An evaluation of the technique of photothermal radiometry for the non-destructive testing and characterisation of plasma-sprayed coatings

Patel, Pravinkumar M.

Award date:
1988

Awarding institution:
University of Bath

TITLE

An Evaluation of the Technique of Photothermal Radiometry for the Non-destructive Testing and Characterisation of Plasma-sprayed Coatings.

Submitted by
Pravinkumar M. Patel BSc, MSc.
for the degree of Doctor of Philosophy
of the University of Bath
September 1988

COPYRIGHT

ProQuest LLC
789 East Eisenhower Parkway
P.O. Box 1346
Ann Arbor, MI 48106-1346

To

Jayna, Anil and Methoon.

ABSTRACT

A review of five photothermal radiometric techniques based on the amplitude or spatial modulation of an incident energy source for materials testing is presented. Measurements are reported demonstrating the potential capability of the periodic heating method for noncontact thickness gauging, subsurface defect detection and characterisation. Effects of coating structure such as surface roughness and porosity on the recorded photothermal signal are also assessed experimentally and theoretically.

Two test systems were evaluated using laser illumination for sample heating. One using a 5 watt argon ion laser and the other, a 0.5 watt GaAlAs laser diode with its emission coupled to a 250 μm diameter optical fibre. In the latter system an ellipsoidal mirror collector was used to enhance the infrared detection efficiency. In the evaluation of these systems a study was undertaken to determine the magnitude of phase angle error with the detection of coherrent infrared noise signals, incident laser power and spot size, sample or detector misalignment, and intrinsic phase noise of the measurement system.

ACKNOWLEDGEMENTS

I wish to thank the technical support staff of the School of the Materials science; in particular Peter Taylor and Ian Turner for the construction of various mounts for holding optical components, test specimens and light tight enclosure. To Dr. S. Gorman for designing and maintaining various electrical 'black boxes' required for this research program and Brain Gosling for his assistance and advice in optical micrography.

I also wish express my deepest gratitude to Drs Darryl P. Almond and Harry Reiter for their encouraging discussions throughout the research program.

CONTENTS

List of Tables

List of Latin symbols

	Definition	Units
b_{ij}	thermal impedance ratio	
c	speed of light in free space	m/s
d	mean free path	m
e	exponential constant	
f	light modulation frequency fractional volume porosity	Hz
h_i	rms roughness	m
i	integer	
j	complex root of minus one	
k	thermal conductivity	W/(m K)
k_m	harmonic mean thermal conductivity	W/(m K)
m	integer	
r	radial distance surface optical reflectivity radius of contact	m
r_g	gaussian beam $1/e^2$ radius	m
t	time	s
u	distance between the mean plane of the rough and flat surfaces	m
x	distance	m
A_c	apparent area of contact	m^2
A_t	true area of contact	m^2
C	Specific heat capacity	J/(Kg K)
D*	Specific Detectivity	$m\ Hz^{-1/2}\ /w$
F	accommodation form factor	
I_o	laser beam intensity	$W\ /\ m^2$
L_i	layer thickness	m
K_c	bulk thermal conductivity of air	W/(m K)

K_g	modified thermal conductivity of air	W/(m K)
M	molecular mass	Kg
N	number of contact spots per unit area	m^{-2}
P	material hardness	N/m^2
P_o	laser power	W
R	coating-substrate thermal wave reflection coefficient	
R'	thermal contact resistance	m^2 K /W
R_m	thermal contact resistance of rough surfaces in contact	m^2 K /W
S	applied stress	N/m^2
T	material temperature	K
	coating-substrate thermal wave transmission coefficient	
$T_m(\lambda)$	infrared optics transmission factor	
Z_1	thermal impedance	$W/(m^2 K)$

List of Greek symbols

α	thermal diffusivity	m^2/s
β	optical absorption coefficient	m^{-1}
δ	electromagnetic skin depth	m
ϵ	emissivity	
η	light to heat conversion factor	
θ_o	infrared collection angle	degree
λ	wavelength of light	m
	thermal wavelength	
μ	thermal diffusion length	m
μ	permeability of metal	
μ_o	permeability of free space	
ρ	material density	Kg m^{-3}
σ	electrical conductivity	$(\Omega m)^{-1}$
	thermal wavevector	m^{-1}

$\overline{\sigma}$	Stefan-Boltzmann constant	W/(m K^2)^2
τ	time constant	s
ω	angular frequency	radian s^{-1}
Γ_t	Thermal wave reflection coefficient	
Ω_{IR}	Solid angle of infrared radiation detection	steradian

Chapter 1

Photothermal Infrared Techniques

CHAPTER 1 PHOTOTHERMAL INFRARED TECHNIQUES

1.1 INTRODUCTION

PLASMA SPRAY COATINGS AND THEIR QUALITY CONTROL

Surface coatings applied by plasma spraying are being increasingly utilised in the power generation and aerospace industries to provide functionally effective surfaces [1-3]. The coating process combines into a single operation the melting, quenching and consolidation stages of materials processing. With plasma spraying the coating process involves the melting of powdered coating material in a plasma flame and the acceleration of the molten material at sonic velocities towards the substrate. On impact with the substrate these particles rapidly deform, quench and solidify on the substrate (or previously solidified coating material). This capability of the technique allows materials to be deposited with compositions independent of thermodynamic limitations, the control of coating microstructure and its physical properties.

Common applications of plasma sprayed coatings include the protection of bare metallic surfaces from wear, erosion, corrosion, oxidation; for thermal or electrical insulation/ conduction and for reclamation of worn components. Coating thicknesses applied range between .1 and 1 mm, and metals, alloys, ceramics, cermets and plastics can be deposited on almost any substrate. The growing applications of plasma sprayed coatings in many high-tech industries has led to increases in the demands for coating quality and suitable control methods for assessing coating

integrity, during both deposition and its service life. Present quality control methods of plasma sprayed coatings include [4]:

a) process control,
b) destructive and
c) non-destructive testing.

The production of high quality deposits with uniform microstructure and coating thickness requires a careful control of the coating material and spraying parameters. Current efforts in guaranteeing reproducible high quality deposits include the development of spraying systems featuring computerised control of spraying parameters and automation of component handling.

Destructive test methods requires the use of coupon samples with the reservation that the test sample may not have the same cross-section nor have been prepared in exactly the same manner as the component. Destructive examination procedures include adhesion (ASTM C633-79) and hardness tests, metallographic examination using optical and scanning electron microscopy.

Apart from dimensional checks the usefulness of non-destructive testing (NDT) methods for monitoring coating quality has yet to be demonstrated with the development and application of a suitable inspection technique(s).

Figures 1.1a-c, summarise respectively, the plasma spray surface coating process, the common coating

materials currently utilised and the principle defects found in these coatings. The abnormal coating conditions include, coating/ substrate, coating/ coating delamination, surface breaking cracks, porosity, surface/ interface and coating thickness variations. The main requirements of the inspection technique may be summarised as follows.

1) Single-sided, non-contactive and non-destructive.
2) Provide defect detection and thickness measurement.
3) Be applicable to a wide range of coating materials and complex shaped components.
4) Offer remote capability and speed in operation.

1.2 REVIEW OF PHOTOTHERMAL NDE TECHNIQUES

During the past decade there has been renewed interest in the application of thermal infrared techniques for materials testing and characterisation. This has made been possible due the commercial availability of stable medium power laser sources, High sensitivity 8-14 μm infrared (IR) detectors capable of detecting a millidegree change in surface temperature, and advances in electronic signal processing equipment.

There are in the United Kingdom six research groups currently exploiting photothermal IR technology for quantitative materials characterisation and non-destructive evaluation. Two independent research teams are at the University of Strathclyde and one at each of the following establishments. University

College London, Harwell NDT research centre, CEGB Marchwood Laser applications centre and the University of Bath.

In the following paragraphs several photothermal IR techniques are reviewed discussing in general their principle of operation, their merits and suitability for inspecting various types of coated components.

Thermal inspection methods are based on the detection of local variation in heat propagation in a sample. The presence of a defect or a thermal impedance change has a disturbing effect on the heat flow passing through the sample. This disturbance is transmitted to the surface, where it appears in the form of a local change in the sample surface temperature. Photothermal radiometry (PTR) is a measurement technique which can monitor these thermal variations through the synchronised detection of emitted thermal radiation following radiative heating. To date, a variety of techniques have been developed on this measurement principle for the non-destructive near surface examination of materials [5-21]. These thermal methods offer several advantages over conventional NDT techniques such as ultrasonics, X-ray radiography and eddy current. They are non-contactive, single-sided and offer remote capability. They allow the inspection of a wide range of materials and complex shaped components and several complementary techniques based on the same detection principle are available.

Applications reported in the open literature include:

a) thickness measurements, defect detection, imaging, thermal property determination and monitoring thermal cycling damage of coatings [6,8,9,22-25]

b) detection and imaging of impact damage, fibre debonding and effective thermal property evaluation of composite polymeric materials [26-28]

c) semi-conducting materials examination for detection of processing defects, imaging of doped regions, determination of carrier electronic properties and bonding defects in soldered joint [29-31]

d) inspection of biological materials [32,33]

e) spectroscopic studies of opaque and translucent materials [34,35].

1.2.1 PHOTOTHERMAL RADIOMETRY AND THERMOGRAPHY

PTR is a dynamic measurement method relying on the active heating (or cooling) of the sample to reveal its internal structure. In the absence of an active thermal stimulus, the technique is more commonly known as thermography or thermal imaging [36]. Thermography is a passive IR inspection method monitoring the thermal emission difference during heat exchange between the sample and its environment to reveal possible internal non-uniformities.

An image obtained by mapping the photothermal signal amplitude is a superposition of an optical image, thermographic image (arising from structures of average temperature and IR emissivity), and an image of thermal structures. This latter piece of information is the most relevant for thermal NDT. In addition, the time

information contained with the photothermal signal can be processed to provide a new signal that is only sensitive to the thermal and geometric parameters of the sample. Hence, a complete description of the samples' subsurface thermal structure may be possible. Finally, table 1.1 summarises the relative merits and non-merits of thermographic and photothermal IR methods.

1.3 DESCRIPTION OF PTR TECHNIQUES

The photothermal effect is the generation and propagation of heat in a sample by the absorption of optical radiation. Heat is generated in the sample through a variety of non-radiative relaxation processes almost instantaneously, typically less than 10^{-10} seconds for conductors and insulators. The depth of heat generation in the sample is determined by the optical absorption coefficient of the sample. With optical illumination on metallic samples light absorption is confined to the surface typically a few tenths of a micrometer. The depth of light absorption can be determined to a first approximation by the electromagnetic skin depth for the sample [37]:

$$\delta = \sqrt{\frac{\lambda}{\pi \sigma c \mu \mu_o}} \qquad (1.1)$$

where λ is the wavelength of the light, c , the speed of light, σ, is the electrical conductivity of the metal, μ and μ_o are permeability of the metal and free space respectively. Using the Drude free electron theory of metals, it can be shown that the fraction of incident power absorbed by a metal is given

approximately by [37]

$$A = 4\sqrt{\frac{\pi c \mu}{\lambda \sigma}} \qquad (1.2)$$

Hence short wavelength light sources (e.g. in the visible and ultra-violet) are more efficient for sample heating as reflection losses are then at a minimum. The difference between the various photothermal techniques arise from the form of sample heating and the IR detection schemes used. Generally lasers and incoherent optical sources are used for sample heating. Heating can be periodic, pulsed, step intensity modulated, spatially modulated or scanned on the sample surface. The heating can also be localised to a point, line or an area on the sample. The thermal detection can also be localised as the heat source and the sampled region can be centralised, partially displaced from or directly opposite the heated region.

The following sections discuss various photothermal infrared methods. Special attention being given to the periodic photothermal technique discussing its instrumentation and methods of signal analysis.

1.3.1 PERIODIC PHOTOTHERMAL HEATING

In figure 1.2 a schematic illustration is presented showing the basic components of a periodic photothermal NDT system. In this technique chopped square wave or sinusoidal continous-wave (CW) optical illumination is used for sample heating followed by lock-in detection of periodic thermal emission to observe thermal variations in the sample.

Almost all the current lasers have been used for

sample heating. However, the Ar^+ ion laser appears to be the most widely used. This laser provides a highly stable CW emission source with which conventional optical components can be used without special selection.

Beam modulation is either by a mechanical chopper or an acousto-optic device. Early experiments with this technique used mechanical choppers which covered a frequency range up to a few kilohertz. Mechanical choppers have the advantages of simplicity and a 100% depth of modulation. Their main disadvantages are phase jitter noise at low modulation frequencies. And an upper limit on the modulation frequency which effectively set the thermal image resolution (see section 2.5).

Acousto-optic modulators are now generally used. They provide a digital control of the modulation frequency over a wide range, 0 to tens MHz and immunity from the phase jitter associated with low frequency modulation from mechanical choppers. The exciting wave form can also be selected (sine or square waves) and the modulation depth can be as high as 90%.

Thermal emission from the sample have been remotely sensed by a variety of IR detectors. Golay cell and pyroelectric ($LiTaO_3$, PVF_2, TGS...) devices in the frequency range less than, 200 Hz. Semiconductor (CMT, InSb, PbSnTe) devices are used for high frequency operations up to 100 KHz [5-9,38].

SIGNAL PROCESSING AND INTERPRETATION

The photothermal signal generated in solid samples

is quite weak. It is therefore necessary to increase the electrical output from an IR sensor by a low noise pre-amplifier. This electronic circuit is already present in most commercially available IR detectors. The output from the detector can then be directly applied to the lock-in amplifier. Using the reference signal from the optical modulation driver, the lock-in amplifier can provide two components of the photothermal signal:

a) the magnitude and phase.
b) the in-phase and quadrature signal.

When only the amplitude and phase of the detected signal is monitored, the phase information of the signal is most useful as it is only related to the thermal and geometric properties of the sample.[1] When the in-phase and quadrature components are recorded, the quadrature is sensitive to subsurface thermal structure and the in-phase component mainly to the surface optical structure.

Another type of signal analysis used with this technique is phase angle adjustment. Here the phase of the reference signal is adjusted to detect selectively the photothermal signal with a specified phase delay. If lock-in detection is done digitally then this latter method of signal analysis enables the user to reconstruct a subsurface thermal image of the sample at any desirable depth from the surface.

1 This is discussed in detail in section 2.4.1

The simplicity of the experimental apparatus and a well developed theory have provided the main driving force for the rapid exploitation of this technique since its demonstration for materials testing by Nordal and Kanstad and Luukkala in 1980 [5]. Rear side [6,23] and displaced detection [7] schemes have also been investigated. An advantage of the former detection scheme is a greater depth of inspection, a few millimetres, limited only by the experimental signal-to-noise ratio. Two disadvantages of this transmission detection method are the requirement of access to the rear surface and a loss in the ability to determine the depth of a subsurface defect. This follows from the fact that the signal changes recorded reflect only a projection of the internal thermal structure [6] in analogy with images obtained by x-ray radiography.

When the heating and IR detection spot on the sample surface are partially displaced, the technique is sensitive to thermal changes parallel to the surface [7] and thus more suitable for detecting surface breaking cracks and thermal property variations along the surface.

A recent development on the above basic technique is the parallel detection of a large number of sample points with an IR video camera and digital phase-sensitive signal processing. Rapid inspection of large component areas is now feasible. Modulation frequencies up to 200 Hz have been demonstrated with this method [39,40]. The upper limitation on the

modulation frequency is determined either by the thermal image digitisation rate or the pixel processing rate of the IR camera detector element.

1.3.2 PULSED PHOTOTHERMAL HEATING

The pulsed photothermal technique is the most widely exploited of all the photothermal methods and has been realised in two commercial instruments; Laser inspect 2000 from Vanzetti Inc. [31] and Thermal wave impedance scanner from Hanford Engineering laboratory [13]. Three schemes of inspection have been developed with pulsed heating: "point" heating with "point" detection, line heating with line IR detection and area heating with area detection by an IR camera.

POINT HEATING WITH POINT INFRARED DETECTION

In this arrangement, figure 1.3a, sample heating is provided by a short pulse N_2, Nd-YAG, or CO_2 laser. The evolving transient thermal emission signal is detected by a fast IR semiconductor detector, (Indium antimonide in the 3- 5 μm band or Cadmium mercury telluride in the 8- 14 μm band). A large bandwidth transient recorder is used for signal recording and averaging over a number of pulses. Measurement times range from a few milliseconds for metals to several seconds for insulators. Common applications reported with this method include the rapid detection of subsurface defects, thermal and optical property determination and automated inspection of soldered joints.

LINE HEATING WITH LINE INFRARED DETECTION

A schematic illustration of this technique is shown

in figure 1.3b. A hot air jet of 5 millisecond pulse duration is used to heat the sample surface. The sample is then moved a short distance and the decaying thermal emission is detected by a line IR scanner at two predetermined time intervals. Sample translation is required to avoid thermal emission interference from the heat source. The IR sensor samples the surface at a rate of 256 lines /second and the digitised output is averaged over a finite time interval to enhance the signal to noise ratio. Large sample areas can be inspected by this technique by continuously stepping and pulse heating the sample. The use of laser heating has yet to be demonstrated with this line scanning technique and measurements have only been reported on thermal spray coatings [13,41-43].

AREA HEATING AND INFRARED CAMERA DETECTION

An IR camera is a versatile thermal radiation detector allowing point, line and area detection of the thermal radiation. In an area sensing mode of operation the camera offers the ability to monitor and record transient thermal diffusion effects in a sample by parallel scanning with good spatial, temporal and temperature resolution. Operating at video-frame rates a thermal scene can be imaged in 20 milliseconds. Two types of thermal imagers have been evaluated for use with this mode of heating: cooled semiconductor and pyroelectric vidicon camera. The latter provides room temperature operation and is a cheaper alternative to the semiconductor camera [26].

An arrangement of this area sensing pulsed thermographic technique is shown in figure 1.3c in a

transmission mode of operation. High energy flash and IR lamps with conventional mirror optics is used to uniformly heat the sample. The transient thermal signal from the sample is then recorded by the camera collecting some 10,000 point measurement on the sample every 20 milliseconds. At the same time the image is recorded on a video tape. The recorded image can then be analysed visually by playing back the images a frame at a time and single lines from the image can be extracted for more quantitative study. Image processing techniques incorporating transient thermal diffusion models can also be readily applied to the thermal images [15-17, 26-28].

1.3.3 STEP PHOTOTHERMAL HEATING

Step intensity modulation offers another variant to transient thermal techniques. Its application to thermal property measurements has shown that low power lamps (rather than pulsed lasers) can be used to step excite the sample with much reduced overall heating of the sample [44,45]. A schematic illustration of a step heating technique using a laser source is shown in figure 1.4 . When measurements times are long, the transient emission can be chopped at a high frequency and recorded by phase sensitive detection. This removes the need of transient recorder to capture the signal. Thickness and thermal resistance measurement on thermal barrier plasma sprayed coating have been reported by Cielo and Dalliare [46] using this technique.

1.3.4 COORDINATE MODULATION PHOTOTHERMAL HEATING

In this technique heating is alternated between two adjacent spots on the sample surface as shown in figure 1.5. Phase sensitive IR detection is then used to monitor the thermal variation between the heated spots. If the sample properties are identical at the heated regions then a null signal will be obtained. Thus making the technique sensitive to small variations in the thermal properties of the sampled region. Letho et al [20] have investigated this technique for thickness measurement of plasma sprayed tungsten carbide on steel. Their results showed that thickness a resolution of 25 μm is possible with this coating system.

1.3.5 SCANNING PHOTOTHERMAL HEATING

By scanning a localised heat source in a raster fashion on a sample surface and detecting the thermal radiation from the heated spot, rapid inspection of large sample area can be made, figure 1.6. This arrangement was widely exploited in the late 1960's using a single element IR detector and external optical scanning to focus the heated spot onto the detector element [47,48]. The modern version of this technique uses the built in optical scanning facilities of an IR camera to sense the changing thermal emission from the sample [49]. Sub-surface defects and fatigue cracks detection has been demonstrated with this technique [47-50]. To maximise contrast from defects an optimum scanning speed need to be predetermined experimentally,

or by numerical modelling. Scanning too rapidly will lead to a reduction in the signal-to-noise, to image blurring and poor resolution.

1.4 SUMMARY OF PTR NDE METHODS

The above photothermal IR techniques operate on a principle similar to ultrasonic pulse-echo materials testing. Subsurface imperfections in a materials are revealed by detection of the reflected thermal wave or pulse (see section 2.2). In opaque materials with pulsed surface heating, the time interval for the delayed signal to appear at the surface is given by L^2/α, where L is the depth of the defect (or interface) and α the thermal diffusivity of the material. This simple relationship shows that long measurement times will be required for low diffusivity materials (i.e. ceramics and polymers) and defects deep in the material. The same inferences also apply to the other thermal methods (periodic and scanned heating) since any thermal pulse can be decomposed into wave components through a Fourier transformation [51].

Table 1.2 summarises the main advantages and disadvantages of all the PTR methods discussed above. The primary advantages of transient methods over periodic pulse techniques are their short measurements times and complete subsurface thermal information in a single heating pulse. Their disadvantages are the requirement of signal processing, numerical modelling and extensive computational support. In contrast, periodic pulse heating techniques offer several important advantages over transient methods.

Phase-sensitive detection removes signal (noise) components that are not at the same frequency as the photothermal signal.

The output from the lock-in amplifier provides directly to the user the signal amplitude and phase angle information.

The phase angle signal is sensitive only to the samples' thermal and geometric parameter.

Thermal diffusion analysis is relatively simple for many NDT problems.

Fine tuning of the test system is possible for optimum performance by adjusting the modulation frequency.

To obtain similar signal information with transient PTR methods it will be necessary to compute the logarithmic derivative of the transient thermal signal.

1.4.1 SELECTION OF PTR TECHNIQUE

The choice of which particular PTR technique to apply will depend on the inspection problem. Some of the parameters that will require consideration may be :

a) the thermal degradation temperature and the thermal properties of the material,
b) the type of measurement required (i.e. thickness gauging, defect detection or imaging),
c) component size and geometry,
d) inspection speed,
e) system portability, and
f) economics.

Figure 1.7 outlines one selection procedure in identifying the most appropriate PTR method for coating thickness measurement. The selection criteria is based on the magnitude of the thermal delay time defined above. For a relatively thin and/ or highly conductive surface coating, the periodic heating technique will

offer excellent signal-to-noise (S/N) ratios and short measurement times due to the high modulation frequencies required for testing (see section 2.4.1). If the coating thickness is large and its thermal conductivity low, a transient excitation PTR system is more suitable as measurement times with a modulated PTR technique can be large, typically several 10's of seconds. In the intermediate cases the selection between the the various PTR techniques will need to be determined experimentally.

The inspection of large components areas requires the application of an area sensitive PTR method, i.e. IR detection with either IR line scanner or IR video camera. The selection of the appropriate PTR technique then essentially follows that for coating thickness measurements except when very thin surface layers are to be inspected. In this case the moving line source PTR technique with synchronised line IR will need to be investigated [49].

Table 1.1: Advantages and disadvantages of thermographic and photothermal radiometric materials testing.

Technique	Advantages	Disadvantages
Thermography	No active heating necessary Large area inspection Complex objects	Surface emissivity variations Weak sensitivity to subsurface defects
Photothermal radiometry	Several techniques available Large area inspection Complex objects Emissivity independent High sensitivity to subsurface defects Quantitative thermal analysis	Sample heating required Laser hazard Accurate thermal diffusion models required for quantitative analysis

Table 1.2: Advantages and disadvantages of PTR NDE techniques.

METHOD	ADVANTAGES	DISADVANTAGES
PERIODIC	Simple test apparatus. High noise rejection. Emissivity independent. Depth profiling, thickness measurement and defect detection. Thermal property evaluation.	High background heating. Depth profiling requires several frequency measurements.
PULSED	Minimum background heating. Fast. Remote capability. Complete subsurface information in a single measurement. Thickness measurement, defect detection and thermal property determination.	Extensive computer support required for signal processing and numerical analysis. Accurate thermal diffusion model(s) needed for quantitative analysis. Signal averaging required to improve signal-to noise ratio.
STEP	As above. Reduced measurement times. Smaller dynamic temperature change.	As above
COORDINATE MODULATION	Simple test apparatus. Sensitive to small changes in thermal properties.	Comparative measurements only. Uniform surface optical properties required.
MOVING SOURCE	Fast. Detection of fatigue cracks and thin films.	Uniform surface optical properties required. Optimum scanning speed needs to be determined for subsurface inspection.

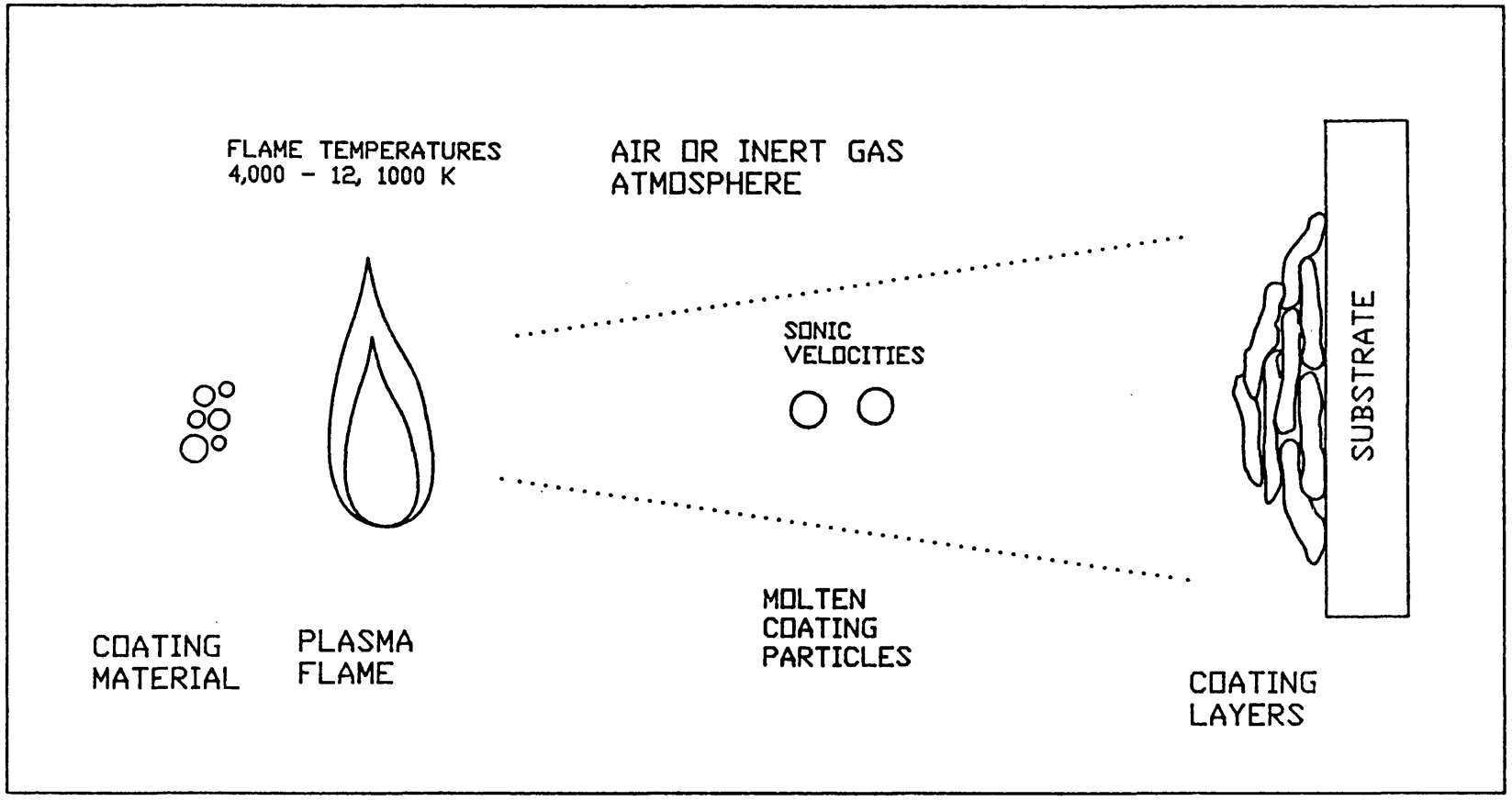

Figure 1a: A schematic illustration of coating deposition by plasma spraying.

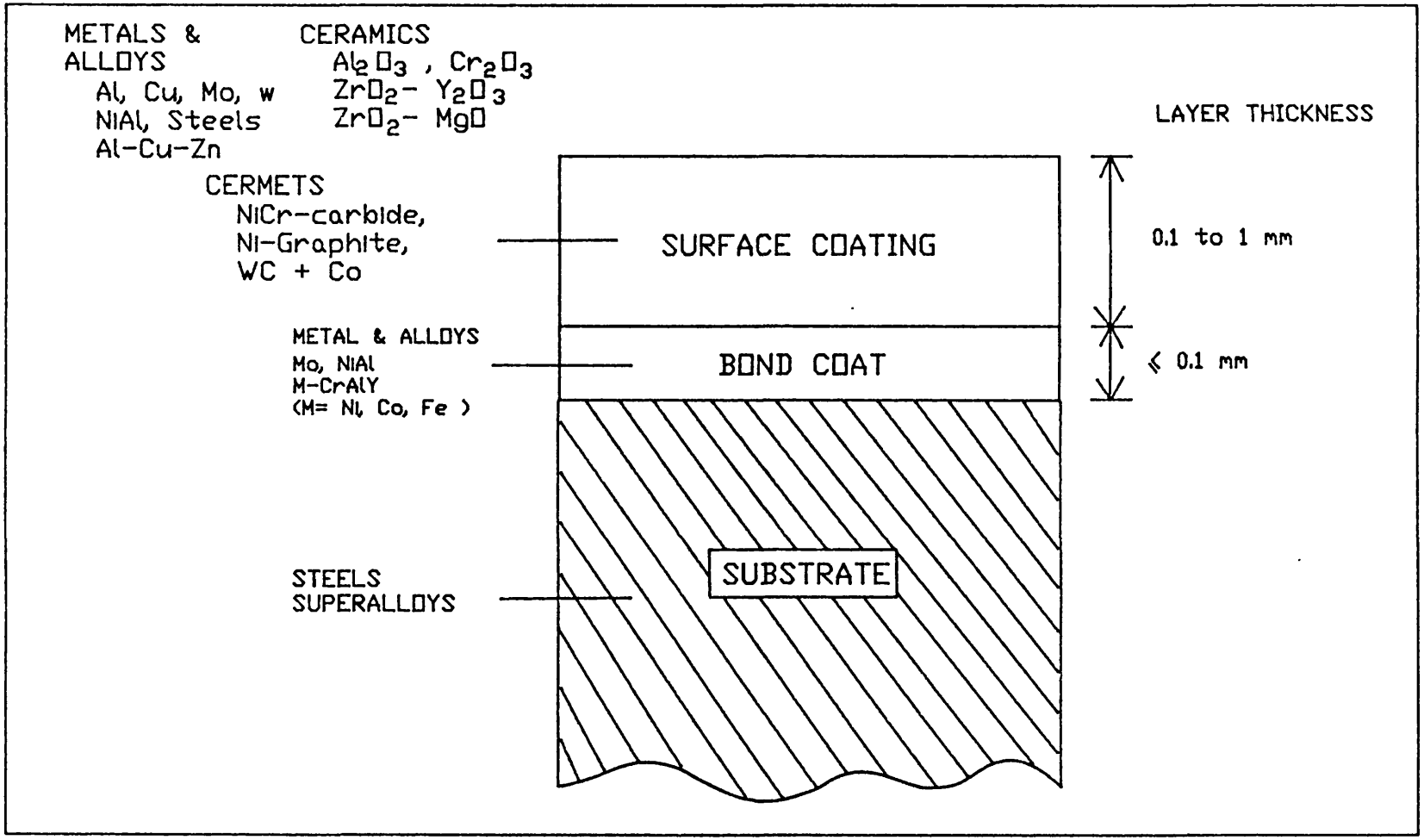

Figure 1b: Frequently used materials and the coating/ substrate system in plasma spraying.

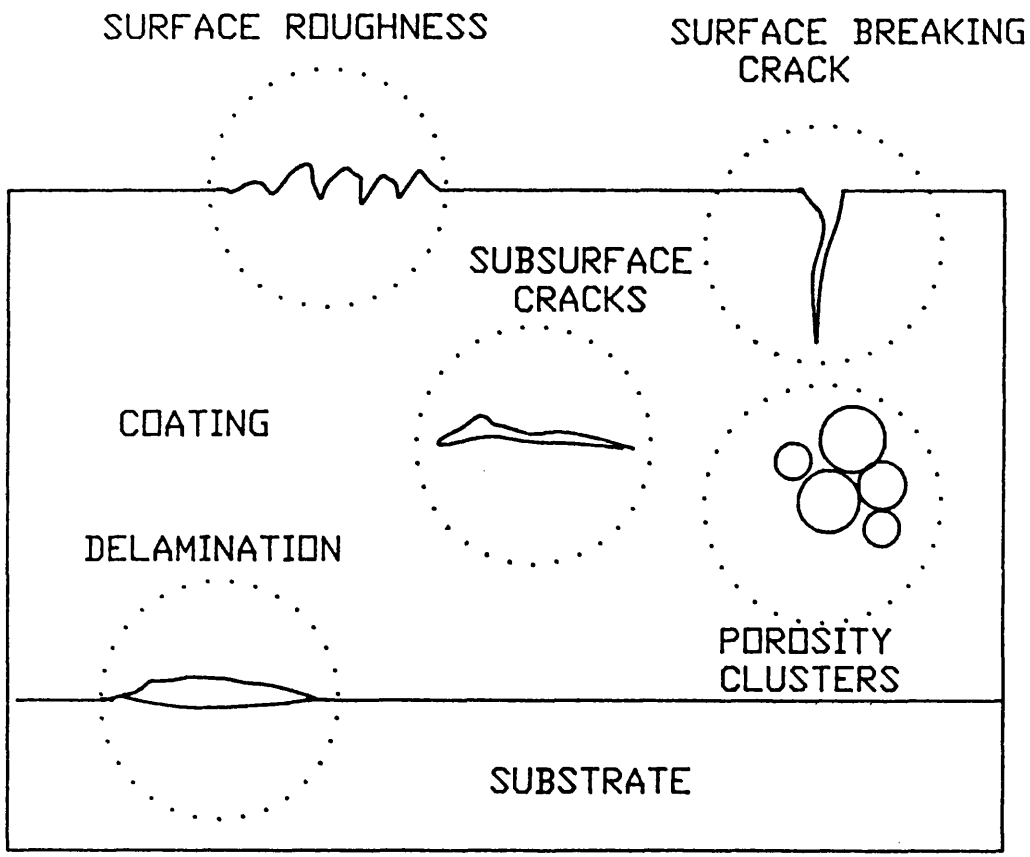

Figure 1c: Some common defects in plasma sprayed coatings.

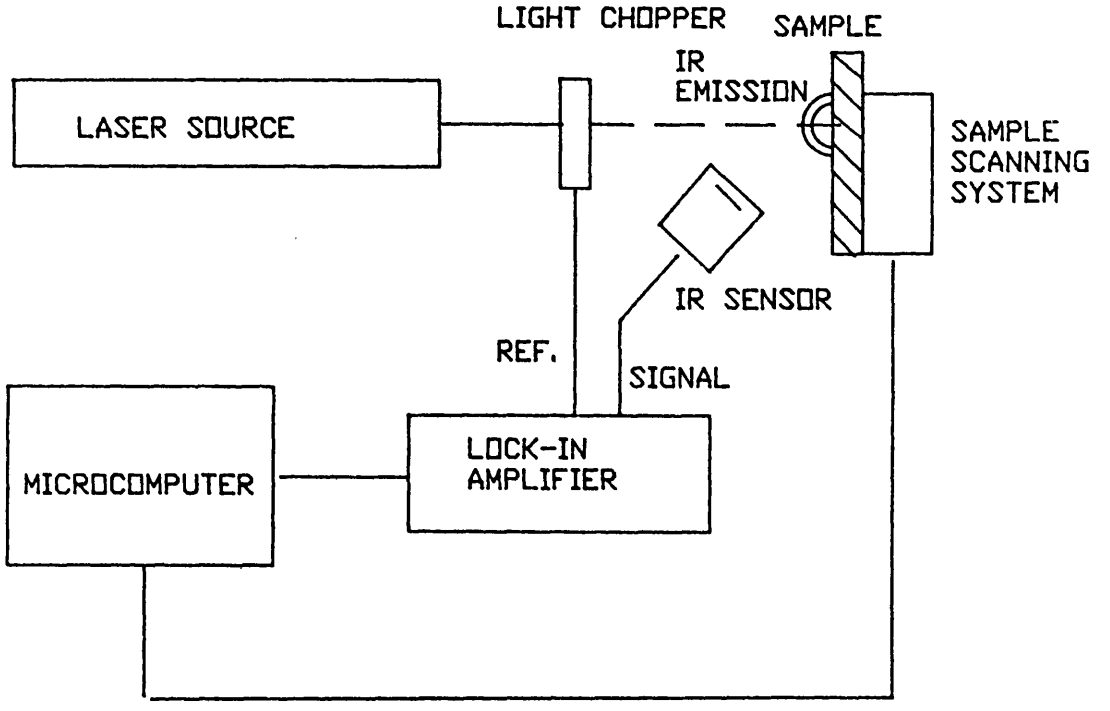

Figure 1.2: A periodic PTR inspection system.

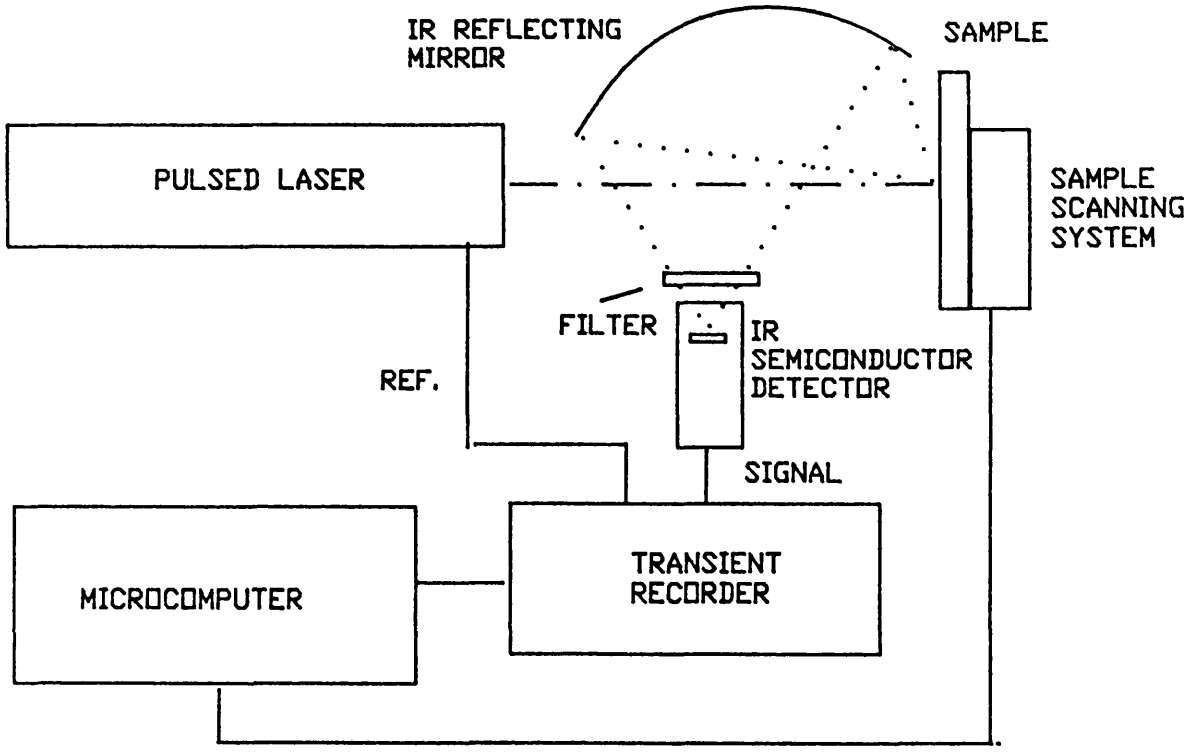

Figure 1.3a: A pulsed PTR instrumentation with spot illumination.

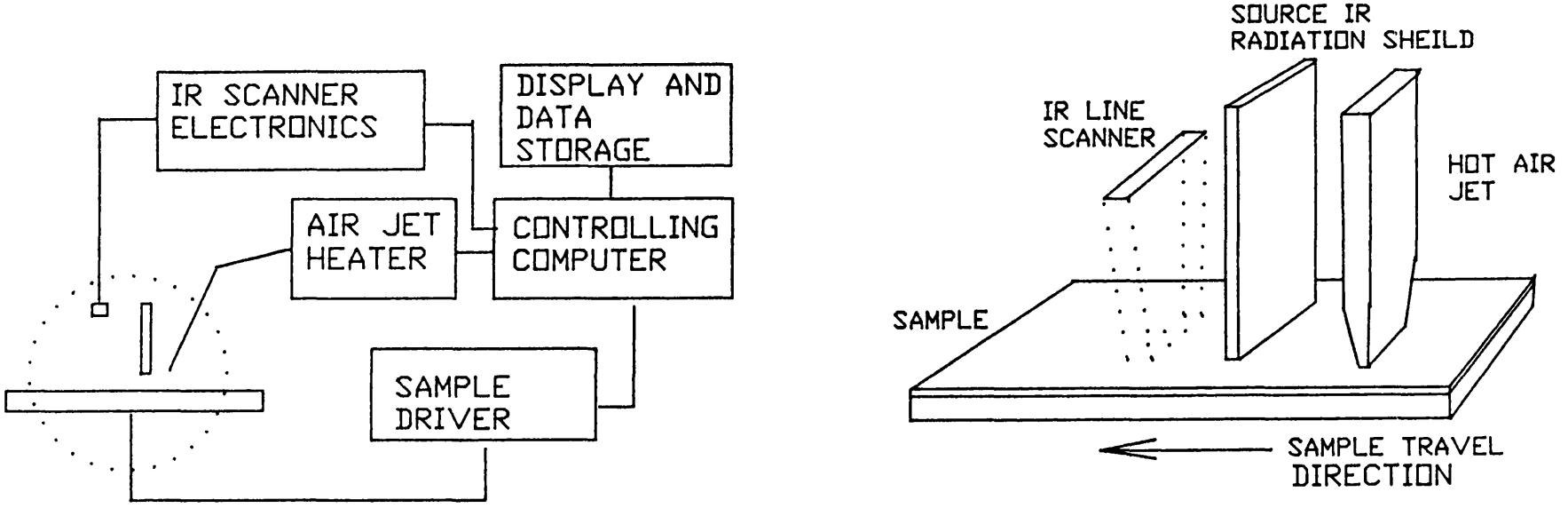

Figure 1.3b: A pulsed PTR instrumentation with line heating.

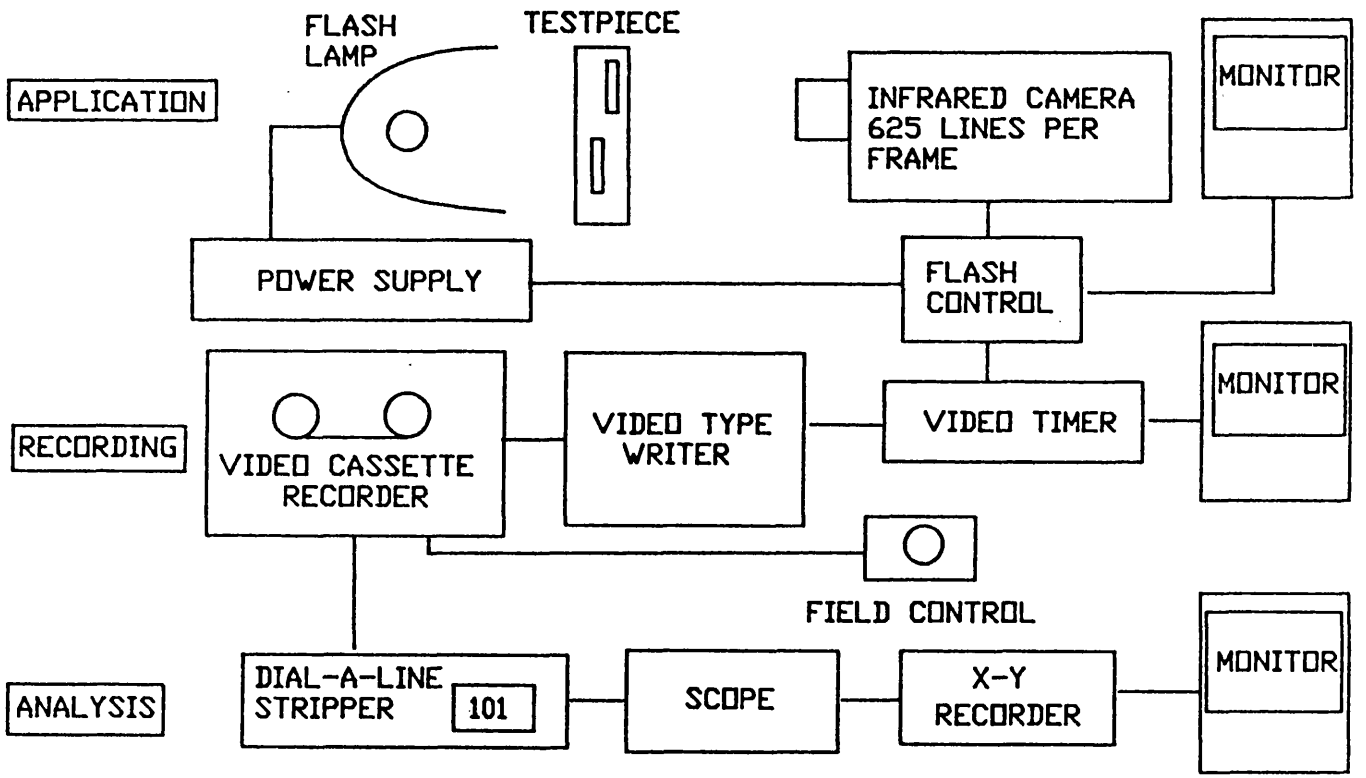

Figure 1.3c: A pulsed PTR transmission set-up with area heating.

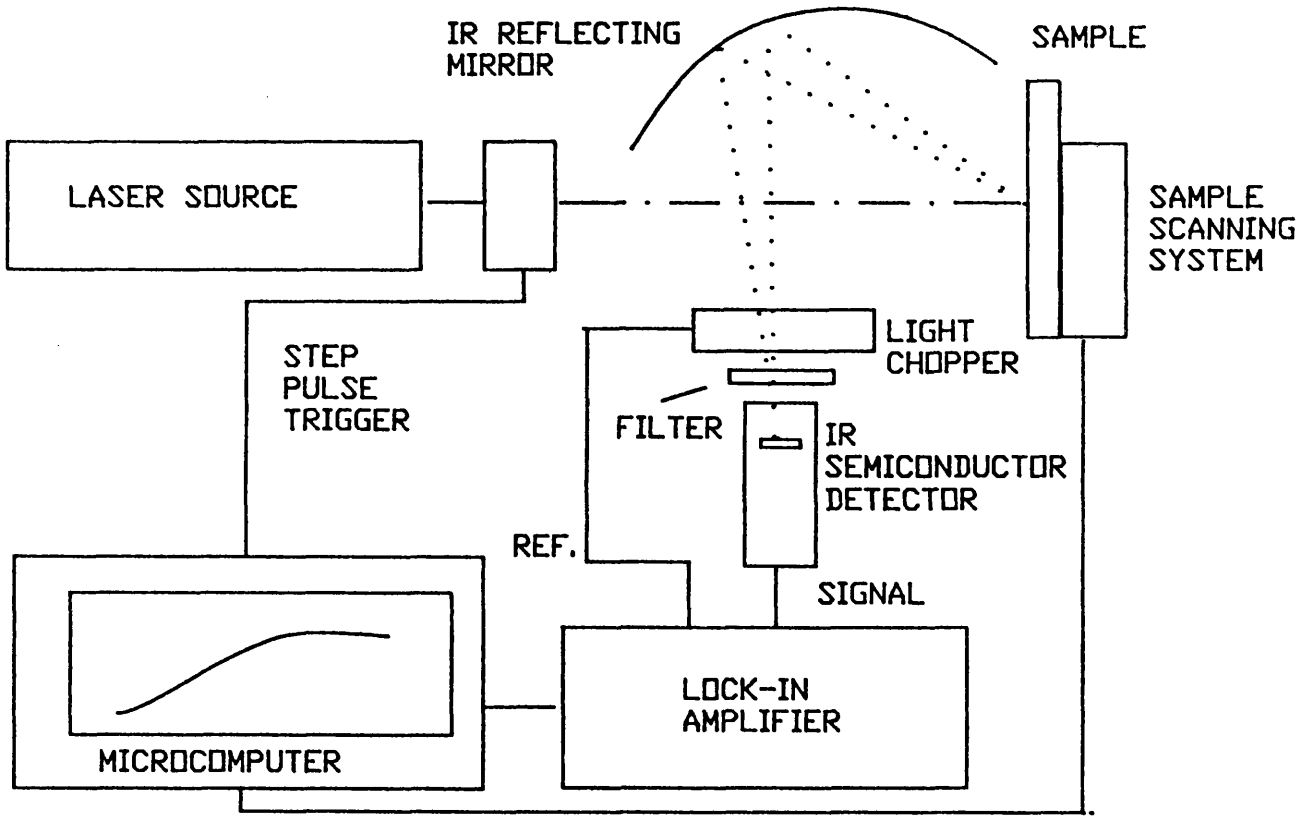

Figure 1.4: A step heating PTR inspection system.

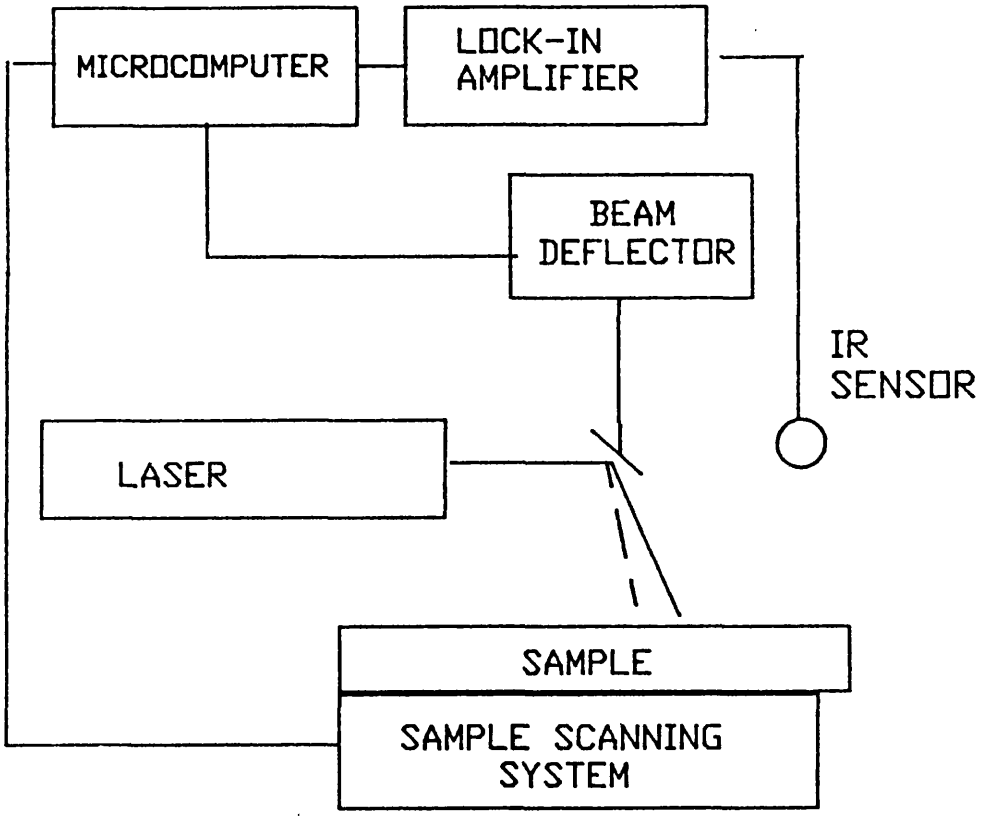

Figure 1.5: A coordinate modulation PTR arrangement.

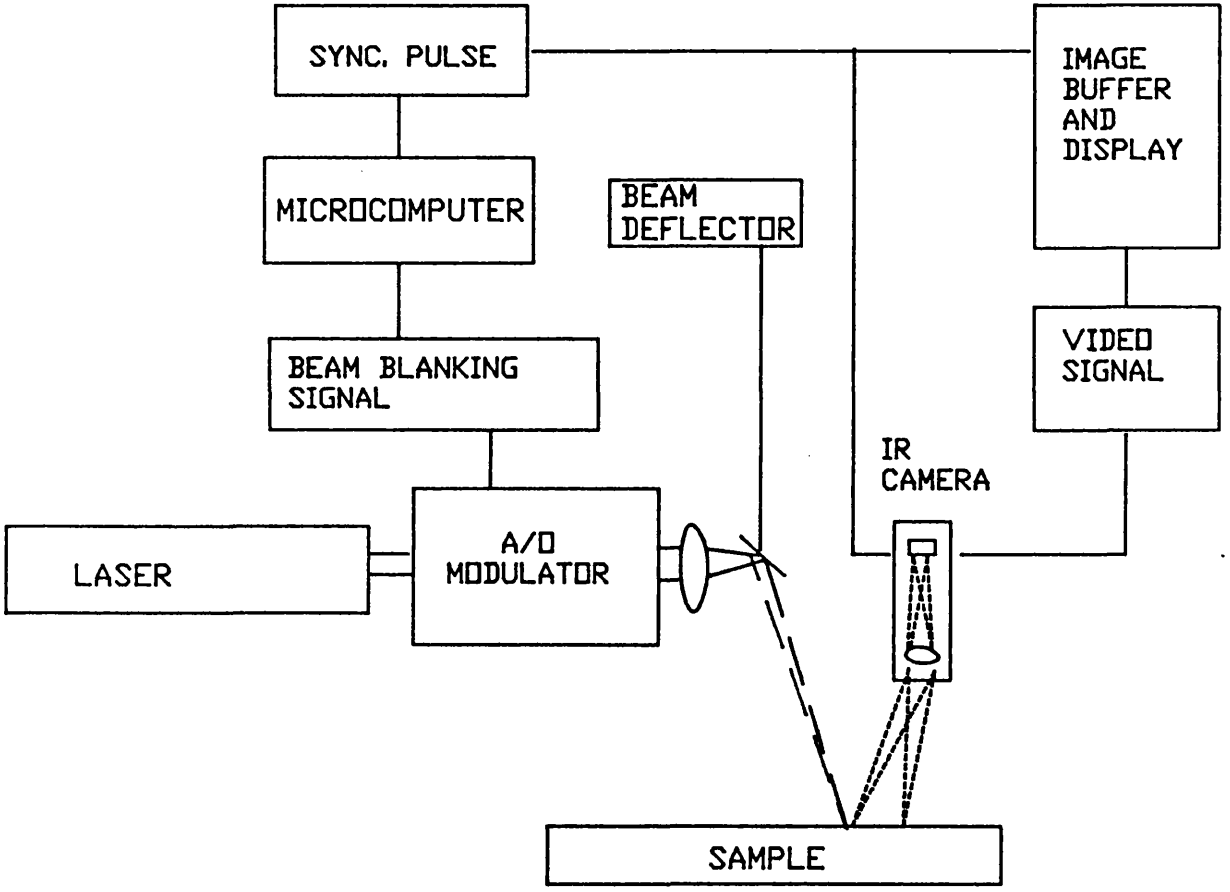

Figure 1.6: A schematic illustration of a moving source PTR inspection system. [49]

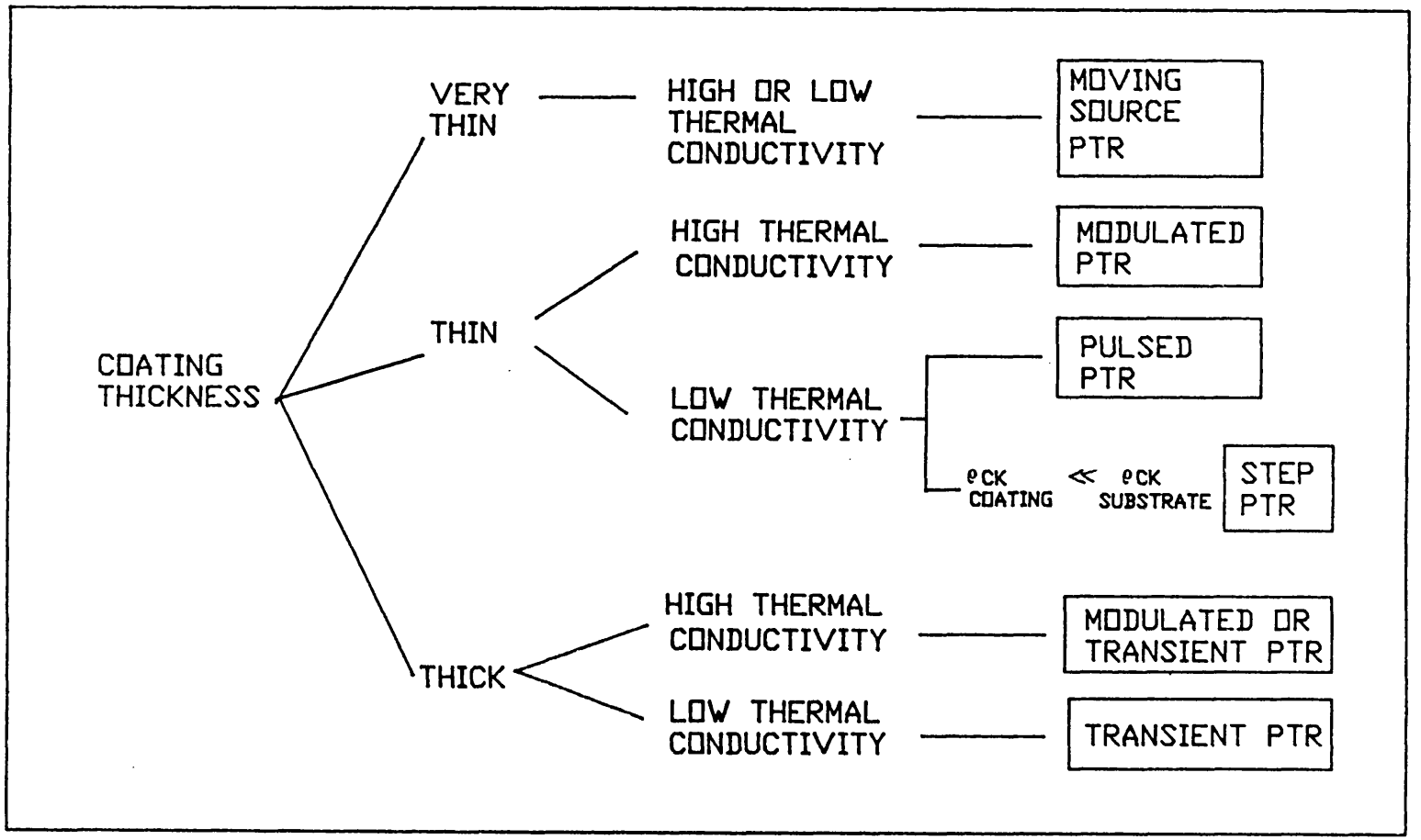

Figure 1.7: A selection guide of the most appropriate PTR inspection technique for thickness measurement.

Chapter 2

Phothermal Radiometric Detection Theory

CHAPTER 2 PHOTOTHERMAL RADIOMETRIC DETECTION THEORY

2.1 INTRODUCTION

The technique of photothermal radiometry involves modulated optical heating of a sample and the detection of emitted thermal infrared (IR) radiation from somewhere on the sample. The increased blackbody thermal emission signal recorded in a photothermal measurement can generally be given through an expression like [52]:

$$Signal \propto S_1 . S_2 . S_3 \quad . \tag{2.1a}$$

S_1, S_2 and S_3 are signal contribution terms determined respectively by the temperature and thermal properties of the sample, IR collection efficiency of the test system and the IR detector sensitivity. These terms can be expressed as follows:

$$S_1 \propto \frac{\partial}{\partial T}\left[\int_{\lambda} \epsilon(\lambda,T) W(\lambda,T) d\lambda\right].\delta T \tag{2.1b}$$

$$S_2 \propto A_{rad}\,\Omega_{IR}\int_{\lambda} T_m(\lambda) d\lambda$$

$$S_3 \propto D^* \quad .$$

Where

T	is the absolute temperature of the sample,
λ	is the emission wavelength,
$\epsilon(\lambda,T)$	is the IR emissivity of the sample[1],
$W(\lambda,T)$	is the blackbody spectral radiant excitance,
δT	is the induced temperature increment,
A_{rad}	is the thermal emission area on the sample,
Ω_{IR}	is the solid angle over which the thermal radiation is collected,

1 Ignoring the directional dependence of surface thermal emission.

$T_m(\lambda)$ is the spectral transmission of the IR collection optics,

D^* is the IR detector sensitivity.

In the following paragraphs a detailed discussion is given of the term S_1 which contains the thermal emission characteristics and the induced surface temperature change of a sample following optical heating. Particular emphasis is given to opaque layered structures harmonically heated by a laser beam. A wave description of heat diffusion in a sample is introduced and some common applications to thermal NDT are examined. Topics discussed include the reflection and transmission of heat at an interface and interference and interferometry with heat waves. A discussion of the terms S_2 and S_3 is provided in chapter 3.

2.1.1 THERMAL EMISSION CHARACTERISTICS

The spectral distribution of surface radiance from a sample varies with its temperature and can be represented explicitly by Planck's radiation function [53]:

$$(2.2) \quad W(T,\lambda) = \frac{2\pi hc^2}{\lambda^5}\left[\frac{1}{\exp(hc/\lambda kT)-1}\right]$$

for an ideal blackbody emitter. h, and k are respectively, the Planck and Boltzmann constant, c the speed of light and T the absolute temperature. The incremental change in the radiance with changes in the sample temperature, corresponding to the derivative of

the Planck's function , is given by the expression:

$$(2.3)\quad \frac{\partial W(T,\lambda)}{\partial T} = \frac{2\pi h^2 c^3}{kT^2\lambda^4}\exp\left(\frac{hc}{\lambda kT}\right)\left[\frac{1}{\exp(hc/\lambda kT)-1}\right]^2$$

In figure 2.1 and 2.2 these functions are plotted for different sample temperatures. Figure 2.2 corresponds to the modulated thermal IR emission signal detected in a photothermal measurement. For samples heated to near ambient temperatures peak thermal emission lies between 9 to 10 μm. Also, at lower wavelengths the thermal emission decreases rapidly and at longer wavelengths the decrease is gradual and nearly independent of temperature. When these functions are integrated across the emission spectrum, the total radiance is proportional to the fourth power of the temperature (Stefan-Boltzmann Law). The incremental change in radiance with temperature is proportional to the third power of the steady state temperature of the sample and directly proportional to δT for a small change in the sample surface temperature:

$$(2.4)\quad \delta W = \epsilon\bar{\sigma}\left[(T_o + T_{dc} + \delta T)^4 - (T_o + T_{dc})^4\right]$$

$$\approx 4\epsilon\bar{\sigma}(T_o + T_{dc})^3\delta T$$

T_∞ is the ambient sample temperature; T_{dc} is the steady state temperature rise of the sample and $\bar{\sigma}$ = 5.67 x10^{-12} W cm $^{-2}$ K^{-4} is the Stefan-Boltzmann constant. The cubic temperature dependence of δW can be exploited to increase the signal-to-noise ratio of the detected signal. However, this will be at the expense of an increased coherent noise signal due to changes

ΔT in the sample's background temperature:

$$\Delta W = \partial \frac{\delta W}{\partial T} \Delta T = 3\delta W \frac{\Delta T}{T} \qquad (2.5)$$

Examination of figure 2.2 shows that the this noise signal will be reduced if IR detection is at long IR wavelengths.

2.1.2 THERMAL WAVES

When a surface is subjected to plane harmonic heating, the equation describing the diffusion of heat into that sample has a wavelike solution for the temperature distribution [54]:

$$T(x,t) = I_o \frac{\mu}{2k} \exp\left(-x/\mu - j\left(x/\mu - \frac{\pi}{4} + \omega t\right)\right). \qquad (2.6)$$

T(x,t) is the temperature rise above the equilibrium ambient temperature, I_o magnitude of the surface heat flux and μ is the thermal diffusion length

$$\mu = \sqrt{\alpha / \pi f} \qquad (2.7)$$

with α = the thermal diffusivity and f the modulation frequency. The thermal diffusivity is equal to

$$\alpha = k / \rho C \qquad (2.8)$$

where k is the thermal conductivity, ρ the density and C the specific heat capacity. Like normal propagating waves, the thermal wave has an oscillatory spatial dependence of the form 'exp(ikx)', with a wavevector given by $1/\mu$. However, unlike normal propagating waves, the thermal wave is also very heavily damped ($\exp(-x/\mu)$) with a damping coefficient $1/\mu$. In one thermal wavelength, $2\pi\mu$, the amplitude of the thermal wave is reduced by a factor $\exp(-2\pi) = 0.0019$. The

thermal diffusion length can range from a few millimetres (mm) at low modulation frequencies to fractions of mm at higher modulation frequencies. Table 2.1 lists the thermal properties and thermal diffusion lengths for various common engineering materials and thermal spray coatings.

The above plane thermal wave equation can also be used to derive the thermal wave reflection and transmission coefficient at a thermal boundary (see appendix 1). For two homogeneous media in perfect thermal contact the reflection and transmission coefficient for normally incident thermal waves are given by the equations [55]:

$$(2.9) \qquad R = \frac{1-b}{1+b} \quad ; \quad T = \frac{2b}{1+b}$$

$$\text{where} \quad b = \sqrt{\frac{(\rho_2 C_2 k_2)}{(\rho_1 C_1 k_1)}}$$

for thermal waves incident from medium one to medium two. As an example, if the thermal impedance mismatch ratio 'b' between two contacting surfaces is a half, then a third of the incident thermal energy is reflected and two-thirds is transmitted.

It is important to note that these thermal wave reflection coefficients are real and independent of the modulation frequency. This is not the case, as will be seen later, when the contact between two media is partial. In this situation these coefficients become complex and frequency dependent.

Equation 2.6 also shows that the surface temperature is inversely proportional to the square root of the

modulation frequency and the phase lags the heating source by 45 degrees. This independence of the surface phase angle from the modulation frequency for a semi-infinite sample can be utilised in normalising experimental phase angle data for quantitative analysis.

2.2 ONE DIMENSIONAL SURFACE TEMPERATURE EXPRESSIONS

When periodically chopped light illuminates an opaque sample the resulting surface temperature distribution assuming one dimensional (1D) heat flow, can be written as a sum of three temperatures [56]:

$$T(x) = T_o + T(x)_{dc} + T(x)_{ac} \qquad (2.10)$$

where T_o is the ambient temperature of the sample, T_{dc} the steady state and T_{ac} the periodic temperature of the sample due to optical heating (see appendix 2). For an opaque semi-infinite sample the ratio of the dc/ac surface temperature can differ by an order of magnitude as shown in the following example for an LC1B plasma spray coating.

Let the coating optical reflectivity be 0.5, optical heat generating efficiency n=1, layer thickness 200 μm, the incident laser power P_o, of 1 watt over an area of .65 mm radius.[2] The steady state surface temperature can then be evaluated form:

$$T_{dc} = \frac{(1-r)}{2}\left(\frac{P_o}{\pi r_g^2}\right)\frac{L_1}{k} = 8.5 \ ^{\circ}C$$

and the periodic surface temperature at a modulation frequency of 81 Hz [3]:

$$T_{ac} = \frac{(1-r)}{2}\left(\frac{P_o}{\pi r_g^2}\right)\frac{1}{k\sigma} = 1.5 \ ^{\circ}C$$

---

2 Laser beam radius corresponds to the Argon ion laser used in the investigations.

3 At this frequency the .2 mm layer will be semi-infinite to the thermal wave.

Table 2.2 summarises the principle one dimensional surface temperature expressions for thermal wave inspection of surface coatings. Rewriting the periodic surface temperature expression for an optically opaque layer on a thick substrate as:

$$(2.11)\quad T_{ac} = \frac{(1-r)I_o}{2k\sigma}\left[\frac{1+\Gamma\exp(-2\sigma L)}{1-\Gamma\exp(-2\sigma L)}\right]$$

$$= \frac{(1-r)I_o}{2k\sigma}\left[1+\frac{2\Gamma\exp(-2\sigma L)}{1-\Gamma\exp(-2\sigma L)}\right]$$

the presence of a surface layer is seen to add a correction term to the temperature that would have been obtained for a semi-infinite layer. The magnitude of the correction term depends on the thermal wave reflection coefficient, Γ, at the coating/ substrate interface and on the thermal thickness (L/μ). Further expansion of this equation shows that the surface temperature is composed of many thermal wave reflections from the coating/ substrate and the coating/ gas interfaces:

$$(2.12)\quad T_{ac} = \frac{(1-r)I_o}{2k\sigma}\left[1+2\sum_{n=1}^{\infty}\Gamma^n\exp(-2n\sigma L)\right]$$

This description of thermal wave propagation in the surface layer (or layered media) is analogous to that of optical interference in thin translucent films. Thus equations 2.11-2.12 physically represent thermal wave interference in a thin optically opaque film [57]. It is this phenomena that allows thermal wave techniques to be utilised as a sensitive interferometric method for non-contact thickness measurements.

2.3 THREE DIMENSIONAL SURFACE TEMPERATURE EXPRESSIONS

As mentioned in chapter 1, laser beams are widely used for optical heating in photothermal NDT. The heated region is very often a small spot on the sample surface and heat diffusion cannot be simply regarded as 1D. The temperature distribution now has an additional degree of freedom. Radial heat diffusion in now possible. The surface temperature of the sample can be separated into three components:

$$/2.13/ \quad T(r,z)=T_o(r,z)+T_{dc}(r,z)+T_{ac}(r,z)$$

where r is the distance from the centre of the heating beam. A number of analytical methods have been developed to solve the three dimensional (3D) thermal diffusion equation with the end result of evaluating the periodic surface temperature by an integral [58], series summation [59,60], or a fast Fourier transform [61]. In table 2.3 the series representation of the complex harmonic surface temperature is given for a semi-infinite opaque substrate and a thin opaque layer on a thick substrate. In both cases it is seen that the 3D surface temperature is composed of 1D surface temperature term and correction term for the radial diffusion of heat. Inspection of the 3D surface temperature term shows that one can readily write down 3D surface temperature expressions by replacing the 1D thermal wavevector, $\sigma = (jw/\alpha)^{1/2}$, with $(\gamma_m^2 + (jw/\alpha))^{1/2}$. One important consequence of this substitution is the increased decay rate of the surface temperature. Figures 2.3a-c summarise the depth decay of a plane thermal wave (2.3a) and the radial and depth

decay of the 3D temperature field (2.3b,c). For a purely 1D heat flow the magnitude of the surface temperature decreases by 1/e in a distance of one thermal diffusion length. The 3D surface temperature decays more rapidly, decaying by 1/e in a distance of $\mu/3$, for the test parameters shown in figure 2.3b.

With localised heating and localised IR detection a further complication is introduced in interpreting the recorded photothermal signal. Figure 2.3d shows the variation of the signal phase with optical spot size and IR detection area for an opaque semi-infinite sample. (It is assumed that the heating and IR detection spot are coincident). The photothermal signal is then computed from an integration of the surface temperature over the extent of the IR detection region. For point IR detection the phase angle is predicted to show a phase advance as the optical spot size is decreased (curve 1). The phase angle approaches the 1D value at optical-spot size/μ ratio >20. Hence, to apply 1D surface temperature expressions to interpret experimental phase angle data the above condition needs to be satisfied. With an increase in the IR sampling region, curves 2-4, the phase advance is reduced and returns to the value expected for 1D heat flow, namely -45 degrees. This additional dependence of the phase angle on the optical spot size and the finite IR detection area presents a difficult problems in interpreting experimental phase angle data quantitatively.

2.4 APPLICATION TO THERMAL SPRAY COATINGS

In the following sections the thermal wave response from optically opaque thermal spray coatings is examined. It is assumed that the surface coating(s) and the substrate have uniform thermal properties and 1D heat flow conditions apply. Signal variations under 3D heat diffusion are also considered. Coating parameters examined include: variations in coating thickness, thermal properties, surface roughness and subsurface defects.

2.4.1 COATING ON A SUBSTRATE

The effects on the surface temperature amplitude and phase angle from a thin opaque coating on a semi-infinite substrate are shown normalised against the thermal thickness, L/μ, and for different coating/substrate thermal wave reflection coefficients in figures 2.4a and b. The normalisation is with respect to the complex surface temperature from a semi-infinite coating. These two figures represent universal diagrams that can be used to predict the variations of the photothermal signal amplitude and phase from any combination of an opaque coating on a substrate when heat diffusion is 1D. The main elements of these amplitude and phase diagrams are summarised below.

1) The larger the differences between the thermal effusivity values of the coating and the substrate (hence a large thermal wave reflection coefficient magnitude) the greater are the changes in the amplitude and phase of the photothermal signal.

2) For a given coating/ substrate reflection coefficient changes in the coating thickness generate the locus specified for the coating/ substrate system, see figure 2.5a.

3) Any variation in the thermal properties of the coating and /or the substrate will alter the coating/ substrate thermal wave reflection coefficient to a different value thus causing the phase angle to shift to a new reflection coefficient locus, see figure 2.5b.

4) Phase angle measurements have the advantages over amplitude recording of greater depth sensing, up to 1.5x thermal diffusion length, and being unaffected by variations in the surface optical properties, absorptivity and emissivity, of the sample. The latter point can be seen explicitly by writing the argument of equation 2.11 [57] :

$$(2.14) \qquad \Delta\phi = \tan^{-1}\left[\frac{-2\Gamma\exp(-2L/\mu)\sin(2L/\mu)}{1-\Gamma^2\exp(-4L/\mu)}\right]$$

or qualitatively through the phasor diagrams of figure 2.6

Since thermal wave interference effects can only be observed up to 1.5 times the thermal diffusion length[4], the test frequency for inspection can as a first approximation be determined by setting:

$$(2.15) \qquad L/\mu = 1 \quad \Rightarrow \quad f = \frac{\alpha}{\pi L^2}$$

For a 250 μm layer of Al_2O_3, LC1B, ZrO_2-Y_2O_3, the test frequencies are found to be 11.1, 6.4 and 1.3 Hz respectively. In general a low modulation frequency is required for inspecting large coating thicknesses or low thermal diffusivity coatings.

Figure 2.7 shows the theoretical phase angle

4 For thermal wave generation and detection at the sample surface.

variation of the surface temperature when heat diffusion in the sample is three dimensional. The surface coating is LC1B and the substrate 316 stainless steel. As noted earlier, when the laser beam diameter is small compared to the thermal diffusion length, deviations from the 1D phase locus occurs, the magnitude of which depends on the relative ratios of the above two dimensions and IR detection area [58,62]. For laser beam diameters greater than 500 μm, the phase curves generated from the 3D and 1D surface temperature equations coincide. In general, to apply 1D thermal diffusion analysis in PTR NDT a laser beam diameter of 20 times the layer thickness is required when point IR detection used. This requirement can be relaxed, at the expense of reduced image resolution, if the IR detection spot on the sample surface is increased.

2.4.2 COATING POROSITY EFFECTS

Local variations in the coating thermal properties due to porosity can be modelled by replacing the bulk coating thermal parameters with those corrected for porosity. For spherical pores the correction terms are [63]:

$$(2.16) \quad \rho C \approx (1-f)\rho C_o \,, \qquad k \approx \frac{(1-f)}{(1+0.5f)} k_o$$

From these relationships it is seen that the coating thermal effusivity changes more rapidly with increasing porosity than the sample's thermal diffusivity:

$$(2.17) \quad \rho C k \approx \frac{(1-f)^2}{(1+0.5f)} (\rho C k)_o$$

where f is the volume porosity fraction and suffix o refers to the bulk thermal properties. In figure 2.8 a plot of the normalised phase angle variation against square root frequency for a 200 μm LC1B coating on 316 stainless steel sample is presented with different porosity fractions. With increasing coating porosity, the phase angle is predicted to increase with respect to the "zero" porosity coating value. This phase advance is due to the increase in the thermal impedance mismatch and hence the thermal wave reflection coefficient between the coating and substrate (see equation 2.9).

2.4.3 SURFACE ROUGHNESS

Thermal spray coatings have inherently rough as-sprayed surfaces. Surface roughness can range up to 25 μm rms, almost 10% of the coating thickness used in many applications. In addition to the surface roughness the coating/ substrate interface is irregular due to the initial roughing of the substrate to promote coating adhesion. To model thermal wave propagation in such a structure it is assumed that the 'rough' surfaces of the coating can be replaced by a discrete layer of different thermal properties, as shown in figure 2.9. The surface temperature of such a layered sample, where the surface layer is optically opaque, can be evaluated by applying the Ospal-Rosencwaig depth profiling theory [64]:

$$T_{ac} = \frac{(1-r)\eta I_o}{Z_1^{in}} \qquad (2.18)$$

$$Z_i^{in} = Z_i\left[\frac{Z_{n+1}^{in} + Z_n \tanh u_n}{Z_n + Z_{n+1}^{in} \tanh u_n}\right]$$

$$Z_i = k_i\sigma_i \qquad u_i = \sigma_i L_i$$

where layer n is the number of surface layers and the uppermost layer is number 1. Z_i are the thermal input impendances.

Consider first the effects of a thermal conductivity variation in a coating changing step wise from a value of 11 at the substrate to a value of 1 at the surface. Let the coating thickness be 100 μm. Figure 2.10a and b show the changes in signal amplitude and phase angle with root frequency of a 1, 2, 4, and 8 layer coating structure. The figure shows that with increased layers and a more gradual thermal conductivity change the thermal wave interference is more 'diffused' in comparison to the one layer thermal structure.

The thermal wave interference pattern for a modelled surface roughness shown in figure 2.9 is shown in figures 2.11a-b for different thermal properties and surface roughness thickness. The phase plots illustrated in these figures are normalised to a coating thickness of 100 μm. From these figures the following observations can be summarised.

1) With increasing frequency the thermal wave interference effects within the surface layer become increasingly apparent as shown by the phase peaks in these figures. Two interference

peaks are seen, the first from the effective thickness of the whole coating and secondly from the surface roughness layer.

2) With decreasing thermal conductivity of the surface layer from a bulk value of 4.4 to 2.2 W /m K, the thermal wave interference peaks are more pronounced due to increasing difference in the layer/ substrate thermal effusivity.

3) Increasing the thickness of the surface roughness layer the thermal wave interference peak shifts to a lower frequency. The magnitude of the interference peak remains unchanged.

2.4.4 COATING/ SUBSTRATE INTERFACE DEFECTS

Subsurface defects in a coated component fall in either one of the following two categories. The defect can be a localised region of complete separation or consists of regions in partial contact [65,66]. In both cases, the complex surface temperature , see table 2.2, take the same form as equation 2.11 but with Γ replaced respectively with:

$$(2.19) \qquad \Gamma = \frac{\Gamma_1 + \Gamma_2 e^{-2\sigma_2 L_2}}{1 + \Gamma_1 \Gamma_2 e^{-2\sigma_2 L_2}}$$

where

$$(2.20) \qquad \Gamma_1 = \frac{1 - b_1}{1 + b_1} \qquad \text{and} \qquad \Gamma_2 = \frac{1 - b_2}{1 + b_2}$$

for the air gap model, and

$$(2.21) \qquad \Gamma = \frac{1 - b_1 + R' k_2 \sigma_2}{1 + b_1 + R' k_2 \sigma_2}$$

for the contact resistance model.

In figure 2.12 the phase variation of T_{sc} with root frequency is presented for the above two defects in 316

stainless steel 0.5mm below the surface for a range of air gap thicknesses[5] and thermal contact resistances. The figure shows a characteristic phase locus for both defect types. At low modulation frequencies the phase angle shows an advance with respect to the defect free phase curve. With increasing frequency this phase advance turns into a phase lag. These theoretical curves also predict the frequency at which a defect becomes undetectable.

The similarity of the thermal wave phase for both defect models can be seen explicitly by expanding the reflection coefficient for low and high frequency. At low modulation frequencies, the thermal wave vectors σ_1 and σ_2 are both small and Γ reduces to:

$$(2.22) \quad \Gamma \approx \frac{2\Gamma_1 \sigma_2 L_2}{(1-\Gamma_1^2)} \qquad i.e \quad \Gamma \propto \sigma_2 \propto \sqrt{\omega}$$

for the air gap model, and

$$(2.23) \quad \Gamma \approx \frac{Rk_1\sigma_1}{2} \qquad i.e \quad \Gamma \propto \sigma_1 \propto \sqrt{\omega}$$

for the thermal contact resistance model. At high frequencies both expressions for Γ tend to unity and are also frequency independent.

2.4.5 DEFECT DETECTION SENSITIVITY

Figure 2.13 and 2.14 plot the phase difference (phase angle at the defect minus the phase at a defect free region) with square root frequency for an air-gap type defect in coated or bulk materials. The bulk

---

5 including gas thermal conductivity correction at small air gap thickness, see below.

materials chosen are aluminium and epoxy resin as they have an order of magnitude difference in the thermal effusivity with respect to 316 stainless steel, the substrate material in the coated situation. The coated structures consist of a 0.5mm surface layer of aluminium, or LC1B or Yttria stabilised zirconia on 316 stainless steel.

Considering first the air gap defect plots of figure 2.12 and 2.13, when the air gap thickness, L_2, approaches the mean free path of the air molecules ,d , a correction for the gas thermal conductivity must be made. In appendix 3 the gas conductivity correction factor

$$K_g = K_0 / \left(1 + \frac{F d}{L_2} \right) \qquad (2.24)$$

is derived. d and F are taken to be 0.15 μm and 3 respectively (the accommodation factor implicit in F is taken to be 0.5 for both surfaces). In addition to the above discussion on the defect phase locus there are three other main points to note.

1) Air gap defects embedded in high thermal effusivity materials (e.g. aluminium) will be more readily detected than similar sized defects in low thermal effusivity materials. This is due the greater difference in the thermal effusivity between the defect and host material.

2) Contrast between defects of different thicknesses diminishes in high diffusivity material due the rapid approach of the reflection coefficient to unity (or the sample/ backing reflection coefficient) with increasing defect thickness (see equation 2.19).

3) Estimation of defect thickness become more difficult in high effusivity materials due to contrast saturation.

2.4.6 THERMAL CONTACT RESISTANCE

In the phase curves presented in figure 2.12 arbitrary values of the thermal contact resistances between the coating and substrate were used to illustrate the phase angle variation at partially contacting interfaces. In this section a detailed analysis is presented for the calculation of thermal contact resistances values at a rough contacting interface and its application to thermal wave NDT of contacting surfaces [67].

The thermal contact resistance between rough surfaces in contact can be related to the true contact area by applying a statistical description to the surface topography [68]. In the following analysis certain assumptions are made:

i) the thermal contact resistance at a contacting surface may be divided into two components;

a) the thermal resistance due to contact between surface asperities (the constriction resistance), R_m, and

b) the thermal resistance due to the trapped fluid (gas) layer between the mating surface, R_g.

ii) Both R_m and R_g are independent of each other and that the total resistance of the interface is given by;-

(2.25) $$\left(\frac{1}{R}\right)=\left(\frac{1}{R_m}\right)+\left(\frac{1}{R_g}\right)$$

iii) The contact topography of the rough surface follows the plastic contact theory. This theory assumes that when two rough surfaces (rms h_1 and h_2) are pressed into contact, the surface deformation can be modelled as being that of a rigid flat plane onto a surface having a combined roughness $h_c=(h_1^2+h_2^2)^{1/2}$, see figure 2.15. Further, the asperities of the rough surface deform plastically with increasing load and that at any load, the true contact compromises a large number of equi-area circular contacts of radius r.

For a contact surface formed between a rigid flat plane and a rough surface having a normal distribution of conical asperities, the thermal resistance R_m can be obtained by applying the relationships [69] :-

$$(2.26) \qquad \left(\frac{A_t}{A_o}\right)=\left(\frac{S}{P_m}\right)=N\pi r^2$$

$$(2.27) \qquad r=\left(\frac{2}{\pi}\right)\left(\frac{h_c}{u}\right)(3.48h_c+4.69)$$

$$(2.28) \qquad R_m=\frac{1}{(2Nrk_m)}$$

where

A_t is the real area of contact,

A_o is the apparent area of contact,

S is the applied stress,

P_m is the hardness of the deforming material,

N is the number of the contact spots per unit area,

u is the distance between the mean plane of the rough surface and the perfectly flat surface,

k_m is the harmonic mean thermal conductivity.

The thermal resistance, R_g, can as a first approximation be written as :

$$R_g = h_c / k_g \qquad (2.29)$$

and the corresponding change in the magnitude of the thermal wave reflection coefficient , Γ, may be evaluated from equation 2.20 assuming one dimensional heat flow.

In figures 2.16a and b, the variation of the thermal contact resistance, for contact spots in vacuum and air, against the normalised contact area (A_c/A_m) are plotted using surface roughness values of 1 and 10 μm rms and harmonic mean thermal conductivity of 64 and 1 W/m K. These figures show that the thermal contact resistance decreases rapidly with increasing contact area ratio. The thermal contact resistance is lower for contact with smooth surfaces and materials with high thermal conductivity. Air present between the contacting surfaces also reduces the thermal resistance of the joint; the overall reduction being dependant on the spot thermal resistance, R_m.

Figure 2.17a and b show the normalised phase angle variation with normalised depth (depth /thermal diffusion length) for different fractional contact area in mild steel and opaque zirconia samples - assuming thermal waves being generated and detected at the surface. The surface roughness of the contacting faces for these two plots is 1 μm rms. For an experimental phase angle noise of 1 degree, it is seen from the plots that fractional contact areas up to 0.3

can be readily detected by thermal waves for these samples. It is also seen from figure 2.17b that the presence of air between the contact surface of low conductivity material reduces the detectability of this interface.

To compare the sensitivity of thermal and ultrasonic waves to contacting surfaces we assume that for comparable resolution between the two techniques that the thermal diffusion length equals the ultrasonic wave length. This allows the determination of the appropriate thermal wave test frequency. Next it is assumed that suitable noise level be set to the detected signal; 1 degree phase angle noise for thermal waves and a 1 dB signal change for ultrasonics. Figure 2.18 shows the variation of the ultrasonic reflection coefficient magnitude, (computed from equation 19 in [69]), against the normalised contact area for a mild steel sample with a rms interface roughness 1 μm and 10 MHz. ultrasonic wave. In a through transmission ultrasonic test a 1 dB signal change corresponds to detecting a contact area ratio of about 0.1. This value is slightly less then the contact area ratio predicted for thermal waves of 0.3.

2.5 RESOLUTION AND DEFINITION OF SUBSURFACE STRUCTURE

The parameters which determine the resolution in modulated photothermal radiometry are:

a) the optical heating and IR detection spot sizes,
b) the depth and geometry of the subsurface structure and,
c) the modulation frequency.

Resolution of nearby structures is improved as the optical heating and IR detection spot sizes are made smaller then the subsurface structure. With source localisation there will be limited interaction of scattered thermal waves from neighbouring structures. Inglehart et al. [70] have shown that for optically opaque samples image resolution is independent of the modulation frequency, (i.e. thermal wavelength) for subsurface thermal structures very close to the surface. In this extreme near-field limit the image resolution is then determined by the depth of the scatterer. The explanation for this is due to the fact that there is very little thermal wave scattering towards the surface. Only when the source approaches a lateral distance approximately equal to the depth, is there appreciable scattering in this direction [71]. Since the optical wavelength ultimately determines the minimum optical spot size, the resolution in PTR is limited by the optical wavelength rather than the IR focal spot.

When the subsurface defect is far from the surface but within the thermal diffusion length, the lateral resolution is determined by the thermal diffusion length assuming that both the heated and sensing spot are much smaller then this length. Image width in this near-field limit will be dependent on the modulation frequency and defect geometry [72-74]. The observed image width will be larger then the actual defect size due to thermal wave diffraction and good correlation of the observed image width will only be obtained at high

frequencies where image blurring by thermal wave diffraction is reduced [75]. Finally, if the optical spot size is much larger than the thermal diffusion length the lateral resolution is determined by optical spot size. The depth resolution will still be set by the thermal diffusion length. Figure 2.19 provides a summary of the various resolution limits for thermal wave NDT. Besides the above parameters, resolution can also be limited by engineering details of the inspection system. In particular the step size of the sample/ optical beam scanning system, focusing lens imperfections and finite IR detection spot size.

2.6 SUMMARY

A detailed account of the theory for photothermal radiometric detection and NDT has been given above. The thermal emission characteristics, thermal wave propagation and interaction with the subsurface thermal microstructure have been discussed in relation to surface coating inspection. The variables dictating the choice of modulation frequency for thickness measurements and defect detection have been identified. Expected deviations from the simple one dimensional theory due to heat diffusion in three dimensions have also been discussed. In the following chapters the predictions of the above theory are compared with experimental results.

Table 2.1: Thermal properties of some common materials and plasma-sprayed coatings.

Material	Density	Specific heat capacity	Thermal conductivity	Thermal diffusivity x 10^{-6}	Thermal effusivity x 10^{6}	Thermal diffusion length (in μm)		
	Kg /m^3	J/Kg K	W/m K	m^2 /s	(J/ m^2 K) ^{2} s	1 Hz	16 Hz	64 Hz
Aluminium	2702	903	237	97.1	578.26	5560	1390	695
Mild steel	7850	580	63.6	16.5	298.60	2292	573	287
316 Stainless steel	8238	468	13.4	3.48	51.66	1052	263	131
Titanium	4500	522	21.9	9.32	51.44	1722	430	215
Germanium	5360	322	59.9	34.7	103.40	3323	831	415
Silicon	2330	712	148.0	89.2	242.36	5328	1332	666
Ploycrystal-line Alumina	3970	765	36.0	11.9	109.33	1946	487	243
High density Graphite	1940	630	150	123	183.33	6257	1564	782
Epoxy Resin	1250	1200	0.20	0.13	0.30	203	51	25
Air	1	1005	0.025	24.9	0.000025	2813	704	352
		PLASMA	SPRAYED	COATINGS				
- Al_2O_3	3540		6.35	2.18	18.58	833	208	104
ZrO_2	5320	470	1.3	0.52	3.25	407	102	51
ZrO_2-8 wt% Y_2O_3	5670	491	0.72	0.26	1.88	288	72	36
ZrO_2-Cr_2O_3	5410	475	1.40	0.55	3.56	418	105	52
Ni-Cr Carbide (LC1B)	6400	550	4.4	1.26	15.36	633	158	79
WC+12 wt% Co	12500	217.7	9.20	3	25.03	977	244	122
NiCrAlY	6980	410	5.77	2.02	16.51	802	200	100
NiAl			18.4	4.6	73.6	1210	302	151

Table 2.2: One dimensional surface temperature expressions for thermal wave NDT of opaque surface coatings.

Semi-infinite solid.	$\dfrac{\eta(1-r)I_o}{2k\sigma}$
Thin coating on a semi-infinite substrate.	$\dfrac{\eta(1-r)I_o}{2k_1\sigma_1}\left[\dfrac{1+\Gamma\exp(-2\sigma_1 L_1)}{1-\Gamma\exp(-2\sigma_1 L_1)}\right]$ $\Gamma=\dfrac{1-b_1}{1+b_1};\qquad b_1=\dfrac{k_2\sigma_2}{k_1\sigma_1}$
Air-gap defect at coating / substrate interface.	Replace Γ above with: $\Gamma=\dfrac{\Gamma_1+\Gamma_2\exp(-2\sigma_2 L_2)}{1+\Gamma_1\Gamma_2\exp(-2\sigma_2 L_2)}$ $\Gamma_2=\dfrac{1-b_2}{1+b_2};\qquad b_2=\dfrac{k_3\sigma_3}{k_2\sigma_2}$
Interface contact resistance.	Replace Γ above with: $\Gamma=\dfrac{1-b_1+Rk_2\sigma_2}{1+b_1+Rk_2\sigma_2}$

Table 2.3: Series summation representation of the three dimensional surface temperature distribution with Gaussian beam illumination.

General term	$\theta(r) = \sum_{m=0}^{\infty} T_m \cdot S_m \cdot J_0(\gamma_m r)$
T_m S_m	Thermal wave generation term. Source illumination term. $I(r) = I_o \exp(-2r^2/r_g^2)$ $S_m = \frac{I_o}{2J_o^2(\gamma_m r_c)}\left(\frac{r_g}{r_c}\right)^2 \exp(-\gamma_m^2 r_g^2/8)$
γ_m r_c J_o, J_1	Given by $J_1(\gamma_m r_c) = 0$ Radius on sample at which heat flux is zero. Zero and first order Bessel functions respectively.
Opaque Semi-infinite solid	$T_m = \frac{1}{2k\sigma(m)}$ $\theta(r) = \frac{I_o}{2}\left(\frac{r_g}{r_c}\right)^2 \sum_{m=0}^{\infty} \frac{C_m}{k\sigma(m)}$ $\theta(r) = \frac{I_o}{2}\left(\frac{r_g}{r_c}\right)^2 \left[\frac{1}{k\sigma} + \sum_{m=1}^{\infty} C_m \cdot T_m\right]$
Opaque thin coating on a thick substrate	$T_m = \frac{1}{k_1\sigma_1(m)}\left[\frac{1+\Gamma(m)\exp(-2\sigma_1(m)L_1)}{1-\Gamma(m)\exp(-2\sigma_1(m)L_1)}\right]$ $\theta(r) = \frac{I_o}{2}\left(\frac{r_g}{r_c}\right)^2 \left[\frac{1+\Gamma\exp(-2\sigma_1 L_1)}{k_1\sigma_1(1-\Gamma\exp(-2\sigma_1 L_1))} + \sum_{m=1}^{\infty} C_m \cdot T_m\right]$
C_m	$= J_o(\gamma_m r) \cdot \exp(-\gamma_m^2 r_g^2/8)/J_o^2(\gamma_m r_c)$ $\sigma^2(m) = \gamma_m^2 + \frac{2j}{\mu^2}$
μ $\Gamma(m)$ $b(m)$	sample thermal diffusion length. complex thermal wave reflection coefficient. $= 1 - b(m)/1 + b(m)$ $b(m) = k_2\sigma_2(m)/k_1\sigma_1(m)$

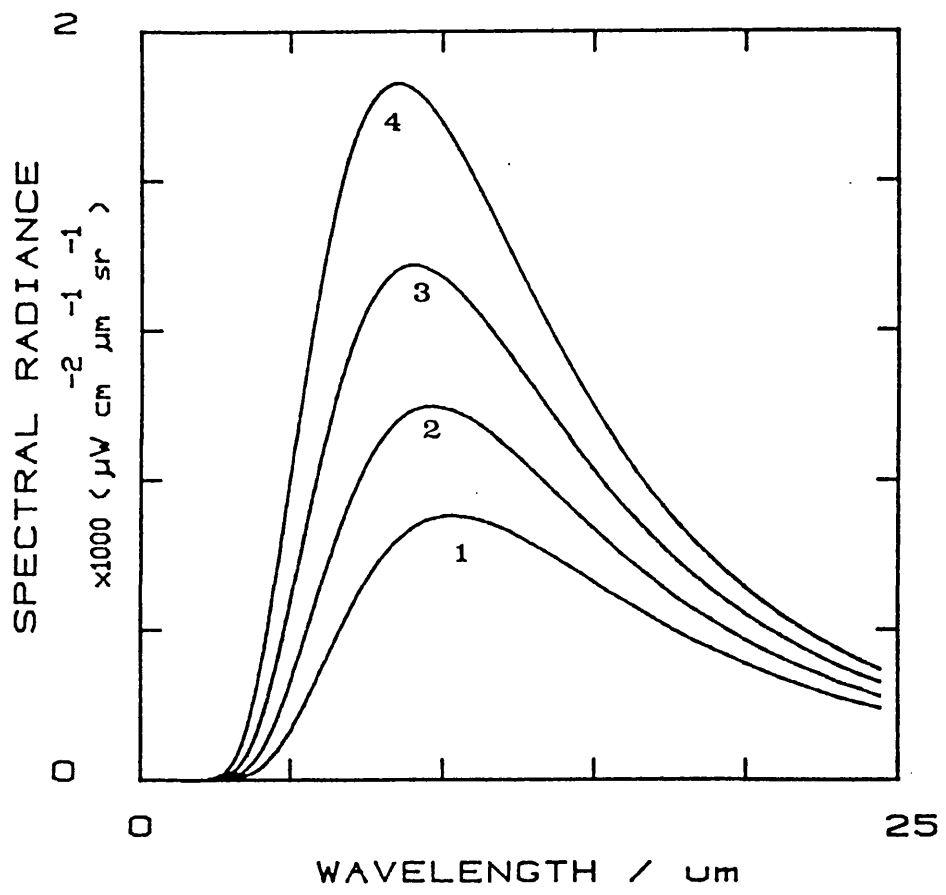

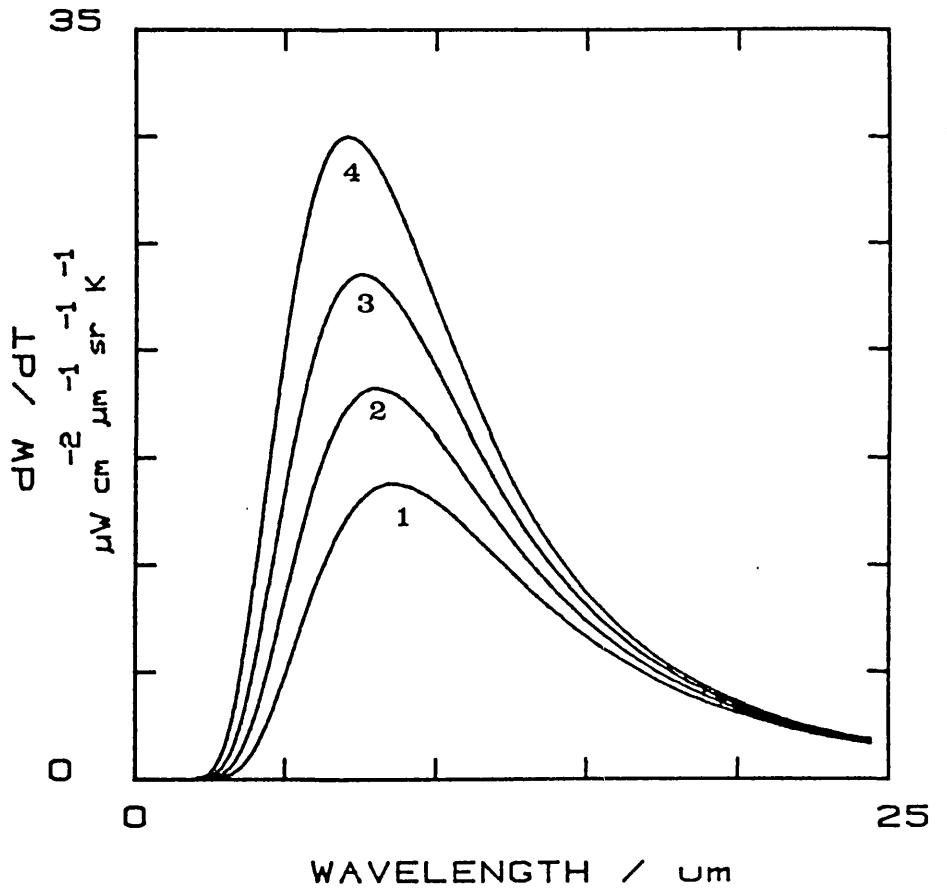

Figure 2.1: Spectral emittance verses emission wavelength for samples temperatures of 1) 280, 2) 300, 3) 320 and 4) 340 K.

Figure 2.2: Derivative plot of the spectral emittance for the sample temperatures given in figure 2.1

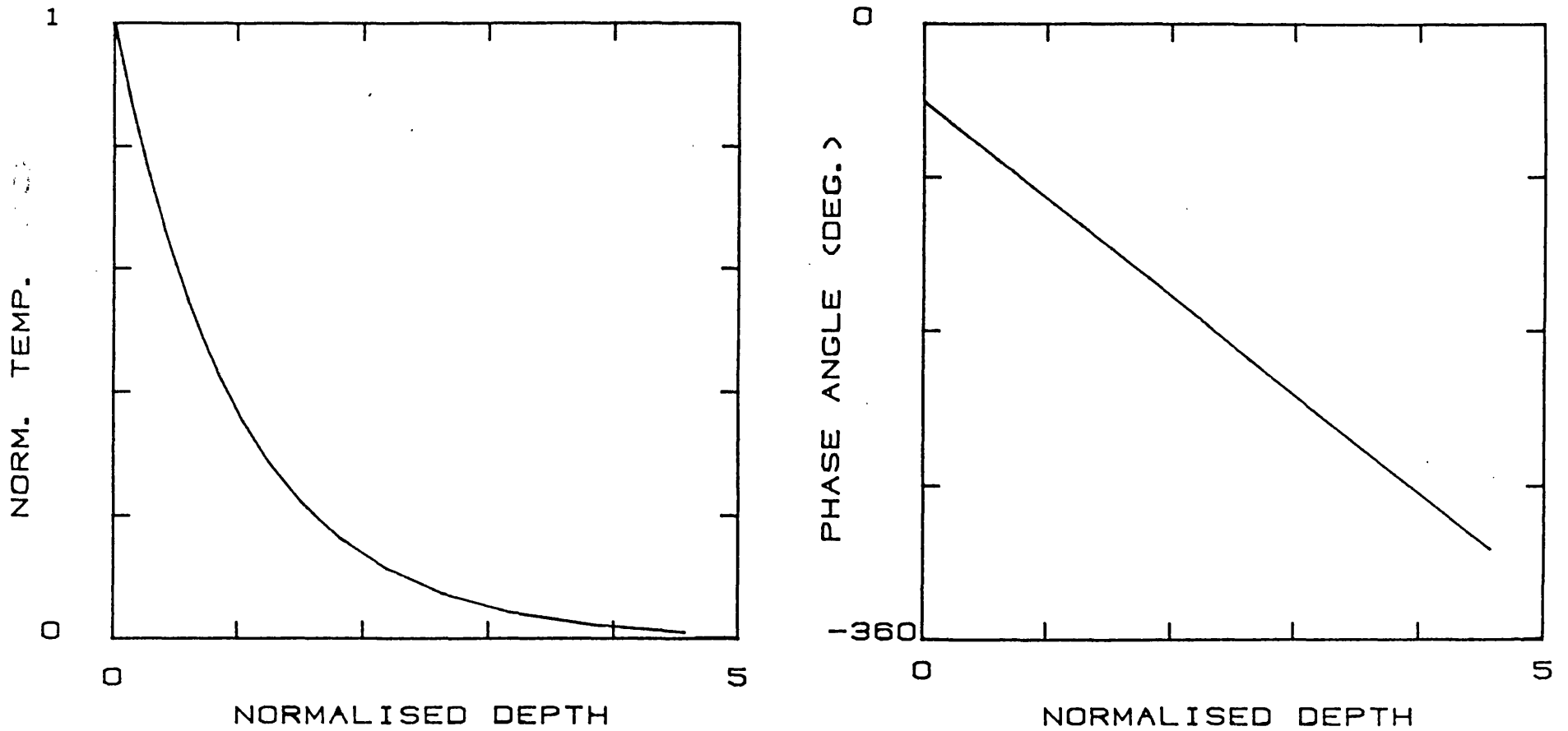

Figure 2.3a: Amplitude and phase angle variation of plane thermal waves with normalised depth, x/μ.

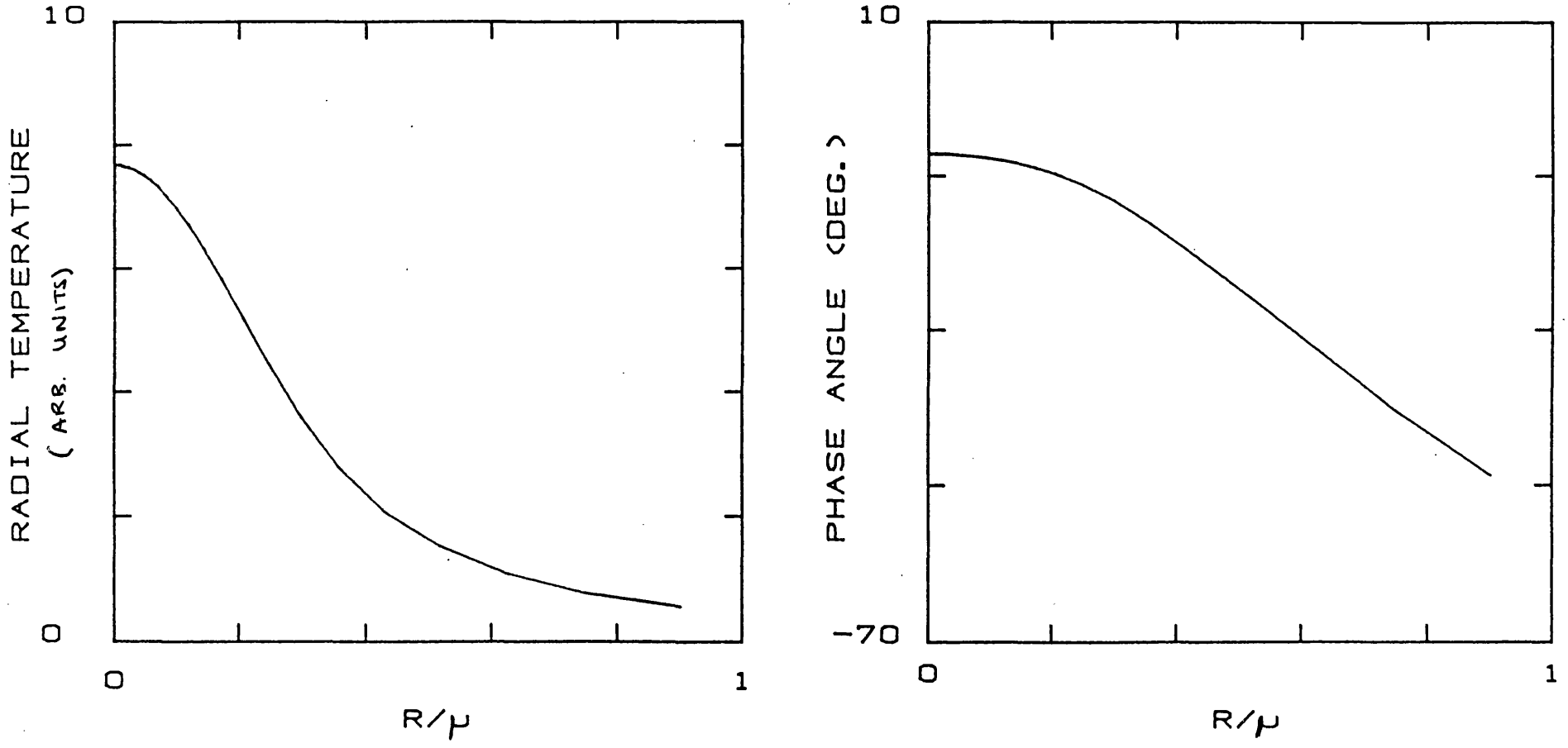

Figure 2.3b: Amplitude and phase angle variation of the three dimensional surface temperature against the normalised radial distance r/μ. The sample is mild steel, 1/e beam radius is 0.5mm and the modulation frequency is 10 Hz.

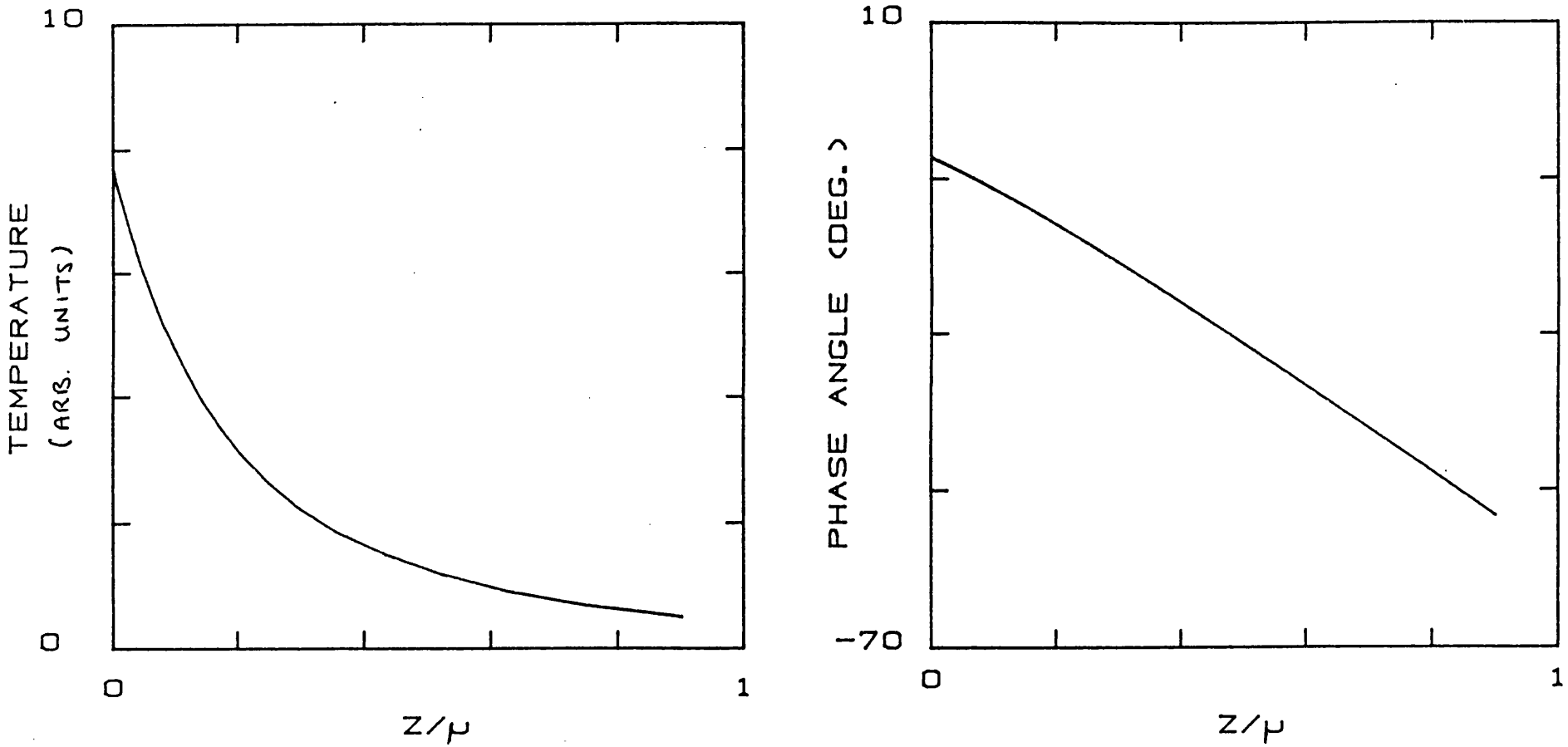

Figure 2.3c: Amplitude and phase angle variation of the three dimensional surface temperature against the normalised depth z/μ. The sample is mild steel, 1/e beam radius is 0.5mm and the modulation frequency is 10 Hz.

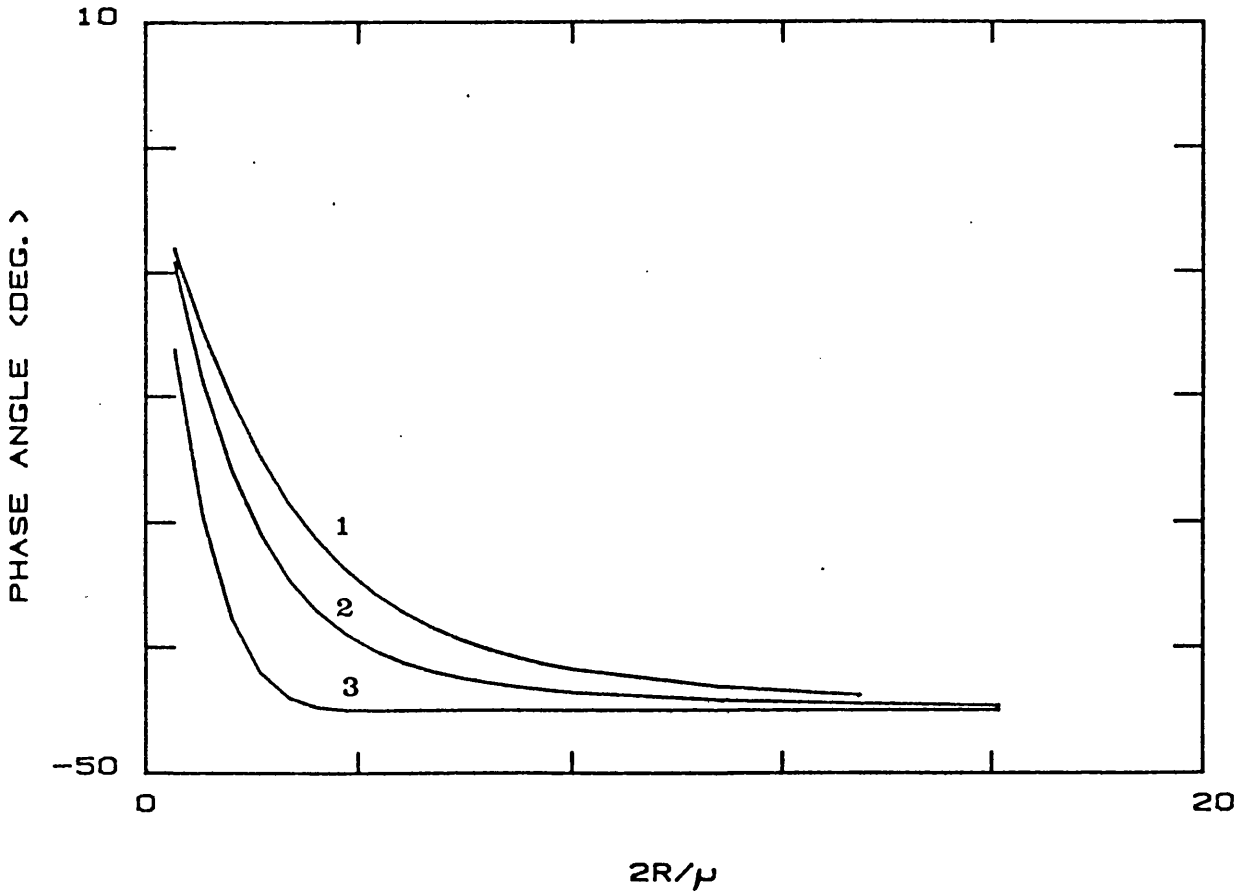

Figure 2.3d: Phase angle variation of the three dimensional surface temperature against the normalised parameter, $2R/\mu$, for various infrared detection spot diameters of 1) point, 2) 4 mm and 3) 8 mm. The sample is aluminium and laser beam 1/e radius is 1.5 mm.

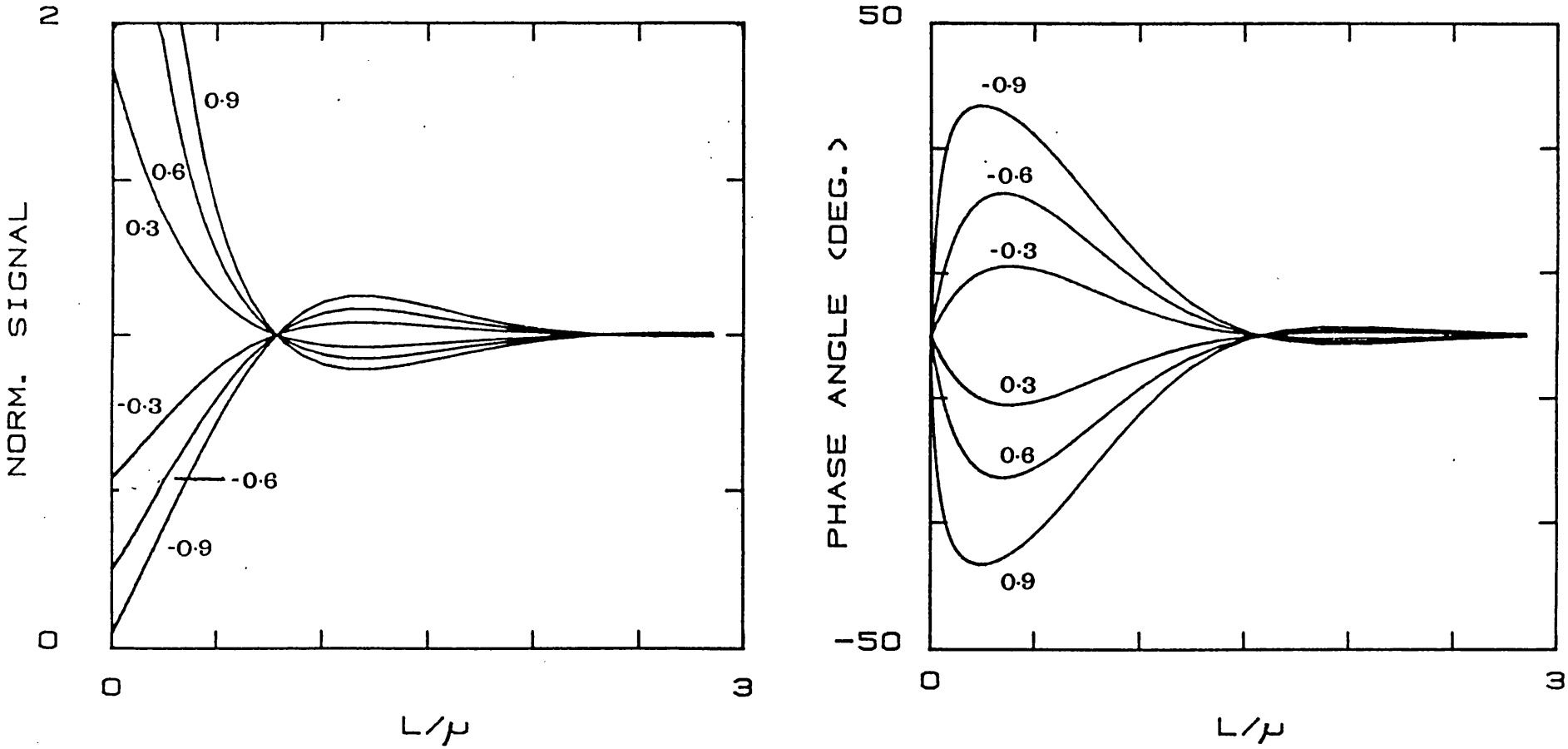

Figure 2.4: Normalised thermal wave interference plots showing the variation of the amplitude, fig. 2.4a and phase angle, fig. 2.4b, against the thermal thickness, L/μ, for various coating/ substrate thermal wave reflection coefficient.

FIG. 2.5 a

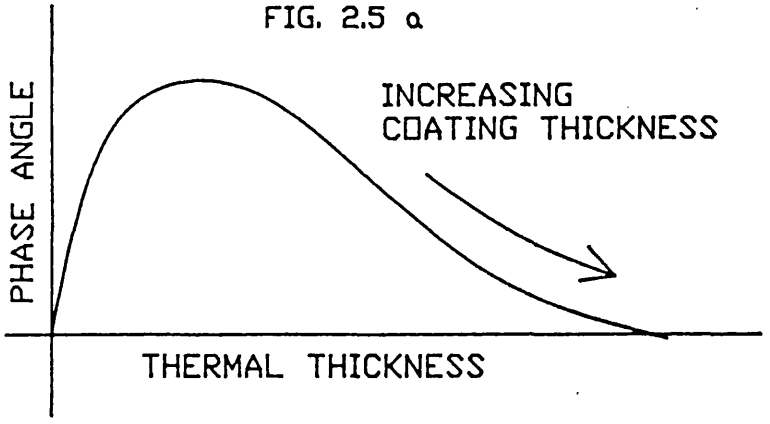

FIG. 2.5 b

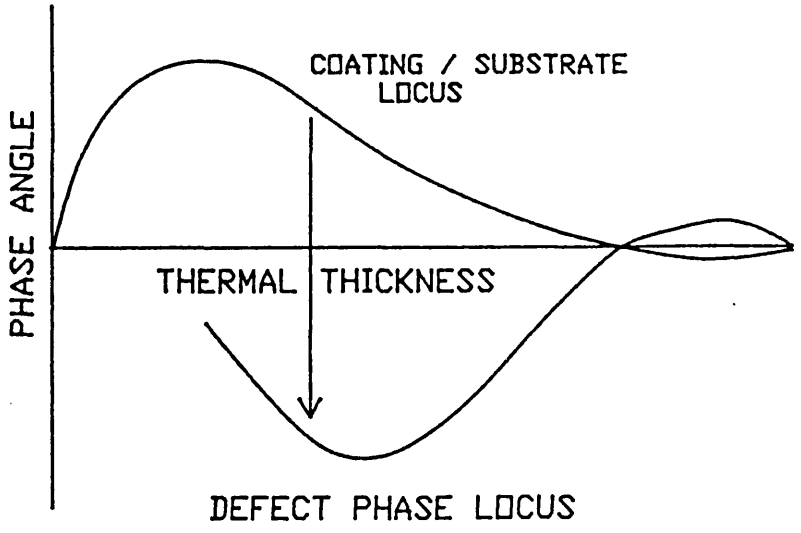

Figure 2.5: Schematic illustration of the change in the observed phase angle with changes in the coating thickness fig. 2.5a, and interface defect, fig. 2.5b.

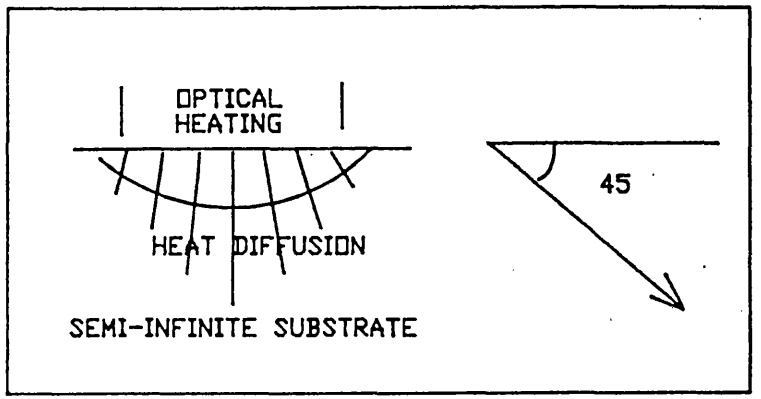

Figure 2.6a: A phasor representation of the surface photothermal signal for a semi-infinite opaque sample.

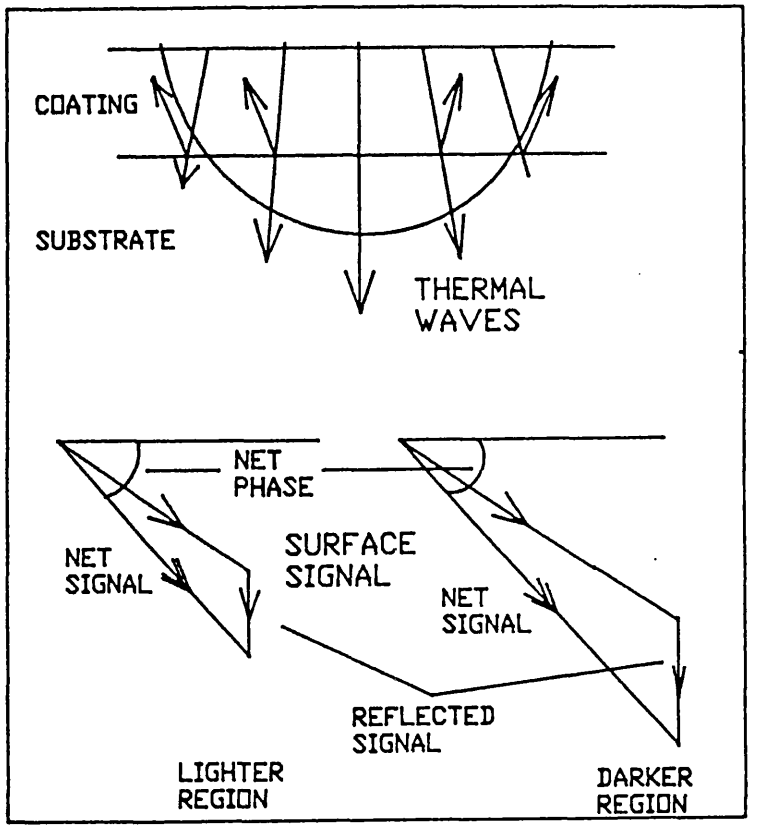

Figure 2.6b: Phasor diagram illustrating the development of the final photothermal for an opaque coating on a substrate, (left), and the invariance of the net phase angle of this signal due to increased light absorption at a 'darker' region on the sample surface (right) .

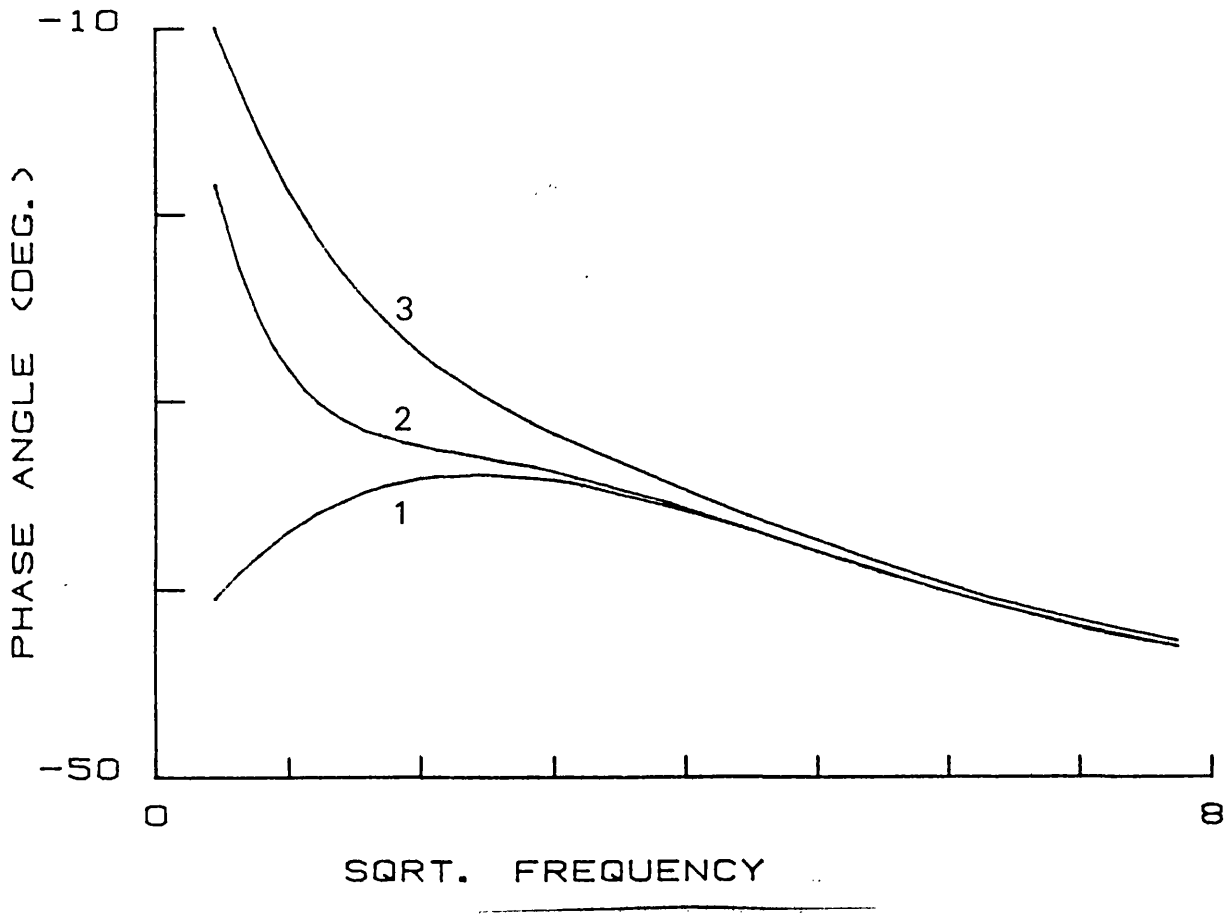

Figure 2.7: Phase angle variation with root frequency for different diameter laser spot sizes 1) infinite, 2) 2 mm, and 3) 4 mm. Phase values are taken at the centre of the laser beam. The sample is a 100 μm LC1B coating on stainless steel.

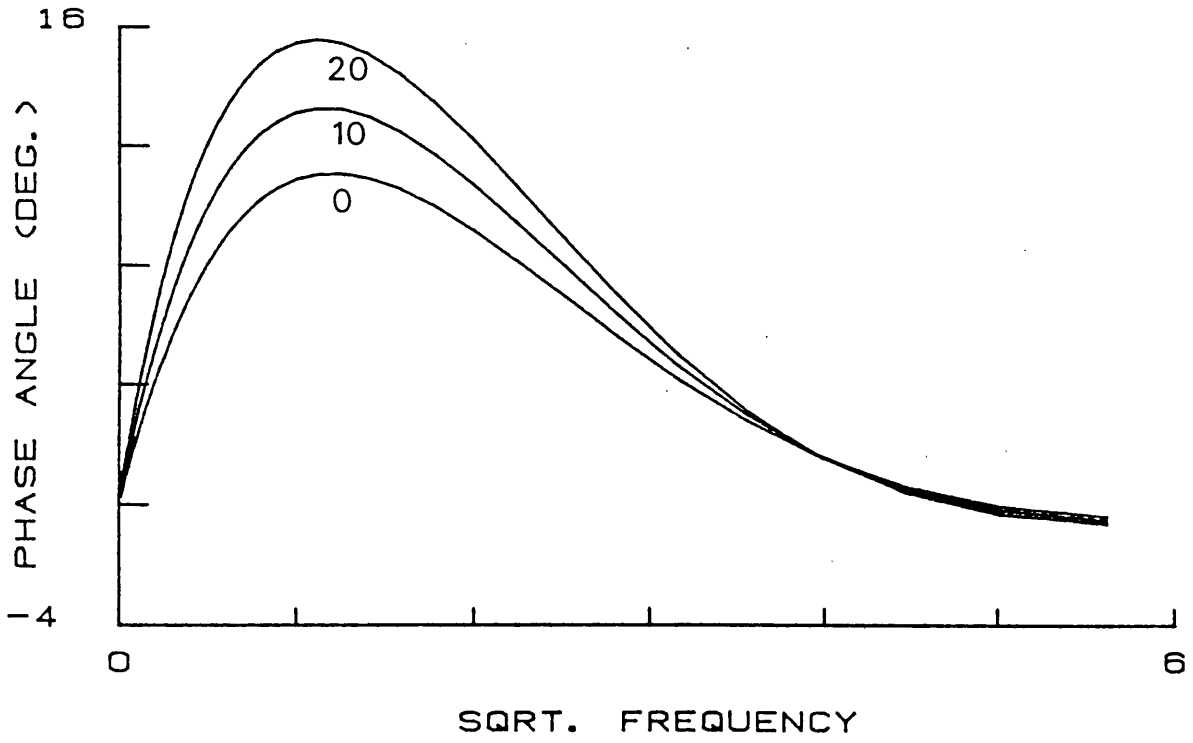

Figure 2.8: Influence of coating porosity on the phase angle root frequency plot for a 200 µm LC1B coating on stainless steel. 1) 0, 2) 10 and 3) 20 % porosity.

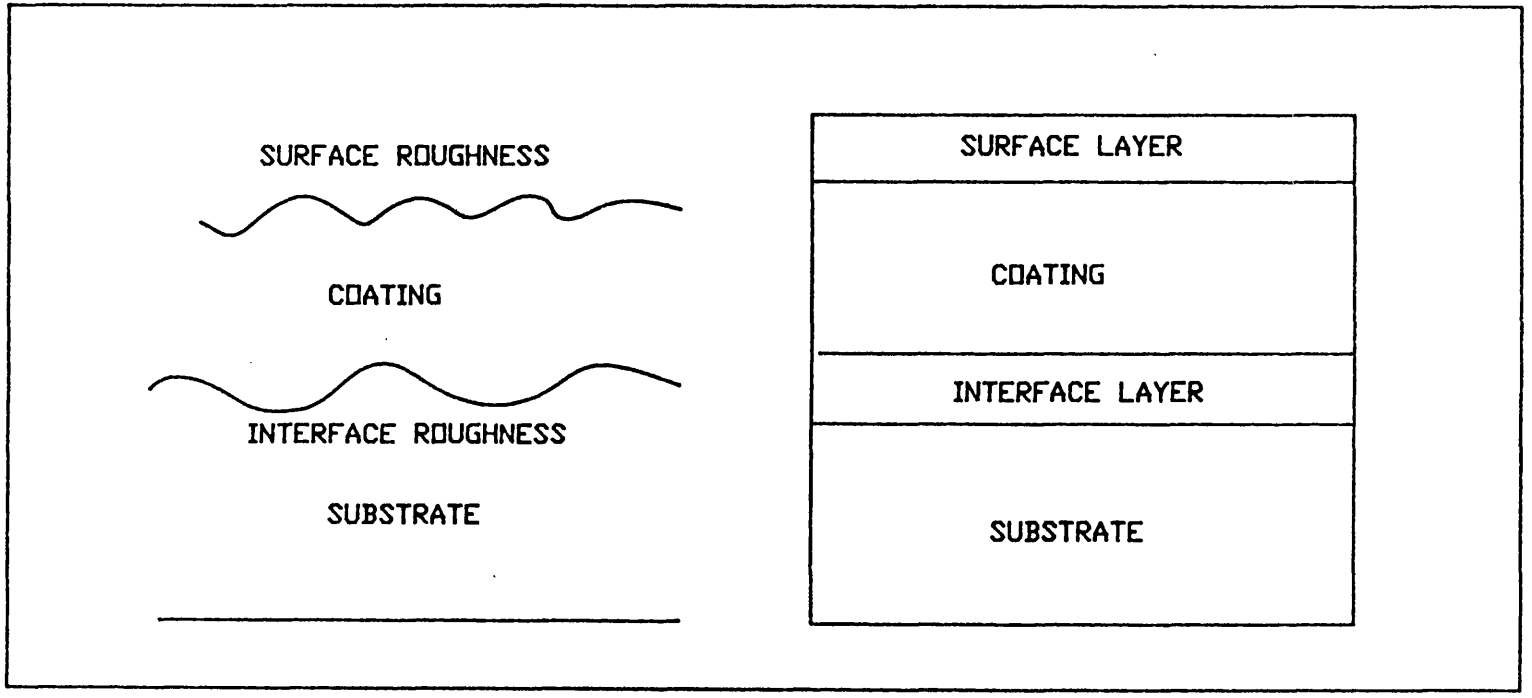

Figure 2.9: Schematic representation of surface roughness with a discrete layer of uniform thickness and thermal properties.

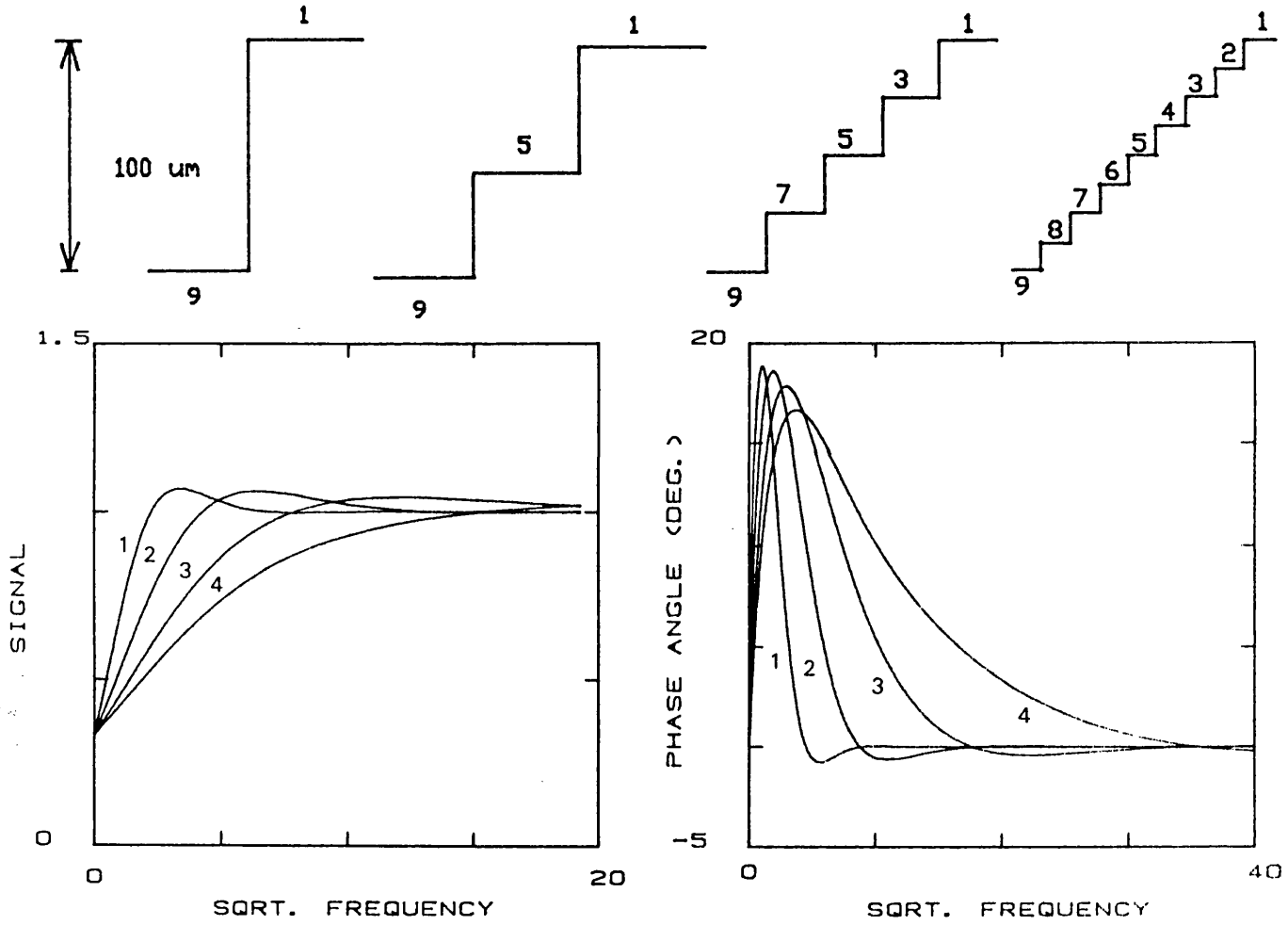

Figure 2.10: Amplitude and phase angle variation with root frequency of a layered sample exhibiting step changes in thermal conductivity. Layer thickness is 100 μm. The substrate has a thermal conductivity of 9 and the surface layer of 1 W /(m K). Top diagram shows the thermal conductivity values when the 100 μm layer is divided in 2,4 and 8 equal parts. The heat capacity of all layers are equal.

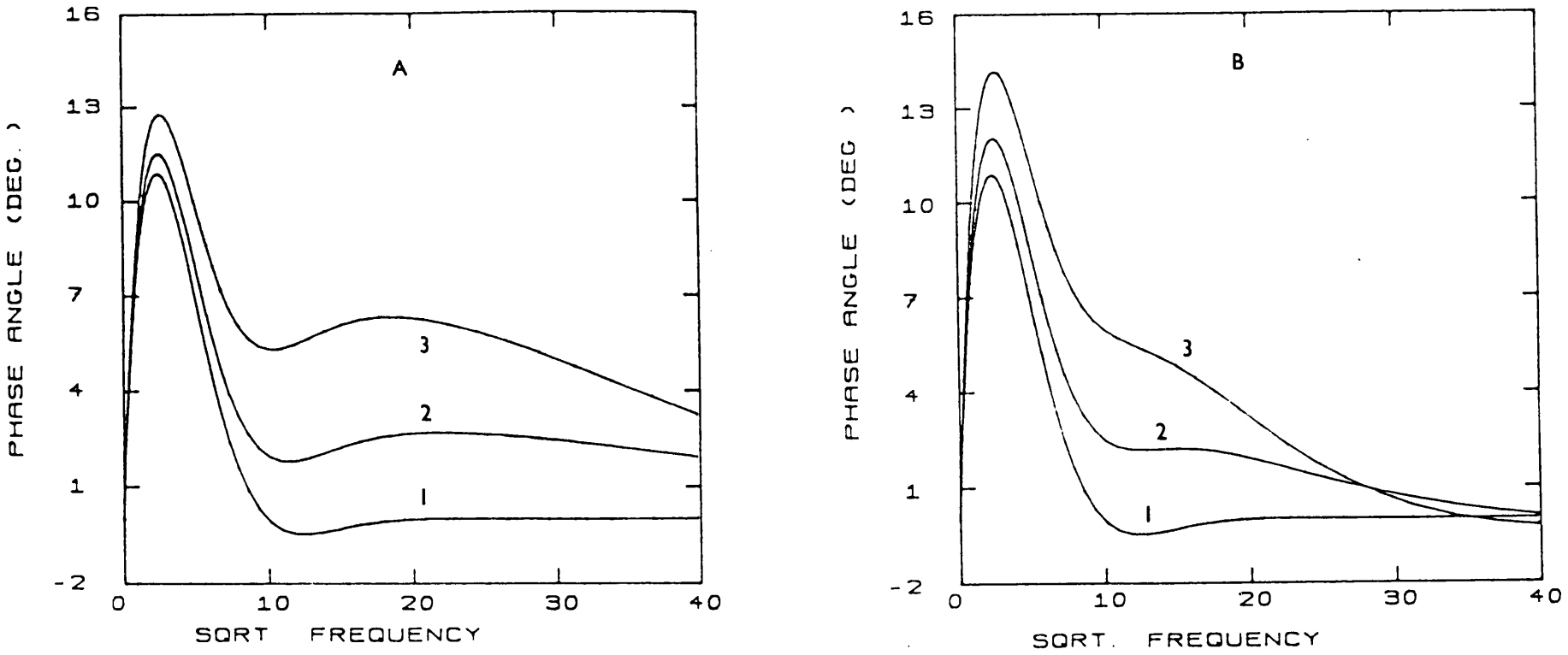

Figure 2.11a and b: Phase angle verses root frequency plots for a 10 and 20 μm surface roughness layer with several different thermal conductivity values: 1) 4.4, 2) 3.3, and 3) 2.2 W/(mK). The coating material is a nickel-chrome carbide on 316 stainless steel. The total coating thickness including the rough surface layer is a 100 μm.

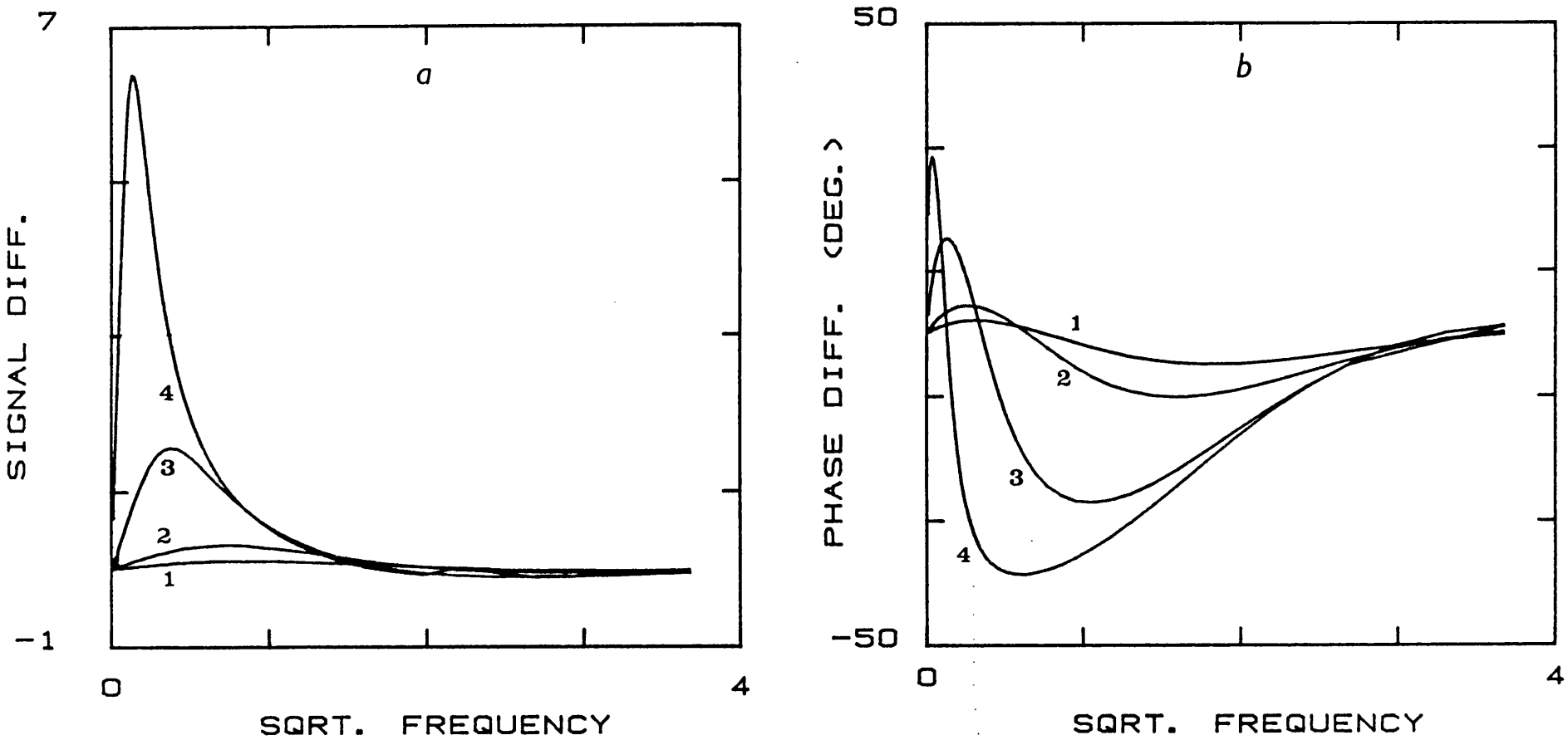

Figure 2.12 a and b: Normalised amplitude and phase angle variation with root frequency for air-gap thicknesses 1) 0.1, 2) 1, 3) 10 and 4) 100 μm 0.5mm below the surface in bulk 316 stainless steel. Heat flow is one dimensional.

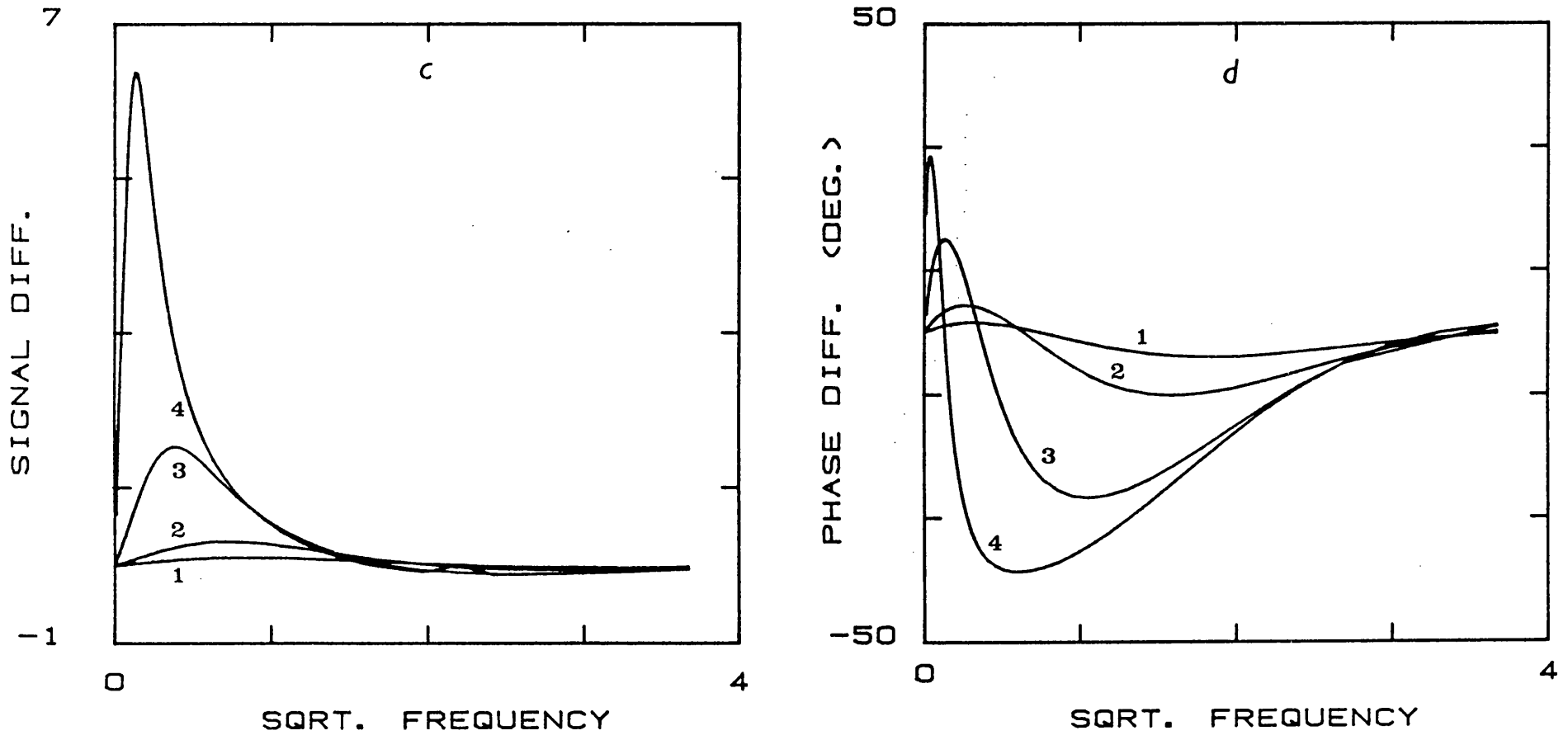

Figure 2.12 c and d: Normalised amplitude and phase angle variation with root frequency for thermal contact resistances of 1) 4E-6, 2) 4E-5, 3) 4E-4 and 4) 4E-3 m^2 K /W 0.5 mm below the surface in bulk 316 stainless steel. Heat flow is one dimensional.

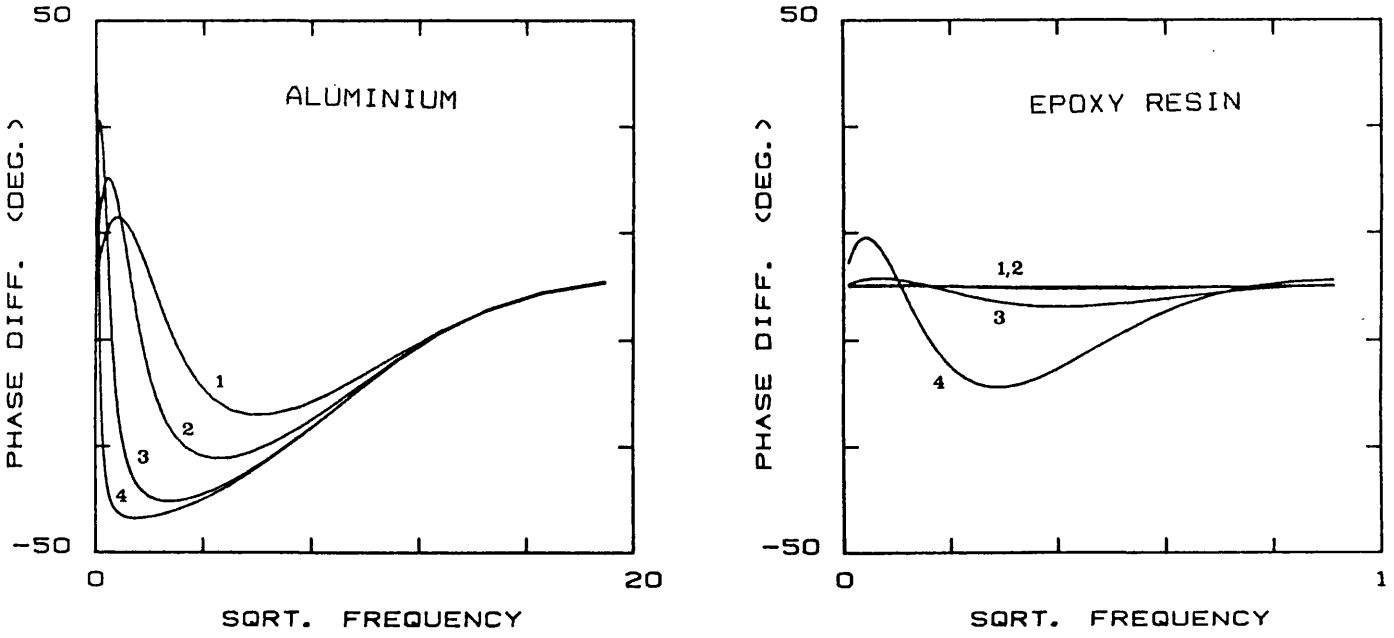

Figure 2.13: Phase angle variation with root frequency for air-gap thicknesses 1) 0.1, 2) 1, 3) 10 and 4) 100 μm 0.5mm below the surface in bulk aluminium and epoxy. Heat flow is one dimensional.

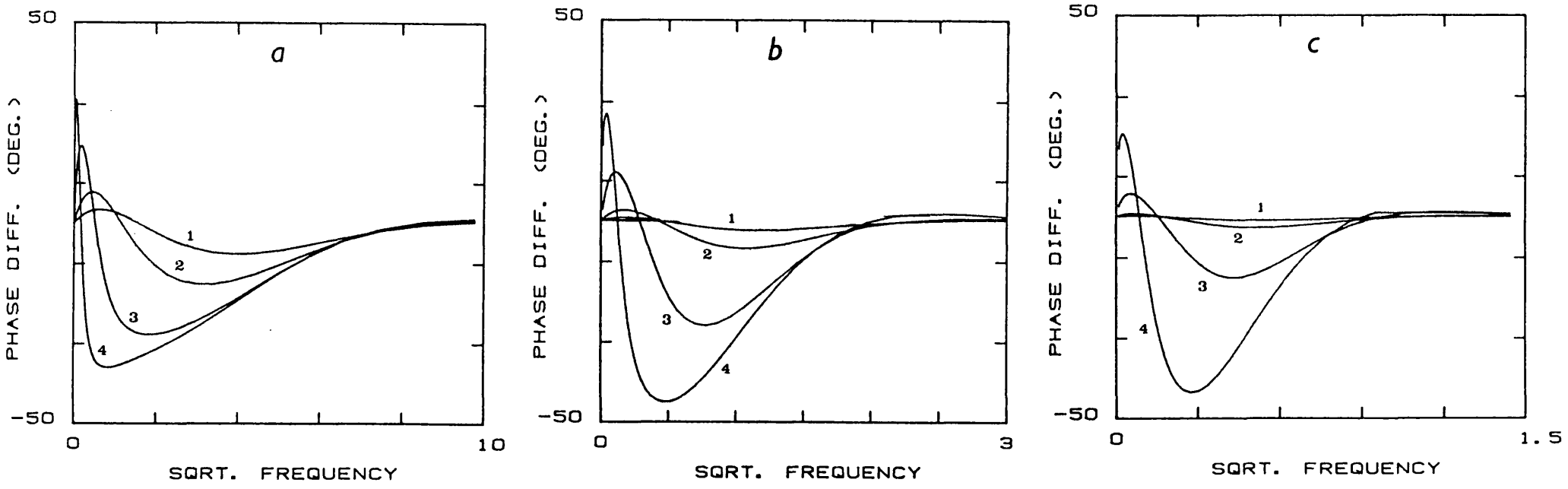

Figure 2.14: A phase difference verses root frequency plot for air-gap thicknesses 1) 0.1, 2) 1, 3) 10 and 4) 100 μm 0.5mm below the surface in a) aluminium, b) LC1B and c) Yittria stabilised Zirconia on stainless steel. Heat flow is one dimensional.

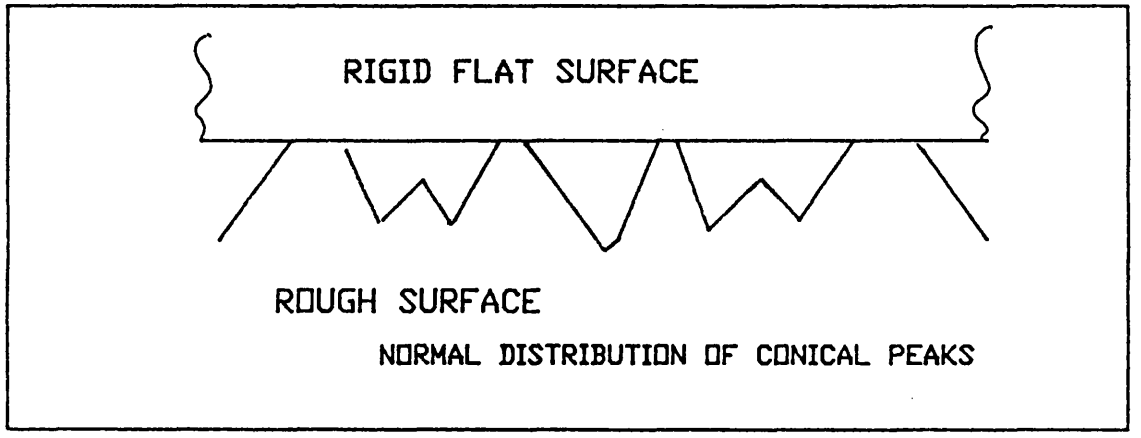

Figure 2.15: Contact between real surfaces modelled as being due to flattening of conical peaks. [68]

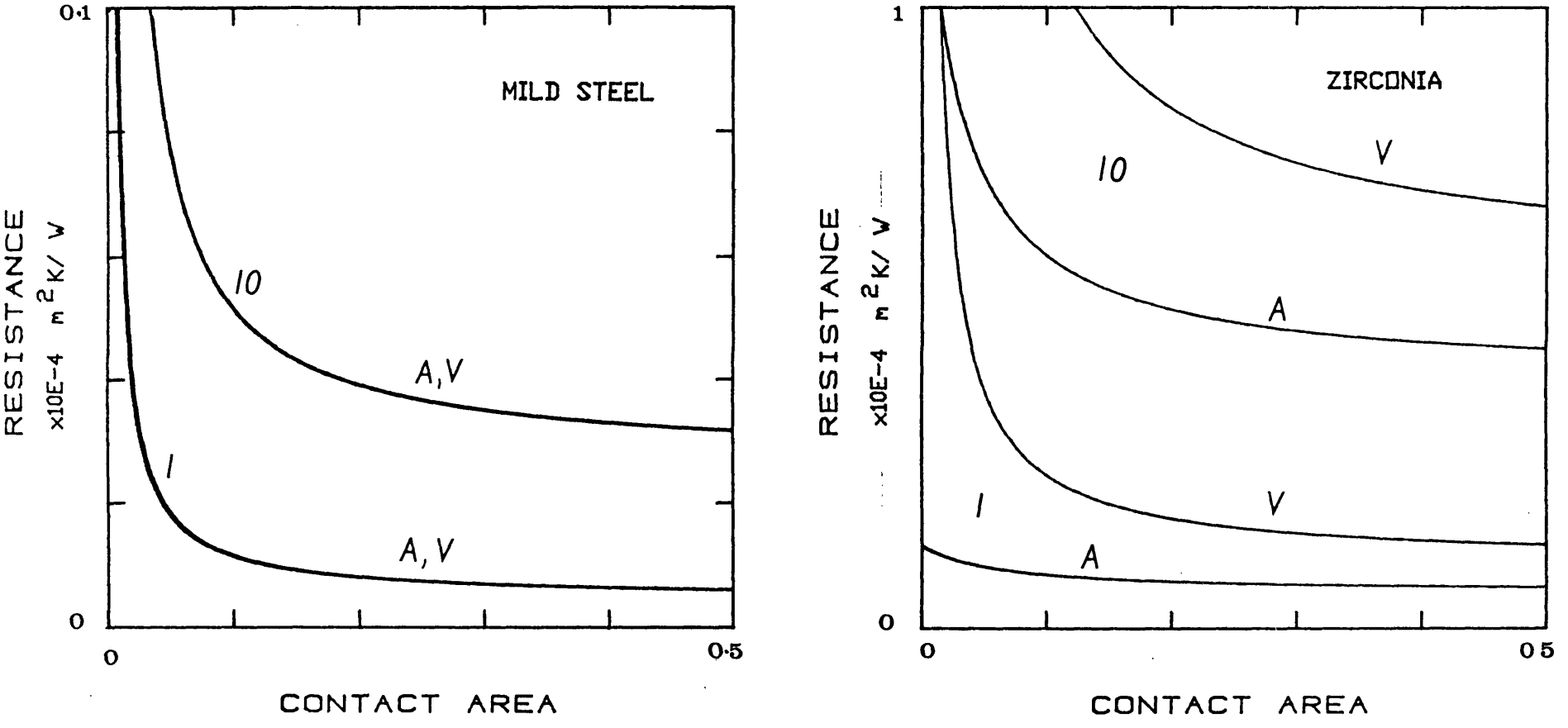

Figure 2.16: The change in thermal contact resistance with increasing fractional contact area. A= contact in air, V= contact in vacuum. Figure 2.16a contact in mild steel and 2.16b contact in zirconia.

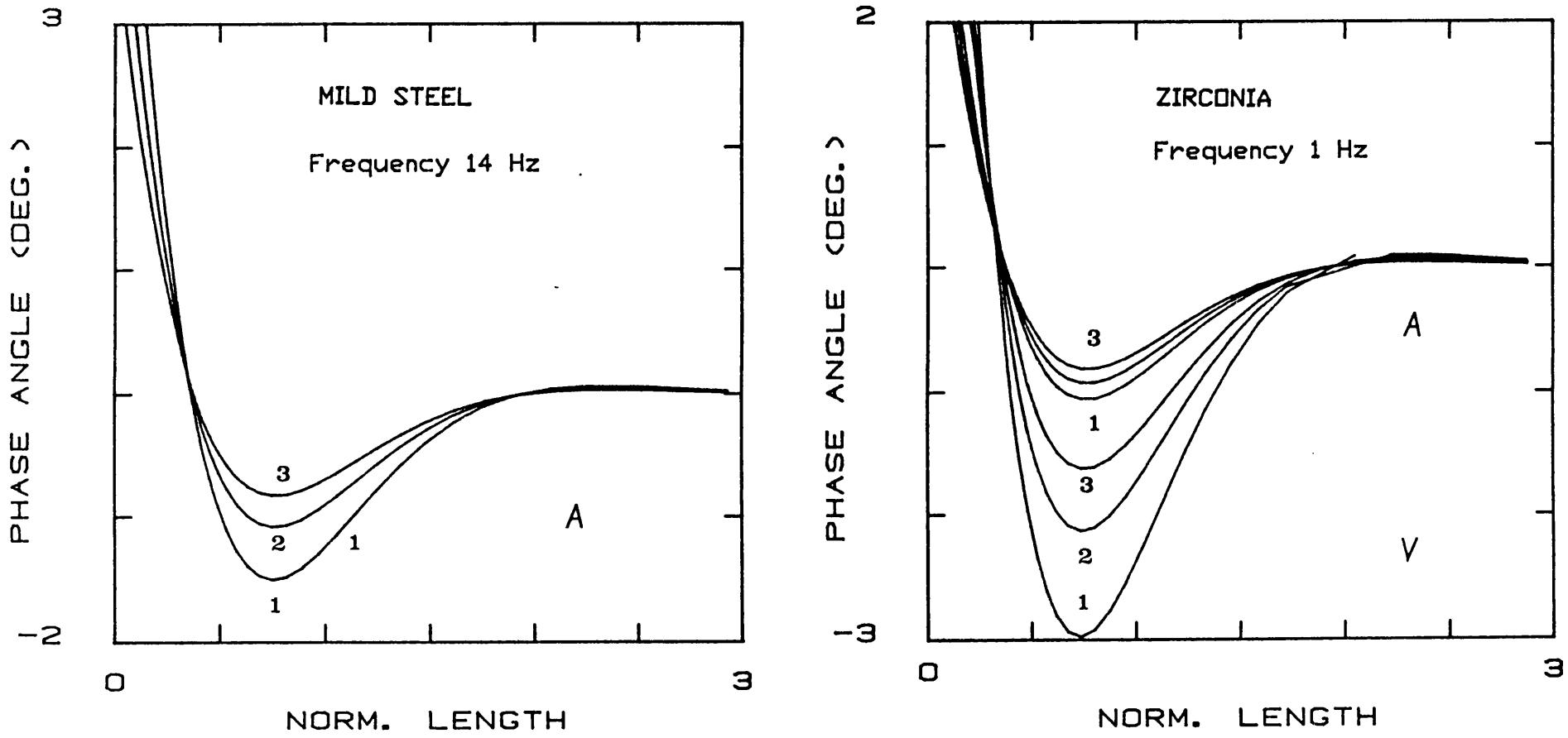

Figure 2.17: Plots of the thermal wave phase angle variation with normalised depth and fractional contact area of 1) 0.1, 2) 0.2 and 3) 0.5 of partially contacting interfaces in mild steel, fig. 2.17a, and zirconia, fig. 2.17b, with a roughness of 1 μm. A= contact in air, V= contact in vacuum.

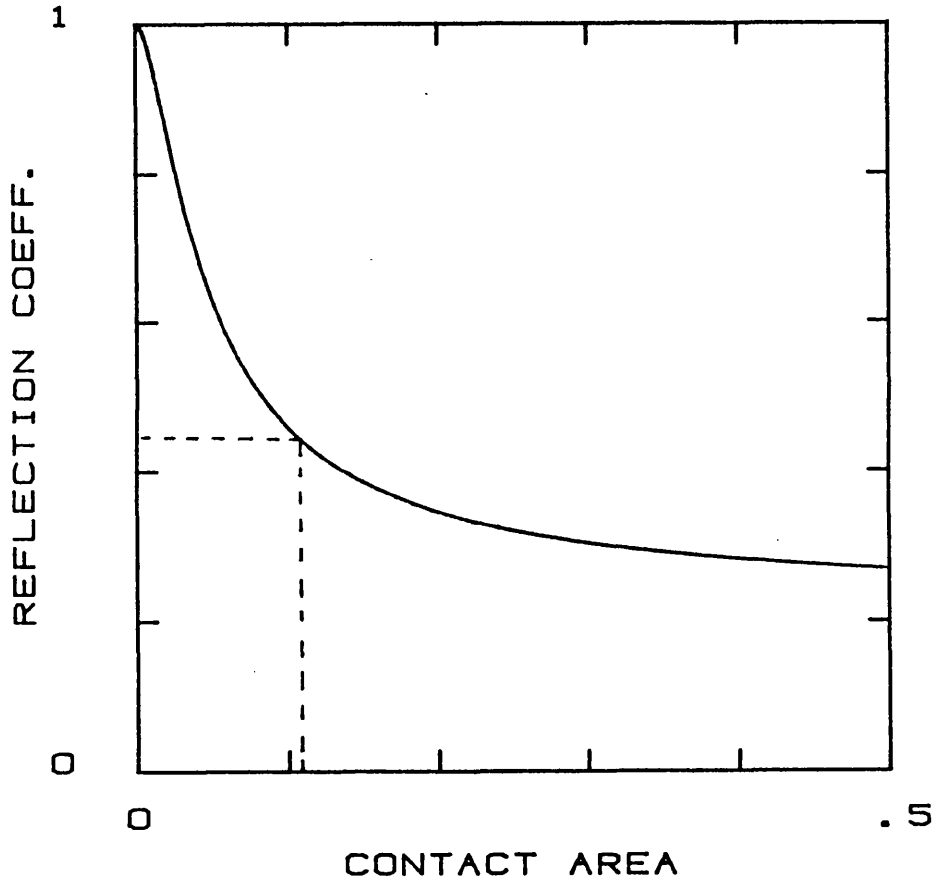

Figure 2.18: A plot of the change in the ultrasonic reflection coefficient magnitude with fractional contact area in mild steel sample of roughness 1 μm and an ultrasonic frequency of 10 MHz.

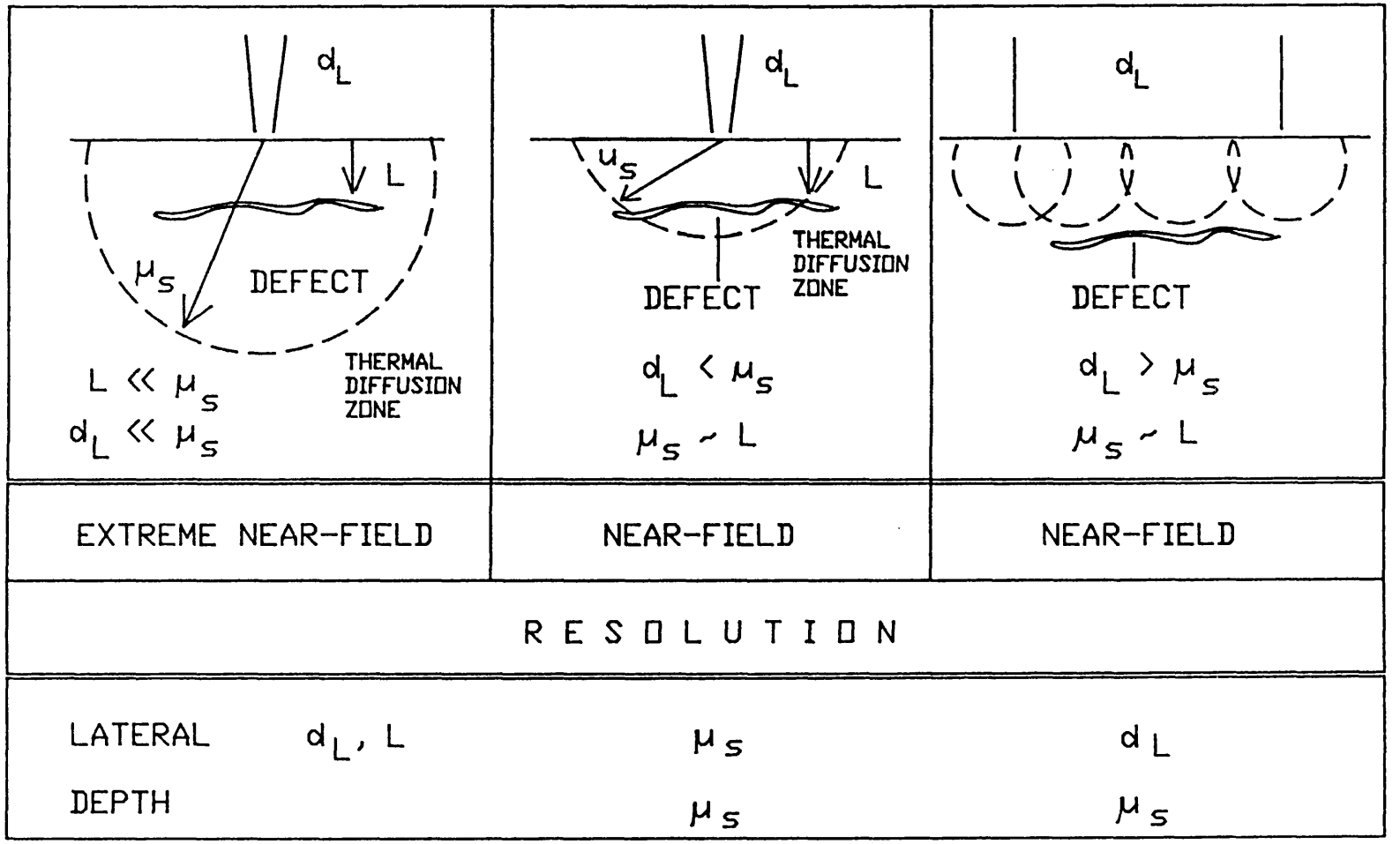

Figure 2.19: Schematic illustration of various resolution limits in PTR.

Chapter 3

Experimental Description

CHAPTER 3 EXPERIMENTAL DESCRIPTION

3.1 PHOTOTHERMAL SYSTEM

A study of figure 1.2 shows that there are essentially six basic components in a modulated photothermal NDT system. A laser source, a beam modulator, an IR sensor, a lock-in analyser , a controlling computer and a sample (or light beam) scanning unit. The measurements reported in section 4.1 used a 5 watt continuous wave Argon ion laser [76] for sample heating and a sectored blade mechanical chopper for beam modulation [77]. The harmonic thermal emission from the sample were detected by a Mullards TGS pyroelectric detector [78] and demodulated using an EG&G 5206 two phase lock-in analyser [79]. An IBM PC XT microcomputer controlled through an IEEE 488 interface, the data acquisition and sample translation [80] in horizontal and vertical directions using interpreted basic computer code. A rotating table provided manual control over the angular positioning of the sample. The IR detector, sample travelling and rotation stages were mounted on an optical bench and the whole set-up, including part of the laser head, were enclosed in a light tight box to comply with laser safety requirements [81].

To prevent the generation of coherent signal noise by the absorption of scattered/ reflected laser light at the IR detector window, a dielectric interference filter [82] was used to selectively reflect away the incident laser radiation and transmit the IR. Figures

3.1a and b show the reflectance and transmittance spectra of this interference filter and the detector window material in the optical and IR region.

3.2 DETECTOR SELECTION

The IR detector may be chosen according to its spectral, temporal, and noise characteristics, its operating temperature and robustness. For room temperature inspection of materials, 300 K, the main spectral requirement is that the IR detector element is sensitive to wavelengths greater than 3 μm, as shown in figure 2.2. The temporal requirements, especially for evaluating low diffusivity materials, are that the device has low electrical noise at low frequencies (< 100 Hz). The IR detector should also have a sufficiently fast response time (<0.001 second) so that the detected signal follows the modulated emission signal. The former requirement is unusual for most electronic applications but is necessary in PTR as low modulation frequencies are required for inspecting thick and/ or low thermal diffusivity coatings. A low noise preamplifier is an essential requirement of the IR detector.

The noise properties of IR detectors at a frequency f are given by the normalised Detectivity, D* in cm $Hz^{1/2}$ W^{-1} , which determines the noise-equivalent-power NEP [83]:

$$NEP = \frac{(A\Delta f)^{1/2}}{D^*} \qquad (3.1)$$

For the detector-sample geometry shown in figure 3.2,

the expression for the minimum detectable temperature can be put in the form:

$$\delta T \approx NEP \cdot \frac{1}{4\epsilon\sigma T_o^3 A_{rad}} \cdot \frac{1}{T_m(\lambda)\sin^2\theta_o} \qquad (3.2)$$

This equation assumes that the IR detector is sensitive to all wavelengths. The first term in equation 3.2 shows the dependence of detector parameters, the second term accounts for the total emission from the sample and the third term the IR collection efficiency. Hence to detect the smallest temperature perturbation, a low NEP value (or high D*) is required for the detector, high emissivity for the sample and high collection efficiency for the IR optics. In this study an ellipsoidal mirror [84] was evaluated to assess the improvement in the IR collection efficiency and determine any practical problems in its usage. In table 3.1 a summary is presented of the principle characteristics of the Argon ion laser, the IR detector and the ellipsoidal collector.

3.3 SEMI-CONDUCTOR LASER

In addition to the above experimental set-up, a GaAlAs semi-conductor laser was studied for its application as a sample heat source. Figure 3.3 show a schematic block diagram of the laser system, Model 7200-Y2, acquired from Spectra Physics [85]. This unit consisted of two of the above laser diodes with their output fed into a .25 mm diameter optical fibre. The laser emission from the diodes lies in the near IR

region, 810 - 820 nm. Coupled with this laser radiation there is also incoherent emission in the visible red region, 630 nm. A high quality current source drives the laser diodes and a thermoelectric cooling system is employed to prevent diode damage from over heating and stabilise laser emission. The continuous wave power output emerging from the fibre end could be varied between zero and 0.5 watt. Provision is also provided for externally modulating the laser emission and the whole assembly is packaged into a size no larger than an A4 page with a depth of 10 cms.

The invisibility of the laser radiation present two practical problems in its usage; locating the radiation on the sample and operator safety. The first problem is partly overcome by making use of the visible "red" emission from the laser. The red emission can be readily seen when it is incident on a white surface. Alternatively an IR fluorescent card can also be used. The second problem of operator safety is discussed below, both for this laser and the argon ion laser.

3.4 LASER SAFETY

Safety requirements of laser products and systems, and for users is covered by the BS4803 (part 1,2 and 3, 1983) regulation. Both laser radiations if viewed by the unprotected eye (directly or through specular reflections) can lead to permanent blindness. This is directly due to the 10^{5} fold increase in energy density focused on the retina by the eye. For the IR laser the

eye damage can be retinal burns or lead to cataracts. With argon ion laser radiation there is potential for photochemical and thermal retinal injury to the eye and also to skin burns at high laser powers.

To comply with the safety requirements for the two lasers, both these lasers were operated in a closed room and protective eye goggles were worn to attenuate the laser radiation by an optical density of 13 (10^{13} reduction of incident radiation).

3.5 SAMPLE AND MEASUREMENT DETAILS

The experimental investigation reported is divided into three parts: An evaluation of the photothermal system based on the Argon ion laser to the sensitivity of the detected signal to sample and detector set-up, Measurements on coated samples to assess the effects of surface roughness and subsurface defects, and Measurements of coating thickness using the semi-conductor laser for sample heating.

The materials studied in these investigations are as follows. LC1B (Nickel-chrome carbide), fine and coarse plasma sprayed coatings and high density nuclear graphite for surface roughness studies. As sprayed and surface polished LC1B coatings for defect detection studies by photothermal and ultrasonic methods. Air gap defects in mild steel/ stainless steel and mild steel/ mild steel diffusion bonded plates. Contacting surface detection with pressed aluminium plates. Figures 3.4-3.7 provide a detailed summary of the samples used in the above tests and table 3.2 lists the experiments undertaken.

Table 3.1 Laser, IR detector and ellipsoidal mirror details

Argon ion laser	
Laser power	0 to 6 Watt in multi-line mode
Wavelength range	488 to 514 nm
$1/e^2$ beam diameter	1.3 mm
Beam divergence	0.005 radians

IR detector	
Dimension	Cylindrical shape 25 mm in diameter and 100 mm in length.
Sensing element	Analine doped tri-glycine sulphate
Element size	2 x 2 mm
Detector window	Bloomed germanium 20 mm in diameter.
Responsivity	1E 5 volts/watt
Noise Equivalent Power	7.7 E-11 Watt/ √ Hz
D* Detectivity	2.6 E 9 cm /watt/ √ Hz
Operating voltage	9 volts DC

Elliposidal mirror details.

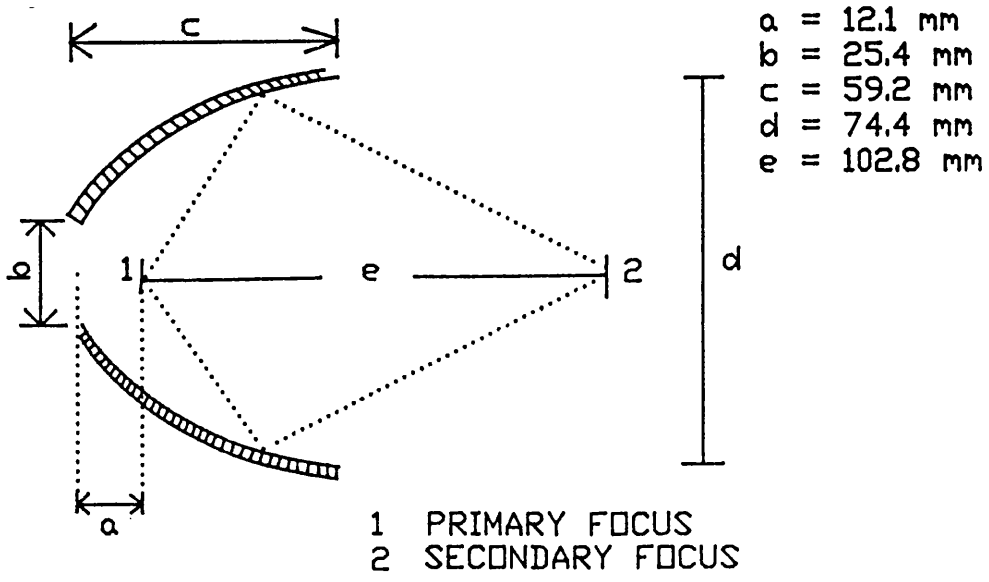

Table 3.2: Experimental investigation summary.

System evaluation
Eliminating IR radiation from the laser tube. Signal and phase variation with laser power and beam diameter. Signal and phase variation with sample or detector rotation. Effects of reflected laser light on signal and phase measurements. Signal and phase variation with laser power using the ellipsiodal mirror collector
Surface roughness study
Signal and phase measurements on LC1B fine and rough coatings. Signal and phase measurements on graphite.
Defect study
Photothermal and ultrasonic measurements on LC1B "defect" samples. Phase angle variation with defect depth and width in diffusion bonded defect samples. Phase angle measurements on partially contacting interfaces.
Semiconductor laser study
Signal and phase angle measurements with laser power Signal and phase angle variation with fibre head positioning. Measurements of coating thickness on an LC1B coating.

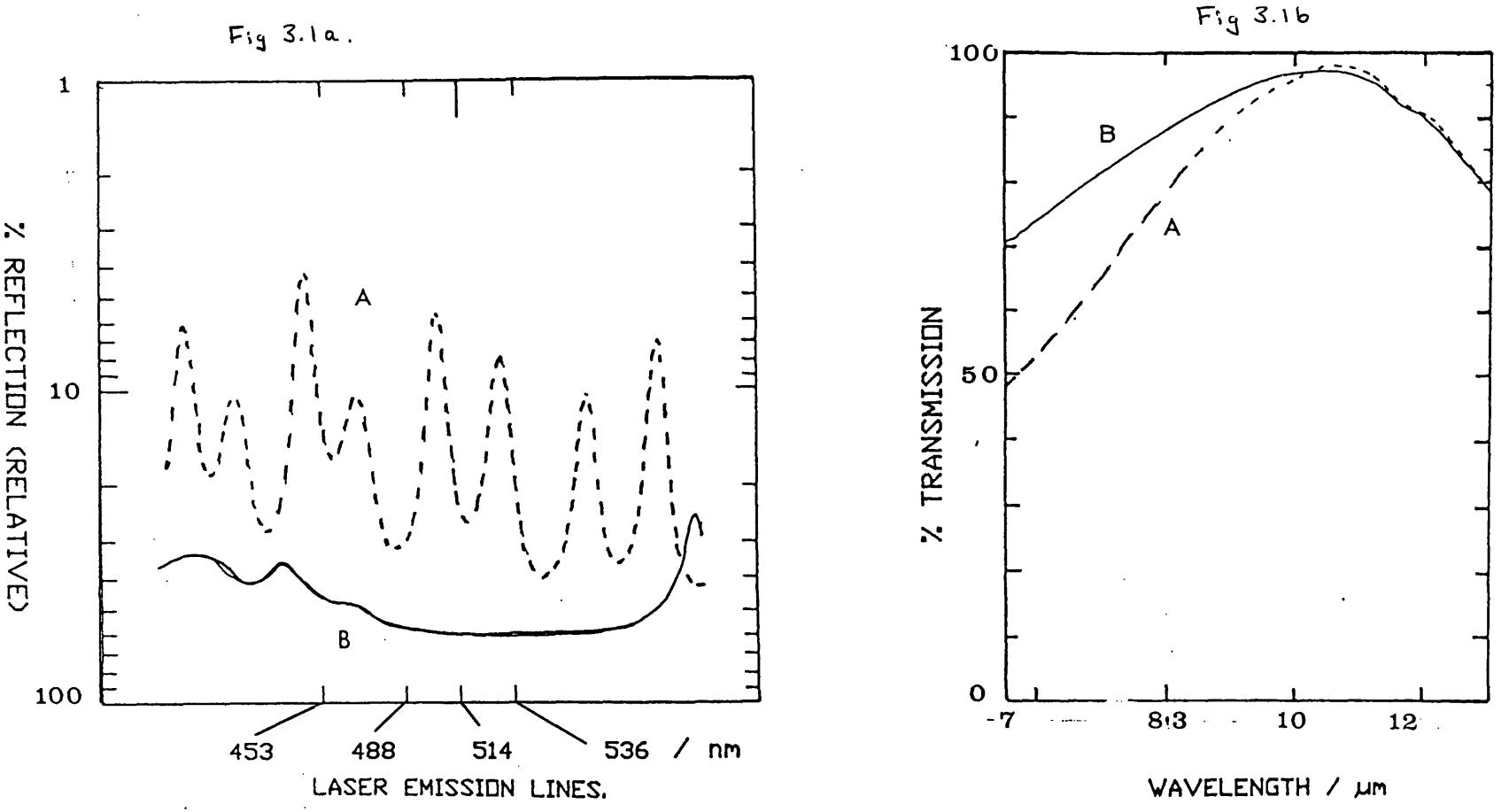

Figure 3.1: Optical and infrared reflectance and transmittance spectra of the infrared detector window material, curve A, and the interference reflectance filter, curve B.

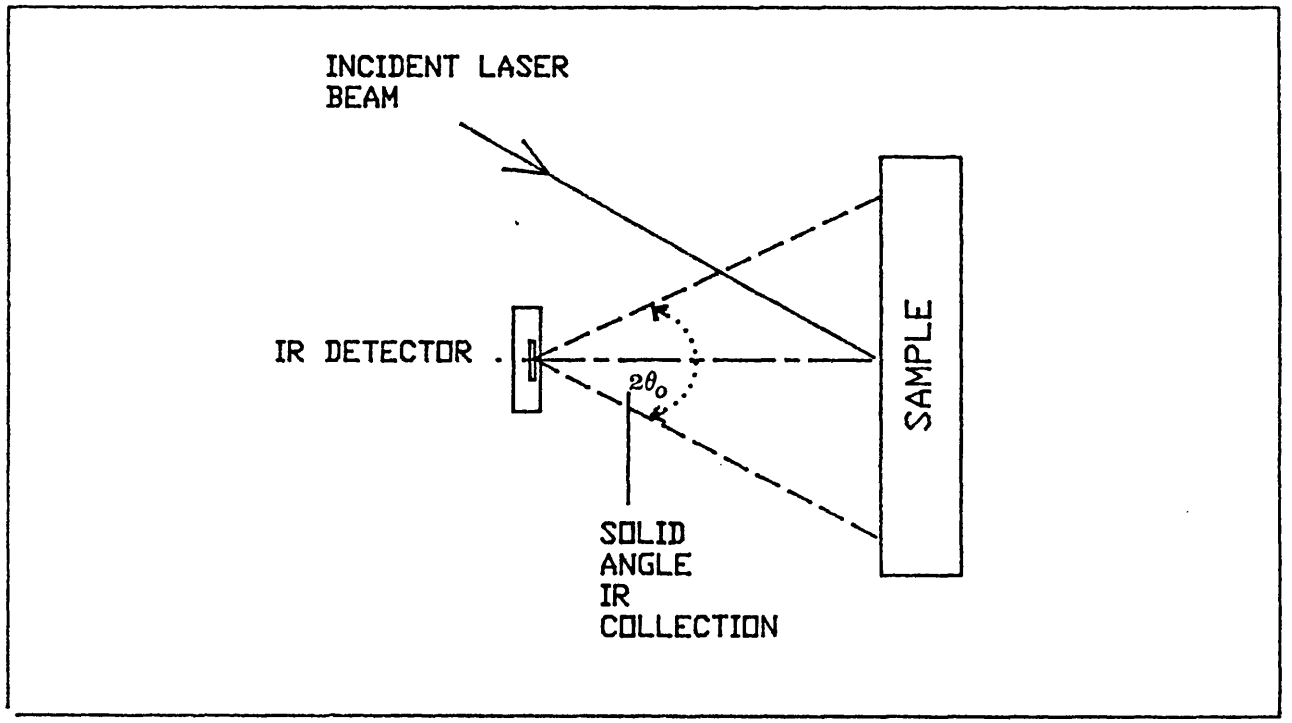

Figure 3.2: Schematic illustration of the sample and IR detector geometry.

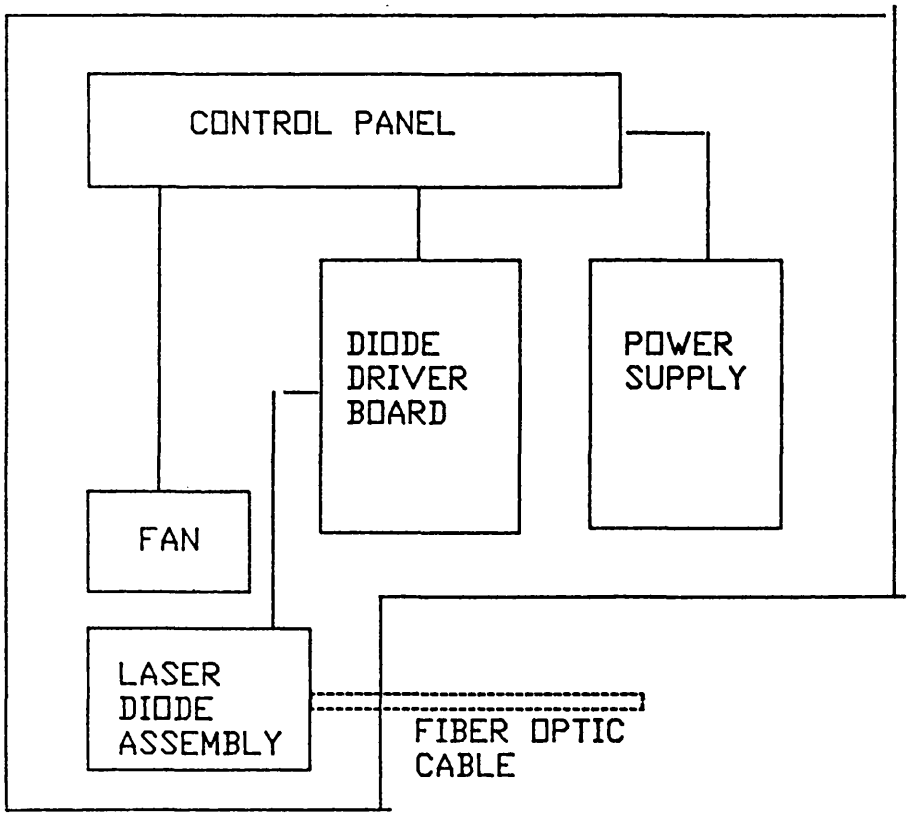

LASER DIODE CHARACTERSTICS	
LASER POWER TEM	0.5 w
BEAM DIVERGANCE	30 Deg.
EMISSION WAVELENGTH	820 nm
FIBER DIAMETER	0.25 mm
DIODE DRIVE CURRENT	0.5 Amp
LASER DIODE LIFE TIME (30 C)	50000h

Figure 3.3: A block diagram of the laser diode system module and beam characteristics.

FIG. 3.4a

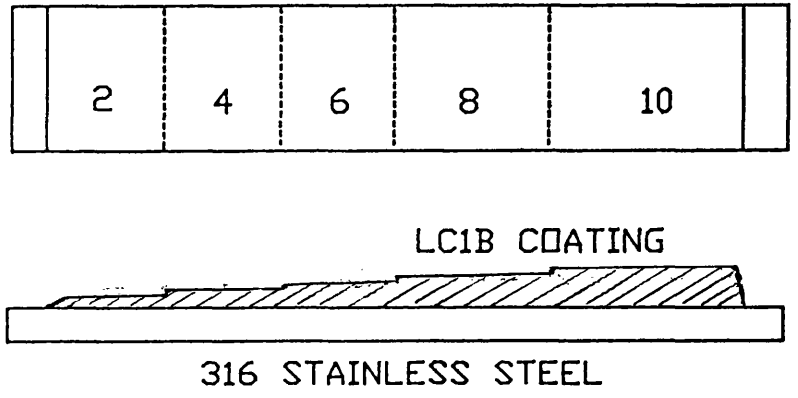

FIG. 3.4b

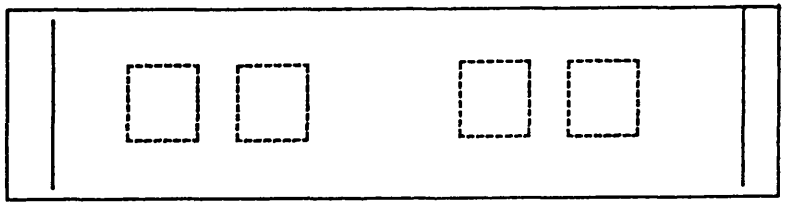

Figure 3.4a: A schematic of LC1B step coating thickness sample. Sample width 25 mm, substrate 3 mm thick 316 stainless steel and length 20 cms. (Thickness step in thousandth of an inch.)

Figure 3.4b: A schematic illustration of subsurface square defects in LC1B coated sample. Specimen dimension as above, coating thickness around 200 μm. Defects 10 mm square and separated by 10 mm.

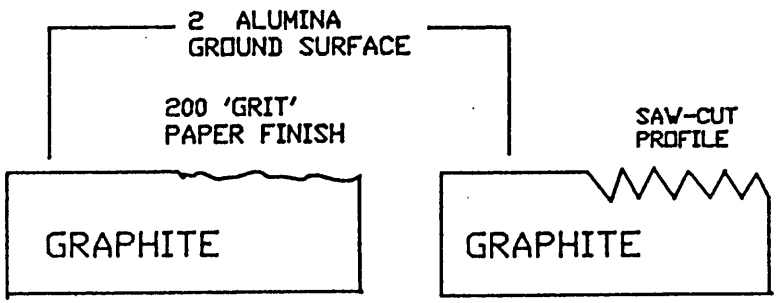

Figure 3.5: Graphite roughness sample geometry. Sample 10 mm square section block, 100 mm long.

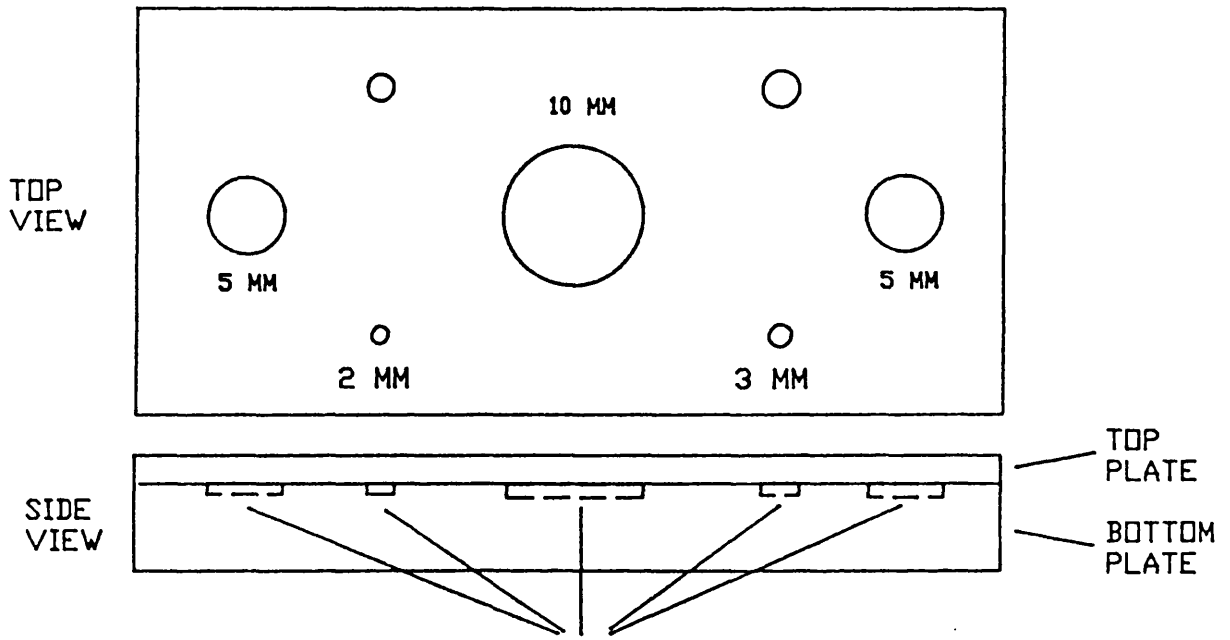

Figure 3.6: Schematic illustration of diffusion bonded defect test sample. Substrate 10 mm thick, 75 mm wide 150 mm long. Surface layer diffusion bonded to substrate and machined down to required thickness.

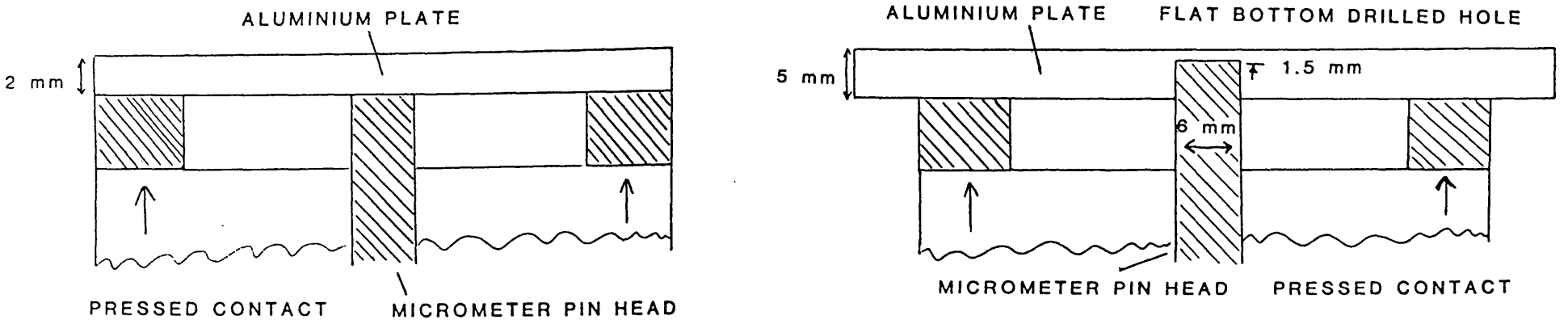

Figure 3.7: A schematic illustration of the sample set-up used to study the detectability of contacting surfaces by thermal waves. Left, a 2 mm thick aluminium plate pressed into contact with a micrometer pin head. Rear surface polished to a 2 μm alumina finish. Right, subsurface contact within a partially flat bottom drilled hole in a 5 mm thick aluminium plate.

Chapter 4

Experimental Results

CHAPTER 4 EXPERIMENTAL RESULTS

4.1 SYSTEM EVALUATION

Figure 4.1 shows a schematic illustration of the general radiation scene viewed by an IR detector in a photothermal NDT system. In addition to the optically generated thermal emission at the sample, there can be three other sources of IR radiation.

a) From the hot plasma tube of the argon ion laser.
b) Signal generated by reflected laser light absorbed at the detector window/ optics.
c) Natural background thermal radiation from the sample and surroundings.

Steps must be taken to eliminate or minimise the detection of these sources. Phase sensitive detection will discriminate against the detection of incoherent signal components such as those arising from background variations in thermal radiation. Reduction of the other IR components require special attention and methods available to prevent their detection are described in section 4.1.1. Photothermal signal variations with laser power, sample and detector set-up are discussed in 4.1.2-3. The findings of the system evaluation are discussed in 4.1.4.

4.1.1 REMOVAL OF UNWANTED INFRARED SIGNAL SOURCES

INFRARED EMISSION FROM THE LASER

Water columns of length 2,4,5,6,8 and 10 centimetres were used to investigate the reduction of IR emission from the laser by absorption. The experimental arrangement used is shown schematically in figure 4.2a. Laser emission was passed through the water column and

allowed to illuminate the detector window/ filter. The incident laser power used was 3 watt and the modulation frequency 10 Hz. The change in signal amplitude and phase angle with increasing water column length was monitored and the results obtained are shown in figure 4.2b. Both the signal amplitude and phase angle decreased with increasing water column length and saturated at column lengths greater than 4 cm. The saturation of the phase angle with increasing water column length suggest that the direct IR component from the laser tube has been reduced or eliminated. The presence of a residual signal even when a laser light reflection filter is used strongly confirm the generation of a secondary signal at the detector IR optics. Hence the direct reflection of laser radiation on to the IR optics must be avoided. In all of the subsequent measurements reported below a 5 cm water column was used to reduce the IR radiation from the laser.

REFLECTED LASER LIGHT

The generation of a secondary coherent signal by the absorption of reflected laser light at the detector window can be reduced by rotating the sample to reflect away the laser light or by employing suitable optical filter(s) to selectively reflect away the laser light and transmit the IR. The effect of sample surface reflectivity is illustrated in fig. 4.3a, which is a trace of the variation of the photothermal phase angle across a test piece compromising of low reflectivity

graphite and high reflectivity titanium. The sharp drop of 20 degrees in the phase angle when going from graphite to titanium is caused by the high reflectivity of the titanium surface. Introducing an interference optical filter to reflect away the laser light the line trace shown in fig. 4.3b is obtained, showing the expected phase angle behaviour on both types of surfaces to be independent of sample optical condition. In figure 4.3c the improvement in rejecting the reflected laser light by sample rotation is presented without the use of a filter.

From these measurements it is clear that the above measures significantly reduce second signal generation at the detector and in practice both measures should be taken when inspecting reflective surfaces.

4.1.2 LASER POWER LEVEL

Figure 4.4 shows the variation of the photothermal signal with incident laser power. The measurements are made on a 250 μm LC1B coating at a modulation frequency of 10 Hz. The interference filter was also used. Below laser powers of 3 watt the signal variation is seen to be linear. For laser powers above 3 watt the signal shows a non-linear variation. A curve fit analysis predicts that the signal variation follows a curve of the form:

$$Signal \approx aI_o + bI_o^2 + cI_o^3 \qquad (4.1)$$

where a,b,c are constants and I_o is the incident laser power. This equation follows directly from equation 2.4 and the surface temperature expressions developed

in appendix 2. The phase angle appears to show little variation with laser power within the experimental noise of half a degree. It also remains unchanged in the non-linear signal variation region. The rise in phase angle at laser power of 1 watt is due to a poor signal to noise ratio at this power level.

The variation of photothermal signal with optical spot size is shown in figure 4.5a for a 250 μm LC1B coating on stainless steel at a frequency of 10 Hz. A converging lens of focal length of 25 cm was used to vary the optical spot size. The measured phase angle showed an advance as the laser spot was brought into focus. The phase angle variations follow a pattern similar to that shown in figure 2.3d curve 1, which plots the theoretical phase variation with the normalised parameter optical spot size/ thermal diffusion length.

Changes in the optical spot size will also affect the phase-thickness calibration curve and hence lead to incorrect thickness measurements. Measurements of the phase variation with coating thickness for different beam diameters is shown in figure 4.5b. The sample was a LC1B coating on stainless steel, the test frequency 10 Hz and a laser power of 3 watt. Decreasing the optical spot size not only shifts the phase-thickness calibration curve into an advance but also reduces the magnitude of the overall phase change. The explanation for the phase advance has been discussed above. The reduction of the total phase change is related to; a) the three dimensional flow of heat in the sample with

small beam diameters and, b) changes in the thermal properties of the coating. Figure 4.5c shows a theoretical plot of the phase angle variation with coating thickness and different optical spot diameters for a LC1B coating on stainless steel. The thermal properties of the coating are assumed to be unchanged at all the optical spot diameters and the phase value plotted is the value at the centre of the heating beam. The general phase variation in this figure agree qualitatively with those obtained experimentally. The main disagreement between the theoretical and experimental data is the magnitude of the total phase change at the smaller optical spot diameter. In the theoretical plot this phase difference is only two degrees compared to nearly ten degrees for the experimental data. This large phase difference is most likely to be related to changes in the coating thermal properties due the increased light beam intensity with beam focusing. This varies from an incident laser power of 3 watt deposited on a spot of 2 mm diameter down to a spot of 0.4 mm diameter. This correspond, roughly, to a steady state temperature change from 20 to 450 K, assuming heat generating efficiency of unity and 50% light absorption.

ELLIPSOIDAL COLLECTOR

In figure 4.6 the variation of the photothermal signal with incident laser power can be seen using an ellipsoidal mirror collector. Comparing this with figure 4.4, using the mirror collector has resulted in

a 30 fold increase in the detected signal. Measurements at laser powers down to 50 milliwatt was possible with a phase noise of one degree. Signal amplitude values at this power level corresponded to those obtained without the collector at a laser power of 1 watt. The phase angle showed little variation for laser powers greater than 2 watts but was observed to fall by 4 degrees with decreasing laser power. The reason for this large change in the phase angle at low power levels is unclear.

Although the detected signal was greater when using the collector there were problems when reflective surfaces were examined. Figure 4.7 shows the observed phase variation with sample rotation for bulk graphite and titanium. The phase angles from both surfaces are not the same despite the use of the interference reflection filter. Sample rotation appears to help the phase angle on the titanium surface to approach that on the graphite surface, but there is still a phase difference of nearly 10 degrees between the samples.

In figure 4.8 the reproducibility of two consecutive line scan traces are presented across a thickness step on an LC1B coating using this system. The laser power was a 100 milliwatt and the chopping frequency 10 Hz. In figure 4.9 the phase change across the thickness step with varying laser power is presented showing its invariance with increasing laser power.

4.1.3 SAMPLE AND DETECTOR ROTATION

A further experimental parameter that needs to be evaluated is the angular positioning of the sample/ detector. In figure 4.10 the variation of the photothermal signal with sample rotation and fixed detector position is shown. (Measurements without the ellipsoidal collector.) At the zero degree position the laser beam is normal to the sample surface. As the sample is rotated both the signal amplitude and phase angle show a maximum between -20 and -10 degree. In this orientation the sample is observed to be normal to the detector. The phase angle variation around the peak is less than one degree for a sample rotation of ± 20 degrees. Figure 4.11 shows the signal amplitude and phase variation with detector rotation. Again the phase angle changes very little when the detector is rotated by as much as 25 degrees.

Figure 4.12a shows the phase difference with sample rotation across a step thickness change on a LC1B coating sample from 150-200 μm. Typical lines traces are shown in figure 4.12b for various sample rotation angles. These measurements also show that within the experimental noise, the phase steps observed are unaffected by sample rotation.

4.1.4 DISCUSSION

The results reported above show that many non-thermal variables influence the phase angle of the detected signal.

a) IR emission from the laser.
b) Reflected laser light.
c) Sample / detector rotation.
d) Optical spot size.

These variables can make calibration curves unreliable and hinder quantitative analysis. The first two variables lead to a coherent noise signal and the last two are dependant on the experimental set-up. In 4.1.1 simple measures were outlined to reduce or eliminate phase variations associated with (a) and (b). In a practical system special dichoric filters will need to be used in separating the optical and IR component from the illumination source.

In 4.1.2-3 the magnitude of phase variations likely to be expected with optical spot size and sample/ detector positioning errors were determined. The relative positioning of the sample/ IR detector had little effect on the phase angle provided that the angular positioning variations were maintained less than 20 degrees. The largest variations in the phase angle resulted with changes in the optical spot size as this dimension became comparable with the thermal diffusion length, 200 μm. It was noted that as long as the laser beam diameter is in excess of 2 mm the phase angle remains constant.

The employment of an ellipsoidal mirror collector resulted in a 30 fold increase in the IR detection efficiency. The large solid angle of IR collection, 0.67 of the collector compared to 0.0016 of the unaided

detector, is the primary reason for the increase in detection efficiency. These figures suggest an expected increase in the detected signal of nearly 400. This has not been realised due to possible high reflection losses at the detector window/ filter for radiation incident at angles removed from the normal. Hence only a limited fraction of the collected IR radiation is focused on to the IR detector element. To regain the lost signal it will be necessary to collimate the incident radiation so that it is normally incident at the IR detector.

With this improvement in IR detection efficiency laser powers down to 50 milliwatt were sufficient for thickness measurements on LC1B type coatings. This power range is well within the capabilities of commercial low powered gas lasers and recently, high powered semi-conductor laser. Current technology offers continuous wave output of 1 watt [85]. In section 4.4 measurements are presented on thickness gauging of LC1B coating using a near IR laser diode for sample heating.

4.2 SURFACE ROUGHNESS

In this section measurements are reported to assess the effects of surface roughness on the phase angle of the photothermal signal. Measurements are first reported from as-sprayed 'fine' and 'coarse' LC1B coatings to determine the magnitude of phase angle

variations[1]. Data is also presented from bulk high density nuclear graphite with its surface roughened with emery paper or mesa cut.

4.2.1 LC1B FINE AND ROUGH COATINGS

The effects of surface roughness on the measured phase angle on plasma sprayed LC1B coatings with different thickness are shown in figure 4.13a-d for modulation frequencies of 10, 25, 36, and 64 Hz respectively. In all cases the phase angle measured on the rough coating shows a phase angle advance with respect to the values obtained on the smooth coating. The phase difference between the rough and fine surfaces rises to a peak as the coating thickness increases and appears to saturate with increasing frequency. In figure 4.14 the phase difference between the rough and smooth sample are plotted against root frequency. The phase measurements are from a 10 mm line average on a nominal 250 μm coating thickness. On removing the surface roughness by polishing (a 600 emery paper finish) the phase angle measured on this surface correlated well, see fig. 4.15, to that measured on the smooth as-sprayed sample.

4.2.2 GRAPHITE SAMPLES

In figure 4.16 the phase angle difference with root frequency from a 200 grit finish and a mesa saw-tooth cut graphite surface are presented. These sample surface conditions represent the widest difference in

1 Fine and coarse refer to the coating powder type used to deposit the coating.

the surface roughness and the surface thermal properties. The phase difference data of figure 4.16 is obtained from line trace measurements across a flat and rough region on a sample. Sample line traces across these surfaces are shown in figure 4.16c for a test frequency of 7 Hz. For the saw-tooth graphite sample the roughness peaks appear to be well resolved. On further investigation it was found that the optical spot size determined the magnitude of the phase peaks and their resolution. To cover the frequency range shown in these figures a cadmium mercury telluride (CMT) IR detector with a germanium lens was used for signal detection. The incident laser power was 5 watts. As with the LC1B coatings samples, the phase difference between the rough surface and flat (1μ alumina finish) shows an advance. The phase advance is also dependent on the modulation frequency. The peak phase advance observed on both sample is around 25-29 degrees. (The error bars shown in the figures are those from a line average of 15 mm on the rough surface and are not associated with electronic noise in the measurement system).

The data of figure 4.16b was fitted to the theoretical phase curves generated by modelling the saw-tooth roughness profile as a layer of finite thickness and differing thermal properties. Figure 4.17 shows the fitting obtained. The layer thickness used is the root mean square surface roughness and the thermal properties are used as the fitting parameters.

Assuming that the data fits the theoretical phase curve for a reflection coefficient of -0.65, then the effective thermal property values indicated in the figure are obtained. The mesa roughness profile behaves as though the thermal effusivity of the surface has been reduced by a factor of 5.

The phase advance on these graphite roughness samples were also found to be dependant on laser power. With increasing laser power the phase advance on the sample increased. Sample rotation had little effect on the observed phase advance on these graphite samples. These observations are summarised in figure 4.18.

4.2.3 DISCUSSION

The above measurements show that surface roughness induces a phase increase relative to that measured on a nominally flat surface. On a rough LC1B coating a phase advance of 2-3 degrees was measured. On a roughened graphite surface the phase advance was as high as 25-30 degrees. These initial observations suggest that the scale of the surface roughness and its thermal properties dictate the magnitude of the phase advance. A detailed study on the graphite roughness samples also showed that the phase advance is dependent on the modulation frequency, laser power and spot size.

Phase data obtained from LC1B roughness samples showed a close similarity to the theoretical phase variation modelled in figure 2.11 in which the surface roughness is represented by a finite layer of well

defined thickness and reduced thermal conductivity. A similar analysis of the phase data from the mesa graphite roughness sample was also possible with the conclusion that thermal effusivity of the surface layer had been reduced by a factor of five.

This surface roughness study has revealed the absence of a phase lag at a rough surface. A phase lag may be expected if one consider phase variations from the edges, corners and mesa structures on the sample surface samples [86]. A numerical analysis is required to determine whether a phase lag or an advance is expected at a rough surface. A difficulty with the test samples used above is that both the surface topography and surface thermal properties were altered with polishing/ roughening. This makes it impossible to correlate the observed phase angle changes with surface topography only. For the samples studied here it appears that the surface thermal properties changes are contributing significantly to the phase advances observed.

4.3 DEFECTS

Subsurface defects have a characteristic phase response with increasing frequency namely a phase advance at low frequencies to a phase lag at high frequencies. In this section measurements are reported on manufactured defect samples to assess the photothermal technique for subsurface defect characterisation and the detection of contacting interfaces. The photothermal system is also compared with ultrasonic measurements.

4.3.1 SQUARE DEFECTS IN LC1B COATINGS

PHOTOTHERMAL INVESTIGATION

In figure 4.19 50 mm line scan traces are presented across the defects in polished and as-sprayed LC1B coating at a frequency of 8 Hz. The line traces are at the positions indicated in figure 4.20. Table 4.1 provides a summary of the phase variation over the defect regions. In both samples defects A,B and D were readily detectable. Defect C failed to be detected. A phase increase of about 1.5 degrees was observed at the defect sites. The defects found in the polished sample showed up more strongly than those detected on the as sprayed sample. To determine whether the phase increase at the defect site is due to adhesion deficiencies a frequency response of defect A in the as-sprayed and B and D in the polished samples were examined. Figure 4.21 shows line traces of the phase variations of these defects with frequency. The absence of a phase lag with increasing frequency suggests that these phase variations are not due to subsurface adhesion defects. The phase advance at the defect is more indicative of localised subsurface thermal property change probably due to increased porosity. This assertion was verified by optical microscopy, figure 4.22, where significant variation in the local microstructure between sites remote and within the defect regions were observed.

ULTRASONIC INVESTIGATION

An ultrasonic examination [87] of the as-sprayed defect sample was also undertaken to compare its performance with the photothermal technique in sensing these defect sites. Measurement on the sample were made difficult due to sample curvature near the defect regions. Figure 4.23 shows line scan traces of signal attenuation across the 'defect' regions in the polished, fig. 4.23a, and as-sprayed, fig.4.23b, sample. Only defects A and B in the as-sprayed sample showed significant perturbation in the signal variation across the defect regions. A decrease in signal attenuation rather then an increase was observed across the defect sites. The decrease in signal attenuation may be explained as being due to the presence of water in the porous microstructure which will result in lower impedance mismatch losses of the transmitted ultrasonic beam.

Both the photothermal and the ultrasonic measurements indicate the absence of interface defects in these samples. There is however a localised change in the coating microstructure.

4.3.2 DIFFUSION BONDED DEFECT SAMPLES

With the difficulty in producing completely delaminated defects in plasma sprayed coatings, defects in diffusion bonded mild steel/ mild steel (MS/MS) and mild steel/ stainless steel (MS/SS) samples were studied. Details of sample geometry and defect sizes are summarised in figure 3.6.

In figure 4.24 line scan traces through the centre of 10 and 5 mm defect in MS/MS sample (sample no. 4) are presented at several modulation frequencies. The sample surface was lightly darkened with soot from a candle flame to increase light absorption and thermal emission. The traces presented show a phase lag at the defect. The magnitude of phase lag goes through a maximum with increasing frequency and disappears in the sample phase noise at higher frequencies. This type of phase variation is characteristic of subsurface adhesion defects.

Figure 4.25 shows a plot of the phase difference[2] with root frequency of the 5 and 10 mm defect diameter in MS/MS fitted to theoretical defect phase loci using literature values for the thermal properties of mild steel and air. The theoretical curves are generated assuming one dimensional heat flow and air-gap defects of finite thickness. The data appears to be a good fit at high modulation frequencies for both defect diameters, 5 and 10 mm. At low frequencies however, there is a significant departure from the one dimensional defect phase locus with the 5 mm diameter defect. The iterative fitting technique used predicts the defect depth to be around 900 μm and defect thickness greater than or equal to 100 μm. The defect depth is in good agreement with the thickness measurement provided with the test sample of 1 mm.

Further line traces from defects of different diameter are presented in figure 4.26a-d for a MS/SS

---

2 phase difference = phase at defect minus phase away from defect.

sample (sample no. 3) and a composite phase difference against root frequency plot is compiled in figure 4.27. With decreasing defect diameter the phase difference at the defect becomes more positive and there is poor correspondence of the observed phase measurement to that of the one dimensional defect model. This departure of the experimental data from the one dimensional defect phase curve is due principally to the three dimensional diffusion of heat at low modulation frequencies. At these low frequencies the thermal diffusion length becomes large (few millimetres) and lateral heat diffusion can no longer be neglected. A three dimensional heat diffusion analysis provides the phase loci shown in figure 4.28 for the phase angle variation at the surface of the above defect sample with different optical spot diameters[3]. The departure of the phase angle at low modulation frequencies is clearly shown in this figure as is the dependence on heating beam diameter.

4.3.3 THERMAL CONTACT RESISTANCE

In figure 4.29 line traces are presented of the phase difference between contacting and non-contacting surfaces demonstrating the ability of photothermal technique in detecting contacting surfaces. The contact geometry for both figures is shown figure 3.7. In both cases the subsurface contact is readily visible and the phase change at the contact is positive. This can be explained qualitatively as illustrated

3 In the phase plot of figure 4.28 no account has been taken of heat diffusion around the defect.

schematically in figure 4.30. With out contact the phase angle recorded represents a defect of infinite contact resistance. With contact, the thermal coupling between the samples significantly reduces this resistance and the contact phase curve is forced into an advance relative to the no contact phase locus. It is the difference of these phase curves which provides the positive phase change shown in figure 4.29.

4.3.4 DISCUSSION

The above investigations show clearly the sensitivity of the thermal wave technique for detecting material porosity, interface defects and pressed contacts. A comparison between ultrasonic and photothermal measurements appear to suggest that the thermal wave technique is more sensitive in detecting abnormal subsurface conditions then ultrasonics. This aspect of the study requires further investigations as the ultrasonic response of the 'square defect' samples were only studied at one arbitrary test frequency of 5 MHz.

Phase angle measurements on the diffusion bonded defect samples of varying diameter and depth illustrate the capability and limitations for quantitative subsurface defect characterisation. To analyse the phase angle data at low frequencies a numerical model needs to be developed which takes into account the finite width and thickness of the defect, the optical heating and IR detection spot sizes on the sample.

4.4 SEMI-CONDUCTOR LASER DIODE SYSTEM EVALUATION

It was noted in section 4.1.4 that the use of an ellipsoidal mirror collector resulted in a 30 fold increase in the detected signal. It was also discussed that this improvement in the IR collection efficiency would allow much lower laser powers to be used for sample heating. In the following sections measurements are reported on the use of an optical fibre coupled semiconductor laser diode for sample heating. Figure 4.31 shows a schematic illustration of the experimental set-up used for evaluating the laser diode NDT system.

4.4.1 LASER POWER LEVEL STUDY

In figure 4.32 the signal amplitude and phase variation with laser power is shown. The modulation frequency was 10 Hz and the sample a 250 μm thick LC1B coating on stainless steel. A linear change in signal amplitude with laser power is observed between 0.05 and 0.3 Watt. Signal levels recorded are roughly a factor of 3 lower when compared with the values obtained with the argon ion laser. The phase angle shows a small variation with laser power and the phase noise is less than 0.5 degrees for laser power above 0.15 Watt.

4.4.2 SIGNAL AMPLITUDE AND PHASE ANGLE VARIATION WITH FIBRE HEAD POSITIONING

With optical fibre coupling of laser emission the heated spot on the sample surface can be located in a variety of position with respect to the area sensed by

the IR detector. An assessment is therefore necessary to determine the effects of fibre positioning on the detected photothermal signal. In figure 4.33 the signal amplitude and phase variation with the distance of the fibre head from the sample is plotted. The signal amplitude initially rises and then fall with increasing distance as the fibre head is moved away from the sample surface. The initial rise of the signal is due to the detector being able to 'see' more of the heated area as the fibre head is retarded. The signal decay and increasing phase lag as the fibre head is further retarded from the sample surface is mainly due to increases in the laser spot diameter on the sample surface as a result of beam divergence. At very short distances from the sample surface the spot size can be expected to be that of the optical fibre diameter, 250 μm. This diameter is approximately equal to the thermal diffusion length in the coating of 200 μm at 10 Hz. A similar phase behaviour was also noted in section 4.1.2, figure 4.5, where the argon ion laser beam diameter is varied.

Figure 4.34 shows the variation of signal amplitude and phase angle as the fibre head is moved through the IR detection spot horizontally. The signal amplitude change is symmetric about the detection spot but the phase angle change is asymmetric. The reason for this is due to a covering of the detection spot by the optical fibre head as it is moved over the region sampled by the IR detector (see fig. 4.31). Moving the fibre head in a vertical direction through the

detection spot, the data shown in figure 4.35 are obtained. In this case both signal amplitude and phase angle show the expected symmetric distribution about the detection spot.

4.4.3 LC1B COATING THICKNESS MEASUREMENTS

In figure 4.36a and b phase angle line scan traces are presented for measurements on LC1B coatings at 10 and 25 Hz, respectively, using a laser power of .3 Watt. Also shown on these figures are the corresponding traces obtained with argon ion laser heating. The latter traces are slightly displaced vertically for clarity. There is excellent reproducibility with consecutive traces obtained with the semiconductor laser and also a close match to the data obtained with the argon ion laser system. The 'noisy' appearance of the line traces obtained with the semiconductor laser is believed to be associated with the finer spot size used for sample heating.

4.4.4 DISCUSSION

These initial measurements with the laser diode system clearly demonstrate the success in using such a laser source for sample heating. The thickness measurements obtained are very similar to those obtained with the argon ion laser. With the focused IR detection system used here a careful control over the IR detection and the illumination spot on the sample is required. There relative positions on the sample need to be maintained fixed to avoid phase angle

variations of the type illustrated in figures 4.33-4.35.

A practical difficulty in the usage of the laser system was the alignment of the laser illumination (which is invisible with protective eye goggles) with the IR detection spot on the sample. The latter is determined by maximising the detected photothermal signal with fine adjustments of the vertical and angular positioning of the IR detector. For a practical system a set-up in which the optical and IR detection spot are coincident is very desirable.

4.5 INFRARED DETECTOR EVALUATION.

In the following paragraphs measurements are presented of the infrared detector frequency response, the photothermal frequency response of bulk titanium and a LC1B coating and the phase angle noise of the detection system.

4.5.1 INFRARED DETECTOR FREQUENCY RESPONSE.

Figure 4.37a and b show respectively, the signal and phase response with frequency of the pyroelectric TGS infrared detector obtained when viewing chopped thermal radiation from a soldering iron at a temperature of 200 C through a 10 mm aperture. The frequency range covered is from 10 to 880 Hz. At frequencies less than 25 Hz the signal variation appears to saturate. With increasing frequency the signal decays very rapidly at a rate approximately proportional to inverse cube frequency. The phase

angle variation also shows a large change. The rate of change being rapid between 10 and 500 Hz and tending to saturate for frequencies greater than 500 Hz.

4.5.2 PHOTOTHERMAL FREQUENCY RESPONSE.

The above frequency measurements can be used to obtain the photothermal frequency response of a test sample. Figures 4.38a and b show respectively, the normalised signal and phase variation of a 10 mm thick titanium and a 250 μm thick LC1B coating on stainless steel. The incident laser power was 4 watt and the IR detector was screened by the laser light reflection filter. The normalised signal data was obtained by evaluating the ratio of the observed signal value to that of the detector frequency response signal. The phase data is obtained by a subtraction of the measured sample phase angle with that of the detector phase at the corresponding frequency. The normalised signal variation for both samples show that the photothermal decays as inversely proportional to square root frequency. The phase angle variation is seen to be flat at high frequencies and increases at low frequencies.

4.5.3 PHASE ANGLE NOISE

Figure 4.39 shows the observed phase noise with frequency measured at a spot on a LC1B coating from 200 measurements in a time period of 5 minutes. The phase noise is seen to be between 0.1 and 0.5 degrees and increases with increasing frequency. In these

measurements it was noted that for signal values below 0.2 millivolts the phase noise can be in excess one degree. Without any laser illumination no signal was detectable by the lock-in amplifier. A minimum detectable signal of approximately 50 microvolts could be measured by the lock-in amplifier. In this case the phase noise recorded using a 3 second time constant was in excess of 5 degrees.

4.5.4 DISCUSSION.

The sharp variations of the detector frequency response is due to the close match of the time constants of the detector signal responsivity [78,83]. A basic expression for signal frequency response of a pyroelectric detector excluding post detection electronic amplifying circuits takes the form:

$$(4.2) \qquad Signal \propto \frac{A\omega}{\left(1+\omega^2\tau_E^2\right)\left(1+\omega^2\tau_T^2\right)}$$

where τ_E and τ_T are respectively, the electrical and thermal time constants for the infrared detector [83]. 'A' is a constant for the detector and represents the pyroelectric, thermal and physical properties of the detector element. This equation predicts at high frequency, a signal variation inversely proportional to frequency. The is in disagreement with the observed signal decay rate of inverse cube frequency. A possible reason for this discrepancy may be due to the neglect in equation 4.2 of the modification of the signal frequency response with associated signal amplifying circuits. These circuits are widely used

to boost the voltage responsivity of the infrared detectors at the expense of a limited frequency response [78].

The inverse square root frequency variation of the photothermal signal for the titanium and LC1B coating indicates that these sample are behaving as semi-infinite opaque media. This frequency variation of the photothermal signal follows that predicted, see table 2.2, by the one heat diffusion theory. Another prediction of this theory is phase angle independence with frequency. This behaviour appears to be satisfied with the experimental data at frequencies above 40 Hz. At frequencies lower than this the normalised phase angle data shows an increase. These increase are due to two different reasons. For the titanium sample the phase increase is related to three dimensional heat diffusion effects, in particular with the increase in the thermal diffusion length with decreasing frequency relative to the laser spot size. For the coating sample the phase increase due to thermal wave interference in the coating. As discussed in section 2.4 a phase angle increase will be obtained from coating systems in which the coating/ substrate reflection coefficient is negative, i.e a coating with its thermal effusivity lower than that of the substrate.

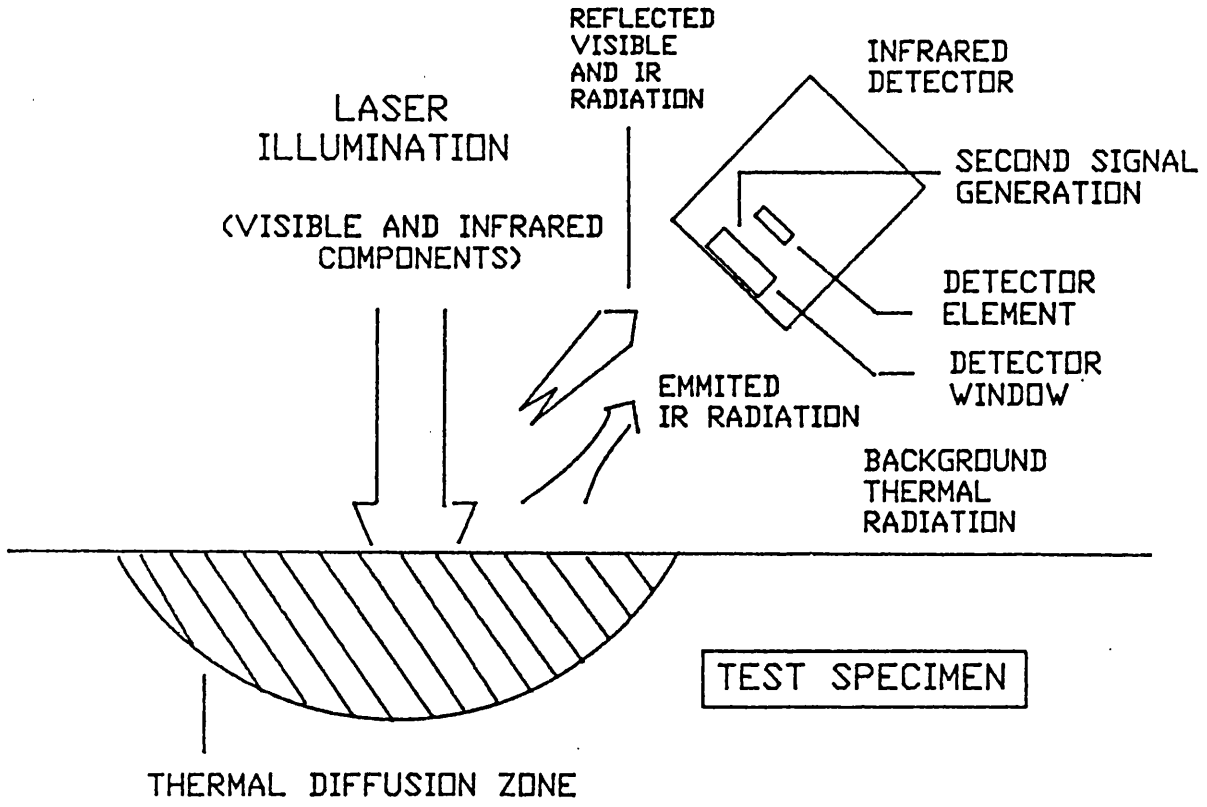

Figure 4.1: Radiation scene viewed by the infrared detector.

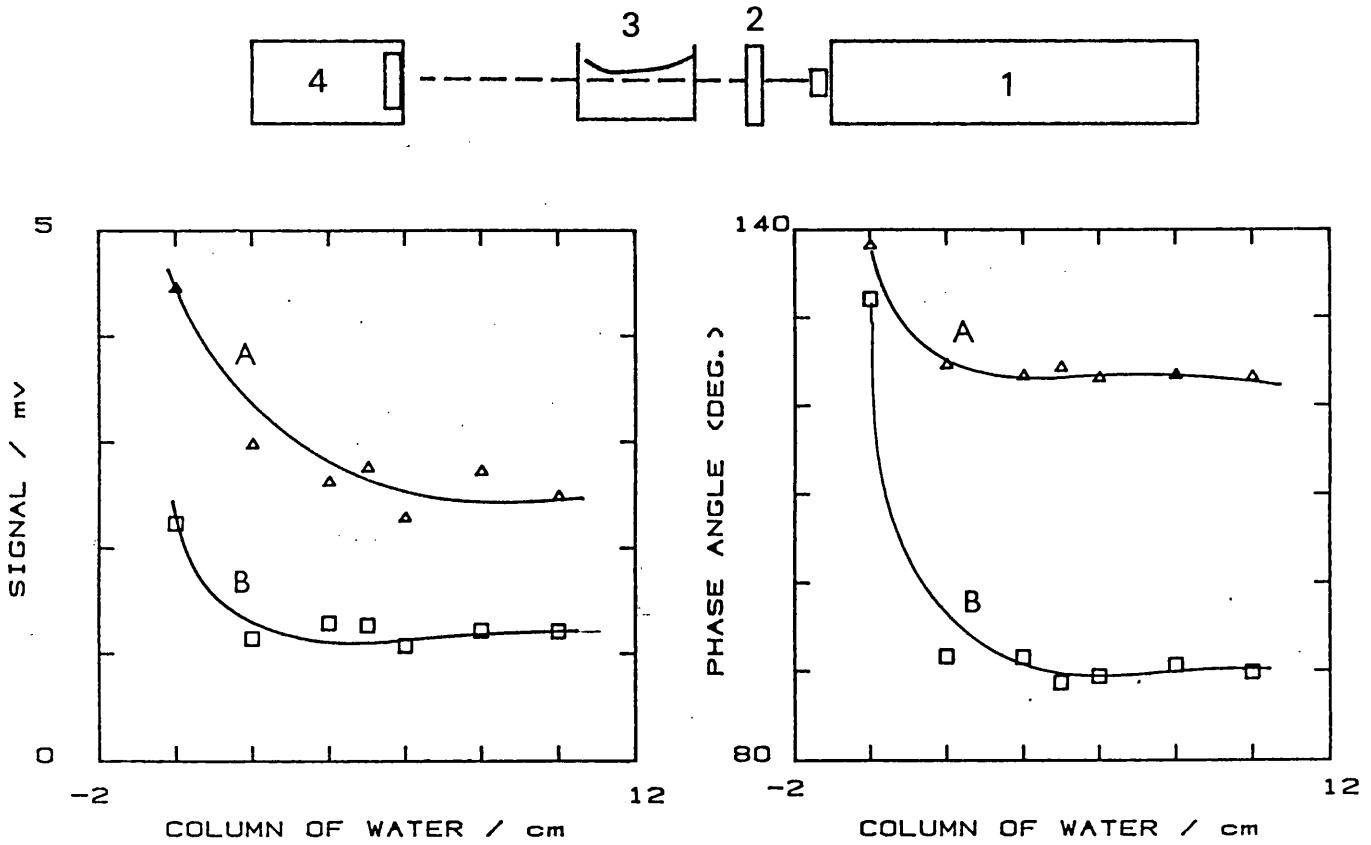

Figure 4.2: Top: A transmission photothermal set-up. 1) Argon ion Laser, 2) Light chopper, 3) water in rectangular container, and 4) infrared detector.
Bottom: Measured signal and phase variation with water column length for laser light normally incident on the detector window (A), and on the interference reflectance filter (B).

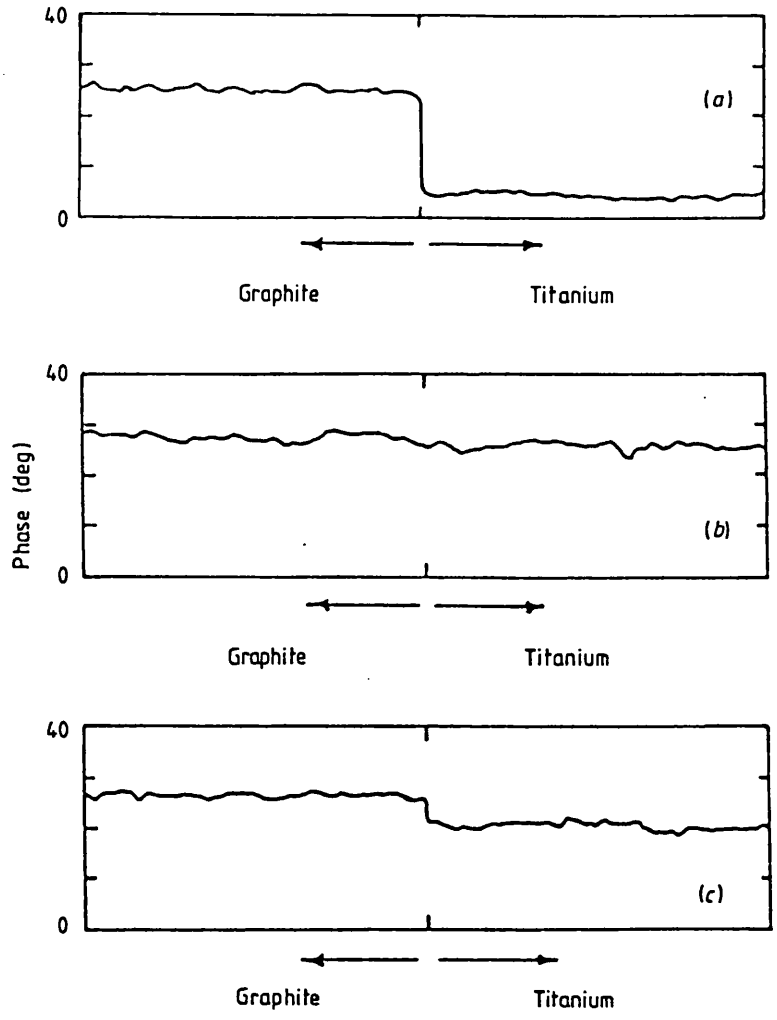

Figure 4.3a: Phase angle trace across a graphite and titanium surface without laser light screening.
b) As above but with interference filter fitted to the infrared detector.
c) As fig. 4.3a above but with sample rotated to reflect away the scattered laser light from the infrared detector.

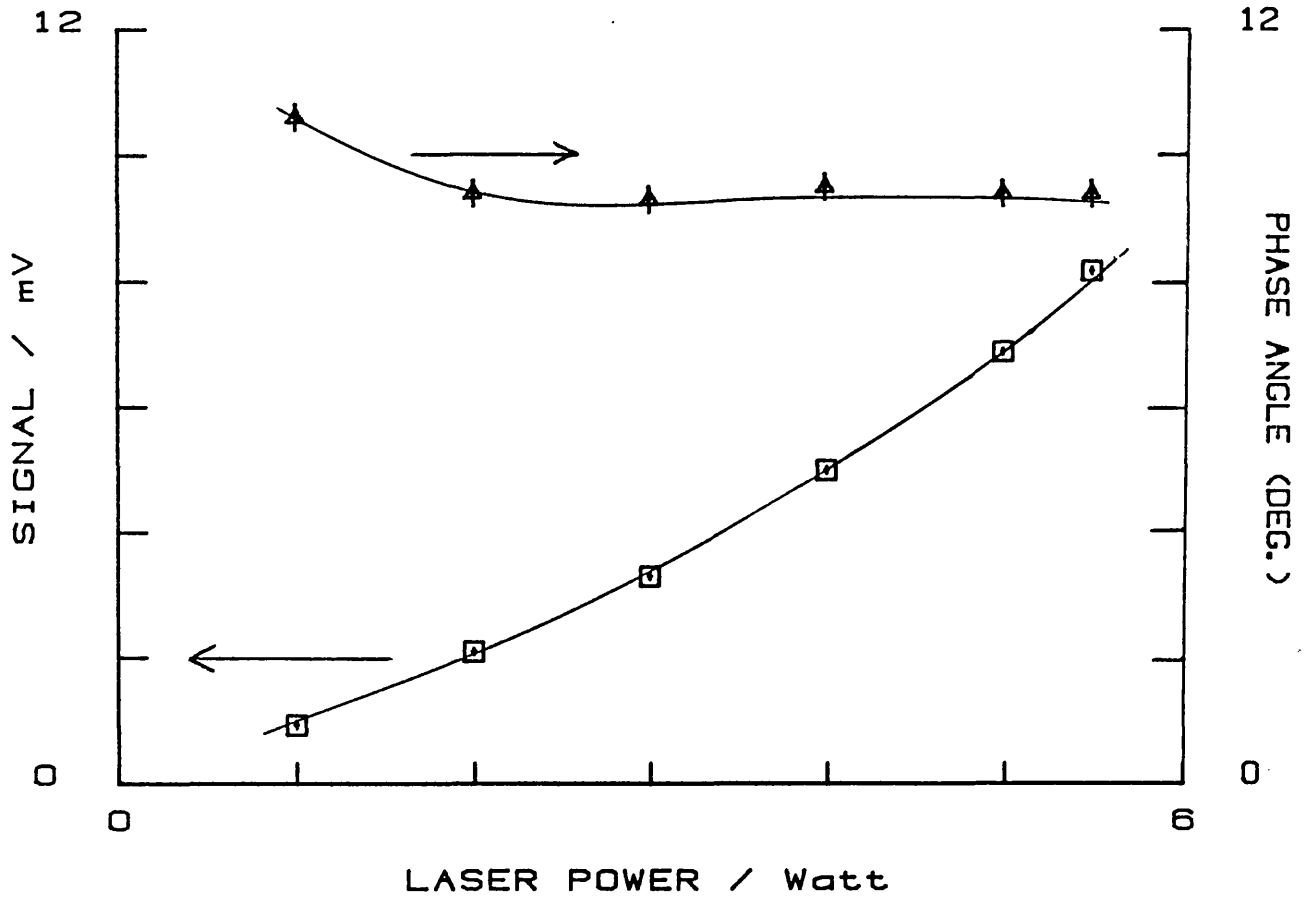

Figure 4.4: Photothermal signal variation with incident laser power on a LC1B coating sample on 316 stainless steel at a modulation frequency of 10 Hz.

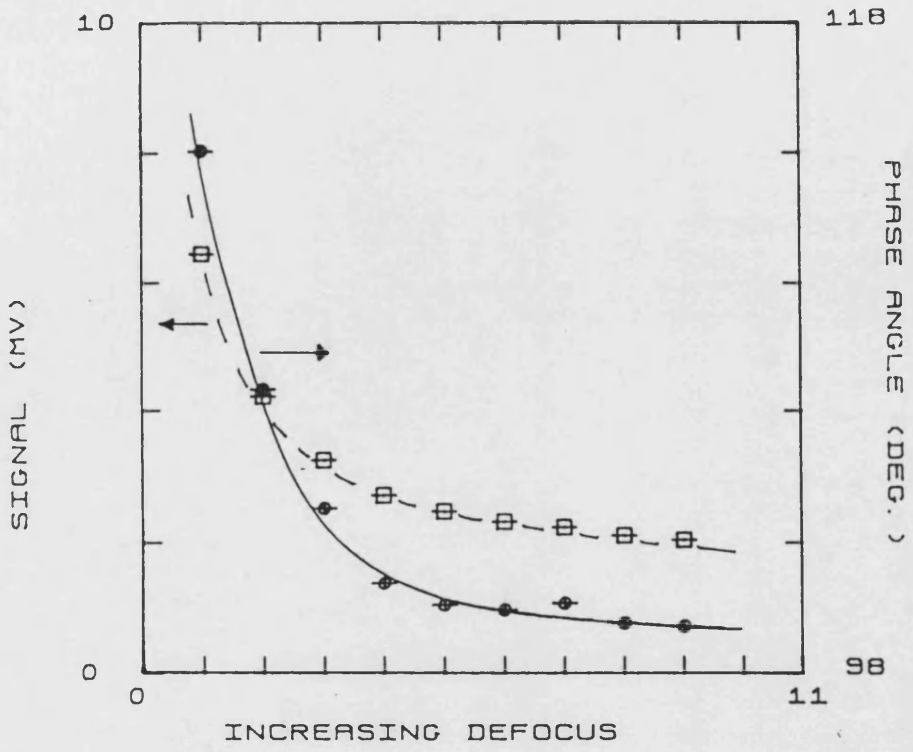

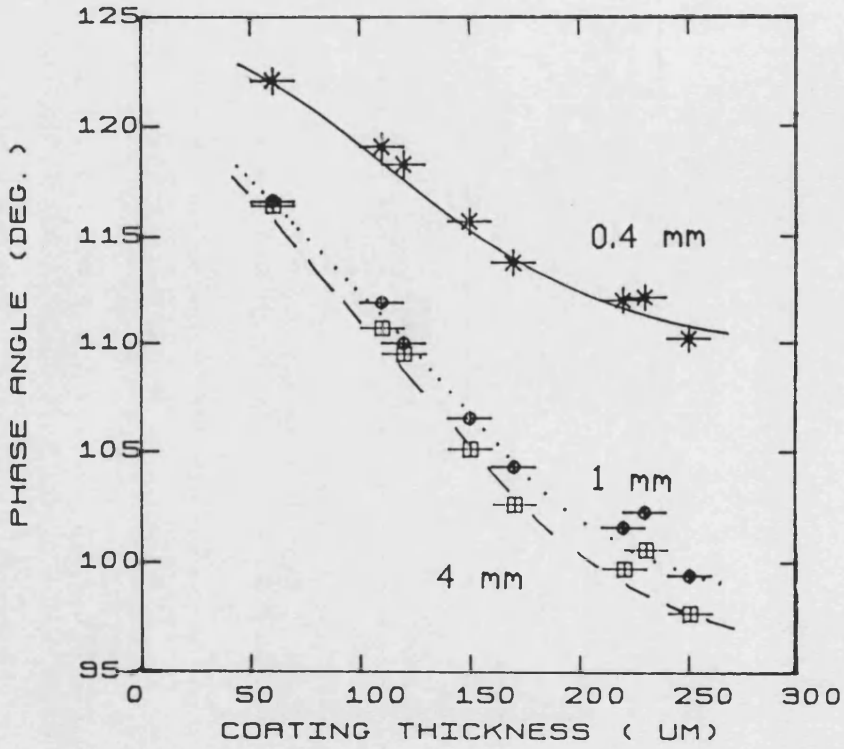

Figure 4.5a: Photothermal signal variation with increasing optical spot size.

Figure 4.5b: Phase angle variation with coating thickness and optical spot size. Test frequency 10 Hz.

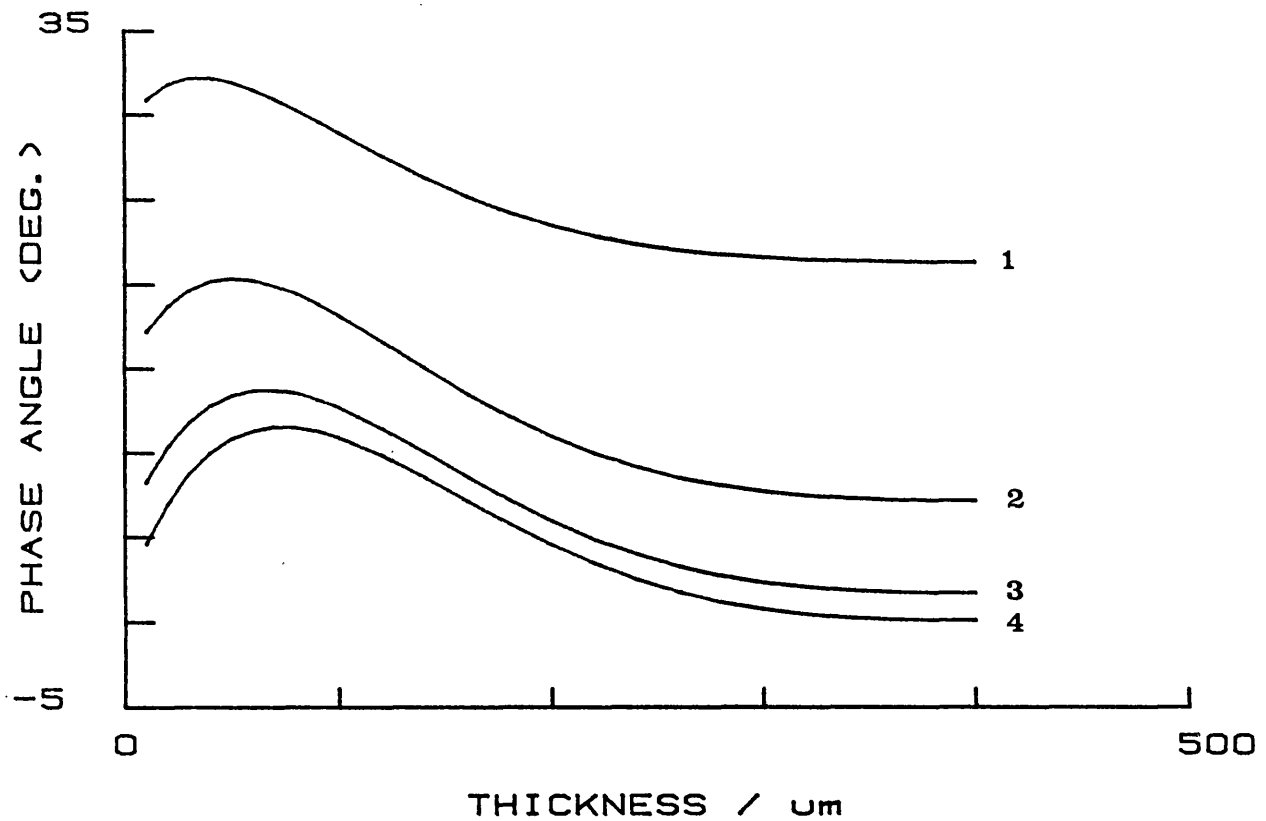

Figure 4.5c: Theoretical phase angle variation with coating thickness and optical spot size. Optical spot size 1) 0.4, 2) 1, 3) 2, and 4) 4 mm. Modelled sample is a LC1B coating on 316 stainless steel and a modulation frequency of 10 Hz. (Note no account has been taken of signal averaging by the IR detector over the detection area.)

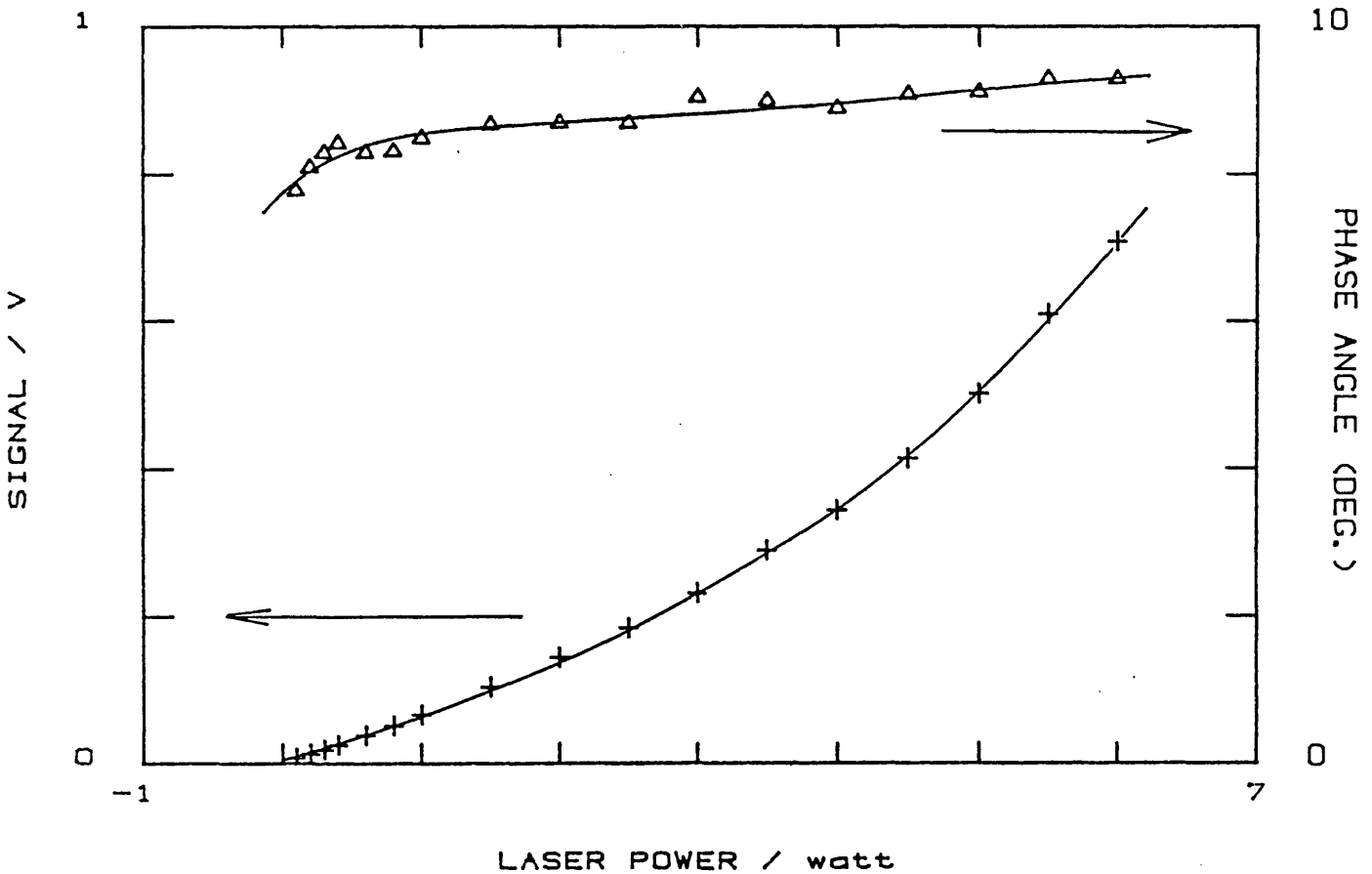

Figure 4.6: Signal amplitude and phase angle variation with laser power using the ellipsoidal mirror collector.

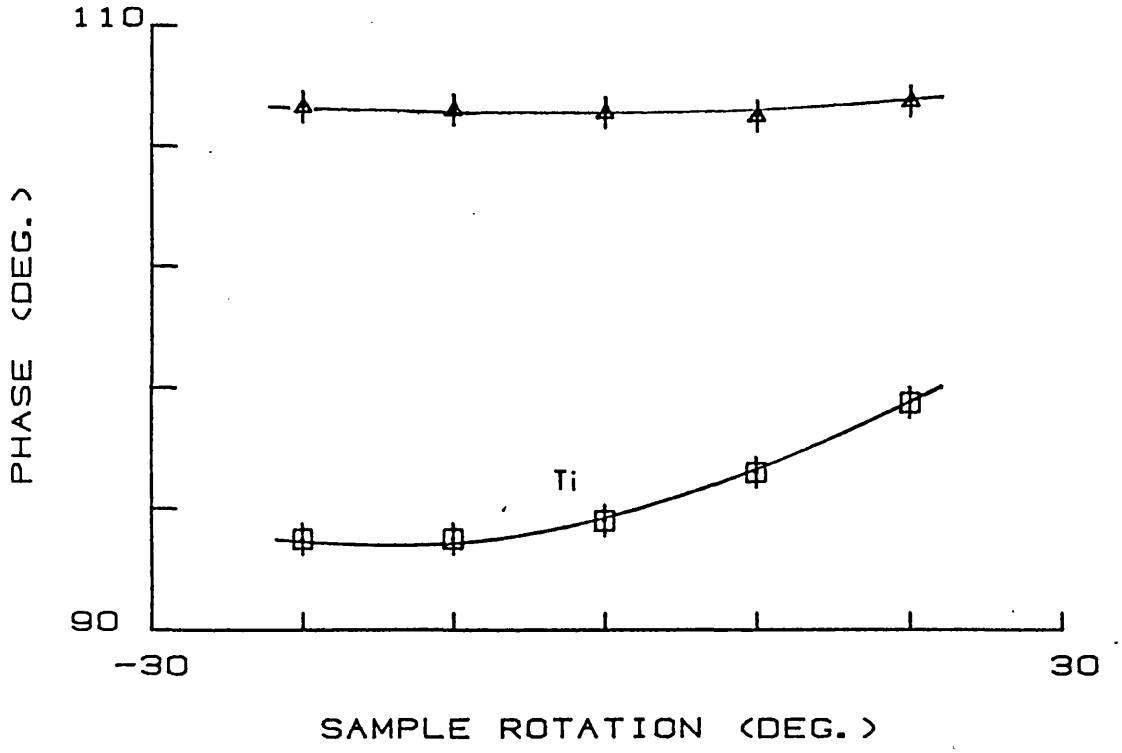

Figure 4.7: Phase angle variation with sample rotation for a graphite and titanium sample. Infrared detection with mirror collector.

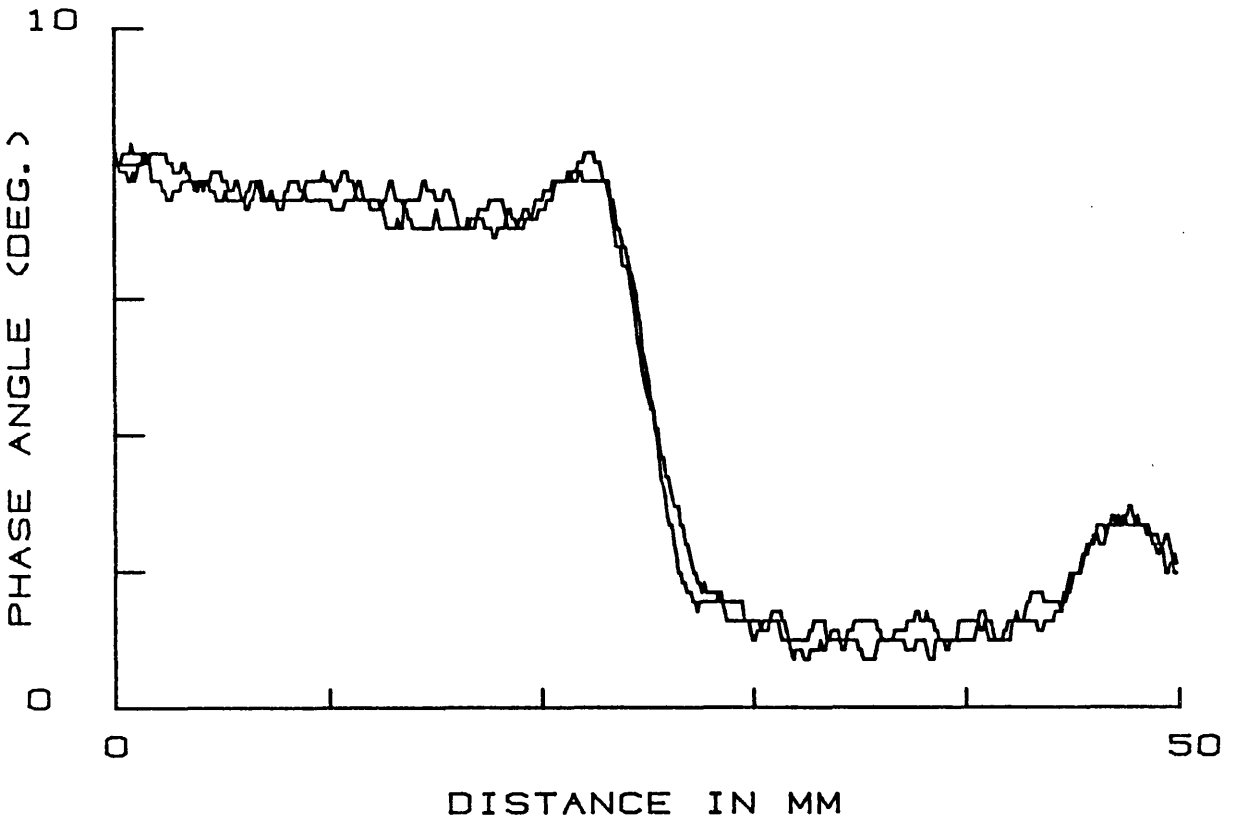

Figure 4.8: Consecutive 50 mm lines trace across a 150-200 μm thickness step on a LC1B coating. Incident laser power is 0.1 watt, the modulation frequency of 10 Hz and infrared detection with mirror collector.

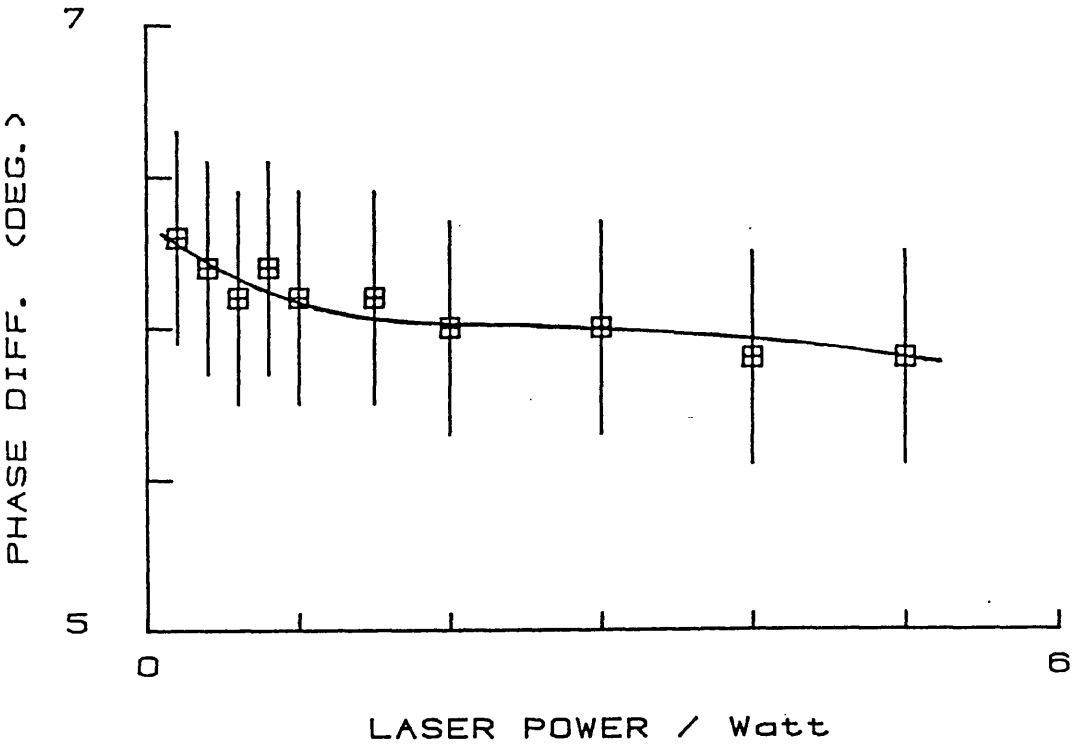

Figure 4.9: A plot of the phase angle change with incident laser power for a 150-200 μm thickness step on a LC1B coating at a modulation frequency of 10 Hz and infrared detection with mirror collector.

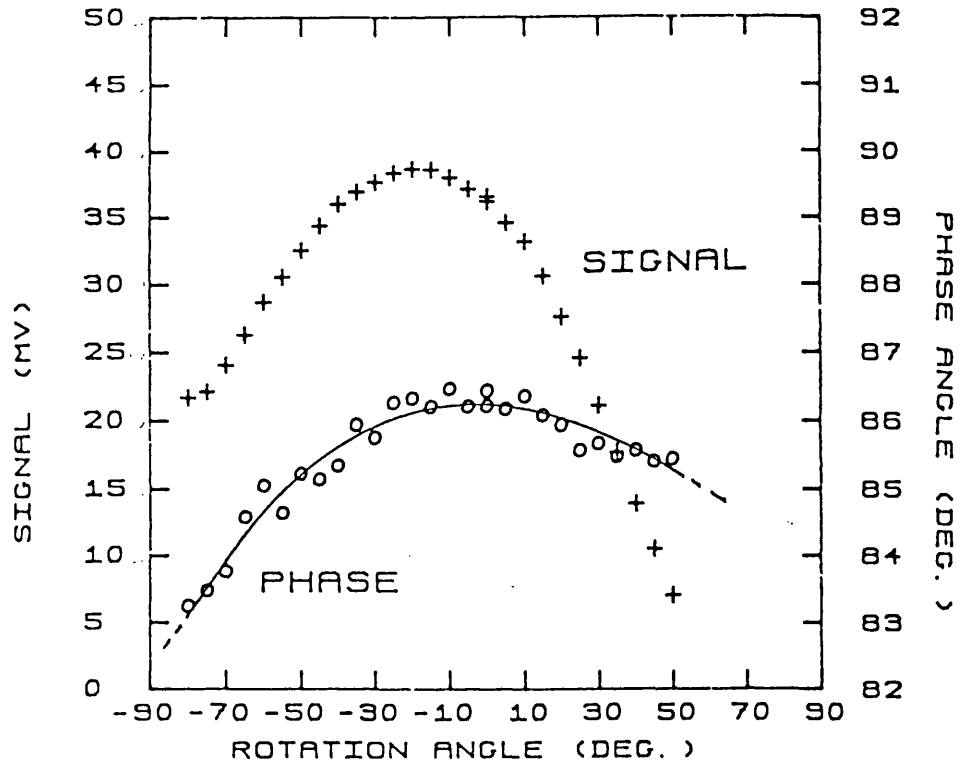

Figure 4.10: Photothermal signal variation with sample rotation.

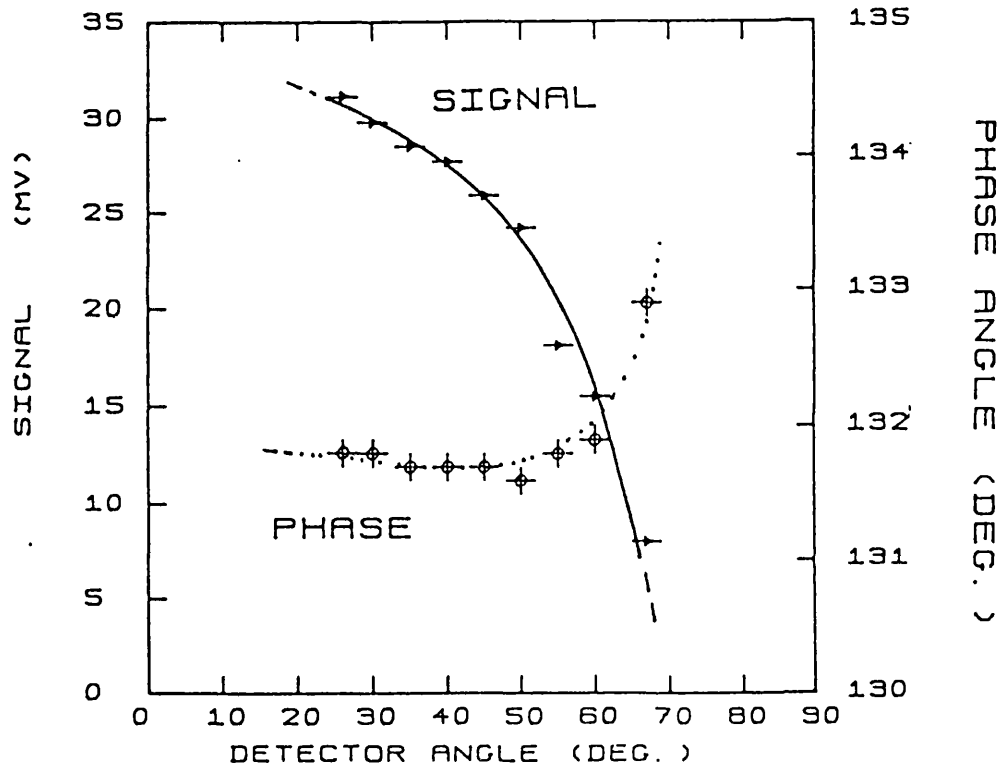

Figure 4.11: Photothermal signal variation with detector rotation.

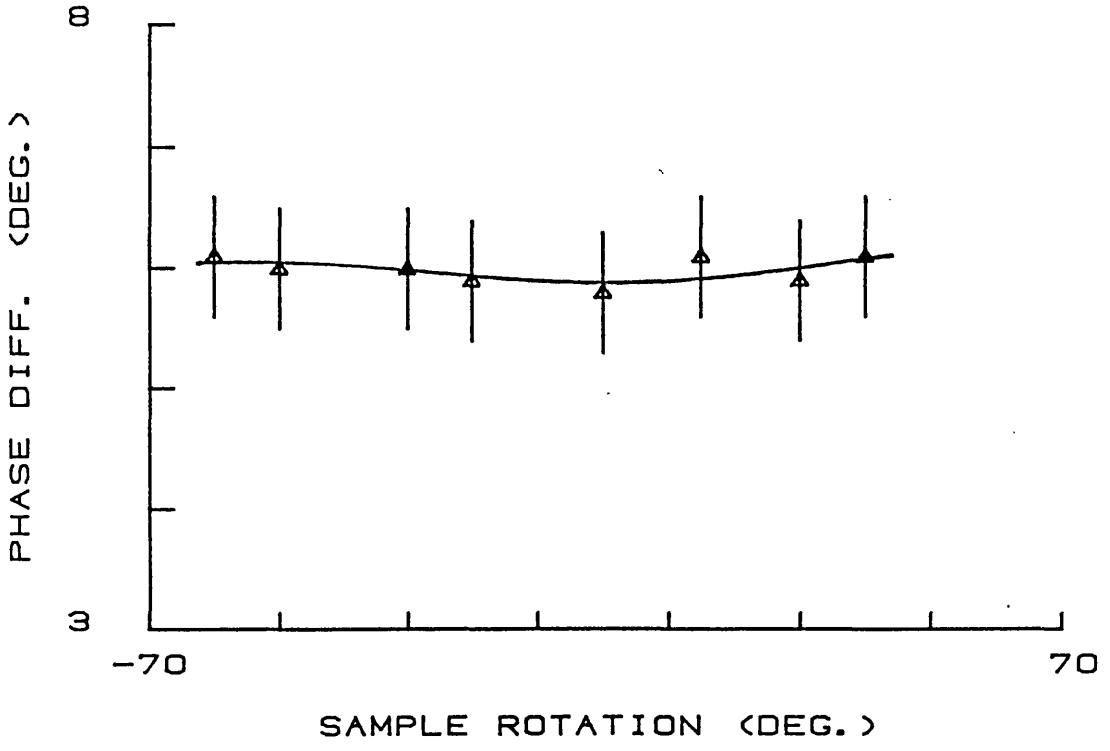

Figure 4.12a: Phase angle variation across a thickness step on a LC1B coating sample for various rotation angles

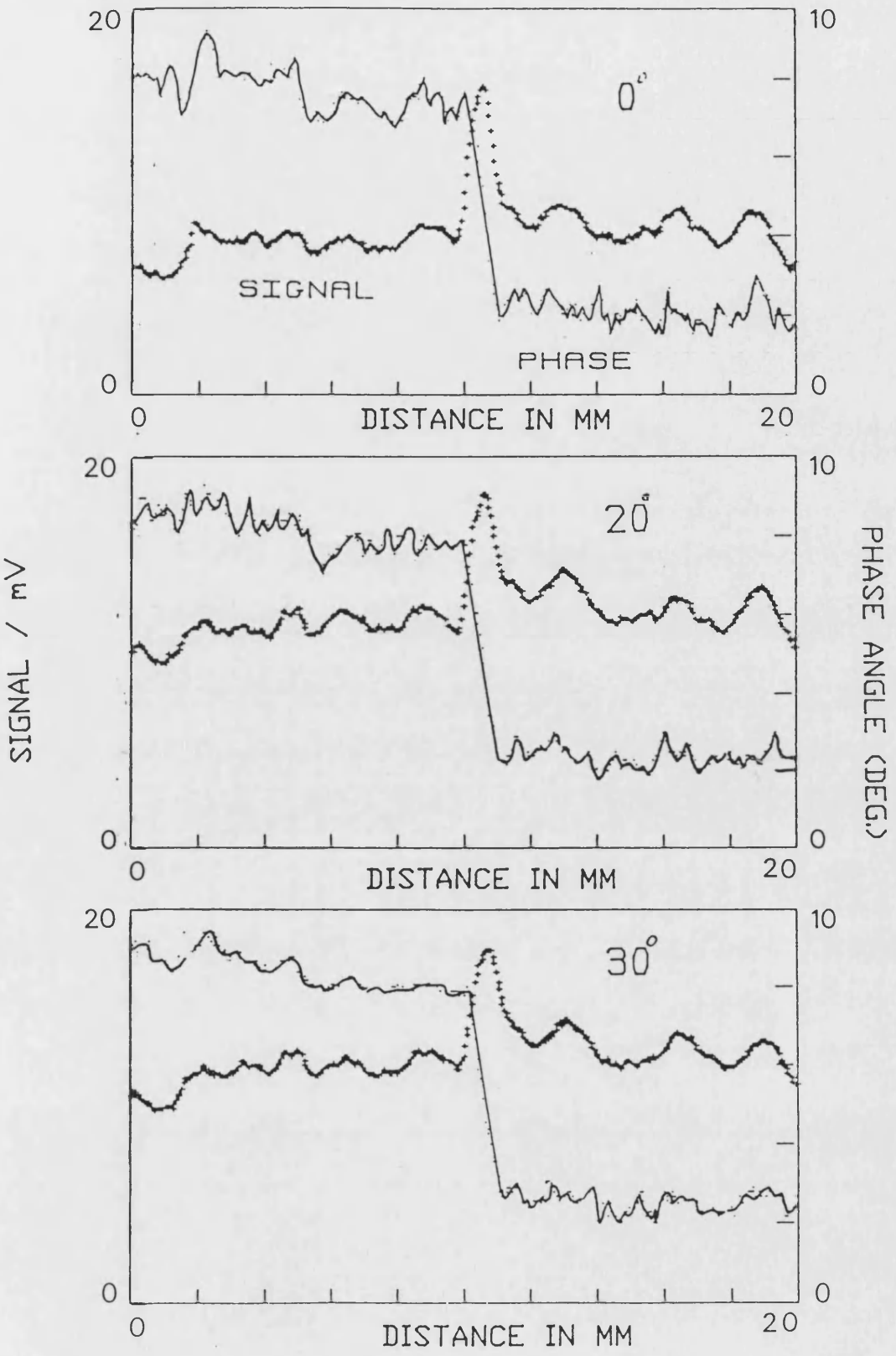

Figure 4.12b: Phase angle line traces across a step thickness change on a LC1B coating sample at various specimen rotation angles.

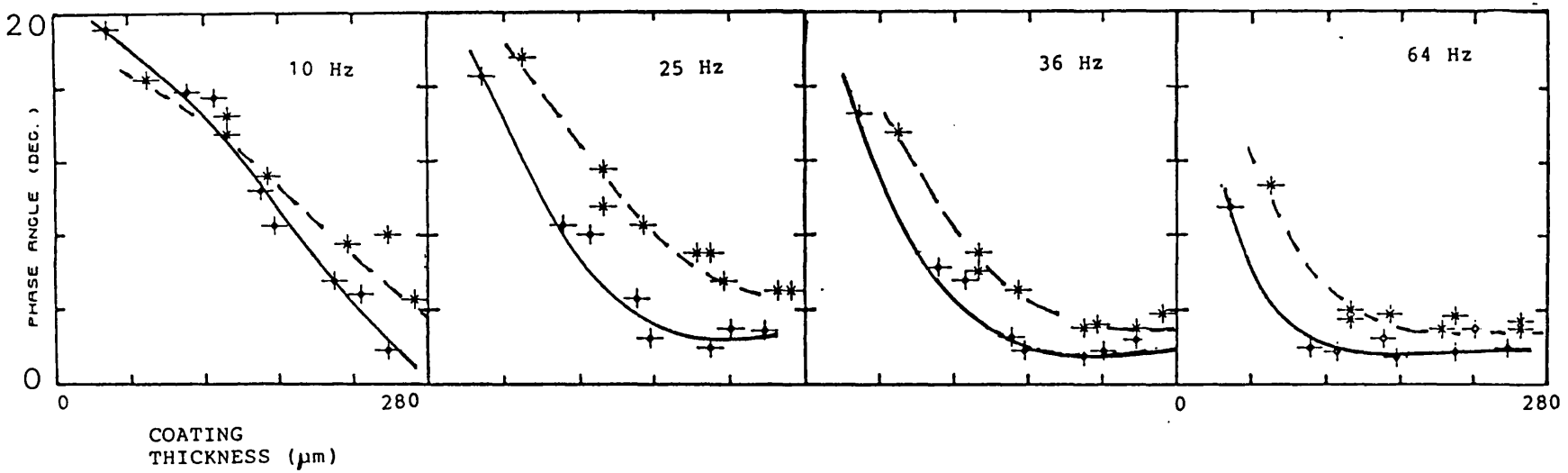

Figure 4.13: Phase angle measurements on fine (_____) and coarse (-----) LC1B coatings on 316 stainless steel at modulation frequencies of a) 10, b) 25, c) 36 and d) 64 Hz.

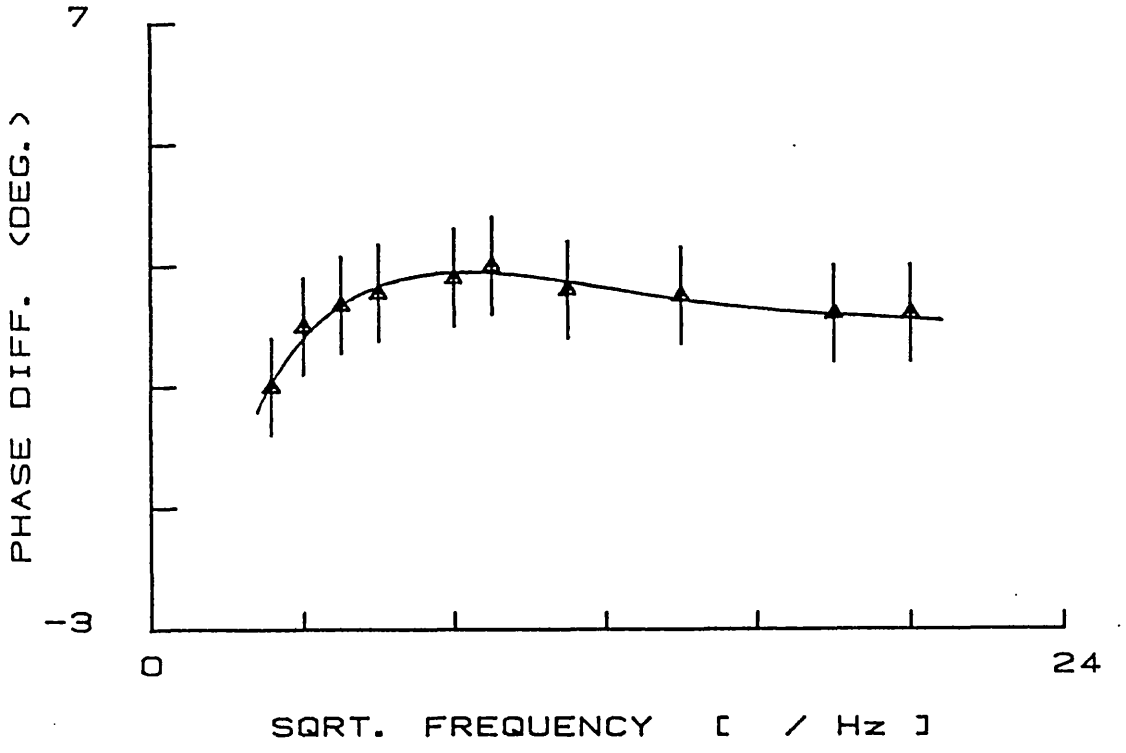

Figure 4.14: A plot of the phase difference with square root frequency between coarse and fine LC1B coating of nominal thickness 250 μm.

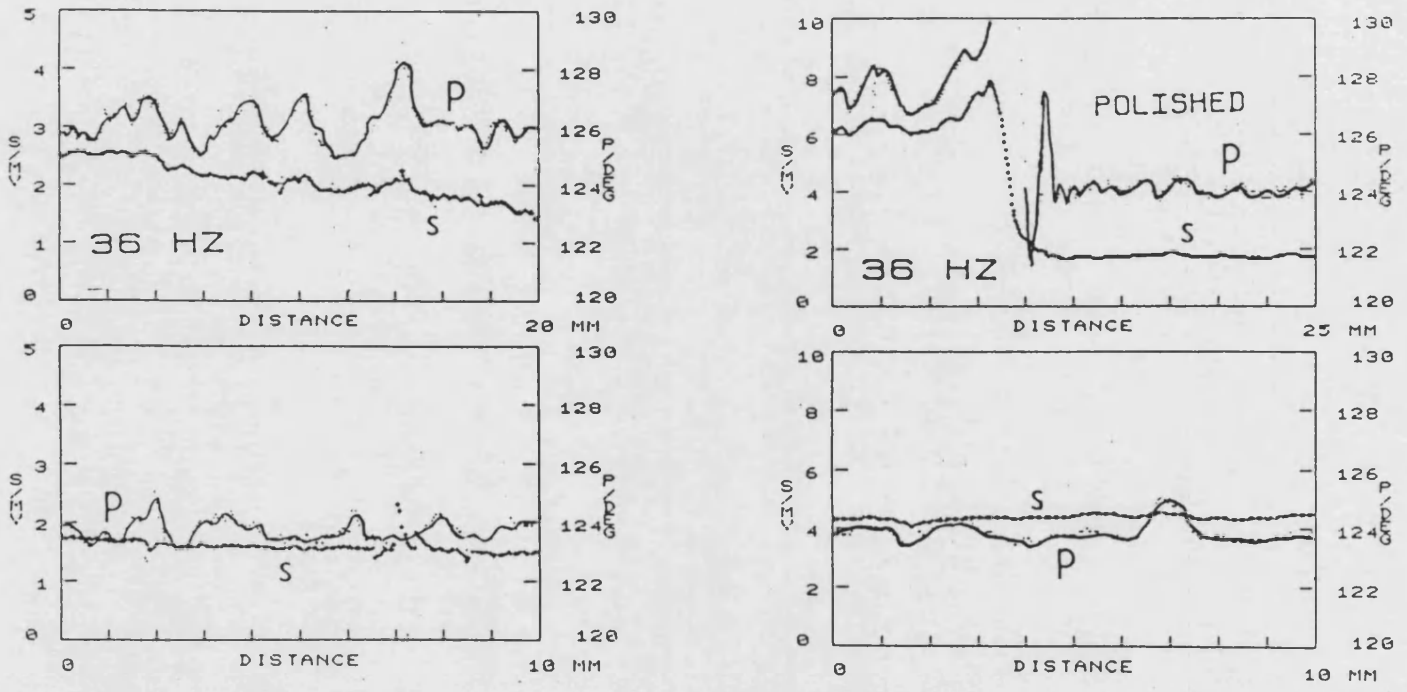

Figure 4.15: Phase angle line traces on coarse and fine LC1B coating before and after polishing. Top figure, phase on coarse sample and bottom figure on fine coating sample.

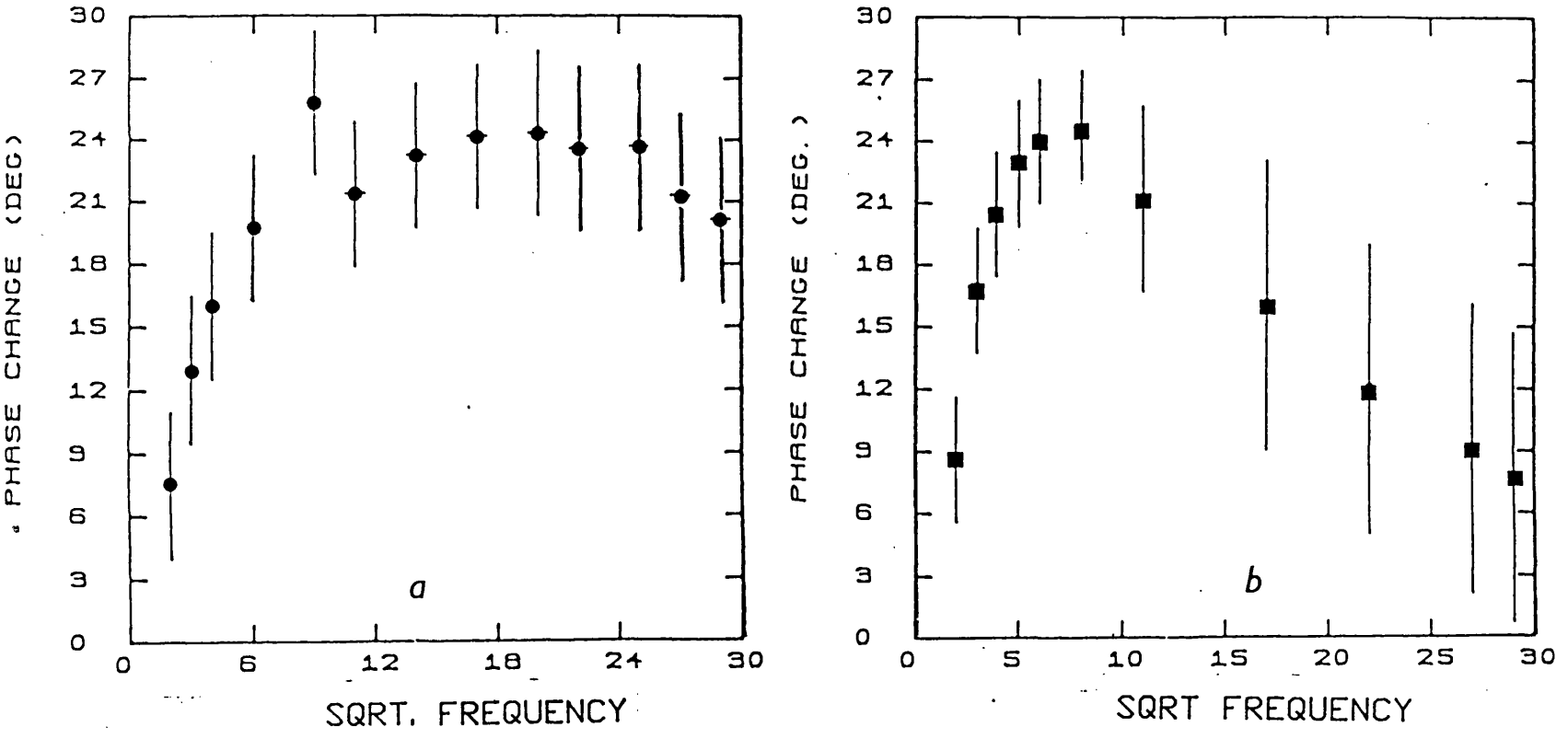

Figure 4.16: Plots of the phase difference (measured relative to a flat graphite surface) with root frequency for a) an sand paper roughened and b) a saw-tooth cut graphite surface.

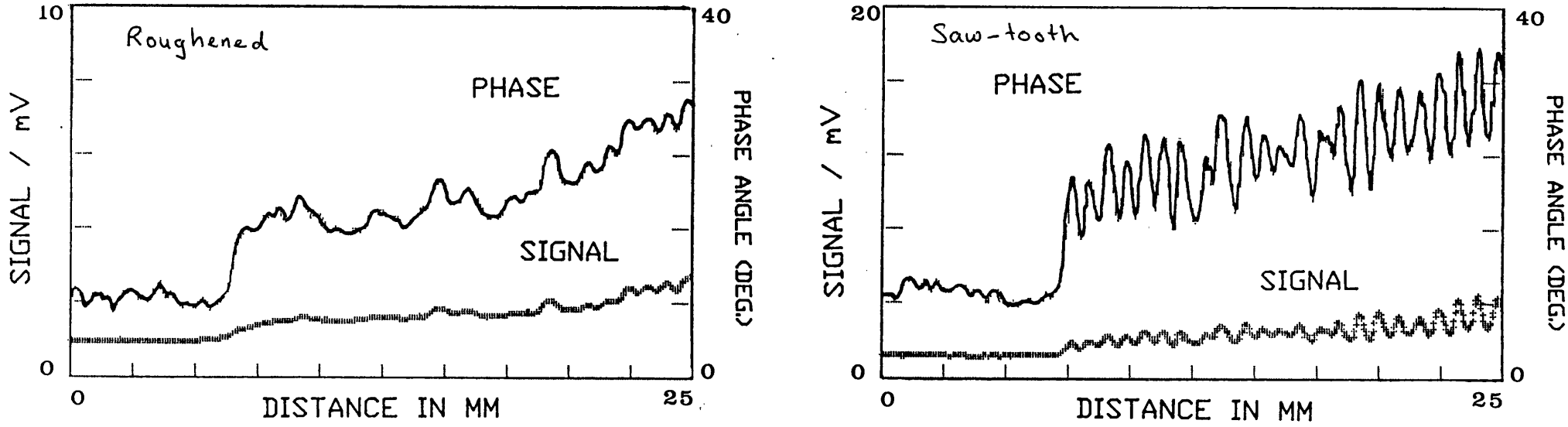

Figure 4.16c: Signal and phase angle line trace across the roughened and saw-tooth cut graphite roughness sample at a modulation frequency of 7 Hz. Incident laser power is 5 watt with infrared detection by a CMT photoconductive detector and infrared collection by a germanium lens.

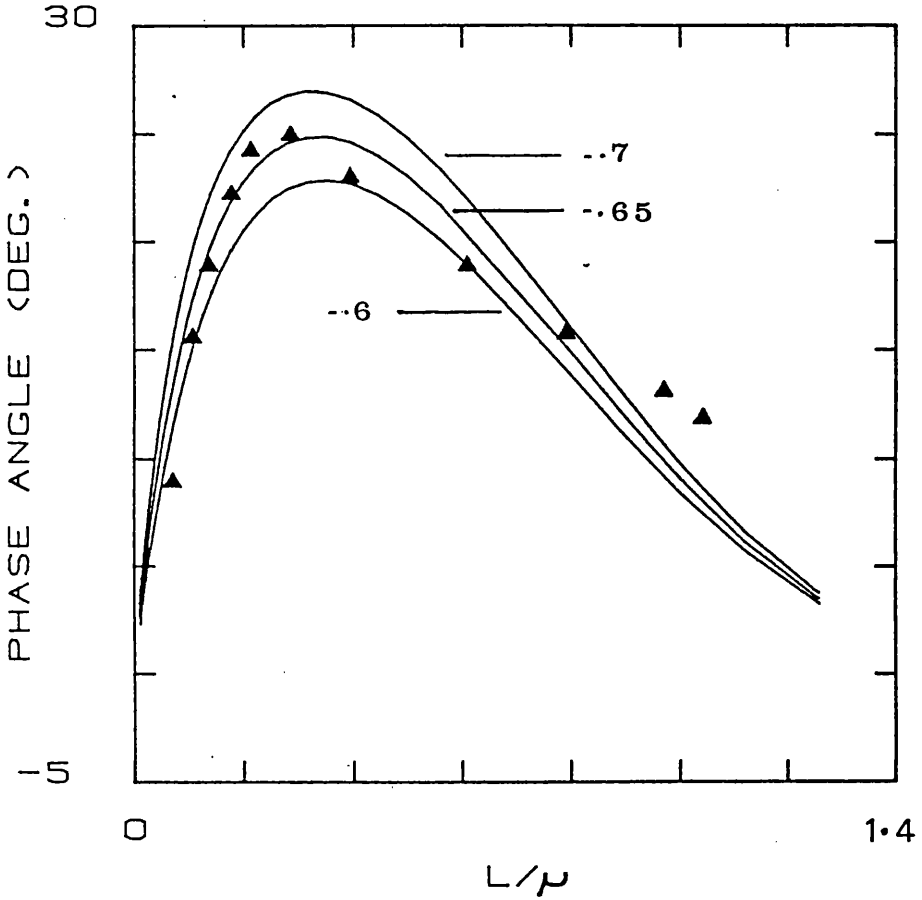

PROPERTY	BULK	SURFACE
DENSITY	1940	
SPECIFIC HEAT	630	
THERMAL CONDUCTIVITY	150	113
THERMAL DIFFUSIVITY	123x10E-6	1,548x10E-6
THERMAL EFFUSIVITY	1.35x10E 4	2,872

PHYSICAL PROPERTY VALUES IN SI UNITS.

Figure 4.17: Fitting of the experimental data of figure 4.16b to a layer on a substrate type structure using equation 2.11 to generate the theoretical phase curves.

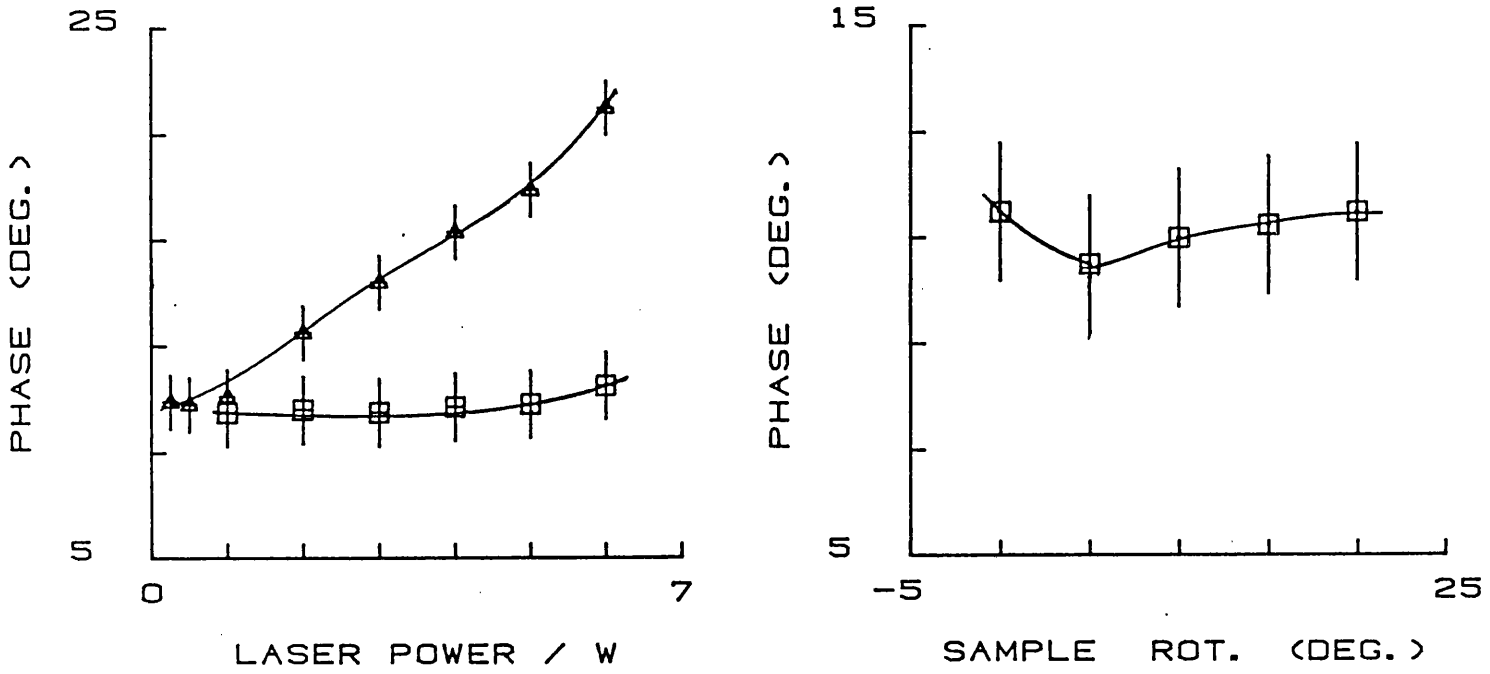

Figure 4.18: Phase angle variation with laser power and sample rotation on graphite roughness samples.

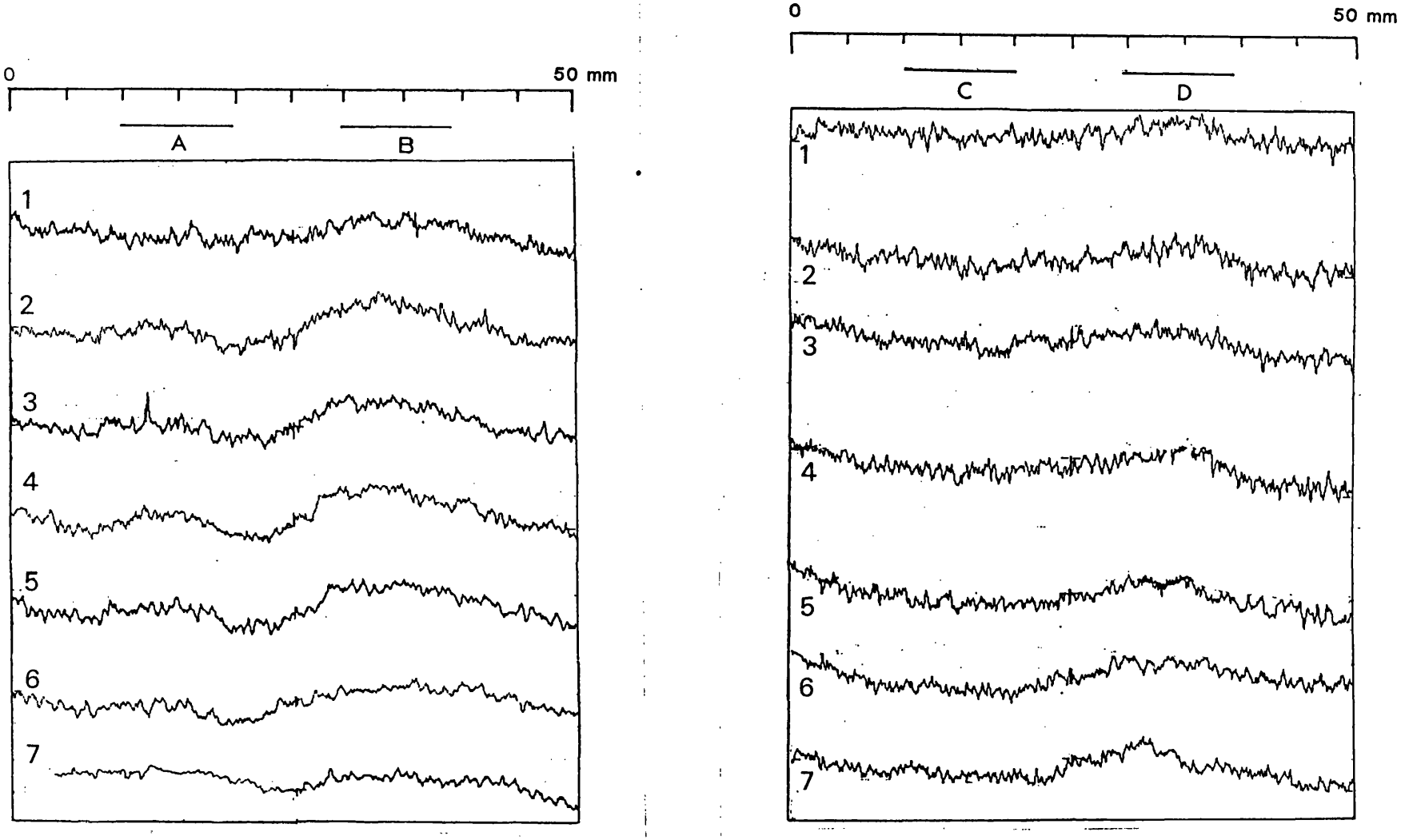

Figure 4.19a: 50 mm phase angle line traces on polished LC1B 'square' defect sample.

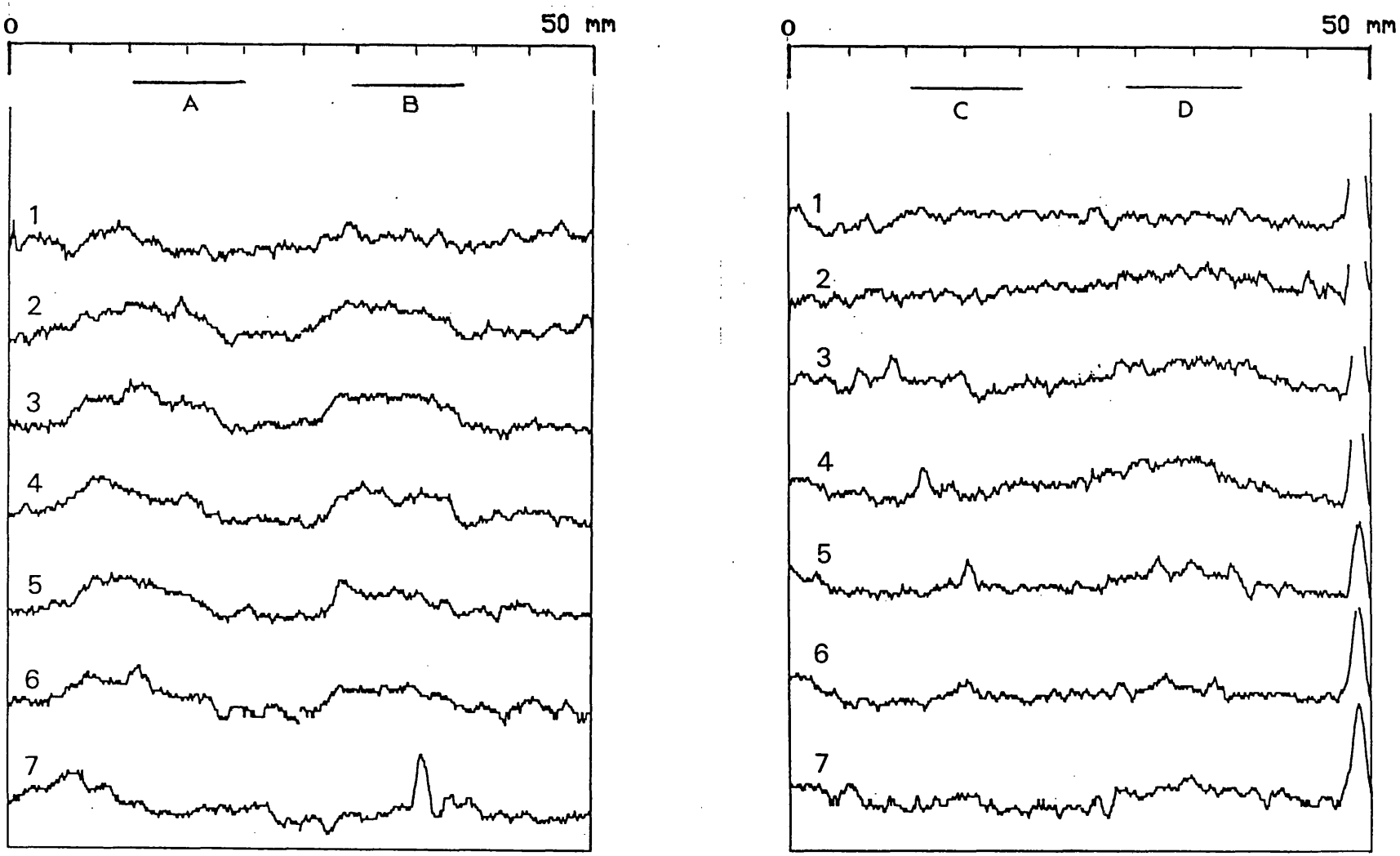

Figure 4.19b: 50 mm phase angle line traces on as-sprayed LC1B 'square' defect sample.

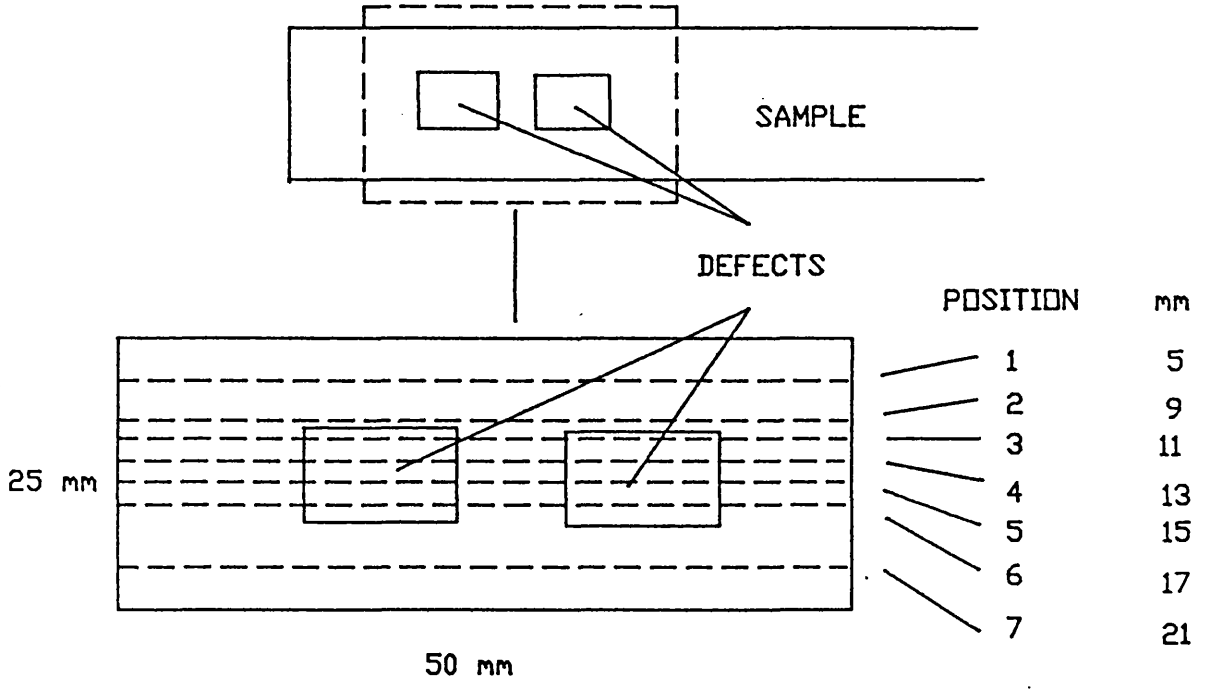

Figure 4.20: Details of 50 mm line trace location on the square defect polished and as-sprayed LC1B coating sample.

	POSITION	POLISHED SURFACE				AS-SPRAYED SURFACE			
		PHASE CHANGE (DEGREES)							
		A	B	C	D	A	B	C	D
PHOTO-THERMAL	1	–	1.3	–	1.0	–	–	–	–
	2	.8	2.5	–	1.0	1.5	1.0	–	.5
	3	.5	2,0	–	1.0	1.0	1.0	–	.5
	4	1	3.0	–	2.0	.75	.75	.5	1.0
	5	1	2.5	–	2.0	1.0	.5	–	.5
	6	–	1.0	–	2.0	.5	.5	–	–
	7	–	1.0	–	2.0	–	–	–	–
ULTRA-SONICS		ATTENUATION CHANGE (dB)							
	5 mm	–	–	–	–	–	–	–	–
	13 mm	–	–	–	–	-3	-2	–	–
	21 mm	–	–	–	–	4	–	–	–

Table 4.1: Summary of the phase angle and ultrasonic attenuation change across the square defect LC1B coating samples.

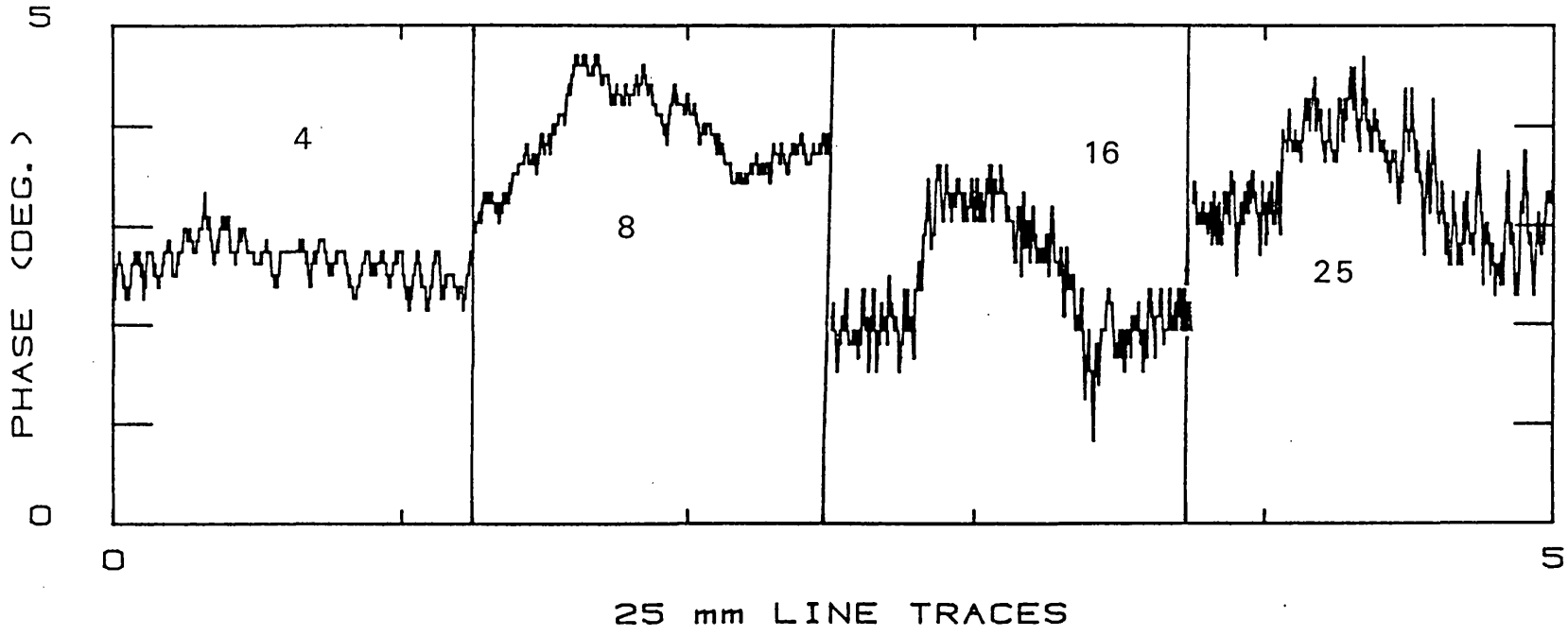

Figure 4.21a: Phase angle line traces at various frequencies for defect A in the as-sprayed sample.

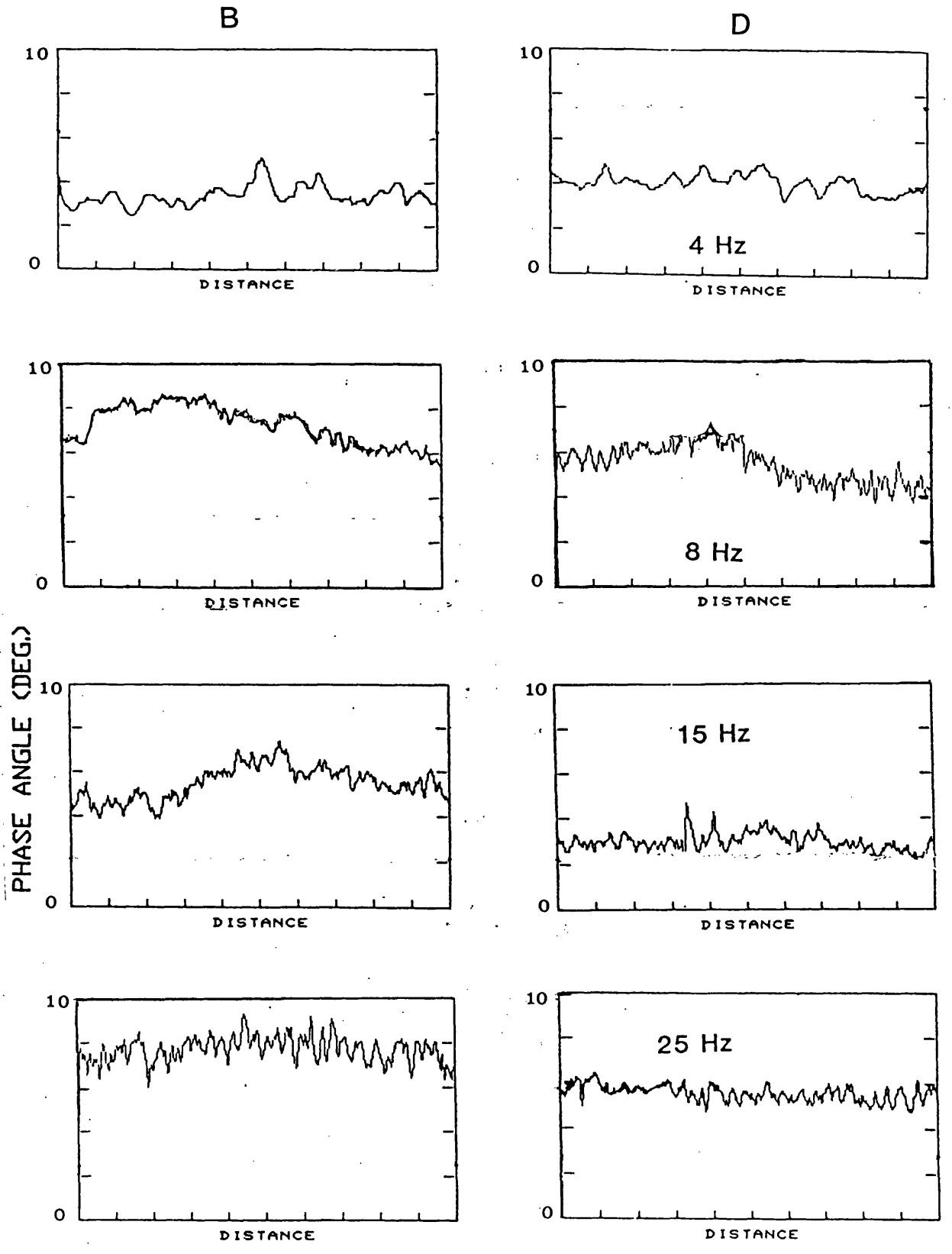

Figure 4.21b: Phase angle line traces at various frequencies for defect B and D in the polished sample.

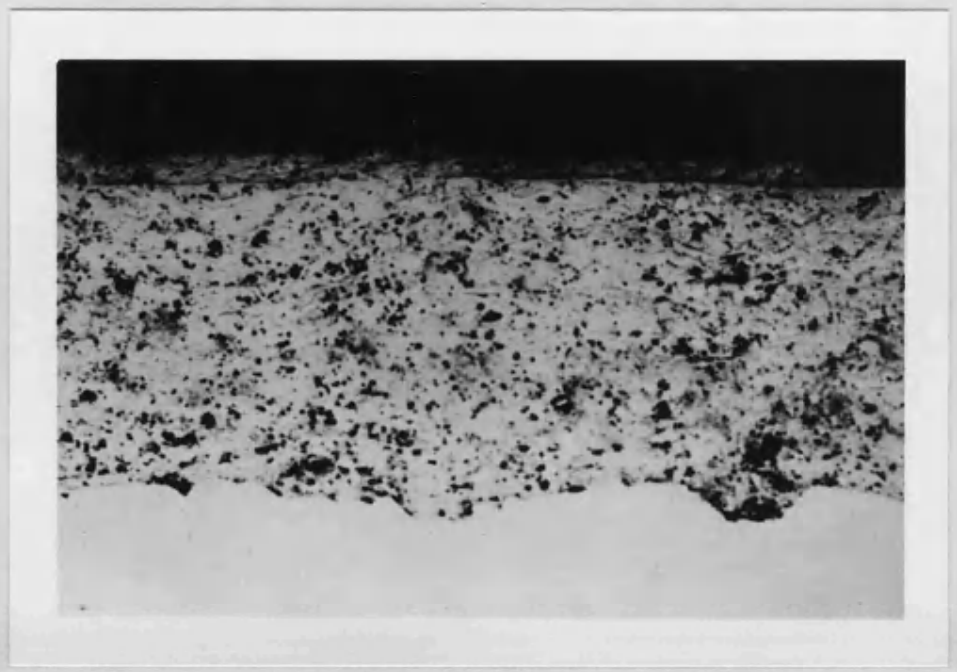

a

b

Figure 4.22 : Optical micrographs of defect B in polished sample.

a) away from the defect; 6 mm from top edge of sample, and

b) within the defect region; 12 mm from top edge of sample.

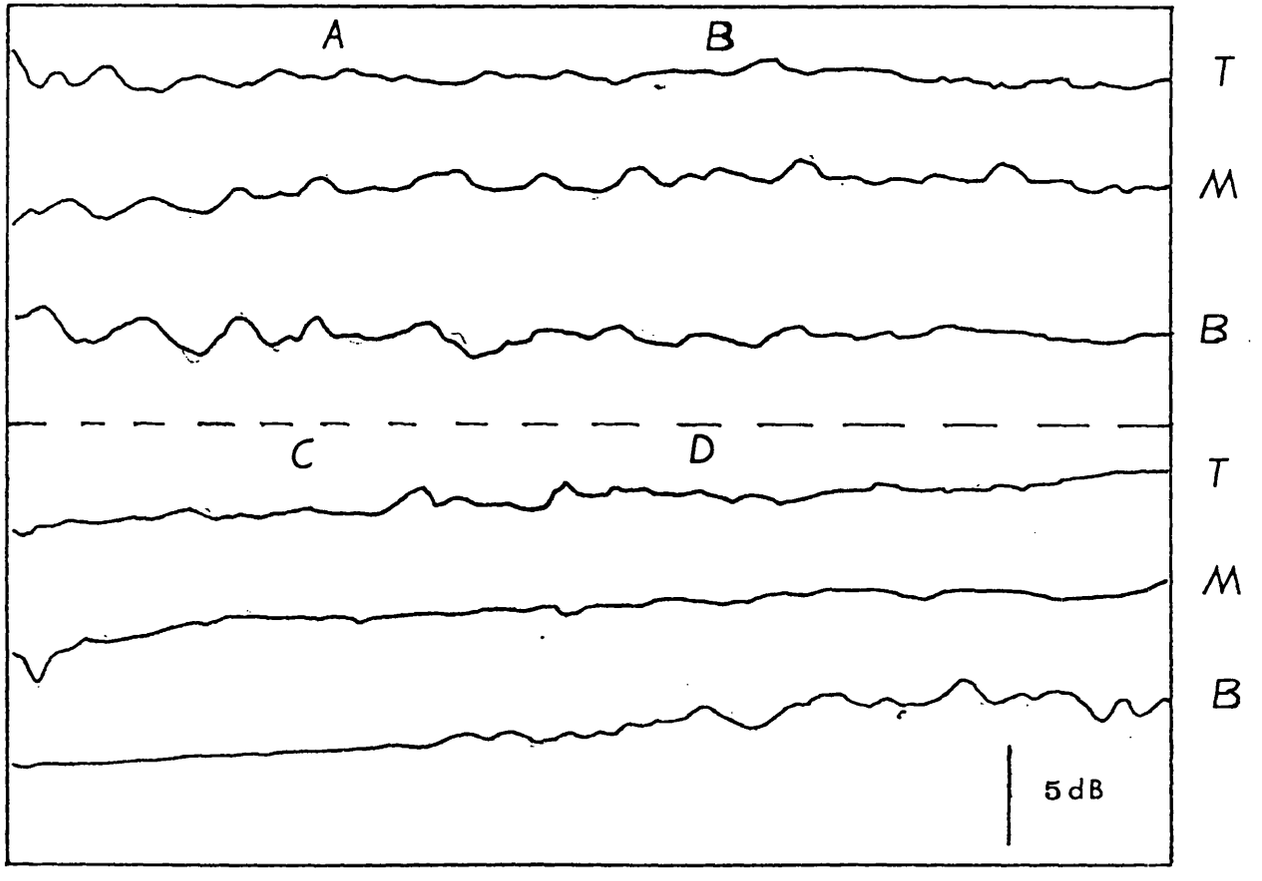

Figure 4.23a: 50 mm ultrasonic attenuation line traces on polished LC1B 'square' defect sample. T and B away from the defect area and M through the middle region of the defect.

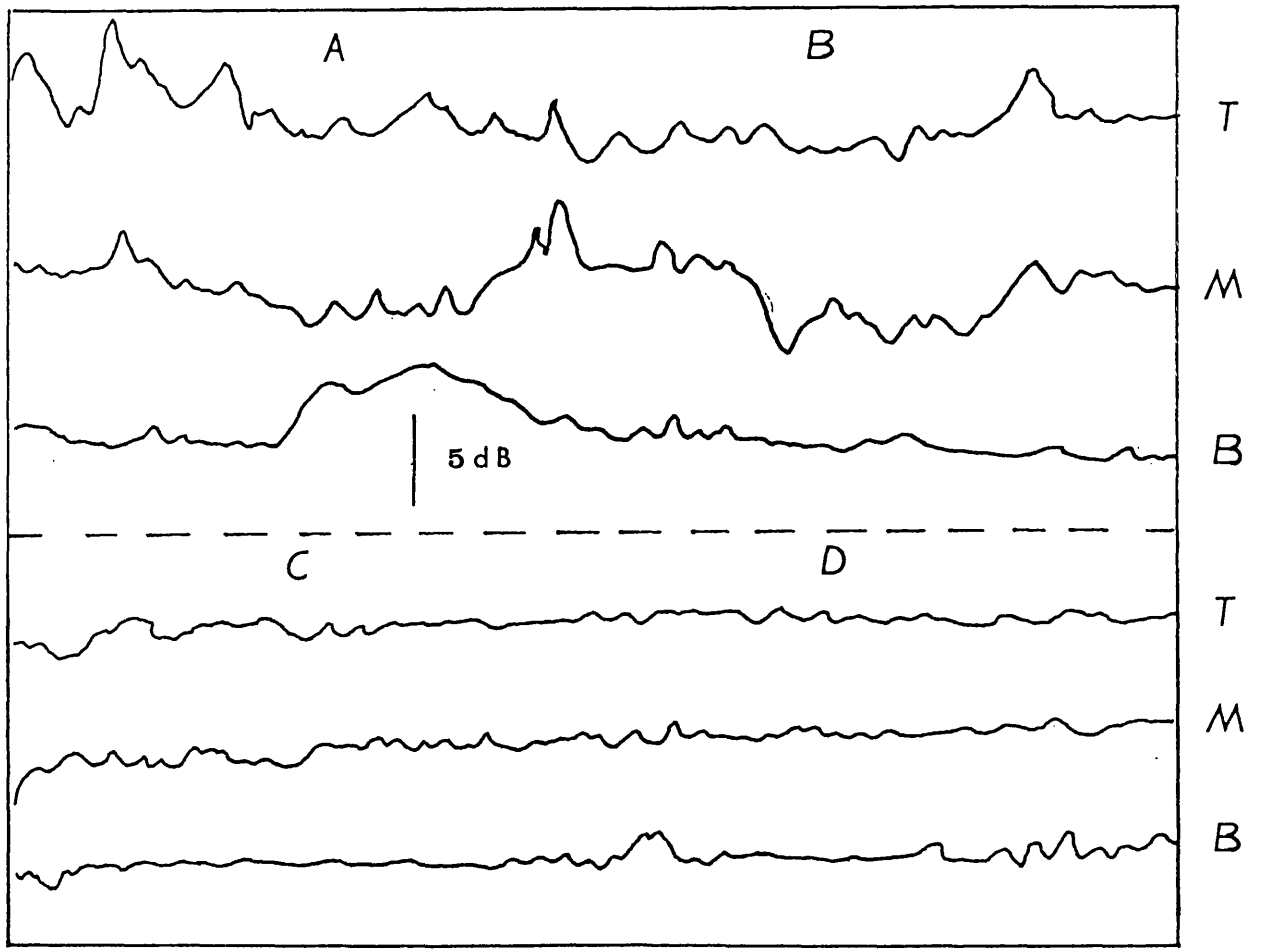

Figure 4.23b: 50 mm ultrasonic attenuation line traces on as-sprayed LC1B 'square' defect sample. T and B away from the defect area and M through the middle region of the defect.

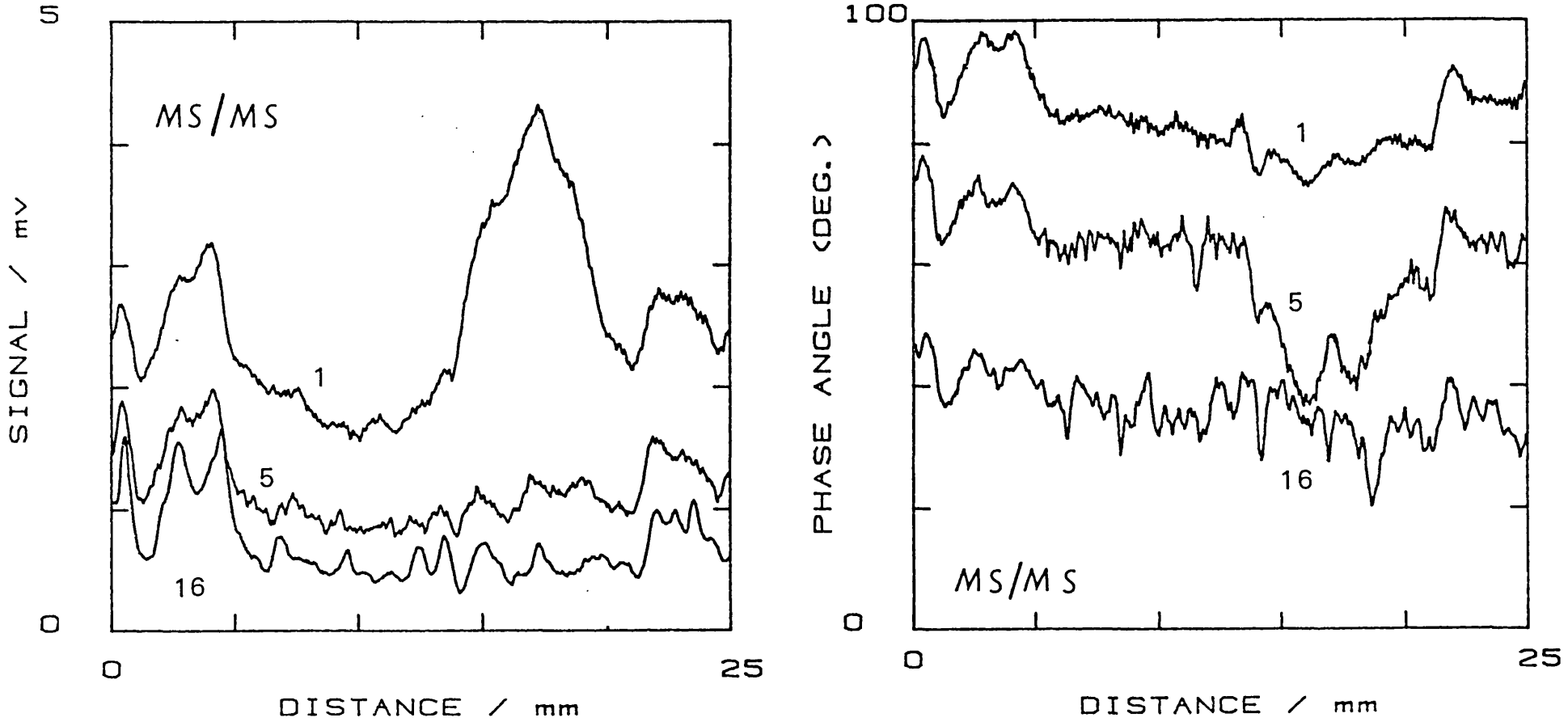

Figure 4.24a: Signal and phase angle line traces at various frequencies through the 5 mm circular defect in mild steel/ mild steel diffusion bonded sample.

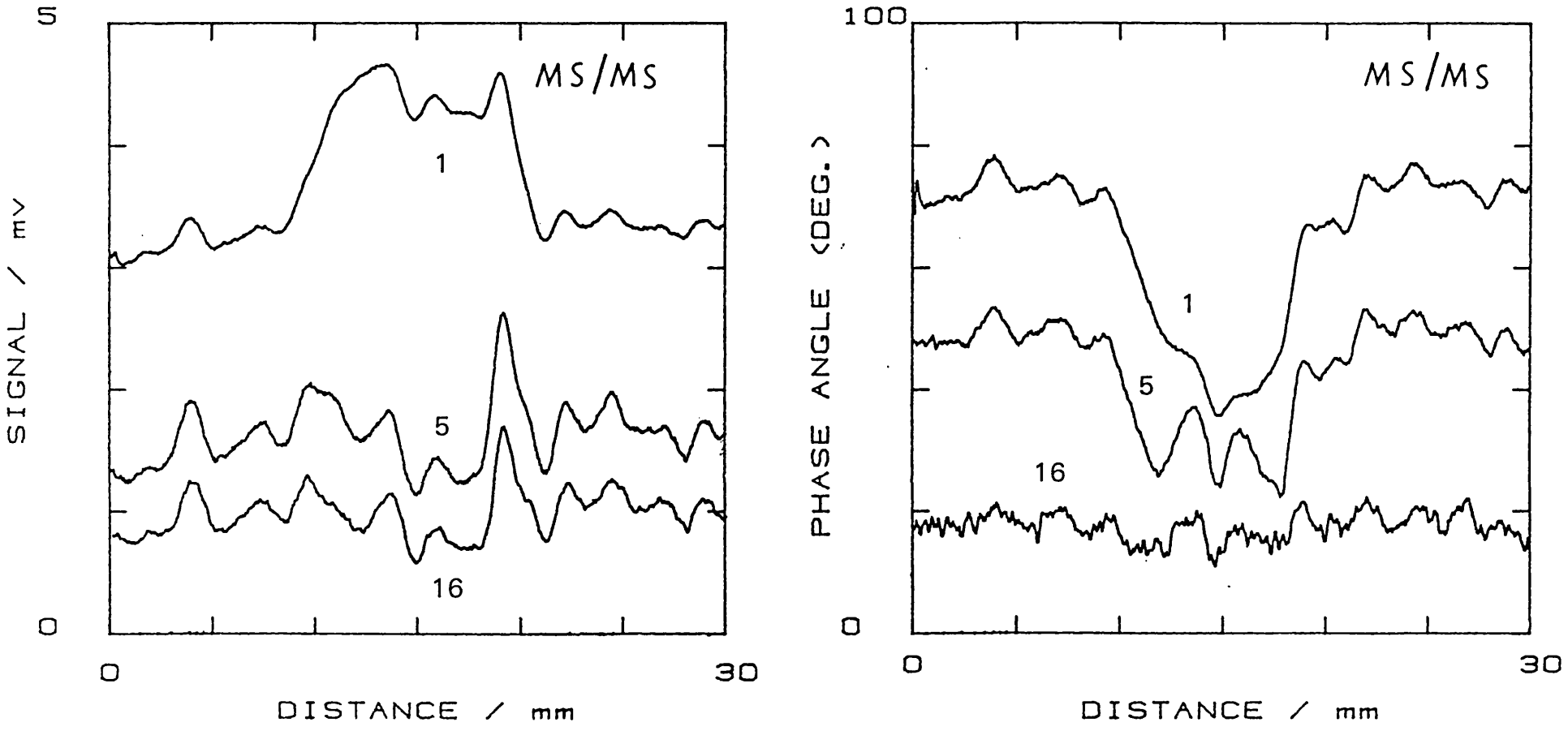

Figure 4.24b: As fig. 4.24a but across a 10 mm diameter defect.

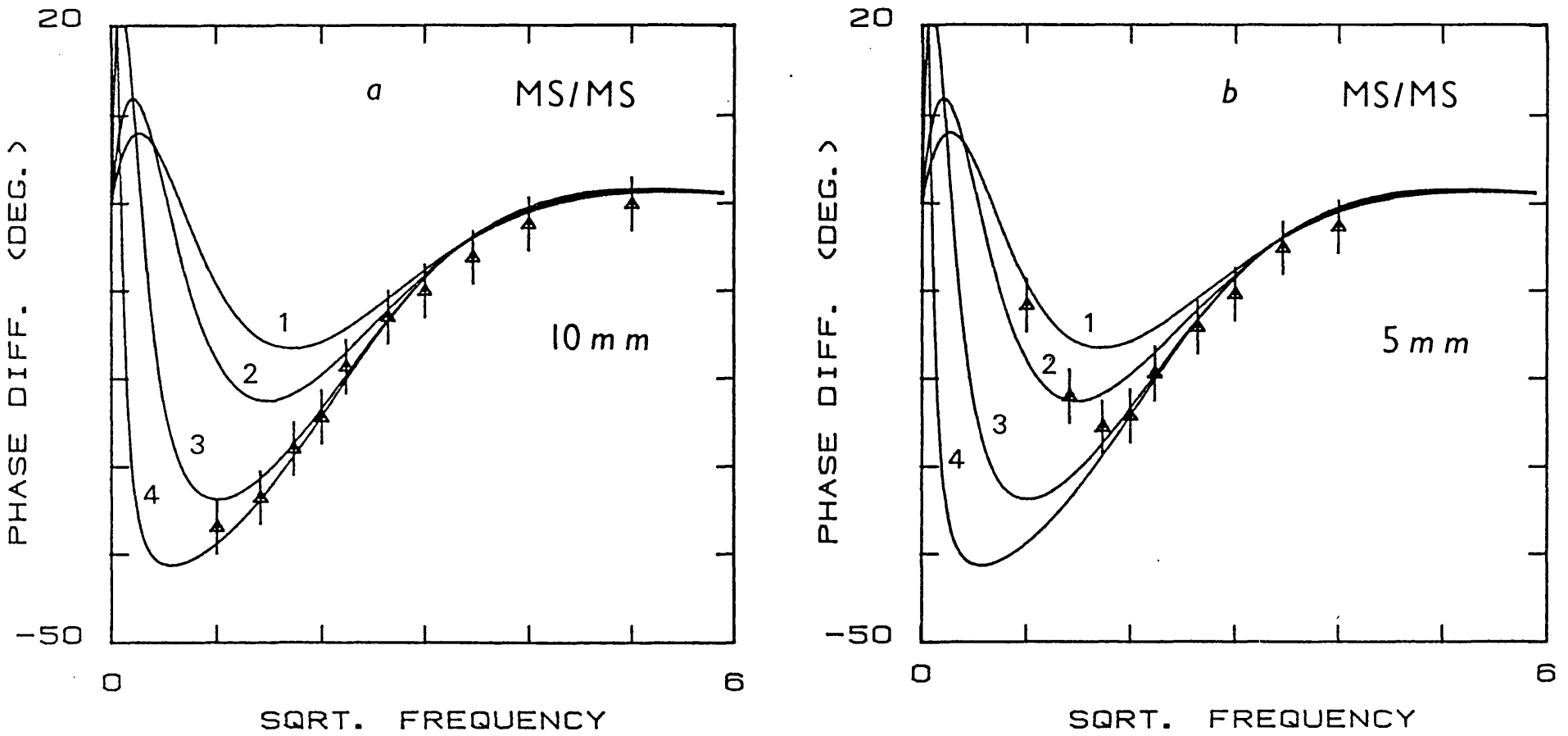

Figure 4.25: Fitting of the experimental phase difference data with root frequency to the theoretical air-gap defect phase curves using the one dimensional surface temperature expression in table 2.2.

a) 10 mm and b) 5 mm diameter defect. Solid curves 1) 0.1, 2) 1, 3) 10 and 4) 100 μm air-gap thickness.

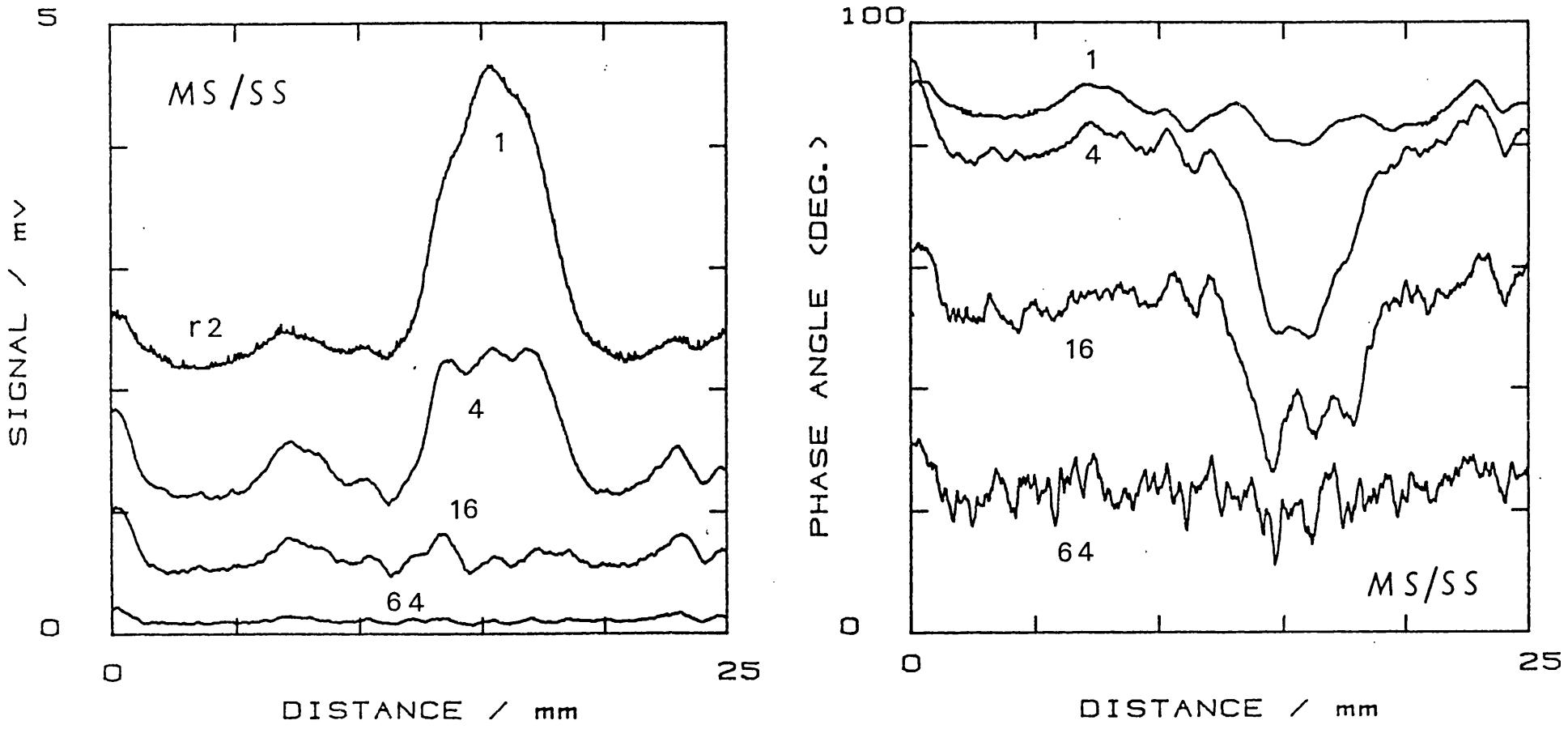

Figure 4.26a: Signal and phase angle line traces at various frequencies through the 5 mm circular defect in mild steel/ stainless steel diffusion bonded sample.

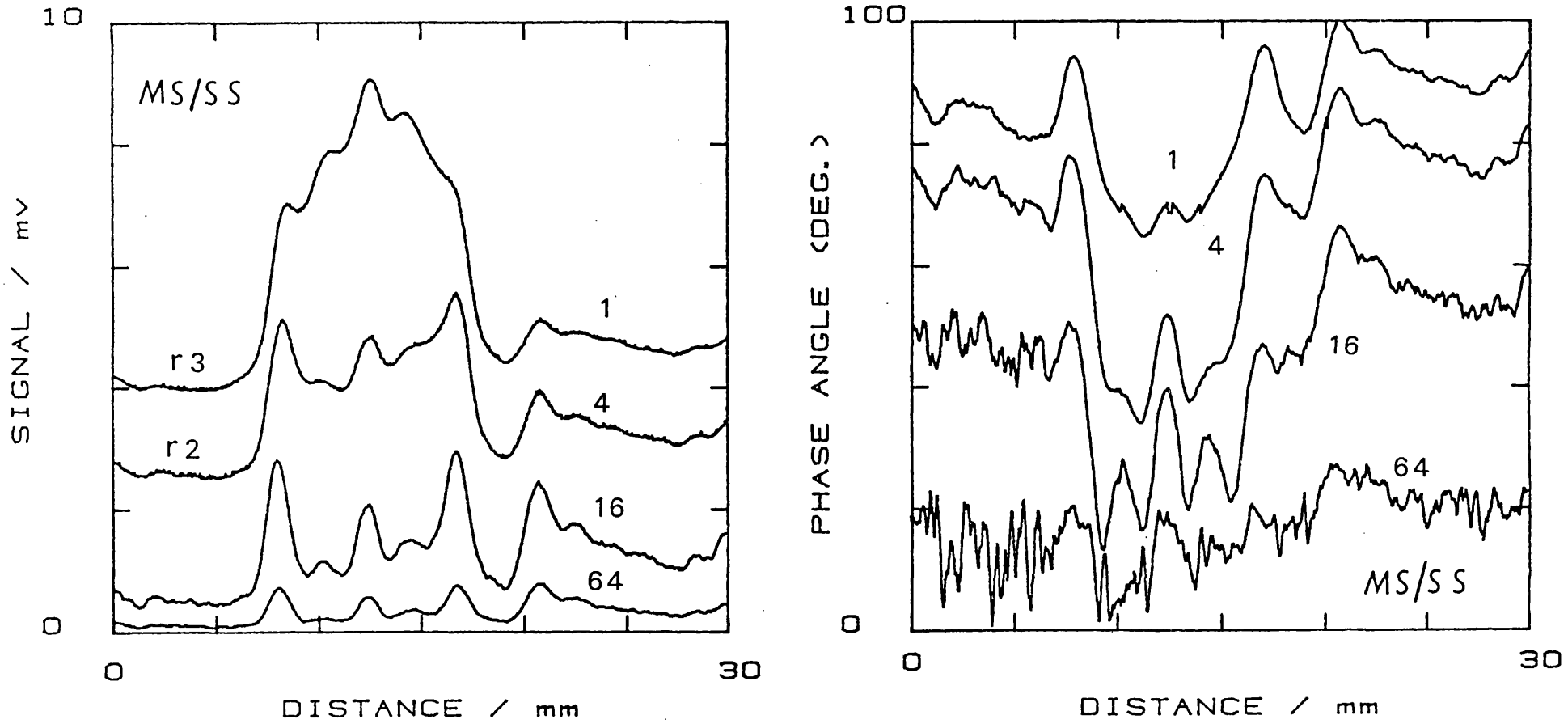

Figure 4.26b: As fig.26a but defect diameter 10 mm.

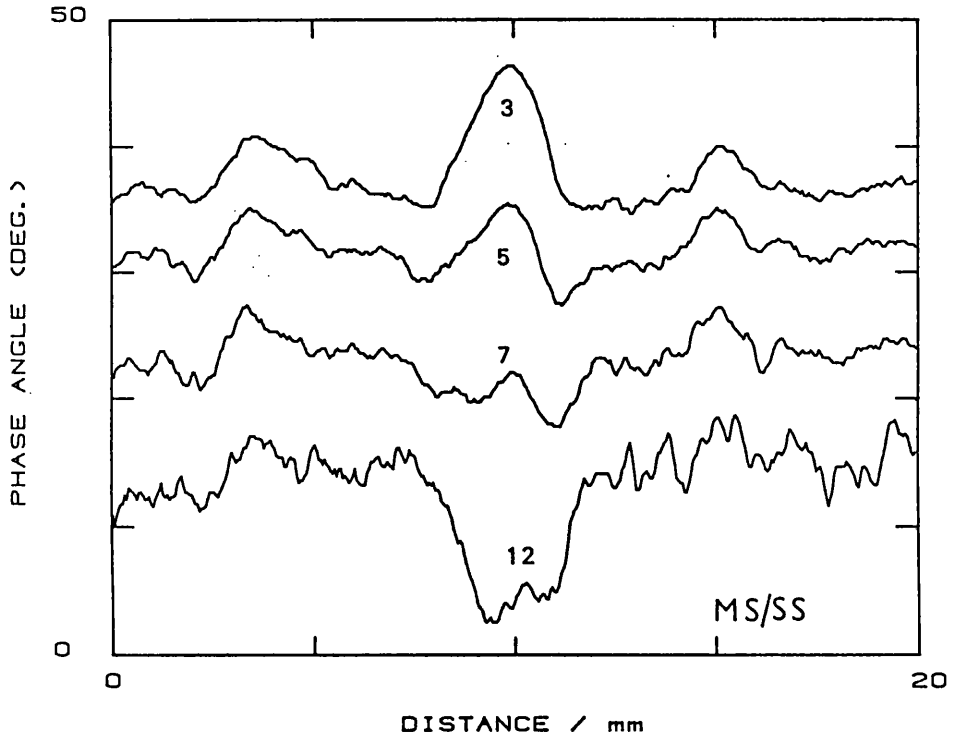

Figure 4.26c: 20 mm phase angle line traces across a 3 mm defect diameter at various frequencies. Mild steel/ stainless steel diffusion bonded sample.

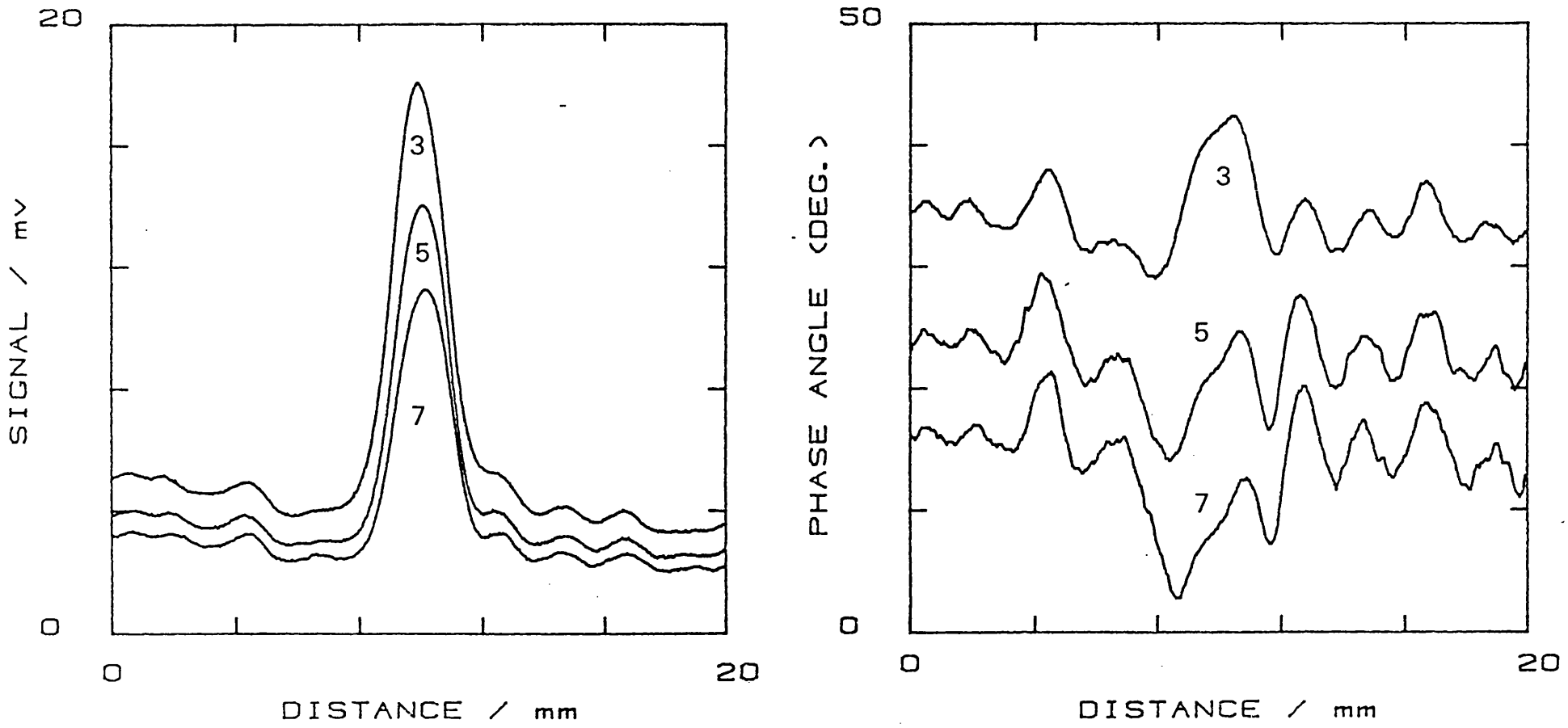

Figure 4.26d: Signal and phase angle line traces at various frequencies through the 2 mm circular defect in mild steel/ stainless steel diffusion bonded sample.

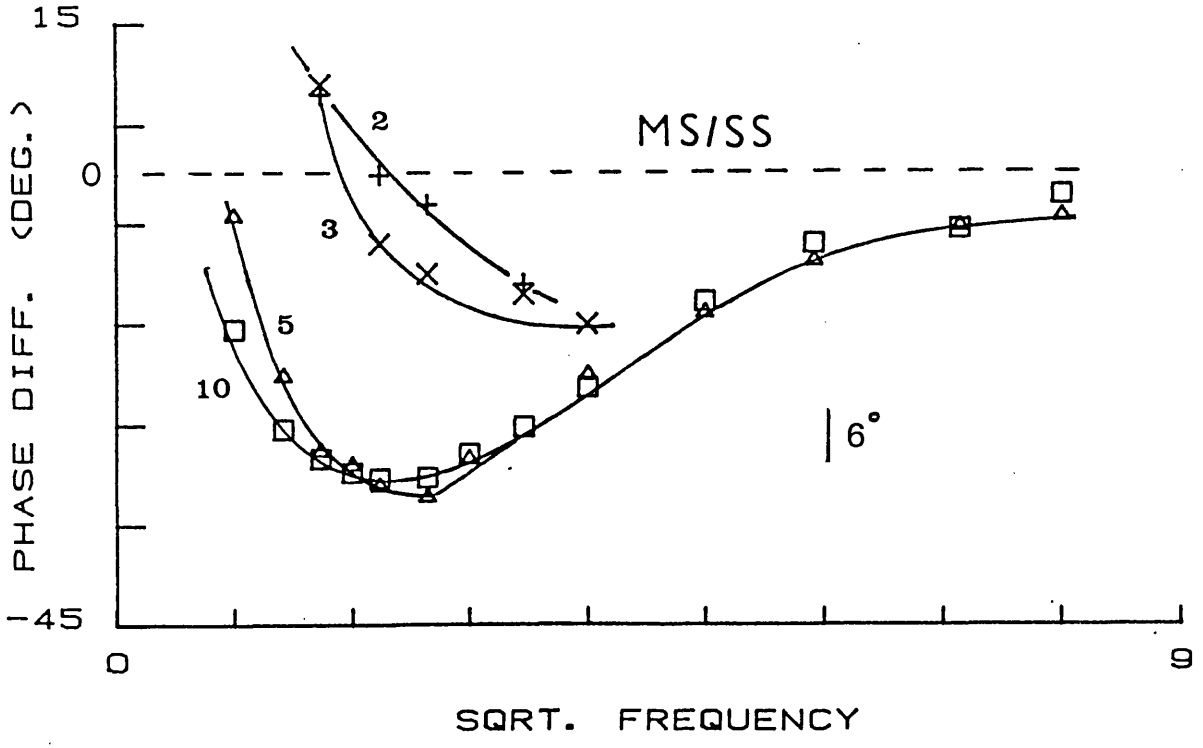

Figure 4.27: A phase difference verses root frequency plot for the 10, 5 3 and 2 mm diameter defects in mild steel/ stainless steel sample.

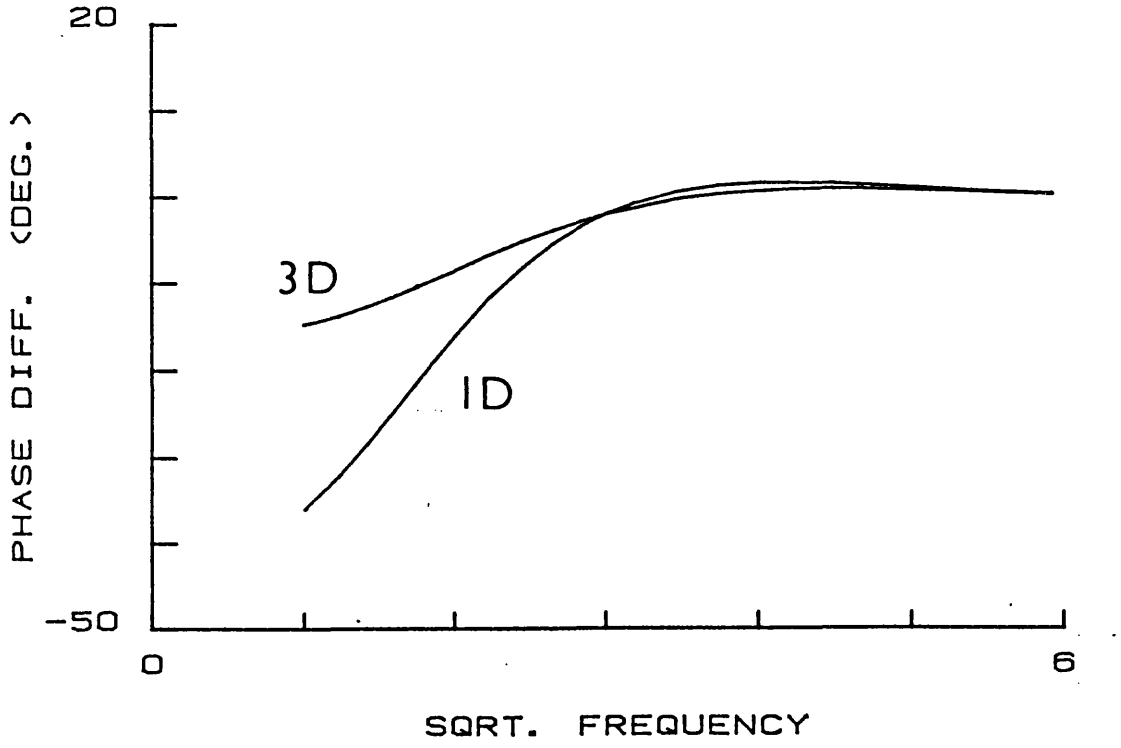

Figure 4.28: A theoretical plot of the phase variation due to subsurface air-gap defect 100 μm thick and 1 mm below the surface in bulk mild steel. Phase curves are plotted for heat diffusion in one and three dimensional. Laser beam diameter 1.5 mm.

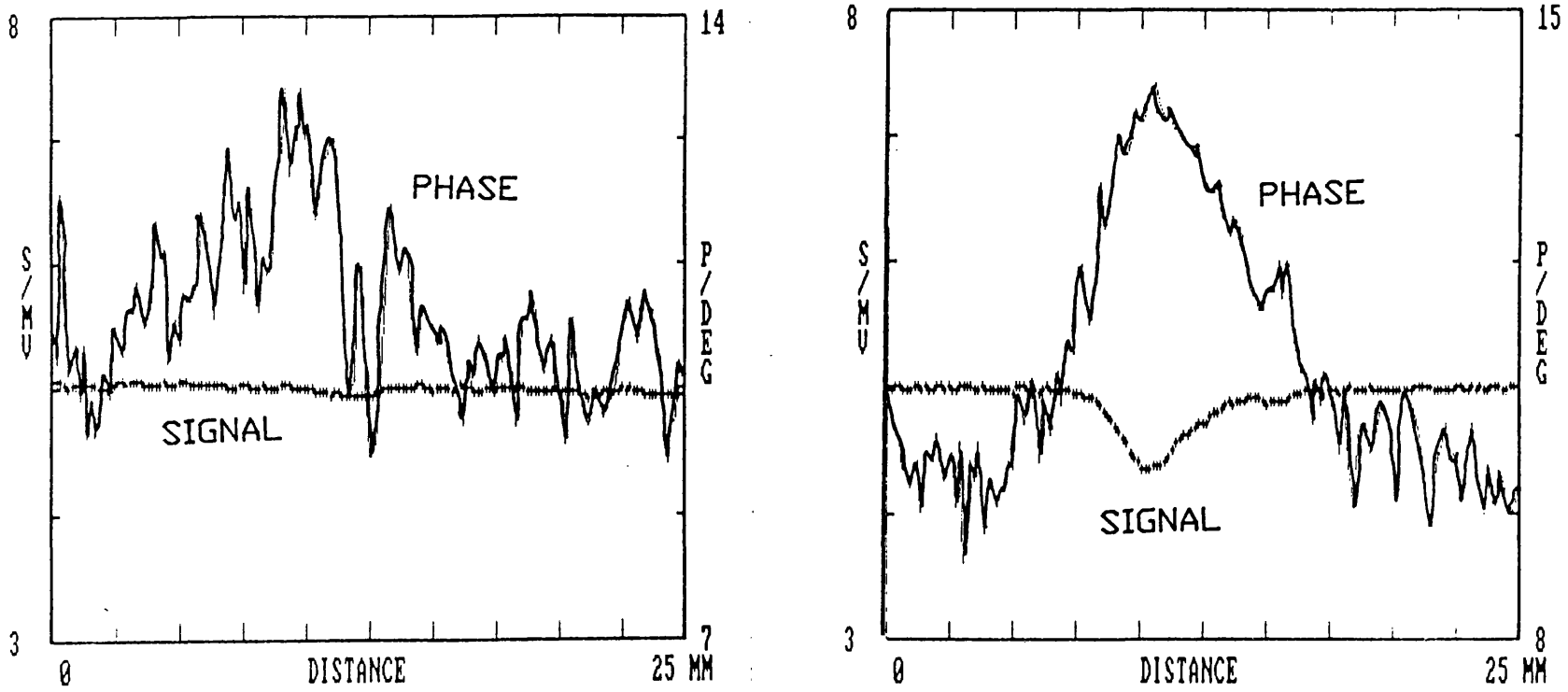

Figure 4.29: a) Signal and phase difference line trace when contact is made between a flat aluminium plate and a micrometer pin head, left, and right, when contact is made inside a partially drilled subsurface hole in an aluminium plate. (Contact geometry shown in figure 3.7)

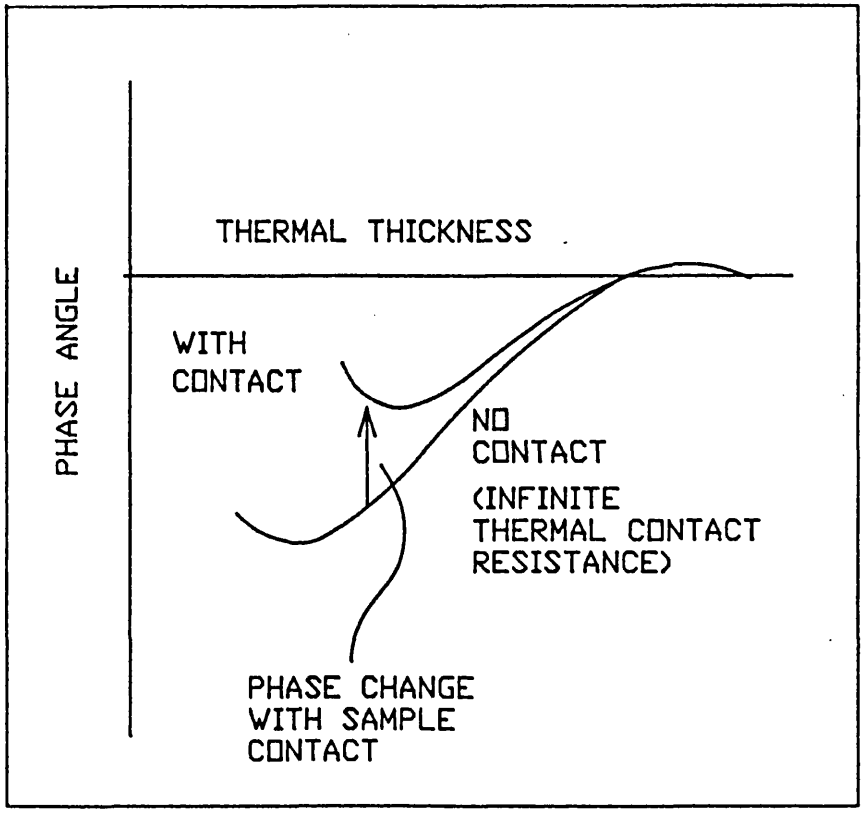

Figure 4.30: A schematic illustration of the phase change between a no contact and contact situation.

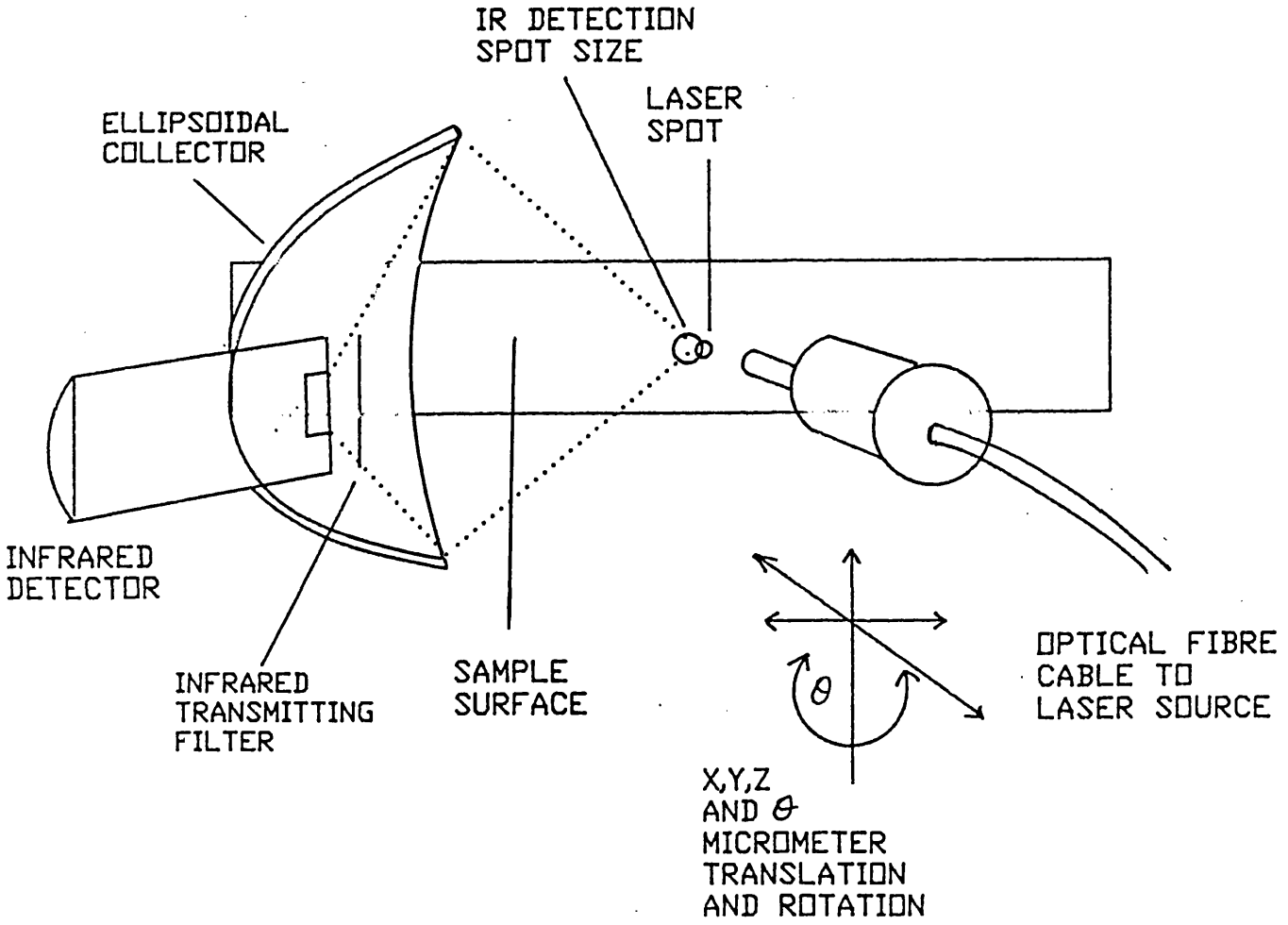

Figure 4.31: A schematic illustration of the IR detector, sample and optical fibre head set-up for measurements taken with the semi-conductor laser.

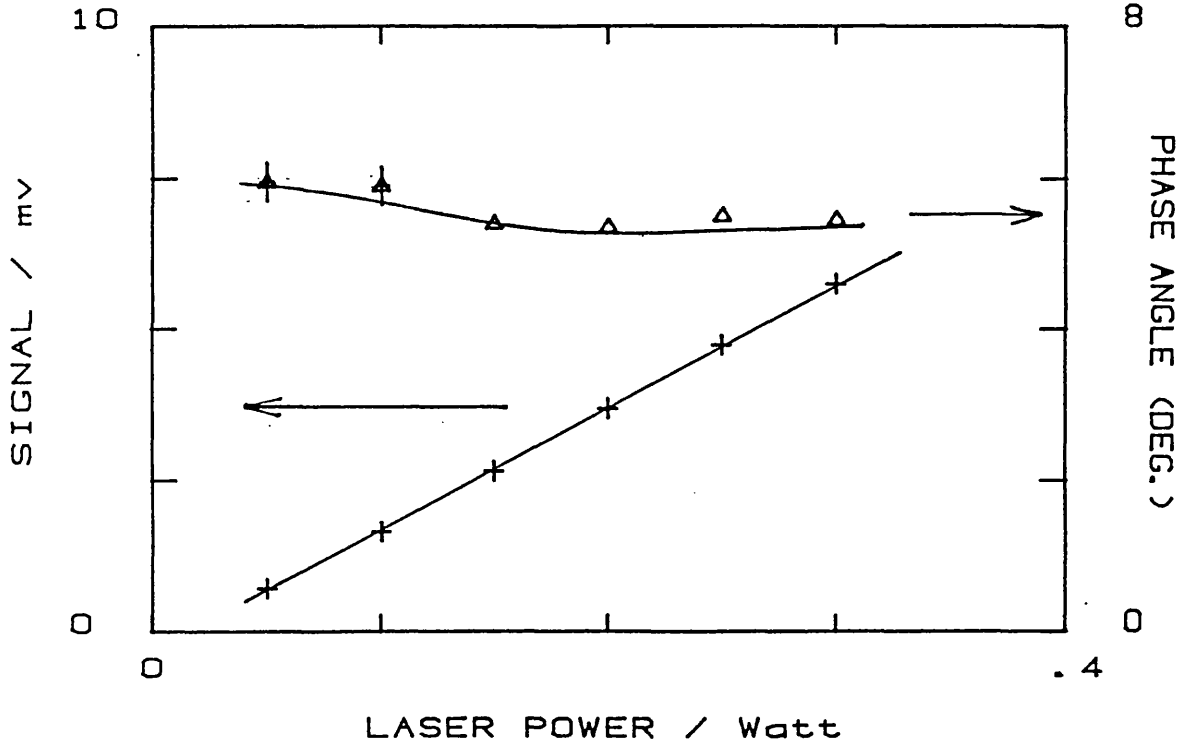

Figure 4.32: Photothermal signal variation with laser power at a modulation frequency of 10 Hz. The test sample is 250 μm LC1B coating on stainless steel.

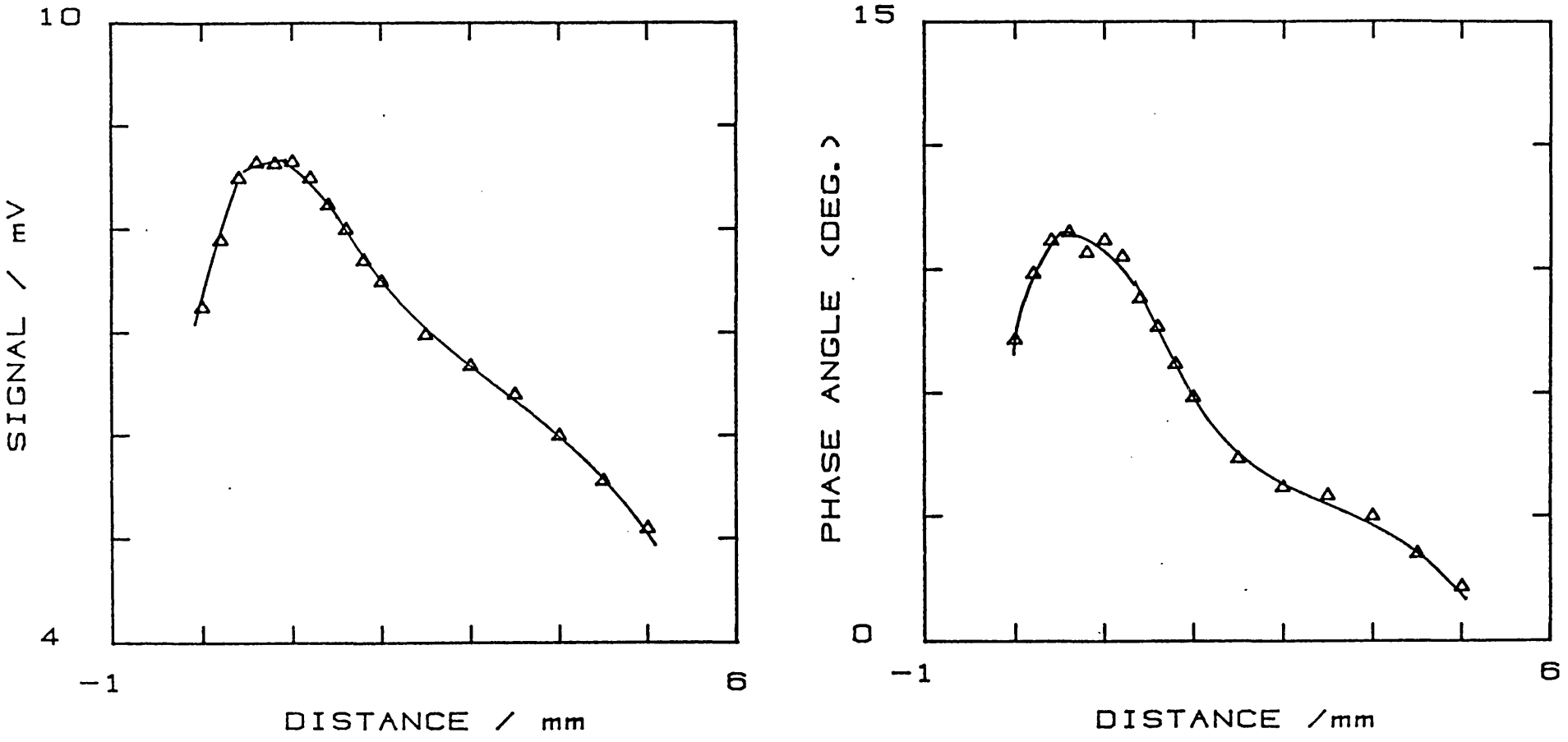

Figure 4.33: Photothermal signal variation as the optical fibre head is retarded from the sample surface.

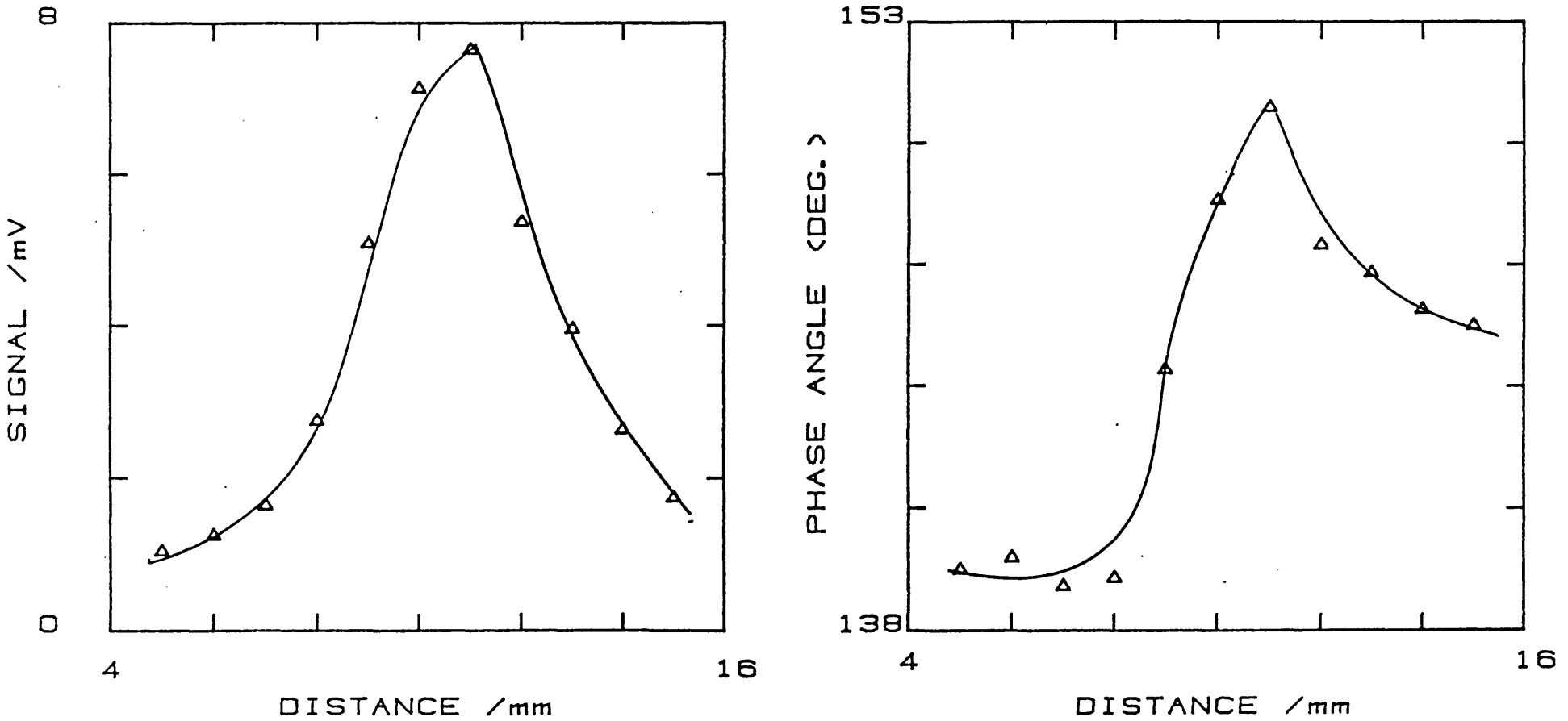

Figure 4.34: Photothermal signal variation as the optical fibre head is moved through the infrared detection region from the right to left. (see fig. 4.31).

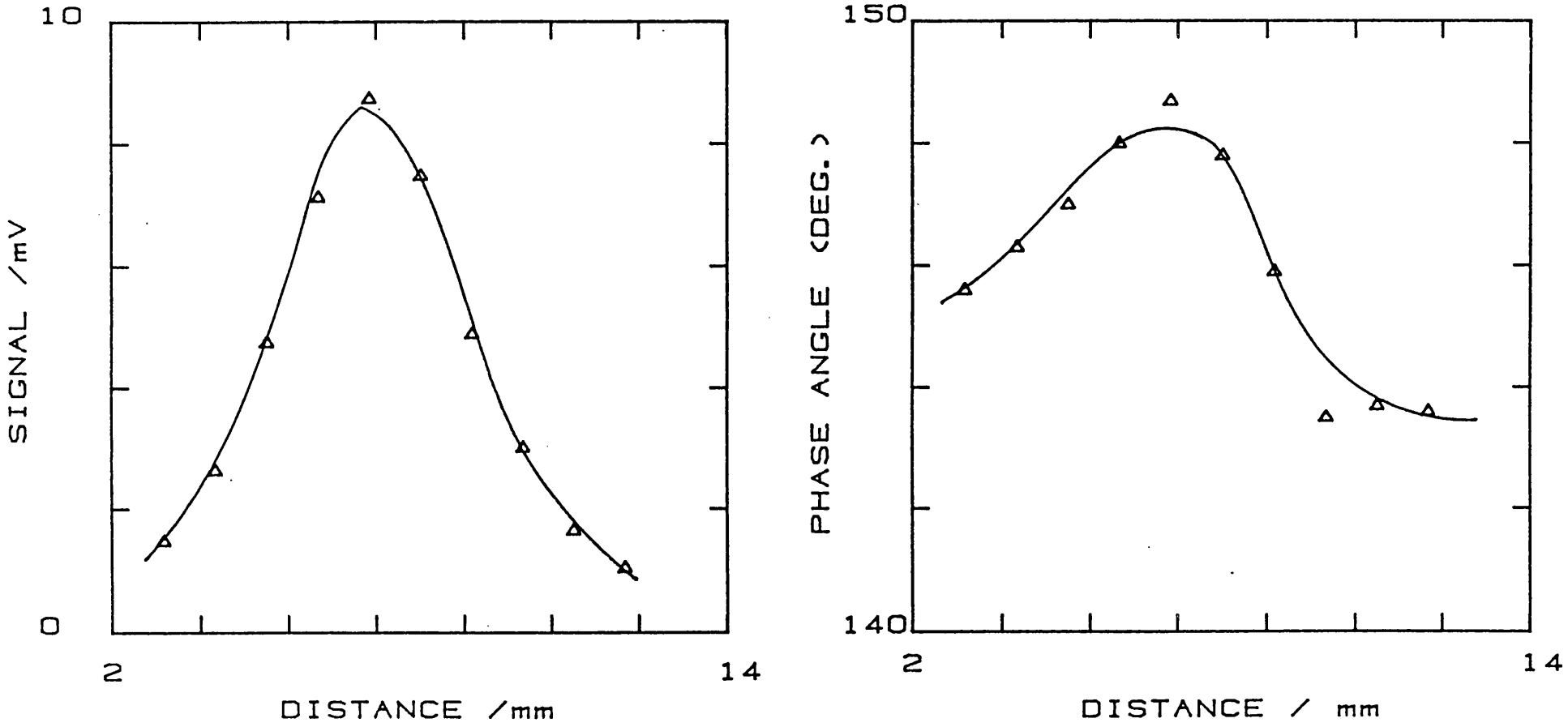

Figure 4.35: Photothermal signal variation as the optical fibre head is moved vertically downwards through the infrared detection region.

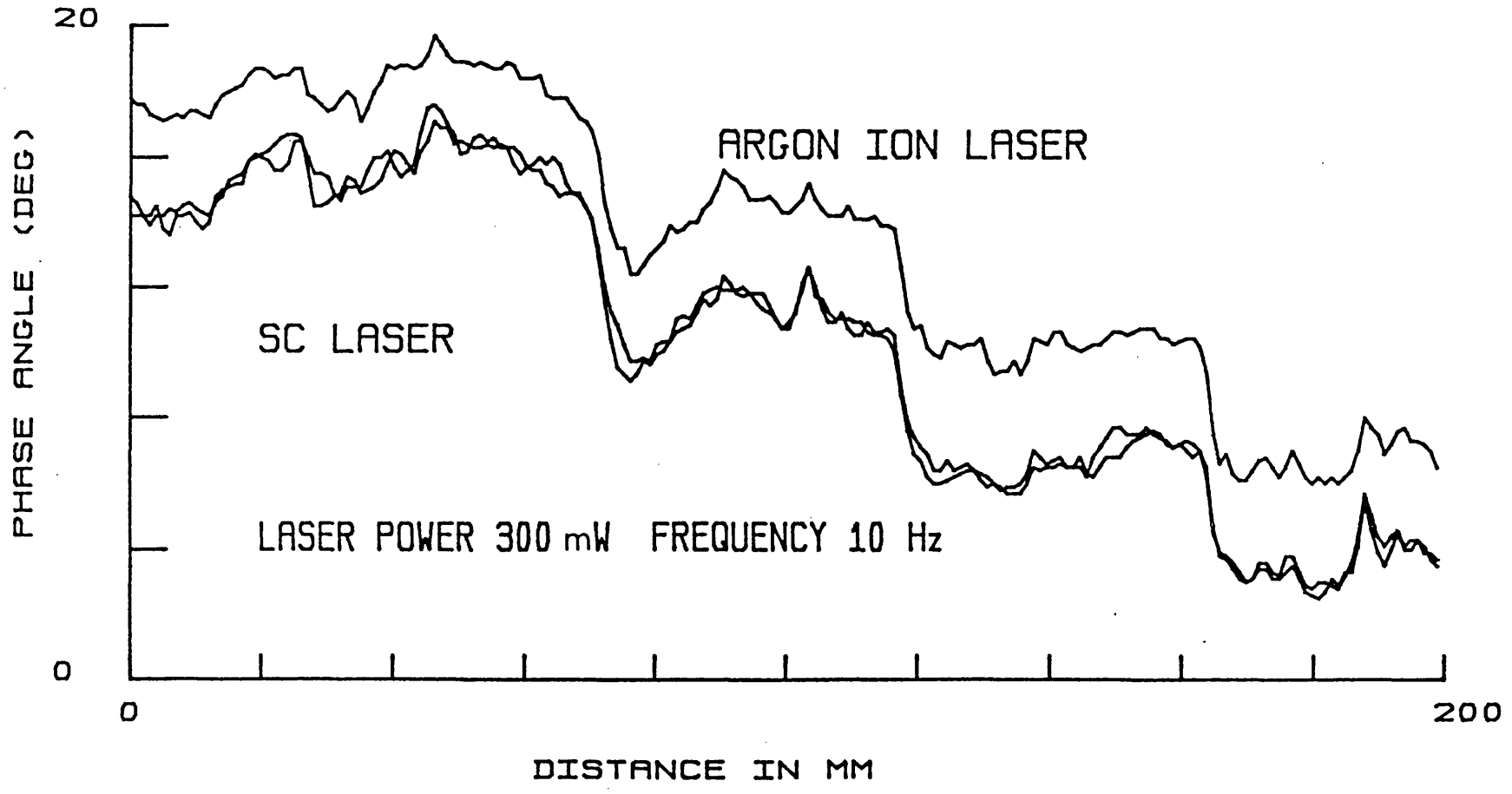

Figure 4.36a: A 200 mm phase angle line trace across a step thickness LC1B coating sample at a frequency of 10 Hz with optical heating by the GaAlAs laser diode and argon ion laser at a laser power of 300 mW.

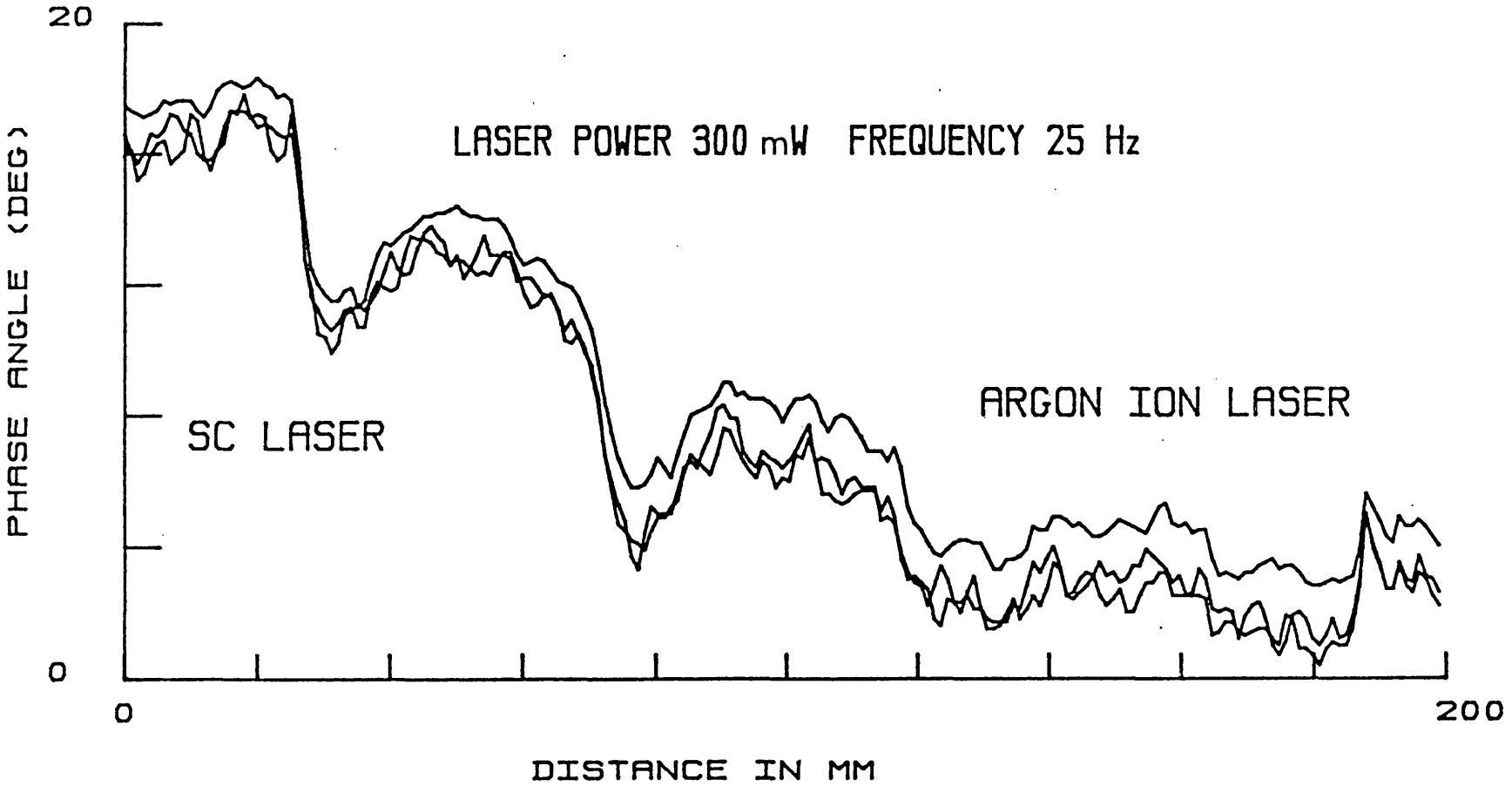

Figure 4.36b: As fig. 4.36a but at a frequency of 25 Hz.

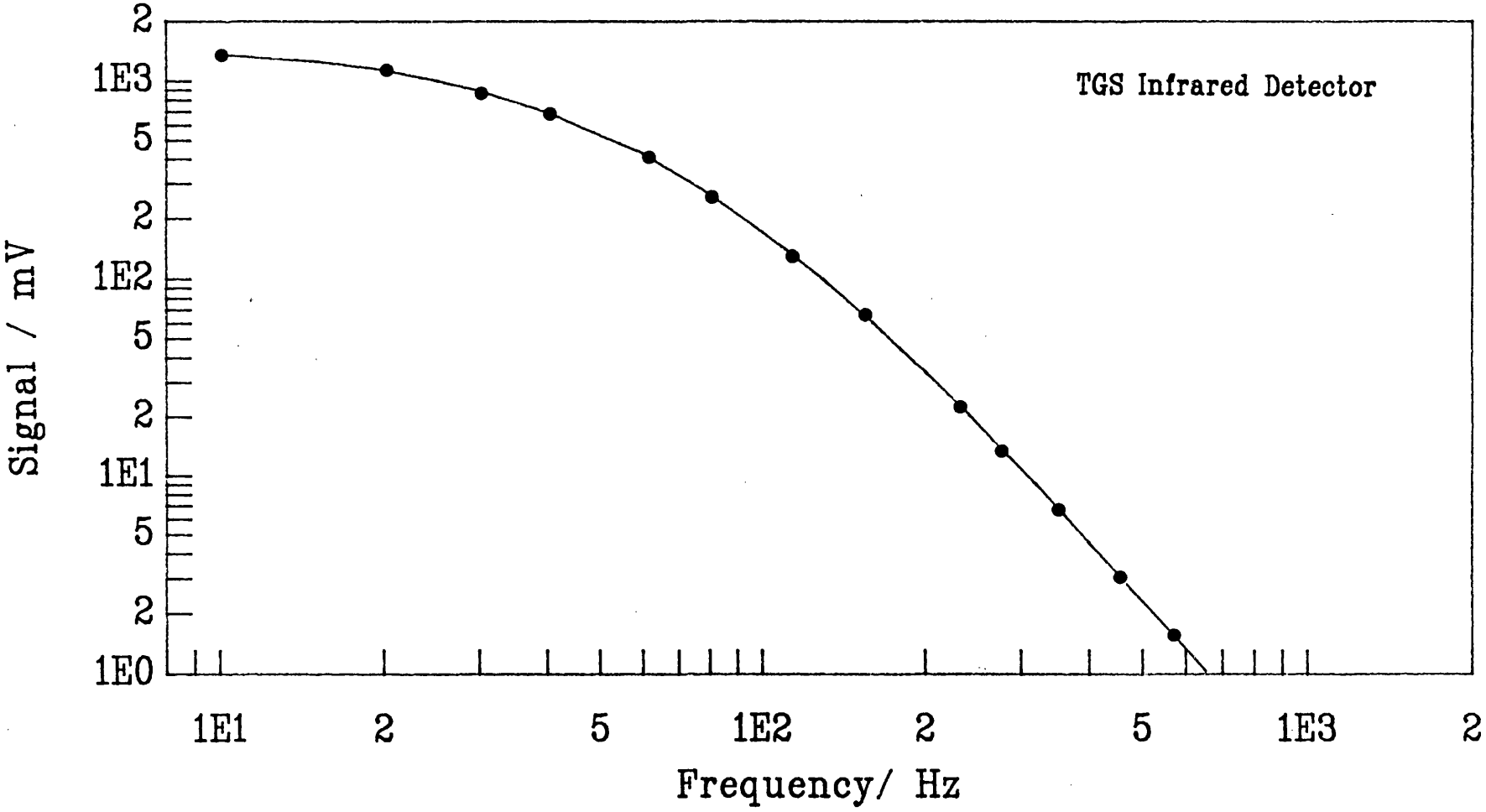

Figure 4.37a: TGS detector signal response with frequency.

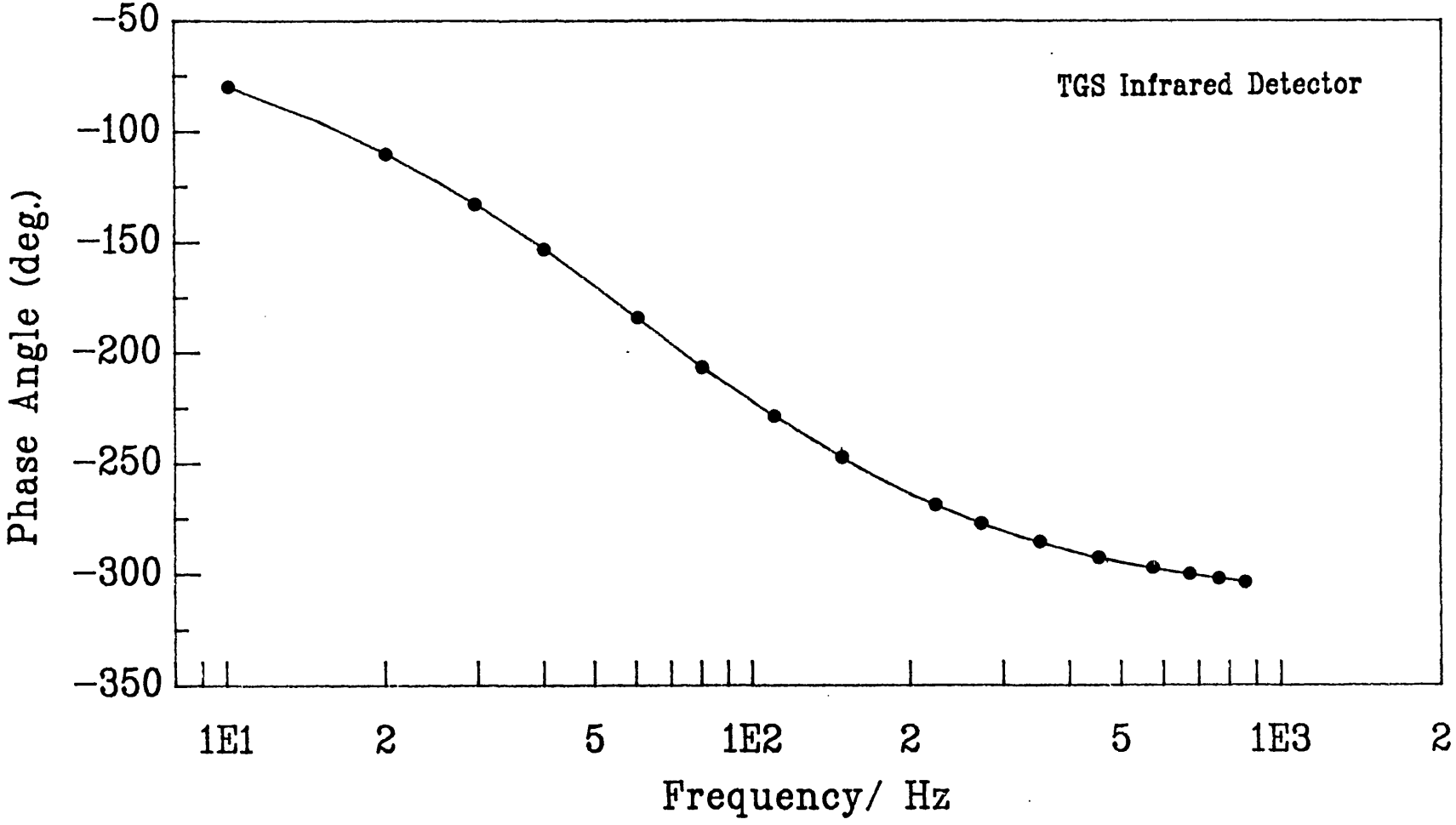

Figure 4.37b: TGS detector phase angle response with frequency.

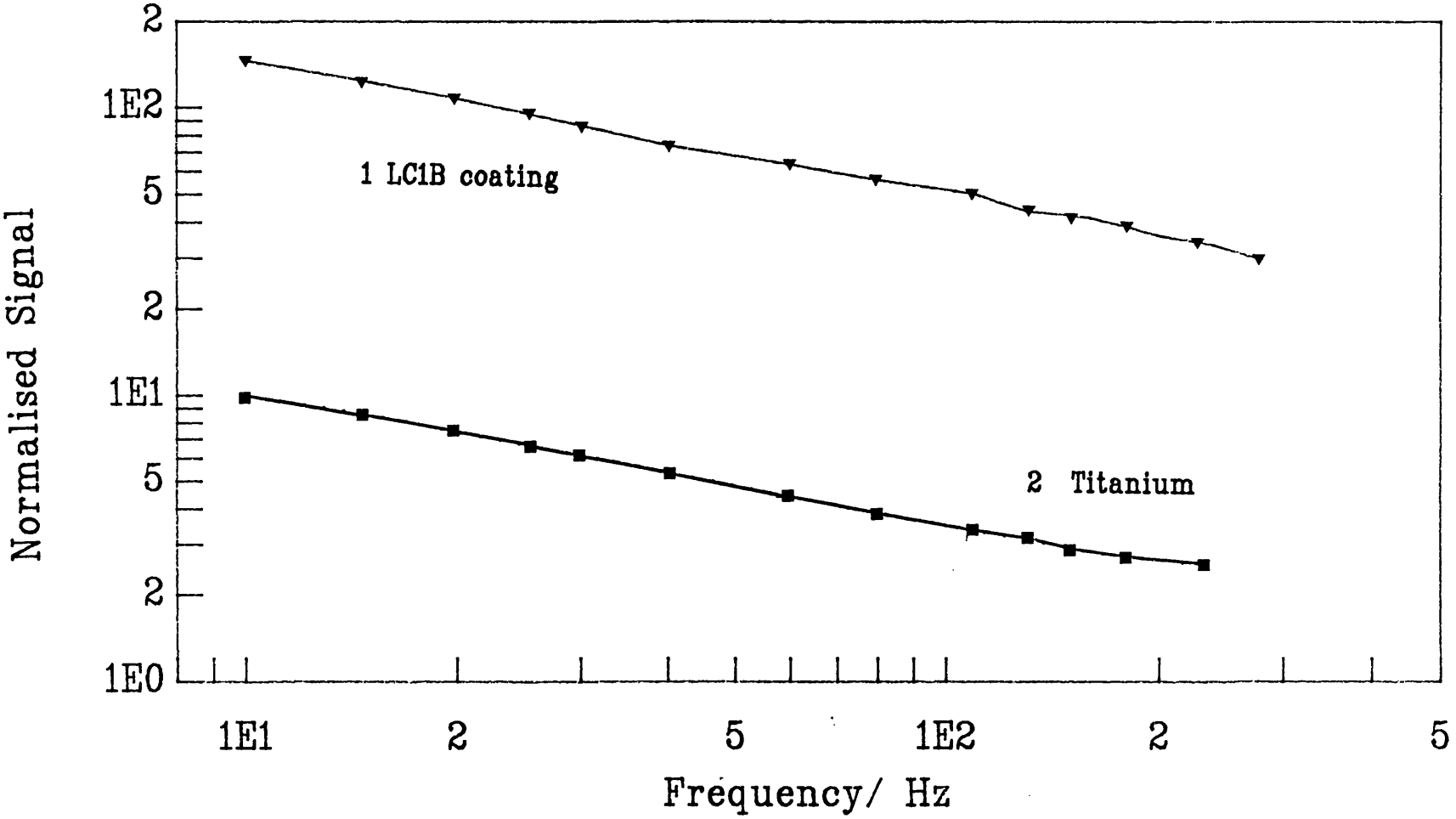

Figure 4.38a: Normalised signal variation with frequency for 1) a 0.25 mm thick LC1B coating on a 3 mm thick stainless steel substrate and 2) a 10 mm thick titanium block. Incident laser power was 3 Watt.

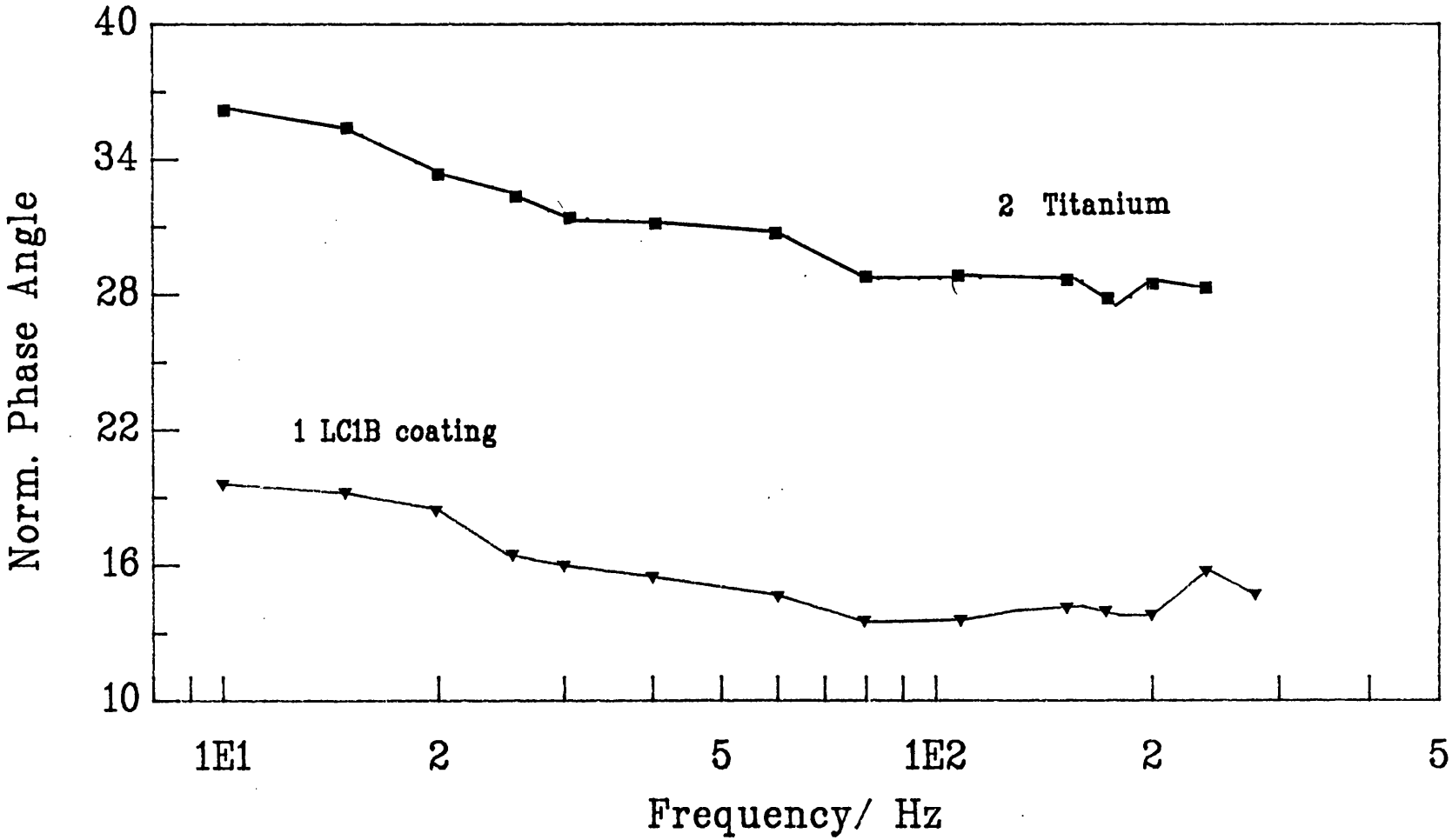

Figure 4.38b: Normalised phase angle variation with frequency for 1) a 0.25 mm thick LC1B coating on a 3 mm thick stainless steel substrate and 2) a 10 mm thick titanium block. Incident laser power was 3 Watt.

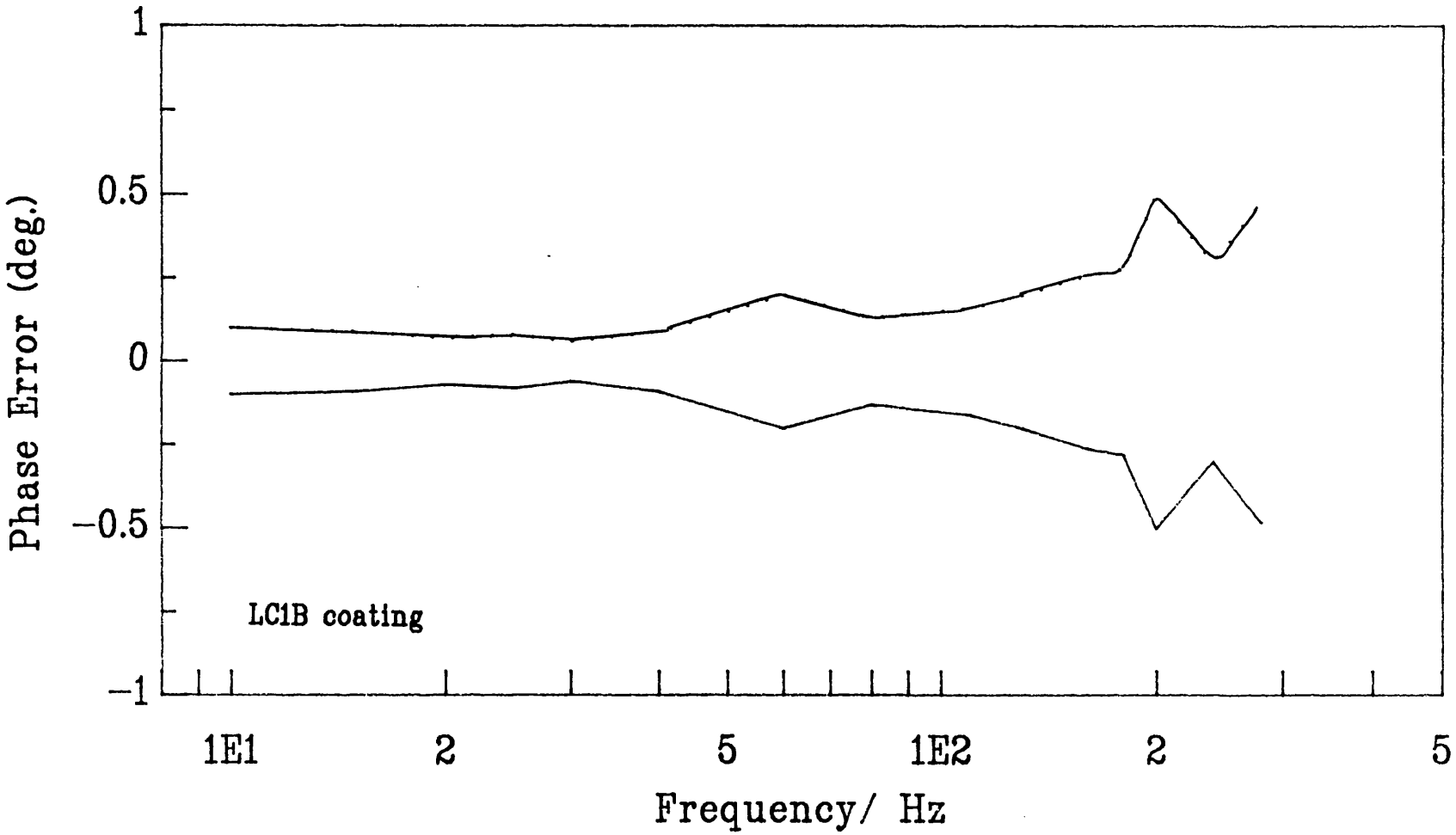

Figure 4.39: A plot of the phase angle error with frequency for spot measurements on an LC1B coating with an incident laser power of 3 watt and a lock-in integration time constant of 3 seconds.

Chapter 5

Discussion

CHAPTER 5 DISCUSSION

5.1 SYSTEM PERFORMANCE ARGON ION LASER VERSES LASER DIODE PTR SYSTEM

Both laser sources proved satisfactory in providing sufficient optical heating for photothermal NDT of plasma sprayed coatings. From the practical experience gained in using both these laser systems table 5.1 compares and contrasts their performance. Particular attention is given to the portability of the laser system, its maintenance requirements and the necessity of any auxiliary equipment. The compactness of the laser diode system favours its usage in a portable inspection system. Further advantages of this laser system over the argon ion laser include limited maintenance costs, elimination of water cooling and special power supply requirements, longer laser life and direct modulation of laser beam intensity. The maintenance costs of this laser system are low because only electronic circuits are required to be maintained. The need for a special maintenance contract for the laser is not necessary.

The main deficiencies of the laser diode system are the invisibility of the laser radiation, its limited power range and the high beam divergence (for the system presently evaluated). The argon ion laser system does not suffer from these problems. However due to its physical size and constraints imposed by water cooling a test system based on this laser source would be more suitable for inspecting components which can be brought to the laser rather than vice versa. If

the laser power requirement was below half a watt then air cooled argon ion laser could be chosen to be used in a portable inspection system.

Over the five years in using the argon ion laser system several problems related to water cooling were noted. Scale build up around the laser tube presents a potentially serious problem. If the scaling is not removed then over heating of the laser tube can lead to its fracture. Although replacements tubes are available, they are expensive, up to £8,000. Another problem with the water cooling system is the frequent necessity of cleaning water filters which would make a continuous operation of the test system difficult. Both these problems can be overcome by using a special water supply system.

The laser power requirement for inspecting sprayed coatings can range from a few watts for an unaided IR detector to a few hundred milliwatts for a well optimised IR detection system. Using a lower laser power also provides further advantages for the inspection system. A wide range of alternative low powered laser sources can be used for sample heating. The laser hazard risk to the operator and related personnel are reduced. It may also be easier for the inspection system to meet the laser safety regulations for industrial usage.

INFRARED DETECTOR

The convenience of operating the pyroelectric TGS IR detector at ambient temperatures, in almost any orientation, its short physical size and high

sensitivity ideally suited its usage in the photothermal testing system. This detector was also observed to have excellent low frequency electronic noise which was an essential requirement if low diffusivity coatings were to be inspected. One short coming of the sensor was its long term stability. It was observed that over a period of 18 months the detector gradually became insensitive and noisy. It became necessary to replace the detector. The problem with the sensor appears to be moisture pick-up by the TGS element[1].

5.2 APPLICATION TO NDT OF SURFACE COATINGS

The experiments reported in chapter 4 demonstrates the capability of photothermal method for thickness gauging and defect detection. Table 5.1 summarises studies reported in this research work and in the published literature of measurements on plasma sprayed coatings made with the periodic optical heating technique with infrared detection.

For thickness measurements the following requirements are essential.

1) A significant thermal impedance mismatch between the coating and the substrate.

2) The experimental phase angle noise averaged over a finite area on the test sample is less than the required thickness resolution.

The first condition is necessary for thermal wave interference effects to occur and hence make thickness measurements theoretically possible. The second

1 Manufactures report, Mullard, Southampton.

condition sets the minimum thickness that can be reliably measured with the system. The thickness sensitivity of the thermal interference technique improves as the magnitude of the thermal wave reflection coefficient increases. Results presented in the previous chapter have indicated that thickness sensitivities better than 25 μm/ degree are readily attainable for LC1B coating on stainless steel (see figures 4.36). The minimum detectable thermal wave reflection coefficient magnitude with the argon ion based test system developed in this work would be about 0.1, assuming that the phase noise of the test sample is less than 1 degree.

Coating properties that limit accurate thickness measurements include surface roughness, thickness fluctuations and changes in the subsurface thermal microstructure resulting from porosity, foreign inclusions etc. Phase angle measurements on fine and rough as-sprayed LC1B coatings have shown that the phase is perturbed by the surface roughness. Thus showing that care must be taken in using calibration curves for thickness measurements on rough surfaces. Accurate thickness values will only be obtained from sample of similar surface roughness.

A variety of subsurface conditions have been detected with this photothermal technique: porosity, partial contact between coating and substrate and completely separated interfaces. Defects as represented by the latter two examples have a

characteristic phase locus with increasing modulation frequency: a phase advance going to a phase lag. The visibility of subsurface defects was discussed theoretically in chapter 2. For thin laminar defect parallel to the surface, the phase contrast was predicted to be large when the defect is sandwiched in a high thermal effusivity material. Submicron defect thicknesses were also predicted to be readily detectable. The visibility of defects at depths greater than 1.5 thermal diffusion length of the surface layer is poor for all defect thicknesses. In summary the main requisites for defect detection are given below.

1) The modulation frequency must make the thermal diffusion length larger than the defect depth.

2) Several frequency measurements are made to distinguish the observed phase angle variations from thickness and microstructure related changes.

3) The sample phase angle noise is less than the minimum defect thickness to be sensed.

For defects of finite widths it has been theoretically shown that they may be detectable up to a depth equal to its diameter [71]. This prediction appears to valid for the disc shaped defects tested in 4.3.2.

5.3 FURTHER DEVELOPMENTS

Two intrinsic limitations of modulated PTR are the slow inspection rate, typically few seconds/ point and the necessity of making several frequency measurements to differentiate between thickness and defect related

phase changes. As noted in section 1.3.1, surface inspection rates may be increased by employing an area wide lock-in detection technique. To overcome the second difficulty Mandelis etal [88,89] have recently shown that by applying a frequency chirp excitation for photothermal heating, both the frequency and time domain response of layered samples can be obtained simultaneously in a relatively short period of time. Other advantages of this excitation method include:

a) conventional lock-in single frequency measurements can also be measured with the same equipment,
b) a pulsed laser is not required to obtain transient thermal propagation information, and
c) reduced sample heating due to sequential deposition of laser energy.

This alternative excitation technique appears to have a greater potential for full quantitative materials characterisation and NDT. Both these characteristics are urgently sought after in future inspection systems.

Table 5.1: A summary of PTR measurements on plasma spyayed coatings.

	MEASUREMENT				
Coating/ Substrate System	Frequency Hz	Thickness μm	Thermal Diffusivity $x10^{-6}$ m^2/s	Defects	REF.
Mo	15	200-610	6.5		24
NiAl/ MS	28	15-490	4.4		24
Al/ MS	4-180	490		Interface	66
Al_2O_3/ MS	16	0-400	2.2	Interface	8
ZrO_2-Y_2O_3/ Nickel superalloy	0.35	50-1000	0.1		90
LC1B/ SS	10,25	50-250	1.26	Interface, Porosity	22
WC + Co/ Ti	36	50-400	3		91

. MS Mild Steel
. SS Stainless Steel

Table 5.2: A comparsion and performance of the gas and semiconductor lasers for sample heating.

	Argon ion laser	GaAlAs Laser Diode
Laser beam visibility	Yes	No
Laser power range (Watt)	0 to 5	0.05 to 0.3
Useful life time	Up to 1500 hrs	10,000 hrs
Special requirements	Filtered water supply, water cooling, and 3 phase power supply.	None
Laser system portability	No	Yes
Maintenance costs	High (Replacement tube)	Low
System cost/ mW		8x the Argon ion system
Signal Magnitude	3x the Laser diode	
Phase angle noise (at 0.3 Watt)	< 0.5 degrees	< 0.5 degrees

Appendix

Appendix 1

1 THERMAL WAVE REFLECTION AND TRANSMISSION COEFFICIENTS.

Assume that the boundary separating two media (1,2) is the plane x=0, and that the incident, reflected and transmitted plane thermal wave makes the angle Ω_i, Ω_r and Ω_t with respect to the x-axis, as shown in figure 1. Let the expression for the plane thermal waves, τ_i, τ_r and τ_t, the incident, reflected and transmitted waves be given by:

$$\tau_i = Ae^{-\sigma_1 x\cos\Omega_i - \sigma_1 y\sin\Omega_i + j\omega t} \tag{1a}$$

$$\tau_r = ARe^{\sigma_1 x\cos\Omega_r - \sigma_1 y\sin\Omega_r + j\omega t} \tag{1b}$$

$$\tau_t = ATe^{-\sigma_2 x\cos\Omega_t - \sigma_2 y\sin\Omega_t + j\omega t} \tag{1c}$$

where A is the initial amplitude of the incident thermal wave; R and T are the thermal wave reflection and transmission coefficient at the interface x=0.

For the continuity of temperature at the interface x=0, we have:

$$Ae^{-\sigma_1 y\sin\Omega_i} + RAe^{-\sigma_1 y\sin\Omega_r} = ATe^{-\sigma_2 y\sin\Omega_t} \tag{2}$$

Since this condition must be true for all y position, the exponents in the above equation must be all equal. Thus we have

$$\sigma_1 y\sin\Omega_i = \sigma_1 y\sin\Omega_r = \sigma_2 y\sin\Omega_t \tag{3}$$

from which the law of reflection and refraction follows:

(3a) $\Omega_t = \Omega_r$ law of reflection

(3b) $\sigma_1 y \sin\Omega_t = \sigma_2 y \sin\Omega_t$ Snell's law

For continuity of flux at the interface the following equation is obtained:

(4) $$k_1\sigma_1\cos\Omega_t - Rk_1\sigma_1\cos\Omega_r = Tk_2\sigma_2\cos\Omega_t$$

as $\Omega_i=\Omega_r$ and I=(1-R) (at y=0), the thermal wave reflection and transmission coefficient can be written as:

(5a) $$R = \frac{k_1\sigma_1\cos\Omega_t - k_2\sigma_2\cos\Omega_t}{k_1\sigma_1\cos\Omega_t + k_2\sigma_2\cos\Omega_t}$$

(5b) $$R = \frac{\cos\Omega_t - b\cos\Omega_t}{\cos\Omega_t + b\cos\Omega_t}$$

(5c) $$T = \frac{2k_2\sigma_2\cos\Omega_t}{k_1\sigma_1\cos\Omega_t + k_2\sigma_2\cos\Omega_t}$$

(5d) $$T = \frac{2b\cos\Omega_t}{\cos\Omega_t + b\cos\Omega_t}$$

where b= $k_2\sigma_2/k_1\sigma_1$. For normally incident thermal waves, $\Omega_i=0$, the reflection and transmission coefficients at x=0 reduce to:

(6) $$R = \frac{1-b}{1+b} \quad \text{and} \quad T = \frac{2b}{1+b}$$

Appendix 2

1 ONE DIMENSIONAL COMPLEX SURFACE TEMPERATURE DERIVATION.

1.1 THIN OPTICALLY ABSORBING LAYER ON A NON-ABSORBING SEMI-INFINITE SUBSTRATE.

Consider a plane periodic optical source illuminating a layered sample with intensity I_o at an angular frequency w:

$$(1) \qquad I = \frac{I_o}{2}[1 + \exp(j\omega t)].$$

The surface temperature of the sample can then be written as the sum of three temperatures:

$$(2) \qquad T = T_o + T_{dc} + T_{ac}$$

where T_o, T_{dc} and T_{ac} are, respectively, the ambient, steady state and periodic temperature of the sample. To derive the periodic surface temperature of a thin optically absorbing layer on a nonabsorbing semi-infinite substrate we proceed as follows. Let r, ß , and n be the surface reflectivity, the bulk optical absorption coefficient and the light-to-heat conversion efficiency, respectively, of medium 1. Assume that heat flow is one dimensional and that the surface layer is in perfect thermal contact with the substrate. Let k_i ,c_i, α_i and σ_i be the thermal conductivity, the specific heat, thermal diffusivity and thermal wavevector of material i, i=0,1 and 2, (see fig. 2). The thermal diffusion equation in each of the media take the form:

(3) $$\frac{\partial^2 T_i(x,t)}{\partial x^2} - \frac{1}{\alpha_i}\frac{\partial T_i(x,t)}{\partial t}$$

$$= \frac{\dot{H}(x,t)}{k_1} \qquad \text{layer 1}$$

$$= 0 \qquad \text{layer } 0,2$$

where H is the net heat density produced at a point x in the sample. If light is exponentially absorbed in the sample (Beer's Law) then H is given by:

(4) $$\dot{H}(x,t) = \frac{(1-r)\eta\beta_1 I_o \exp(\beta_1 x)}{2} Re[1+\exp(j\omega t)]$$

Since I and hence T are harmonic in time;

(5) $$T_i(x,t) = T_i(x)\exp(j\omega t)$$

the above thermal diffusion equations can be rewritten as:

layer 0

(6a) $$\frac{\partial^2 T_o(x,\omega)}{\partial x^2} - \left(\frac{j\omega}{\alpha_o}\right) T_o(x,w) = 0 \qquad x \geq 0$$

layer 1

(6b) $$\frac{\partial^2 T_1(x,\omega)}{\partial x^2} - \left(\frac{j\omega}{\alpha_1}\right) T_1(x,w) = -\frac{\dot{H}(x,\omega)}{k_1} \qquad -L \leq x \leq 0$$

layer 2

(6c) $$\frac{\partial^2 T_2(x,\omega)}{\partial x^2} - \left(\frac{j\omega}{\alpha_2}\right) T_2(x,w) = 0 \qquad x \leq -L$$

The equations 6a-6c are coupled via the boundary conditions of temperature and heat flux continuity at all the interfaces:

$$T_i(\omega, \text{boundary}) = T_j(\omega, \text{boundary}) \tag{7a}$$

$$k_i \partial \frac{T_i(\omega, boundary)}{\partial x} = k_j \partial \frac{T_j(\omega, boundary)}{\partial x} \tag{7b}$$

The time dependant solutions to equation 6 for the periodic temperature distribution in the sample are given by the equations:

layer 0

$$T_0(x,\omega) = C_1 \exp(-\sigma_0 x) \tag{8a}$$

layer 1

$$T_1(x,\omega) = C_2 \exp(\sigma_1 x) + C_3 \exp(-\sigma_1 x) + \frac{(1-r) I_0 \exp(\beta_1 x)}{2k_1(\sigma_1^2 - \beta_1^2)} \tag{8b}$$

layer 2

$$T_2(x,\omega) = C_4 \exp(\sigma_2 x) \tag{8c}$$

The quantity of interest is the function for the temperature field at the surface of medium 1, $T_1(w,0)$. This can be determined by evaluation the coefficient C_1 subject to the boundary conditions of equation 7, which yield the following matrix equation:

$$(9)\qquad \begin{bmatrix} 1 & -1 & -1 & 0 \\ 1 & b_o & -b_o & 0 \\ 0 & X^{-1} & X & -Y^{-1} \\ 0 & X^{-1} & -X & -b_1 Y^{-1} \end{bmatrix} \begin{bmatrix} C_1 \\ C_2 \\ C_3 \\ C_4 \end{bmatrix} = \begin{bmatrix} -E \\ b_o r_1 E \\ EB \\ r_1 EB \end{bmatrix}$$

$$(9a)\qquad \text{or} \qquad [A][C]=[B]$$

and

$$(10)\qquad b_i = \frac{k_i \sigma_i}{k_{i-1}\sigma_{i-1}} \quad , \qquad i = 1,2$$

$$(11)\qquad X = \exp(\sigma_1 L_1) \qquad \text{and} \qquad Y = \exp(\sigma_2 L_1)$$

$$(12)\qquad E = \frac{(1-r)\eta I_o \beta_1}{2k_1(\beta_1^2 - \sigma_1^2)} \qquad \text{and} \qquad EB = E \cdot \exp(-\beta_1 L_1)$$

The solution of the matrix equation 9 is

$$(13)\qquad [C]=[A]^{-1}[B]$$

from which the periodic surface temperature, T_{ac}, follows on evaluating the coefficient C_1 [1]:

$$(14)\qquad T_{ac} = \frac{(1-r)\eta\beta I_o}{2k\sigma(1-\Gamma_0 \Gamma e^{-2\sigma L})} \left[\frac{1-e^{-(\beta+\sigma)L}}{\beta+\sigma} + \Gamma e^{-2\sigma L} \frac{1-e^{-(\beta-\sigma)L}}{\beta-\sigma} \right]$$

1 the suffix 1 referring to the surface layer material properties has been relaxed.

where Γ is the thermal wave reflection coefficient at the layer / substrate interface, $\Gamma=(1-b_{e1})/(1+b_{e1})$ and Γ_e the reflection coefficient at the layer/ air interface, Γ_e = unity for solid-air interface. For an optically opaque surface layer , $\beta_1 L_1 >>1$, equation 14 reduces to:

$$(15) \qquad T_{ac} = \frac{(1-r)I_o}{2k\sigma}\left[\frac{1+\Gamma e^{-2\sigma L}}{1-\Gamma e^{-2\sigma L}}\right]$$

1.2 THERMAL CONTACT RESISTANCE.

The above solution for the periodic surface temperature applies to a thin optically absorbing layer in perfect thermal contact with a nonabsorbing thermally thick substrate. If the layer/ substrate interface is partially bonded then the interface will present a thermal resistance to heat flow. The periodic surface temperature must now be obtained by introducing a 'thermal contact resistance' term, R, to the temperature continuity boundary condition of equation 7a:

$$(16) \qquad T_1(-L_1,\omega) = T_2(-L_1,\omega) + R'k_2\frac{\partial T_2(-L_1,\omega)}{\partial x}$$

The solution for T_{ac} takes the same form as equation 14 but with Γ replaced with:

$$(17) \qquad \Gamma = \frac{1-b_1+R'k_2\sigma_2}{1+b_1+R'k_2\sigma_2}$$

hence making the layer / substrate thermal wave reflection coefficient both complex and frequency dependant.

1.3 AIR GAP DEFECT.

If the layer /substrate interface is locally separated such that an air gap is sandwiched between the layer and the substrate, then the periodic surface temperature can be obtained by solving the heat diffusion equation with periodic boundary conditions of temperature and flux continuity at the air / layer ,layer /air and air / substrate interfaces, see figure 3. The solution for the surface temperature requires the simultaneous solution of six equations which on solving gives for the surface temperature:

$$(18) \qquad T_{ac} = \frac{(1-r)\eta I_o}{2k_1\sigma_1}\left[\frac{1+\Gamma e^{-2\sigma_1 L_1}}{1-\Gamma e^{-2\sigma_1 L_1}}\right]$$

where Γ is defined as:

$$(19) \qquad \Gamma = \frac{\Gamma_1 + \Gamma_2 e^{-2\sigma_2 L_2}}{1+\Gamma_1\Gamma_2 e^{-2\sigma_2 L_2}}$$

$$(20) \qquad \Gamma_1 = \frac{1-b_1}{1+b_1} \qquad \text{and} \qquad \Gamma_2 = \frac{1-b_2}{1+b_2}$$

This representation for T_{ac} is identical in form to the surface temperature expression for an optically opaque

layer on a semi-infinite substrate, see equation 15. Also, as with the thermal contact resistance model, a complex and frequency dependant thermal wave reflection coefficient is obtained for the interface defect.

1.4 STEADY STATE TEMPERATURE: OPAQUE SEMI-INFINITE LAYER.

The steady state , T_{dc}, temperature rise of the sample can also be obtained in a similar manner as that for an absorbing layer on a transparent substrate by putting w=0 in equation 6 and then solving the time independent heat diffusion equations using the boundary conditions of temperature and flux continuity. The solution for the steady state temperature is then given by the expression:

$$(21) \qquad T_{dc} \approx \frac{(1-r)I_o}{2}\left[\frac{L_1}{k_1}-\frac{L_2}{k_2} - \left\{\frac{1-\exp(-\beta_1 L_1)}{k_1\beta_1}+\frac{L_2\exp(-\beta_1 L_1)}{k_2}\right\}\right]$$

For an opaque insulator on a conducting substrate this equation simplifies to:

$$(22) \qquad T_{dc} \approx \frac{(1-r)I_o L_1}{2k_1}$$

Appendix 3

1 EFFECTIVE THERMAL CONDUCTIVITY OF A GAS TRAPPED BETWEEN NARROWLY SPACED PARALLEL PLATES.

There are two distinct modes of gas heat conduction; the molecular heat transfer and continuum heat transfer. In the molecular regime, collisions occur between gas molecules much less frequently then between the gas molecules and the 'hot' or 'cold' surfaces. In this regime molecular heat transfer is directly proportional to the system pressure and is also influenced by the accommodation coefficient, α, which can be defined as the energy exchanged between a molecule and a surface with respect to the maximum energy exchange possible.

In the continuum regime heat conduction is relatively independent of pressure and also has the maximum thermal conductivity. The basic equation for the thermal conductivity of a gas is[1] :

(1) $$K_g = \epsilon \eta C_v$$

$$\epsilon = (9\delta - 5)/4$$

$$\eta = \rho v \lambda / 2$$

$$C_v = R_o / M(\gamma - 1)$$

where

ϵ is a constant,
n is the viscosity coefficient,
C_v is the specific heat.
γ is the specific heat ratio,
ρ is the density,
v is the mean speed,

1 N.V. Tsederberg. Thermal conductivity of gases and liquids. (M.I.T. Press, 1965) Chap. IV.

λ is the mean free path,

R_o is the universal gas constant, and

M is the molecular mass.

By substitution,

$$K_g = \epsilon \rho C_v v \lambda / 2. \quad (2)$$

Defining the mean free path λ as[2]

$$\lambda = \left[\left(\frac{1}{\lambda_p} \right) + \left(\frac{1}{L} \right) \right]^{-1} \quad (3)$$

where λ_p is the particle to particle path length (= kT/$\sqrt{2}$ σ P), k is the Boltzmann constant , σ is the collision cross-section, and L the system characteristic dimensions (volume/ area).

By substitution,

$$K_g = \frac{\epsilon \rho C_v v}{2(1/\lambda_p + 1/L)} \quad (4)$$

This equation allows calculation of the gas thermal conductivity over the range from molecular transfer regime to continuum. Equation 4 assumes an accommodation coefficient of 1 for all the surfaces. In general α lies in the range 0 to 1. To account for this coefficient, the factor F is introduced as follows:

$$K_g = \frac{\epsilon \rho C_v v}{2(1/\lambda_p + F/L)} \quad (5)$$

F represents a accommodation factor resembling the emissivity factor in radiative heat transfer. For parallel plates of equal size, F is given by

$$F = \frac{1}{\alpha_1} + \frac{1}{\alpha_2} - 1 \quad (6)$$

---

2 H.M. Strong etal, J. Appl. Phys. 31 p43 (1960)

From equation 4 or 5 it can be seen that for large separation , L, the thermal conductivity approaches that of the bulk value. When gas is trapped between surfaces with separation approaching the mean free path , then the thermal conductivity of the gas can be reduced significantly. For example for L=0.1μm , and $\alpha = \alpha = 0.5$, the gas thermal conductivity is reduced by 25% from its bulk value:

$$K_g = K_o / \left(1 + \frac{F\lambda}{L} \right) \qquad (7)$$

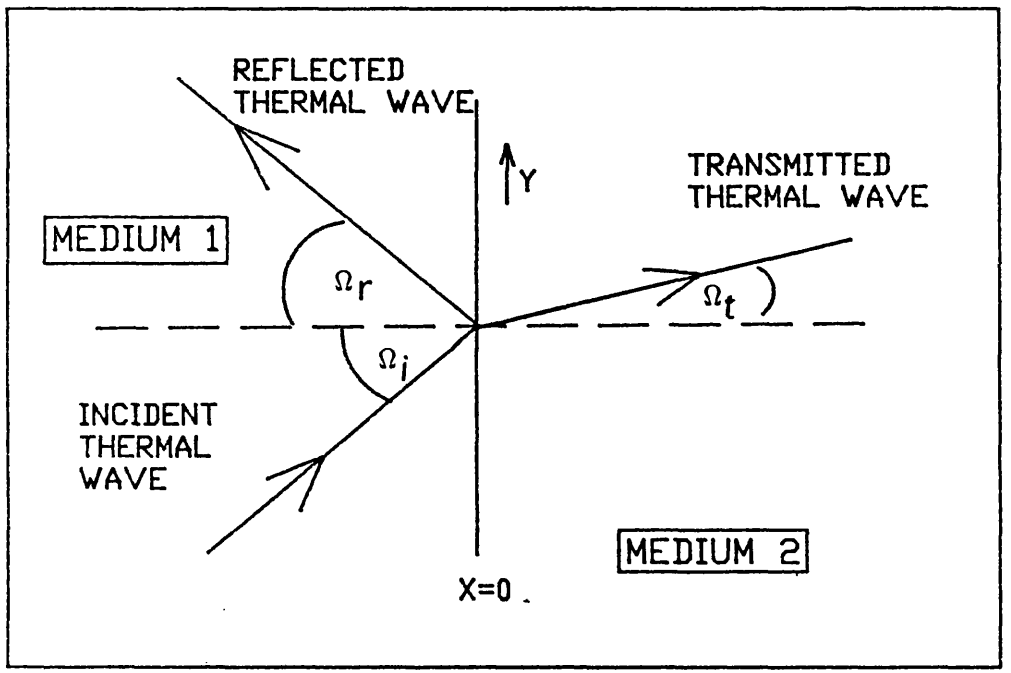

Figure 1: Reflection and refraction of plane thermal waves.

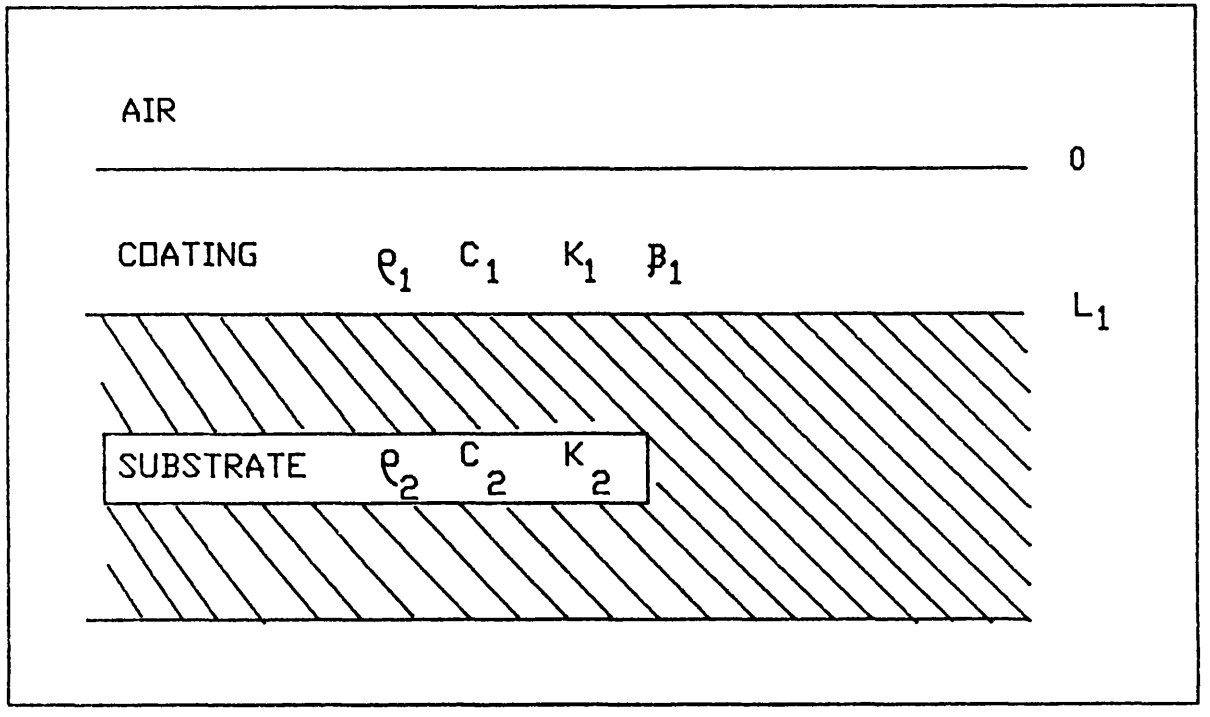

Figure 2: Modelled coating/ substrate system.

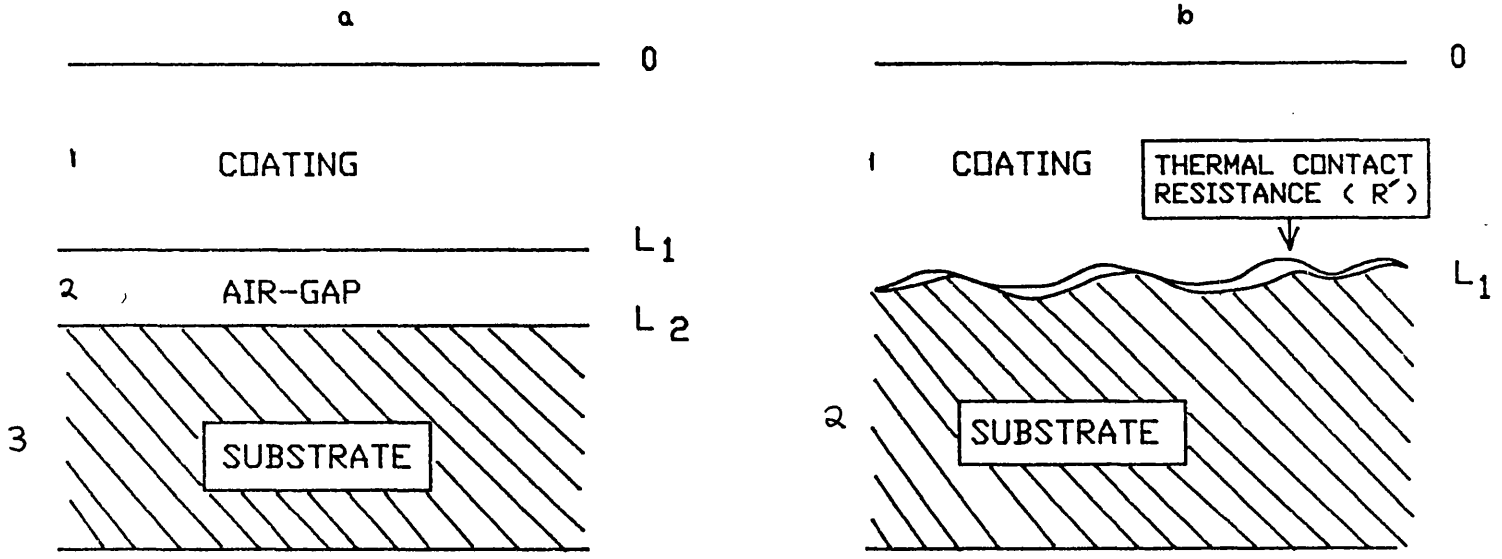

Figure 3: a) Air gap and b) thermal contact resistance interface defects.

References

REFERENCES

1 Proc. 11th Int. Conf. Thermal Spraying (ITSC).
8- 12th Sept. 1986. Montreal, Canada.

2 Eds, I. Kvernes, W.J.G. Bunk and J.G. Wurm
Proc. Advanced Material Research and Development for Transport Ceramic Coatings for Heat Engines." 26-28th Nov., Strasborg, France. (1985)
ISBN 2-86883-024-2

3 Ed, E. Lang
"Coatings for high temperature applications."
Appl. Sci. Pub. (U.K), ISBN 0-85334-221-0 (1983)

4 Anon
"Sprayed coatings.", Chapter 10.
From: Wear resistant surfaces in Engineering.
HMSO Publications. ISBN 0-11513826-9

5 Ed, E.A. Ash
"Scanned Image Microscopy".
Academic Press, England (1980)

6 G. Busse
"Photothermal transmission probing of a metal."
Infrared Phys. 20 p419-422 (1980)

7 M. Luukkala, A. Letho, J. Jaarinen and M. Jokien
"Photothermal imaging and thermal surface waves as a NDT tool for coatings."
IEEE Ultrasonic symp. p591-594 (1982)

8 D.P. Almond, P.M. Patel, H. Reiter
"Potential value of photothermal imaging for the testing of plasma sprayed coatings."
J. de Phys. 44(10) p491-493 (1983)

9 M. Egee, R. Dartois, J. Marx and C. Bissieux
"Analysis of semi-transparent layered material by modulated photothermal radiomerty: Application to the bonding and thickness control of enamel coating.
Can. J. Phys. 64(4) p1297-1302 (Sept 1986)

10 A.C. Tam and B. Sullivan
"Remote sensing application of pulsed photothermal radiometry."
Appl. Phys. Lett. 43(4) p333-335 (Aug 1983)

11 P. Cielo
"Pulsed plotothermal evaluation of layered materials."
J. Appl. Phys. 56(1) p230-234 (July 1984)

12 R.E. Imhof, D.J.S. Birch, F.R. Thornley, J.R. Gilchrist and T.A. Strivens
"Optothermal transient emission radiometry."
J. Phys. E: Sci. Instrum. 17 p521-525 (1984)

13 D.R. Green, M.D. Schmeller and R.A. Sulit
"Thermal NDE method for thermal sprayed coatings."
Proc. IEEE Oceans 1982. Pub: Marine Technology Society.

14 C.S. Welch, D.M. Heath and W.P. Winfree
"Quantitative thermal characterisation of thin plates."
Rev. Prog. QNDE 58 p1133-1139 (1986)

15 W. Reynolds and G.M. Wells
"Video-compatible thermography."
Brit. J. NDT 26(1) p40-44 (Jan 1984)

16 P. Cielo, R. Lewak and D.L Balageas
"Thermal sensing for industrial quality control."
Proc. SPIE (Thermosense VIII) p47-54 (1986)

17 D.L. Balageas, A.A. Deom and D.M. Boscher.
"Characterisation and nondestructive testing of carbon-epoxy composites by a pulsed photothermal method."
Mat. Eval. 45(4) p461-465 (April 1987)

18 K. Kobayasi and T. Kumada
"A method of measuring thermal diffusivity by heating of step function change."
J. Atom. Energy Sco. Jpn. 9 p58-64 (1967)

19 R.R. Bittle and R.E. Taylor.
Step Heating technique for thermal diffusivity measurement of large-grained hetergeneous materials."
J. Am. Soc. Cerm. 67(3) p186-190 (Mar 1984)

20 A. Letho, M.Jokein, J.jaarinen, T.Tiusanen and M. luukkala
"Alternating beam method (ABM) in photothermal microscopy..."
Elect. Lett 17(15) p540-541 (July 1981)

21 I. Kaufaman and A.K. Choudhrgy
"Radiomertic crack detection in moning surfaces."
Appl. Phys. Lett. 46(2) p152-154 (Jan 1985)

22 D.P. Almond, P.M. Patel, I.M. Pickup and H. Reiter
"An evaluation of the suitability of thermal wave interferometry for the testing of plasma sprayed coating.
NDT Int. 18(1) p17-21 (1985)

23 G. Busse and K.F. Renk
"Steroscopic depth analysis by thermal wave transmission for nondestructive evaluation."
Appl. Phys. Lett. 42(4) p366-368 (Feb 1983)

24 P.M. Patel and D.P. Almond
"Thermal wave testing of plasma sprayed coatings and a comparsion of the effect of coating microstructure on the propagation of thermal and ultrasonic waves."
J. Mat. Sci 20(3) p955-966 (March 1985)

25 F. Gitzhofer, C. Martin and P. Fauchais
"Controle par thermographie infrarouge de l'apparition de fissures dans un materiau ceramique projecte par plasma et soumis a un cyclage thermique."
Rev. Gen. Therm (Fr) 26(301) p63-69 (Jan 1987)

26 J.M. Milne and W.N. Reynolds
"The nondestructive evaluation of composited and other materials by thermal pulse video thermography."
Proc. SPIE 520 (Thermosence VII) p119-122 (1984)

27 P. Cielo, X. Maldague, A.A. Deom and R. Lewak
"Thermographic nondestructive evaluation of industrial materials and structures.
Mat. Eval. 45(4) p452-460,465 (April 1987)

28 T.S. Durrani, F. Lotti, K. Boyle, R. Abdel-Aal and A. Hall
"Computer-aided thermal imaging technique for the inspection of composites material."

Esprit 1984: Status report of ongoing work.
Eds, J. Roukens and J.F. Renualt.
Elsevier Sci. Pub. (1985)

29 N. Mikoshiba, H.Nakamura and T.Tsubouchi
"Nondestructive observation of defects in semiconductors with photoacoustic and photothermal radiation microscopes."
IEEE Ultrasonic symp. p651-655 (1984)

30 S.J. Sheard.
"A new configuration for photothermal radiometric microscopy."
IEEE Ultrasonic Symp. p789-792 (1986)

31 R. Vanzetti, A.C. Traub and A.A. Richard
"Laser inspection of soldered joints."
Brazing and soldering 2 p34-37 (1982)

32 S.O. Kanstad and P.-E. Nordal.
"Photoacoustic and photothermal technique for powder and surface spectroscopy."
Applic. Sur. Sci. 6(3-4) p372-91 (1980)

33 J. Marx, C. Droulle, M. Egee, E. Van Schel, F. Potler and G. Potron
"Hemotological parameters effects on the PTR signal during the blood sedimentation."
Rev. Gen. Therm (Fr) 26(301) p (Jan 1987)

34 P.-E. Nordal and S.O. Kanstad
"Visible light spectroscopy by photothermal radiometry using an incoherrent source."
Appl. Phys. Lett. 38(7) p486-488 (April 1981)

35 W.P. Leung and A.C. Tam
"Technique of flash radiometry."
J. Appl. Phys. 52(1) p153-161 (July 1984)

36 Eds, S.G. Burnay, T.L. Williams and C.H.N. Jones.
"Applications of thermal imaging."
Pub. Inst. of Phys. ISBN 0-85274-421-8 (1988)

37 J.T. Luxon and D.E. Parker
"Industrial lasers and their applications." p200-202
Pub. Prentice-Hall, New Jersey (USA). ISBN 0-13-461369-4 (1985)

38 D.P. Almond and P.M. Patel
"Thermal wave imaging and testing." Chapter 8, p226-242.
ibid. ref 36.

39 J.L. Beaudoin, E. Merienne, R. Danjoux and M. Egee.
"Numerical systems for infrared scanners and applications to subsurface control of materials by photothermal radiometry."
Proc. SPIE. 590 p285-292 (1985)

40 P.K. Kuo, Z.J. Feng, T. Ahmed, L.D. Favro, R.L. Thomas and J. Hartikainen
"Parallel thermal wave imaging using a vector lock-in video technique."
Springer series in Optical sciences 58 p415-418 (1987)

41 D.R. Green, C.R. Wadling, M.D. Schmeller and R.A. Sulit
"Feasibility of thermal NDE methods for Naval thermal spray coatings."
Proc. American Soc. NDT Oct. 24th 1983, Dallas, Texas.
HEDL-SA-2986

42 D.R. Green, J.W. Voyles and J.H. Prati
"Automatic thermal impedance scanning (ATIS) system for the NDE of coatings on turbines engine parts."
HEDL -SA-3517-FP (March 1986)

43 R. Travis, C. Ginther and C. Zanis
"Infra-red thermal wave non-destructive evaluation of thermal sprayed coatings."
ibid ref 1. p309-314

44 P. Cielo
"Analusis of pulsed thermal inspection."
14th Symp. on NDE, San Antonio, Texas. April 19-21 1983

45 R.E. Talyor and K.D. Maglic.
"Pulse method for thermal diffusivity measurement. Chapter 8."
Ed., K.D. Maglic, A. Cezairliyan and V.E. Peletsky.
Plenun Press, ISBN 0-306-41424-4 (1984)

46 P. Cielo and S. Dallarie
"Optothermal NDE of thermal barrier coatings."
Proc. AMS metal Congress 12-17th Oct. 1985

47 D.R. Maley
"Two thermal non-destructive testing techniques."
Proc. SNT Spring Conf. (1965)

48 E.J. Kubiak
"Infrared detection of fatigue cracks and other near surface defects."
Appl. Opt. 7(9) p1743-1747 (Sept 1968)

49 P.K. Kuo, I.C. Oppenheim, L.D. Favro, Z.J. Feng and R.L. Thomas
"Time-resolved IR Video imaging with syncronised scanned laser heating."
Springer series in Optical sciences 58 p496-499 (1987)

50 I. Kaufman, P. Chang, A.K. Choundry, R.L. Choudary, D. Shyang and J.R. Sch
"Radiometric detection of cracks on metallic surfaces."
11th World Conf. on NDT p427-434 (1986)

51 F.E. Alzofon
"Retardation and diffraction aspects of the conduction of heat in solids."
Am. J. Phys. 30 p285-293 (1962)

52 P.E. Nordal and S.O. Kanstad
"New developments in photothermal radiomerty."
Infrared Phys. 25(1/2) p295-304 (1985)

53 F.C. Incropera and D.C, De Witt
"Fundamentals of heat and mass transfer." 2nd Edition
Pub: John Wiley and Sons, London. ISBN 0-471-82561-1 (1985)

54 H.S. Carlsaw and J.C. Jaeger
"Conduction of heat in solids". p64-69
Pub: Oxford, Clarendon (1959)

55 G. Green
"Some problems in heat conduction."
Phil. Mag. 3(7) p784-800 (1927)

56 A. Rosencwaig and A. Gersho
"Theory of the photoacoustic effect in solids."
J. Appl. Phys. 47(1) p64-69 (Jan 1976)

57 C.A. Bennet,Jr and R.R. Patty
"Thermal wave interferometry: a potential application of the photoacoustic effect."
Appl. Opt. 21(1) p49-54 (Jan 1982)

58 L.C. Aamodt and J.C. Murphy
"Photothermal measurements using a localised excitation source."
J. Appl. Phys. 52(8) p4903-4914 (Aug 1981)

59 H.C. Chow
"Theory of three dimensional photoacoustic effect with solids."
J. Appl. Phys. 51(8) p4053-4058 (Aug 1980)

60 F. Lepoutre, B.K. Bein and L.J. Inglehart.
"Three-dimensional calculation of the mirage effect with a personal computer."
Can. J. Phys. 64(9) p1037-1041 (Sept 1986)

61 M.V. Iravami and H.K. Wickramasinghe
"Scattering matrix approach to thermal wave propagation in layered structures."
J. Appl. Phys. 58(1) p122-132 (July 1985)

62 M. Beyfuss, R. Tilgner and J. Baumann
"Photothermal evaluation of layered samples with high accuracy based on 3-D analysis of thermal waves."
Springer series in Optical sciences 58 p392-395 (1987)

63 R.C. Progelhof, J.L. Thorne and R.R. Ruetsch
"Methods for predicting the thermal conductivity of composites systems: A review."
Poly. Eng. Sci 16(9) p615-625 (1976)

64 J. Baumann and R. Tilgner
"Determining photothermally the thickness of a burried layer."
J. Appl. Phys. 58(5) p1982-1985 (Sept 1985)

65 F. Lepoutre, D. Fouriner and A.C. Boccara.
"Nondestructive control of weldings using the mirage detection."
J. Appl. Phys. 57(4) p1009-1015 (Feb 1985)

66 P.M. Patel, D.P. Almond and H. Reiter
"Thermal wave detection and charactersation of subsurface defects."
Appl. Phys B43 p9-15 (1987)

67 P.M. Patel, D.P. Almond and H. Reiter
"Analysis of thermal wave reflectivity at rough surfaces in contact."
Springer series in Optical sciences 58 p430-434 (1987)

68 T. Tsukizoe and T. Hisakado
A.S.M.E., J. Lub. Technol. p81-88 (1968)

69 N.F. Haine
"Theory of sound propagation through contacting surfaces."
CEGB Report RD/B/N 4744 (1980)

70 L.J. Inglehart, K.R. Grice, L.D. Favro, P.K. Kuo and R.L. Thomas
"Spatial resolution of thermal wave microscopes."
Appl. Phys. Lett. 43(5) p446-448 (Sept 1983)

71 F.A. McDonald.
"Photoacoustic, photothermal and related techniques: A review."
Can. J. Phys. 64(9) p1023-1029 (Sept 1987)

72 G.C. Wetsel Jr, and F.A. McDonald
"Resolution and definition in photothermal imaging."
J. Appl. Phys. 56(11) p3081-3085 (Dec 1984)

73 F.A McDonald, G.C. Wetsel Jr., and S.A. Stotts
"Scanned photothermal imaging of subsurface structure."
Acoustical Imaging 12 p147-155 (1982)

74 F.A. McDonald and G.C. Wetsel, Jr.
"Resolution and definition in thermal imaging."
IEEE Ultrasonic symp. 622-628 (1984)

75 A. Mandelis
"Hamilton-Jacobi formulation and quantum theory of thermal wave propagation in solid state."
J. Math. Phys. 26(10) p2676-2683 (Oct 1985)

76 Coherent (UK) Ltd, Cambridge Science Park, Cambridge, England.

77 EG&G Instruments Ltd, Doncastle House, Bracknell, Berkshire, England.

78 Mullards Southampton, Millbrook Industrial Estates, Southampton, England.

79 EG&G Instruments Ltd, Doncastle House, Bracknell, Berkshire, England.

80 Ealing Electro-optics Plc., Greycaine Rd, Watford, Hert., England.

81 BS4803 Part 1,2 and 3. (1983).
Radiation safety of Laser Products and Systems.

82 OCLI Optical Coatings Ltd, Hilend Ind. Park, Dunfermilne, Fife, Scotland.

83 J.P. Bentley
"Principles of measurements systems,
Chapter 15: Thermal Radiation Measurements Systems."
Pub.: Longmans Group Ltd, London (1983)
ISBN 0-582-30506-3

84 Melles Griot Ltd, Culdrose House, Aldershot, Hampshire, England

85 Spectra-Physics Ltd, Boundary way, Hemel Hempstead, Herts, England

86 L.C. Ammodt and J.C. Murphy
"Sample edge effects."
Appl. Opt. 21(1) p111-115 (Jan 1982)

87 M. Moghisi and D.P. Almond
"An inexpensive computer-controlled ultrasonic C-scan system."
NDT. Int p9-12 (Feb 1983)

88 A. Mandelis
"Frequency modulated (FM) time delay photoacoustic and photothermal wave spectroscopies: Techniques, instrumentation, and detection. Part I, II, and III."
Rev. Sci. Instrum. 57(4) p617-635 (April 1986)

89 J. F. Power and A. Mandelis
"Photopyroelectric thin-film instrumentation and impulse respose detection. Part I, II and III."
Rev. Sci. Instrum. 58(11) p2018-2038 (Nov 1987)

90 D.P. Almond, P.M. Patel and H. Reiter
"The testing of plasma sprayed coatings by thermal wave interferometry."
Mat. Eval. 45 p471-475 (April 1987)

91 J. Morris, P.M. Patel, D.P. Almond and H. Reiter
"The influence of coating properties on the sensitivity of thermal-wave testing techniques."
Surface and Coatings Technology 34 p51-57 (1988)